Minimum Diagnosable Damage and Optimal Sensor Placement for Structural Health Monitoring

Alexander Mendler

Minimum Diagnosable Damage and Optimal Sensor Placement for Structural Health Monitoring

by

Alexander Mendler

B.Sc., The Technical University of Munich, 2013
M.Sc., The Technical University of Munich, 2016

A THESIS SUBMITTED IN PARTIAL FULFILLMENT OF
THE REQUIREMENTS FOR THE DEGREE OF

DOCTOR OF PHILOSOPHY

in

Civil Engineering

(Defended on December 11th, 2020)

THE UNIVERSITY OF BRITISH COLUMBIA

(Vancouver)

December 2020

The following individuals certify that they have read, and recommend to the Faculty of Graduate and Postdoctoral Studies for acceptance, the dissertation entitled:

Minimum Diagnosable Damage and Optimal Sensor Placement for Structural Health Monitoring

submitted by	Alexander Mendler	in partial fulfillment of the requirements for
the degree of	Doctor of of Philosophy	
in	Civil Engineering	

Examining Committee:

Dr. Carlos Ventura, Professor, Dept. of Civil Engineering, UBC, Canada
Supervisor

Dr. Michael Döhler, Researcher, I4S Team, Inria, France
Co-Supervisor

Dr. Clarence de Silva, Professor, Dept. of Mechanical Engineering, UBC, Canada
University Examiner

Dr. Tony Yang, Professor, Dept. of Civil Engineering, UBC, Canada
University Examiner

Additional Supervisory Committee Members:

Dr. Terje Haukaas, Professor, Dept. of Civil Engineering, UBC, Canada
Supervisory Committee Member

Dr. Reza Vaziri, Professor, Dept. of Civil Engineering, UBC, Canada
Supervisory Committee Member

Dr. Ruben Boroschek, Professor, Dept. of Civil Engineering, University of Chile, Chile
Supervisory Committee Member

Dr. Yavuz Kaya, SHM Engineer, Ministry of Transportation and Infrastructure, Canada
Supervisory Committee Member

Abstract

Structural health monitoring (SHM) can extend the operation of bridges beyond their original life span, increase the safety between scheduled inspections, and allow for a prioritized inspection after extreme events. One of the major challenges is to assess which damages can or cannot be diagnosed (i.e., detected or localized), which is essential to evaluate the value of a SHM system before it is installed, and to optimize the sensor placement accordingly.

This work develops a framework to predict the *minimum detectable damage*, i.e., the minimum change in local structural design parameters that can reliably be detected based on changes in global damage-sensitive features. The diagnosis is considered "reliable"' if the probability of false alarms is low and the probability of detection is high. Equivalently, a damage is "detectable" if it is significant under consideration of typical uncertainties related to ambient excitation and measurement noise and empirical safety thresholds. The approach requires vibration data from the undamaged structure in combination with a numerical model, and is universally applicable to a wide range of structures and damage-sensitive features. Secondly, a method is proposed to analyze the *minimum localizable damage*. The results show that optimal localizability is a compromise between high localization resolution, high detectability, and few false localization alarms. Thirdly, a sensor placement strategy is devised that takes as input the desired minimum diagnosable damage and optimizes the sensor layout and the number of sensors accordingly. The method allows one to focus the global damage diagnosis on local structural components. Ultimately, the monitoring of prestressing forces and support displacements is incorporated into the diagnostic framework, so that they can be analyzed and distinguished from changes in material properties or cross-sectional values.

Besides the performance evaluation, the framework is suitable for quality control of existing instrumentation on real structures. Therefore, self-validation strategies are implemented to verify the input parameters, to validate the theoretical assumptions, and to check its effectiveness based on non-invasive tests using extra masses. The proof of concept studies based on a laboratory steel beam and a cable-stayed bridge show promising results regarding the practical application of the theoretical contributions.

Lay Summary

The structural health of bridges can be analyzed through vibration measurements, where the primary goal is to detect the presence of damage. Damage localization is more challenging but can be achieved by combining the records with information from computer models of the examined structures. Before installing a monitoring system, it is crucial to know which damage scenarios can be detected and how small the minimum localizable damage is. The classical approach is to run a large number of numerical simulations (in the damaged state) or to perform elaborate laboratory experiments. However, this work derives a theoretical formula to predict the minimum diagnosable damage based on the undamaged state. This formula finds numerous practical applications: it helps to analyze the minimum diagnosable damages, to find the optimal sensor layout, to perform quality control checks on existing instrumentation, and to evaluate the value of structural health monitoring in general.

Preface

The work presented in this thesis was conducted by Alexander Mendler under the supervision of Dr. Carlos Ventura at the University of British Columbia (UBC) in Canada, and the co-supervision of Dr. Michael Döhler at the National Institute for Research in Computer Science and Automatic Control (Inria) in France. In the framework of a software license agreement, Inria provided the "SSDDL - Stochastic Subspace-based Damage Detection and Localization," which is a MATLAB® library for the detection and localization of damage based on subspace techniques. The copyright and all other intellectual property rights remain with Inria. During his Ph.D. program, Alexander Mendler spent six-months at the Inria research centre in Rennes, were he worked in close collaboration with the mathematicians Dr. Döhler and his Team Leader Dr. Mevel.

[1] A version of Chapter 5, Section 5.1 has been published [Mendler A., Allahdadian, S., Döhler M., Ventura C., Mevel L. (2019, May), Minimum detectable damage for stochastic subspace-based methods. In Proceedings of the IOMAC - 8th International Operational Modal Analysis Conference, Copenhagen, Denmark. pp.1-11]. Mr. Mendler was responsible for data collection and analysis, validation, and manuscript composition. The work is a continuation of the research by Dr. Allahdadian, who was involved in early stages of concept formation. All supervisory authors were involved throughout the project from concept formation to manuscript edits. Dr. Ventura provided funding.

[2] Another version of Chapter 5, Section 5.1 to 5.2 has been published [Mendler A., Döhler M., Ventura C., Mevel L. (2021). A reliability-based approach to determine the minimum detectable damage for statistical damage detection. Mechanical Systems and Signal Processing]. Mr. Mendler was responsible for data collection and analysis, validation, and manuscript composition. All supervisory authors were involved throughout the project from concept formation to manuscript edits. Dr. Ventura provided funding.

[3] A version of Chapter 7, Section 7.1 and 7.4.1, has been published [Mendler A., Döhler M., Ventura C., Mevel L. (2020, February). The minimum detectable damage as an optimization criterion for performance-based sensor placement. In Proceedings of the IMAC - 38th International Modal Analysis Conference, Houston, United States]. Figure 5.1 is reprinted with permission of the publisher as well as Figures 7.6, 7.7, 7.8 , 7.9, and 7.10. Mr. Mendler was responsible for data collection and analysis, validation, and manuscript composition. All supervisory authors were involved throughout the project from concept formation to manuscript edits. Dr. Ventura provided funding.

[4] A version of Chapter 6, Sections 6.2 and 6.3, has been published [Mendler A., Döhler M., Ventura C., Mevel L. (2020, July). Clustering of redundant parameters for fault isolation with Gaussian residuals. In Proceedings of the IFAC - 21st World Congress of the International Federation of Automatic Control, Berlin, Germany]. Fig. 6.1 is reprinted with permission of the publisher. Mr. Mendler was responsible for data collection and analysis, validation, and manuscript composition. The supervisory authors were involved throughout the project from concept formation to manuscript edits. Dr. Ventura provided funding.

The laboratory tests on the St. Nazaire Bridge (in Section 9.2) were conducted under the supervision of Dr. Yann Lecieux at the Department of Civil and Mechanical Engineering at the University in Nantes, France. Cadoret A. and Freyssinet C. were responsible for the data acquisition and computer modelling.

Table of Contents

Abstract . . . . . **iii**

Lay Summary . . . . . **iv**

Preface . . . . . **v**

Table of Contents . . . . . **vii**

List of Tables . . . . . **xii**

List of Figures . . . . . **xiv**

List of Programs . . . . . **xviii**

List of Acronyms . . . . . **xix**

List of Symbols . . . . . **xxi**

List of Variables . . . . . **xxii**

Acknowledgements . . . . . **xxiii**

I PRELIMINARIES **1**

1 Background **2**

1.1 Introduction 2

1.2 Motivation 4

1.2.1 Lifeline Bridges 4

1.2.2 Monitoring System 6

1.2.3 Anticipated Damage 7

1.3 Methodology 9

1.3.1 Damage Diagnosis 9

1.3.2 Contributions 10

1.3.3 Thesis Organization 12

2 Literature Review . . . 13
2.1 Global Vibration-based Damage Diagnosis . . . 13
2.1.1 Damage-sensitive Features . . . 13
2.1.2 Damage Diagnosis Methods . . . 15
2.1.3 Changes in Boundary Conditions . . . 22
2.1.4 Minimum Diagnosable Damage . . . 24
2.2 Optimal Sensor Placement . . . 25
2.2.1 Performance Criteria . . . 25
2.2.2 Optimization Algorithms . . . 30
2.3 Summary . . . 32

3 Structural Dynamics in Control Theory . . . 34
3.1 Input-output Systems . . . 34
3.1.1 State Space Model . . . 34
3.1.2 Sampled System Response . . . 36
3.1.3 Hankel Factorization . . . 36
3.2 Output-only Systems . . . 38
3.2.1 State Space Model . . . 38
3.2.2 Covariance Function . . . 38
3.2.3 Hankel Factorization . . . 39
3.2.4 Practical Considerations . . . 40
3.3 Stochastic System Identification . . . 41
3.3.1 Subspace Decomposition . . . 41
3.3.2 Eigenvalue Problem . . . 41
3.3.3 Diagonalization . . . 42
3.4 Summary . . . 43

4 Damage Diagnosis Using the Asymptotic Local Approach . . . 44
4.1 Damage Parametrization . . . 44
4.2 Damage-sensitive Residual . . . 45
4.2.1 Subspace-based Residual . . . 45
4.2.2 Covariance Matrix . . . 46
4.2.3 Jacobian Matrix . . . 47
4.3 Statistical Decision-making . . . 52
4.3.1 Damage Hypothesis . . . 52
4.3.2 Generalized Likelihood Ratio . . . 52
4.3.3 Test Distribution . . . 53
4.3.4 Fisher Information Matrix . . . 56
4.4 Damage Diagnosis Tests . . . 56
4.4.1 Parametric Detection Test . . . 57

4.4.2 Non-parametric Detection Test . . . 57
4.4.3 Direct Localization Test . . . 58
4.4.4 Minmax Localization Test . . . 58
4.5 Interpreting the Test Result . . . 61
4.5.1 Empirical Reference Distribution . . . 61
4.5.2 Empirical Safety Threshold . . . 62
4.5.3 Empirical Power of Detection . . . 62
4.6 Summary . . . 63

II CONTRIBUTIONS . . . 65

5 Minimum Detectable Damage . . . 66
5.1 Main Idea . . . 66
5.1.1 Predictive Formula . . . 67
5.1.2 Minimum Detectability . . . 68
5.1.3 Reliability Concept . . . 69
5.1.4 Interpretation . . . 70
5.2 Application to Data-Driven Tests . . . 71
5.3 Numerical Considerations for Large Systems . . . 72
5.4 Proof of Concept . . . 73
5.4.1 Monitoring Model-based Parameters . . . 75
5.4.2 Monitoring with Data-Driven Tests . . . 77
5.5 Summary . . . 81

6 Minimum Localizable Damage . . . 82
6.1 Direct Localization Test . . . 82
6.1.1 Damage Identifiability . . . 83
6.1.2 False Localization Alarms . . . 84
6.1.3 Reliability Despite False Localization Alarms . . . 85
6.2 Minmax Localization Test . . . 86
6.2.1 Damage Identifiability . . . 87
6.2.2 False Localization Alarms . . . 88
6.2.3 Non-centrality Ratio . . . 89
6.3 Optimal Damage Localization . . . 89
6.3.1 Localization Resolution . . . 90
6.3.2 Damage Identifiability . . . 91
6.3.3 False-Alarms Susceptibility . . . 91
6.3.4 Optimal Compromise . . . 92
6.4 Proof of Concept . . . 93

6.4.1 Direct Localization Test . . . 93
6.4.2 Minmax Localization Test . . . 98
6.4.3 Optimal Damage Localization . . . 98
6.5 Summary . . . 101

7 Sensor Placement Optimization . . . 102
7.1 Optimizing the Detectability . . . 103
7.1.1 Minimum Measurement Duration . . . 103
7.1.2 Performance Criterion . . . 104
7.1.3 Optimal Sensor Layout . . . 105
7.1.4 Appropriate Number of Sensors . . . 105
7.2 Optimizing the Localizability . . . 106
7.2.1 Performance Criteria . . . 106
7.2.2 Optimal Compromise . . . 107
7.3 Implementing a Genetic Algorithm . . . 108
7.3.1 Single-objective Optimization . . . 108
7.3.2 Multi-objective Optimization . . . 110
7.4 Proof of Concept . . . 112
7.4.1 Optimizing the Detectability . . . 112
7.4.2 Optimizing the Localizability . . . 116
7.5 Summary . . . 121

8 Monitoring Boundary Conditions . . . 123
8.1 Effect on System Matrices . . . 123
8.1.1 Linear Analysis (Stress Stiffening) . . . 124
8.1.2 Non-linear Analysis (Large Displacements) . . . 125
8.2 Sensitivity Calculation . . . 127
8.2.1 Neglecting Geometry Changes . . . 127
8.2.2 Considering Geometry Changes . . . 128
8.2.3 Discussion . . . 128
8.3 Proof of Concept . . . 128
8.3.1 Pre-stressing Tendon . . . 129
8.3.2 Cable-stayed Bridge . . . 133
8.4 Summary . . . 136

III APPLICATIONS . . . 137

9 Experimental Case Studies . . . 138
9.1 HSS Beam (104 DOF) . . . 138

9.1.1 Experimental Setup . . . 139
9.1.2 Detecting Mass Changes . . . 140
9.1.3 Localizing Mass Changes . . . 147
9.1.4 Optimizing the Sensor Placement . . . 152
9.2 St. Nazaire Bridge Model (1,002 DOF) . . . 154
9.2.1 Experimental Setup . . . 154
9.2.2 Localization Cable Failure . . . 159
9.2.3 Additional Numerical Studies . . . 161
9.3 Summary . . . 163

10 Model Validation . . . 165
10.1 Case Study . . . 165
10.2 Main Input Parameters . . . 168
10.2.1 Time Lags . . . 168
10.2.2 System Order . . . 169
10.2.3 Mode Selection . . . 171
10.2.4 Number of Data Segments . . . 174
10.3 Minimum Data Length . . . 175
10.3.1 Sampling Frequency . . . 176
10.3.2 Measurement Duration . . . 177
10.4 Small Damage Assumption . . . 184
10.4.1 Jacobian Prediction Error . . . 185
10.4.2 Degeneration Check . . . 187
10.5 Summary . . . 189

11 Conclusions . . . 190
11.1 Contributions . . . 191
11.2 Strengths and Limitations . . . 195
11.3 Future Research . . . 199

Bibliography . . . 201

List of Tables

1.1 Performance levels for bridges as per (S6-19, 2019) 6
1.2 Anticipated earthquake damage on cable-stayed bridges, refer to Fig. 1.4 8
1.3 Examined cable-stayed bridges that sustained damage during earthquakes (see Table 1.2) 8

2.1 Damage-sensitive features (Farrar and Worden, 2012) 14
2.2 Optimization criteria categorized with respect to the primary purpose 30

4.1 Classifying the available damage diagnosis tests 64

5.1 Interpreting code-based reliability indices 70
5.2 Input parameter sheet 75
5.3 Minimum detectable change in the modulus of elasticity E for each beam segment . 77
5.4 Minimum detectable change in the modulus of elasticity E for each beam segment . 80

6.1 Input parameter sheet 93

7.1 Input parameter sheet 113
7.2 Finite element specifications 117
7.3 Input parameter sheet 118
7.4 Pareto optimal points P1 - P11 with unscaled objective functions 119

8.1 Input parameter sheet 129
8.2 Input parameter sheet 133

9.1 Input parameter sheet for detection 142
9.2 Finite element specifications 156
9.3 Operational modal analysis results (covariance-driven SSI) 157
9.4 Input parameter sheet 158

10.1 Default input parameters 167
10.2 Relation between the detectable damage and the number of modes 173
10.3 Input parameters for the evaluation of the minimum detectable damage and the non-centrality ratio in Fig. 10.9 176
10.4 Best practices for stochastic subspace-based damage diagnosis 188

11.1 List of contributions of this thesis 192

List of Figures

1.1 Seismic hazard in British Columbia (B.C.) (Earthquakes Canada, 2020) 4
1.2 Major-route and lifeline bridges of Metro Vancouver, Canada 5
1.3 Architecture of the B.C. Smart Infrastructure Monitoring System (BCSIMS) 7
1.4 Anticipated earthquake damage on cable-stayed bridges, see Table 1.2 7

4.1 Chain of sensitivity analyses for Jacobian calculation 48
4.2 Central χ^2-distribution for a varying number of degrees of freedom $\nu \in [1, \ldots, 9]$ . . 55
4.3 Non-central χ^2-distribution for a fixed number of degrees of freedom and varying non-centrality $\lambda \in [0, 1, \ldots, 10]$ 55
4.4 6-DOF mass-and-spring system 56
4.5 Damage detection of a 2% stiffness decrease in Spring 1 57
4.6 Damage localization of a 2% stiffness decrease in Spring 1 58
4.7 Probability of false alarms, safety threshold value, and probability of detection . . . 62
4.8 Flowchart for damage diagnosis 63

5.1 Statistical distribution of the test statistic 67
5.2 Minimum non-centrality as a code-based reliability index 70
5.3 HSS beam with nine material properties and one sensor 74
5.4 Numerical mode shapes and power spectral density of the generated signal 74
5.5 Jacobian computation through the chain rule (reference state) 76
5.6 Fisher information computation (reference state) 76
5.7 Training state 77
5.8 Validation state 77
5.9 Validation state for the structural parametrization 78
5.10 Training state 78
5.11 Training state 78
5.12 Validation state for the modal parametrization 79
5.13 Validation state for the non-parametric test 80

6.1 Statistical distribution of the test statistic for $\nu = 1$ 83
6.2 Comparing the minimum non-centrality for damage detection and localization . . . 86
6.3 Visualizing the hierarchical clustering 90
6.4 Multi-objective optimization with two objective functions 92

6.5 Numerical HSS beam with nine materials and four sensors . . . 94
6.6 Numerical mode shapes and power spectral density of the generated signal . . . 94
6.7 Fisher information for the direct test (left) and the minmax test (right) . . . 95
6.8 Validation of the prediction for the direct localization test . . . 96
6.9 Validation of the prediction for the minmax localization test . . . 97
6.10 Original model (top) and substructured model (bottom) . . . 99
6.11 Objective functions for automated substructuring . . . 99
6.12 Validation of the automated substructuring approach . . . 100

7.1 Elements of reproduction of the genetic algorithm (GA) with integer sensor encoding and $r = 3$ sensors . . . 108
7.2 Flowchart for the genetic algorithm with a single objective . . . 110
7.3 Evolution of sensor layouts in the multi-objective GA . . . 111
7.4 Numerical HSS beam including the possible sensor locations P1 - P8 . . . 112
7.5 Numerical mode shapes . . . 112
7.6 Minimum measurement duration T_h for (a) one sensor at position P2, and (b) two sensors at P1 and P8 . . . 113
7.7 Measurement durations $T(c, r = 1)$ and standard deviations . . . 114
7.8 Optimal measurement time $T_{opt}(c)$ for a varying number of sensors . . . 114
7.9 Measurement durations $T(c, r = 2)$ . . . 114
7.10 Test distribution for a 5% stiffness decrease in stiffness parameter E_1 . . . 115
7.11 HSS beam including the possible sensor locations P1 - P24 . . . 116
7.12 Convergence chart for the genetic algorithm, showing the rank of elite members with respect to their ranking after an exhaustive search (ES) . . . 116
7.13 Schematic bridge with six possible sensor locations P1 - P6 . . . 117
7.14 Modes of vibration . . . 117
7.15 Feasible optimization space with 11 Pareto optimal solutions . . . 119
7.16 Empirically validating the mean test response to the minimum detectable damages 120
7.17 Test response to damage in a deck element (Parameter 6) and a hanger (Parameter 9) for balanced and tuned sensor layouts . . . 121

8.1 2-D Bernoulli beam in local coordinates (undeformed) . . . 126
8.2 Metal string with sensors S1 - S3 and support displacements u . . . 130
8.3 Numerical mode shapes and power spectral density of the generated signal . . . 130
8.4 Validation of the prediction for the minmax localization test . . . 131
8.5 Validating the Jacobian approximation . . . 131
8.6 Validation of the prediction for the minmax localization test . . . 132
8.7 Validating the Jacobian approximation . . . 132
8.8 Validation of the prediction for the minmax localization test . . . 132
8.9 Schematic cable stayed bridge with six sensors . . . 134

8.10 Modes of vibration . . . 134
8.11 Localization of abutment settlement (left) and tower tilt (right) . . . 135
8.12 Validating the Jacobian approximation . . . 135
8.13 Localization of a loss in pretension in cables T_1, T_2, and T_3 . . . 136

9.1 Laboratory HSS steel beam on pin supports . . . 139
9.2 Numerical HSS beam with eight sensor locations P1 - P8 . . . 141
9.3 Experimental power spectral density from eight sensors . . . 141
9.4 Numerical modal analysis with four sensors at P1, P2, P7, and P8 . . . 141
9.5 Block Hankel singular values . . . 142
9.6 Covariance singular values . . . 142
9.7 Fisher information matrix and its singular values . . . 142
9.8 Training procedure to determine the minimum measurement duration . . . 143
9.9 Damage scenarios with extra masses . . . 145
9.10 Validating the prediction for the damage detection tests . . . 145
9.11 Optimal substructure arrangement for $K = 6$ clusters . . . 149
9.12 Automated parameter clustering . . . 149
9.13 Minmax Fisher information with six clusters $K = 6$ and its singular values . . . 150
9.14 Damage localization . . . 150
9.15 Probability of detection for sensor configurations with rank 70, 36 and 1 . . . 152
9.16 Ranking all 70 configurations with $r = 4$ sensors . . . 152
9.17 Performance curve . . . 152
9.18 Relation between the mean test response and the measurement duration . . . 153
9.19 St. Nazaire Bridge (Janberg, 2020) . . . 155
9.20 Experimental setup for the St. Nazaire Bridge . . . 155
9.21 Finite element model of the St. Nazaire Bridge in MATLAB® . . . 156
9.22 First six modes of vibration in the vertical direction (FE Model) . . . 157
9.23 Repeated mode at about 80.5 Hz . . . 158
9.24 Automated clustering of cable cross-section parameters . . . 160
9.25 Non-centrality of the minmax localization test for damage scenario P19 . . . 160
9.26 Singular values of the Block Hankel matrix and the Fisher information . . . 161
9.27 Substructure arrangement for 20 parameter clusters . . . 162
9.28 Comparing the predicted and the measured non-centrality for $\Delta_3 = 50\%$ . . . 162
9.29 Validation state for all 36 damage scenarios . . . 163

10.1 Numerical HSS beam with nine materials and two sensors . . . 166
10.2 Numerical modal analysis . . . 166
10.3 Effect of changing time lags . . . 169
10.4 Minimum detectable damage and non-centrality ratio for increasing noise contamination. The noise is in percent of the output variance . . . 170

10.5 Subspace angles between the FEA-based observability and the data-driven column space of the block Hankel matrix . . . 171
10.6 Fisher information for a simply supported beam with asymmetrical excitation . . . 172
10.7 Relation between the detectable damage and the number of modes . . . 173
10.8 Convergence of the predictions for a varying number of data segments . . . 175
10.9 Increasing the sampling frequency for a fixed measurement duration T (left side) and a fixed sample size (right side). Refer to Table 10.3 for input parameters . . . 176
10.10 Zero mean and unit variance checks in the training state . . . 179
10.11 Gaussianity check, goodness-of-fit test on the parametric residual . . . 179
10.12 Convergence of the minimum detectable damage . . . 180
10.13 Convergence of the Fisher information matrix norm and the covariance matrix norm 181
10.14 Convergence of the Jacobian matrix norm . . . 181
10.15 Gaussianity convergence studies in the reference state . . . 183
10.16 Gaussianity convergence studies in the testing state . . . 184
10.17 Convergence of the non-centrality ratio in the testing phase . . . 184
10.18 Jacobian prediction error (JPE) for the change prediction in natural frequencies (shown for Parameter θ_5) . . . 186
10.19 Jacobian prediction error (JPE) for the change prediction in mode shape coordinates (shown for Parameter θ_5) . . . 186
10.20 Jacobian prediction error (JPE) for the change prediction in natural frequencies (shown for Parameter θ_5) . . . 187

List of Programs

MATLAB®

MATLAB® is a registered trademark of The MathWorks, Incorporated, 3 Apple Hill Drive, Natick, MA, 01760-2098, United States. Additional toolboxes include the Signal Processing Toolbox and the Global Optimization Toolbox.

https://www.mathworks.com/

ANSYS®

ANSYS® is a registered trademark of ANSYS, Incorporated, Southpointe 2600 Ansys Drive, Canonsburg, PA 15317, United States. The Mechanical APDL interface is used in combination with the aaS MATLAB® toolbox.

http://www.ansys.com/

List of Acronyms

AL asymptotic local

B.C. British Columbia

BCSIMS British Columbia Smart Infrastructure Monitoring System

CDF cumulative density function

CLT central limit theorem

DOF degrees of freedom

EOV environmental and operational variable

ES exhaustive search

FE finite element

FEA finite element analysis

GA genetic algorithm

GLR generalized likelihood ratio

HSS hollow structural steel

JPE Jacobian prediction error

LTI linear and time-invariant

NCR non-centrality ratio

NSGA-II 2nd generation of the non-dominated sorting genetic algorithm

OMA operational modal analysis

PDF probability density function

PFA probability of false alarms

POD probability of detection

PSD power spectral density

SHM structural health monitoring

SNR signal-to-noise ratio

SSI stochastic subspace-based system identification

SVD singular value decomposition

List of Symbols

a, A	Scalar
$\mathbf{a}$	Vector
a_a	Vector entry
$\mathbf{A}$	Matrix
$\mathbf{A}_i$	Matrix column i
$\mathbf{A}_{\bar{i}}$	Matrix with removed column i
$\mathbf{A}_{ij}$	Submatrix
A_{ij}	Matrix entry in row i and column j
$\text{vec}(\mathbf{A})$	Vectorization operator to stack columns in $\mathbf{A}$
$\mathbf{A}^T$	Transposed of $\mathbf{A}$
$\mathbf{A}^*$	Transposed conjugated complex matrix of $\mathbf{A}$
$\mathbf{A}^{-1}$	Inverse of $\mathbf{A}$
$\mathbf{A}^\dagger$	Pseudo inverse of $\mathbf{A}$
$\mathbf{I}_m$	Identity matrix of size $m \times m$
$\mathbf{A} \otimes \mathbf{B}$	Kronecker product
$\mathbb{R}$	Set of real numbers
i	Imaginary unit $\text{i}^2 = -1$
$\text{Re}(a)$	Real part of complex a
$\text{Im}(a)$	Imaginary part of complex a
$\hat{X}$	Estimate of variable X
$\bar{x}, \bar{X}$	Complementary event or value of x or X
$\mathbf{E}(X)$	Expected value of a variable X
$\mathbf{E}_{\boldsymbol{\theta}}(X)$	Expected value of variable X under system parameter vector $\boldsymbol{\theta}$
$\mathcal{N}(\mu, \sigma)$	Gaussian distribution with mean value μ and standard deviation σ
$\mathcal{N}(\boldsymbol{\mu}, \boldsymbol{\Sigma})$	Multi-dimensional Gaussian distribution with mean value vector $\boldsymbol{\mu}$ and covariance matrix $\boldsymbol{\Sigma}$
$\chi^2(\nu)$	Central chi-squared distribution with ν degrees of freedom
$\chi^2(\nu, \lambda)$	Non-central chi-squared distribution with ν degrees of freedom and non-centrality λ

List of Variables

$\mathbf{A}$	State transition matrix
$\mathbf{B}$	Input matrix
$c, \mathbf{C}^1$	Damping coefficient and damping matrix
$\mathbf{C}$	Output matrix
$\boldsymbol{\mathcal{C}}$	Controllability
$\mathbf{D}$	Feed-through matrix
h	Parameter number $h = 1, 2 \ldots, H$
$\boldsymbol{\mathcal{H}}$	Block Hankel matrix
$\boldsymbol{\mathcal{J}}$	Sensitivity matrix (Jacobian)
$k, \mathbf{K}$	Stiffness and stiffness matrix
k	Cluster number $k = 1, 2 \ldots, K$
$m, \mathbf{M}$	Mass and mass matrix
N, N^0	Number of samples during training and testing
N_m	Number of modes of vibration
$\boldsymbol{\mathcal{O}}$	Observability
p	Time lag for block columns in block Hankel matrix
q	Time lag for block rows in block Hankel matrix
r, r^0	Number of uni-axial sensors, number of projection sensors
$\mathbf{S}$	Singular values
$\mathbf{U}_0$	Left null space
$\mathbf{U}$	Left singular vectors
$\mathbf{V}$	Right singular vectors
α	False-positive rate (type I error)
β	False-negative rate (type II error)
$\boldsymbol{\delta}$	Statistical change vector
$\boldsymbol{\varepsilon}$	Residual vector
ζ	Critical damping ratio
$\boldsymbol{\zeta}$	Gaussian residual vector
$\boldsymbol{\eta}$	Parameter vector with modal parameters
$\boldsymbol{\theta}$	Parameter vector with structural design parameters
$\boldsymbol{\Sigma}$	Covariance matrix

Acknowledgements

First of all, I would like to thank my research supervisor Carlos Ventura for his support and confidence in my work. He inspired the research proposal and guided me through the challenges of the research program. I am appreciative that he put emphasis on both my academic and professional development by involving me in client projects, and trusted me with valuable measurement equipment. I will be forever grateful for the conferences he sent me to, and the professional network he helped me build. Particular thanks go to my co-supervisor Michael Döhler for his inspiration, mentoring, and patience. His originality, academic excellence, and thoroughness were a humbling experience and driving force throughout my thesis. His supervision and mentoring has set an unprecedented standard. The work environment and team spirit at Inria have shaped my perception of the academic world and left a lasting imprint on my personality.

Furthermore, I would like to express my gratitude for the support I received from my supervisory committee members and the subtle impulses they gave me whenever I needed them. I truly enjoyed the discussions with Ruben Boroschek and his strong and well-founded opinion. Reza Vaziri's knowledge on finite element analysis were extremely helpful. It was a great pleasure to assist Terje Haukaas with teaching, and his knowledge on statistical analysis is much appreciated. Special thanks go to Yavuz Kaya for his supervision in the first year and the insights into the plans of the Ministry of Transportation and Infrastructure. On this occasion, I would like to acknowledge my colleagues at UBC and Inria. Special thanks go to the Manager of the Earthquake Engineering Research Facility, Mehrtash Motamedi, and Project Assistant Terry Moser, who were always available, responsive, and supportive. I would also like to thank my Team Leader at Inria, Laurent Mevel, for his enthusiasm for my work and his mentorship. His many ideas, his point of view, and profound knowledge were a great source of inspiration. Special thanks go to my colleagues Szymon Greś and Eva Viefhues, whose work and expertise I greatly benefited from. Equally, I would like to thank Frédéric Gillot who selfishly helped me through discussions on global optimization.

Finally, I would like to thank my family. My parents Ludwig and Susanne Mendler encouraged me to commence the PhD program and supported me throughout it, despite the sacrifices this meant for them. Due to the large distance, I was unable to say my goodbyes to my grandparents Heinz Kobiela and Lotte Mendler, who deserve to be acknowledged here. Special thanks also go to my grandmother Irmgard Kobiela for her continuous financial support. At the end of this list—though really at the beginning of it all—stands my loving partner and best reader, Jennifer Mah, without whom this thesis would not exist.

Part I

PRELIMINARIES

Chapter 1

Background

"A society grows great when old men plant trees whose shade they know they shall never sit in."
— Greek Proverb

1.1 Introduction

The province of British Columbia (B.C.) is located in one of the most seismically active zones in Canada and the world, and is dependent upon lifeline infrastructure that bridges the coastal rivers and the Pacific inlets. Many of the existing links are designed according to outdated design standards, e.g., the George Massey Tunnel, or are nearing the end of their design basis service life, e.g., the Lion's Gate Bridge and the Second Narrow's Bridge. Since these structures cannot be economically replaced, or because of their iconic value, techniques for bridge monitoring are developed so their operation can be extended beyond their original lifespans.

In the context of civil engineering structures, the process of implementing a damage diagnosis strategy is referred to as structural health monitoring (SHM). Due to the existing monitoring system, this work focuses on vibration-based damage diagnosis. This process involves the observation of the structural vibrations through permanently installed sensors, the extraction of damage-sensitive features, and their subsequent statistical evaluation (Farrar and Worden, 2012). The statistical evaluation includes a data normalization step that removes the effect that changing environmental and operational variables (EOVs) have on the vibration behaviour of the structure (e.g., wind, traffic loads, temperature fluctuations, icing). Some features are robust to changes to EOVs (Balmès et al., 2008a, 2009; Viefhues et al., 2020), which is why they are not explicitly considered in this thesis. The damage diagnosis involves four consecutive steps with increasing complexity, i.e., damage detection, localization, quantification, and the prediction of the remaining lifetime (Rytter, 1993). The real-time information on the health state increases the structural safety between periodically scheduled bridge inspections, and allows for a coordinated emergency response after extreme events, such as storms, tsunamis, or earthquakes. For the urban communities in the Southwest of B.C., the advancement of a bridge monitoring network (and with it, the theoretical developments in SHM) are particularly relevant because there is a one out of ten chance that a megathrust earthquake will strike within the next 50 years (Onur and Seemann, 2004). All emergency response and evacuation services depend on a few lifeline bridges that will turn into the most critical and vulnerable infrastructural links.

SHM poses multiple challenges specific to civil engineering structures. Firstly, no site and bridge are identical, so a structure-specific training of the damage diagnosis algorithm is required, and findings from one bridge cannot straightforwardly be applied to another. Therefore, it is challenging to assess whether certain damages can or cannot be detected and localized querying the value of implementing a SHM system. Secondly, due to the sheer size of bridges, a dense sensor layout cannot be realized and local monitoring approaches cannot be applied, so global monitoring approaches are to be applied in combination with sparse sensor layouts that are strategically laid out for successful damage detection. For instance, the Port Mann Bridge exhibits a length and width of 2,020 m and 65 m, respectively, and 288 stay cables, but the acquisition and maintenance costs for monitoring each cable using local damage diagnosis methods are unreasonable. Thirdly, a lack of real vibration data from damaged structures is impeding the research progress, as bridges are vital links in primary infrastructure and damaging them for research purposes, as it was done in the case of the Z24 Bridge in Switzerland and the S-101 Bridge in Austria, can only be justified after exceeding their life expectancy. Equally, continuous operation is imperative, and bridge closures for dynamic or static testing are unacceptable. Consequently, the damage diagnosis is to be performed during normal operating conditions and under unknown force excitation. With this in mind, this thesis pursues the following objectives:

- *Objective I:* Build a universal framework, which is applicable to a wide range of structures, damage-sensitive features, and anticipated damage scenarios, to calculate the minimum detectable and localizable damage based on global vibration monitoring
- *Objective II:* Devise criteria that describe the detectability and localizability of damage and incorporate them into a sensor placement optimization scheme for large mechanical systems
- *Objective III:* Implement self-validation strategies to test the applicability of the algorithm for real structures, to verify input parameter settings, and to non-invasively test its performance in the absence of damage

All considerations are made for a damage diagnosis method, called the asymptotic local (AL) approach using the subspace-based residual as a damage-sensitive feature. This method allows for an online evaluation with diagnostic capabilities including detection, localization, and quantification. However, all developed tools are universal in that they can be applied to any damage-sensitive feature with Gaussian properties. The tools are of great value to predict the minimum detectable and localizable damage, to optimize the sensor placement, and to assess the value of SHM for bridge monitoring in general. Ultimately, all methods are readily applicable to other civil engineering structures, such as buildings, offshore structures, defence systems, mining structures, or power plants, as well as mechanical structures such as ships, aircraft, and spacecraft.

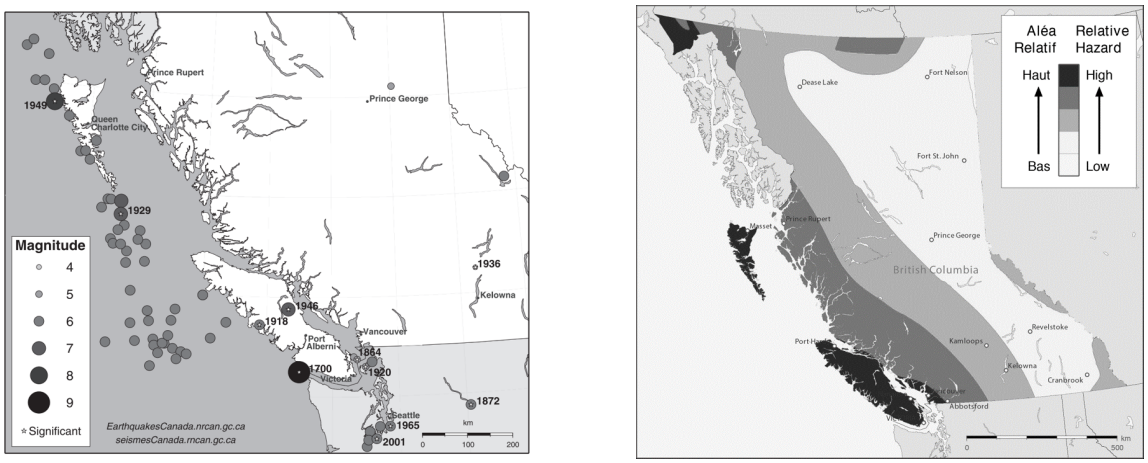

(a) Significant historic earthquakes (b) Relative seismic hazard map

Figure 1.1: Seismic hazard in British Columbia (B.C.) (Earthquakes Canada, 2020)

1.2 Motivation

The Southwest of B.C., including Vancouver and the densely populated Fraser River delta, is one of the most seismically active regions in Canada (Clague et al., 1998). About 150 km off the coast of Vancouver, a locking mechanism at the tectonic plate interfaces causes strain to be built up continuously. Geologic evidence has shown that the strain is released abruptly every 300 - 700 years through subduction interface earthquakes with magnitudes of up to 9.0, with the last one occurring in 1700 (Goldfinger et al., 2012). The relative movement between the two plates since then amounts up to 12 m. Smaller, but still damaging earthquakes within the overlapping crust, or deep down in the subducting slab are omnipresent reminders of the seismic threat. The four most recent and significant ones are the 2001 Nisqually earthquake (M = 6.8), the 1965 Puget Sound earthquake (M = 6.7), the 1949 Olympia earthquake (M = 6.7), and the 1946 Vancouver Island earthquake (M = 7.3), see Fig. 1.1. At the same time, the seaport city is located on a peninsula that is wedged between the Pacific Inlet, coastal mountains and the Fraser River delta, causing the two sea bridges and four river bridges across the 400 m wide main arm of the Fraser River to be among the largest and widest in North America (Svensson, 2013), see Figure 1.2. For example, when the Alex Fraser Bridge was opened to traffic in 1986, it was the longest cable-stayed bridge in the world. The Golden Ears Bridge was opened to traffic in 2009, and is still the longest extra-dosed bridge in North America. Last but not least, with a width of up to 12 traffic lanes (65 m), the Port Mann highway bridge was the widest bridge ever built at the time of its inauguration in 2012, and is still the second longest cable-stayed bridge in North America.

1.2.1 Lifeline Bridges

The bridge monitoring in B.C. follows the lifeline monitoring philosophy. The highway bridge inventory of British Columbia was evaluated in 2017 (Siddiquee et al., 2017) and the report concludes

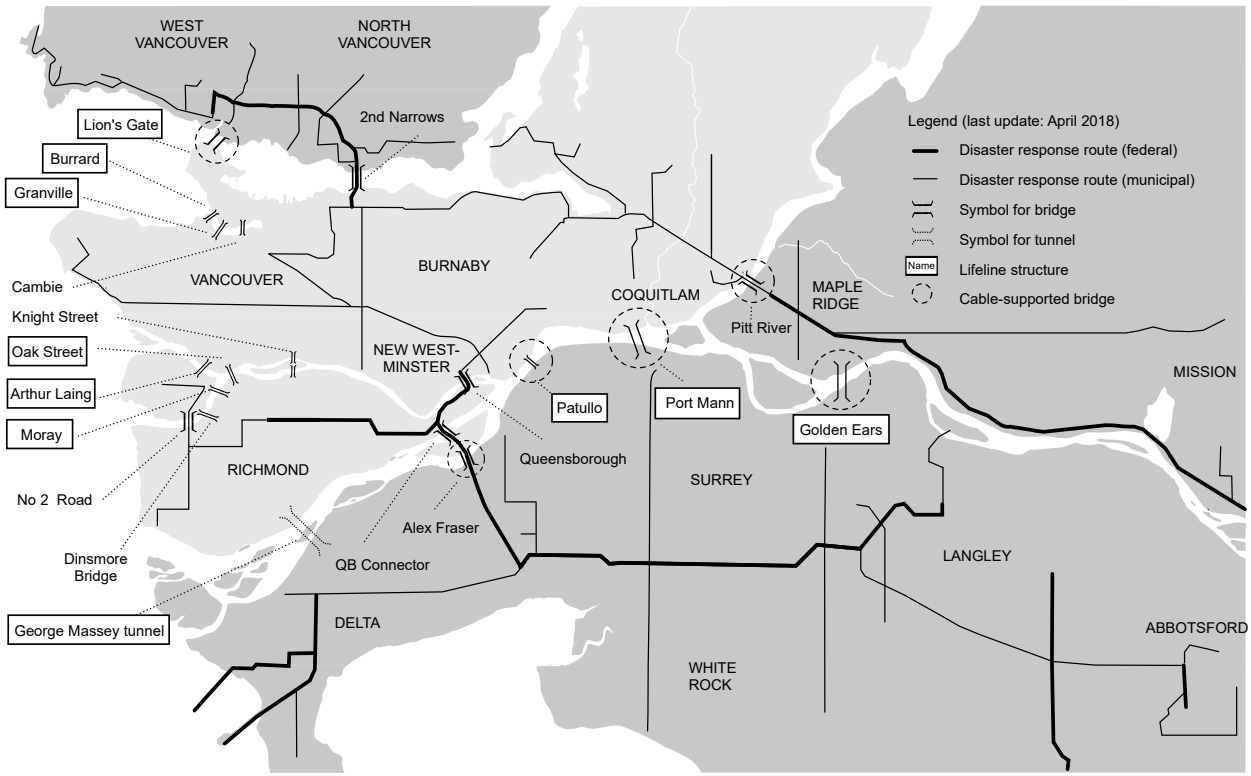

Figure 1.2: Major-route and lifeline bridges of Metro Vancouver, Canada

that 80% of all highway bridges are between 20 m and 100 m long and exhibit simple structural systems, such as simply-supported or continuous multi-span girders. The numbers suggest these bridges are the most relevant infrastructures; however, more than 68% of the population lives in the Southwest of B.C., and among those, two out of three live in Metro Vancouver (Foster et al., 2011), where merely 20.4% of all bridges are located, see Fig. 1.2. The seismic hazard is the greatest in the coastal areas (Earthquakes Canada, 2020), but only 26.5% of all bridges are located here, Figure 1.1b. Since the area with the highest population density overlaps with the most seismically active zone, the bridge design code categorizes the safety requirements for bridges with respect to their importance. On the bases of social, economic and security requirements, the seismic design guidelines distinguish between three importance categories: (a) lifeline bridges, (b) major-route bridges, and (c) other bridges. Major-route bridges are part of the municipal and federal disaster response network and are required to facilitate emergency response and defence purposes. In the event of an earthquake or tsunami, they are designated for use by emergency personnel only, and they are not used for evacuation purposes. Lifeline bridges, on the other hand, serve the general public. They are vital to the integrity of the local transportation network and the ongoing economy. Moreover, particularly large (and expensive) or iconic bridges can be declared lifeline bridges. The importance category determines the design approach and the analysis requirements. More importantly for monitoring applications, it also determines the performance levels, which describe the accepted level of damage as well as the serviceability requirements after an earthquake has

Prob.	Lifeline bridges			Major-route bridges			Other bridges		
in 50 a	Lvl.	Serviceability	Damage	Lvl.	Serviceability	Damage	Lvl.	Serviceability	Damage
10%	(1)	Immediate	None	(2)	Immediate	Minimal	(3)	Limited*	Repairable*
5%	(2)	Immediate	Minimal	(3)	Limited*	Repairable*	(4)	Disrupted*	Extensive*
2%	(3)	Limited	Repairable	(4)	Disrupted	Extensive	(5)	Life safety	Replacement

*Optimal performance levels unless required by the Regulatory Authority or the Owner

Table 1.1: Performance levels for bridges as per (S6-19, 2019)

occurred. In the case of a megathrust earthquake (with a probability of exceedance of 2% in 50 years), lifeline bridges are required to remain operational with minor service limitations and repairable damage. In contrast, non-essential bridges are expected to be closed to traffic and replaced in the aftermath of a megathrust earthquake, refer to Table 1.1. The maintenance effort of bridges correlates with bridge area, and an estimation yielded that 24.3% of all lifeline bridges in Metro Vancouver are already cable supported (neglecting the approach viaducts, this number increases to 53.2%) and additional cable-stayed bridges are in planning. Three out of the six disaster response bridges (major-route bridges) are cable-stayed and so are all bridges across the main arm of the Fraser River—the main evacuation route.

To summarize, the efficiency of disaster response services and the safety of evacuation procedures for a majority of the population depend on the structural health state of cable-stayed bridges, and the ability to assess them rapidly. It would be invaluable for the city of Vancouver and B.C. to have an algorithm in place that can reliably detect and localize damage, and rank the bridges according to the severity of damage sustained during an earthquake.

1.2.2 Monitoring System

In 2009, the B.C. Ministry of Transportation & Infrastructure embarked on a program called the British Columbia Smart Infrastructure Monitoring System (BCSIMS). The resulting online platform makes available the data of two monitoring networks, including a strong motion network with 162 accelerometers and a structural health monitoring network with 15 bridges and one tunnel (Kaya et al., 2017). The instrumentation on the bridges is designed to capture the global vibration behaviour, in order to record strong ground motions and their effect on both the structures and the soil. All sensors record the structural response of the bridges (< 200 Hz) to ambient excitation.

The primary objective of the SHM network is to provide a post-earthquake damage assessment module which assesses the structural health state in real-time, and thus, enable prioritized bridge inspections and rapid deployment or repair measures (Kaya et al., 2017). The second objective is the long-term monitoring for cost-efficient operation over the entire life span of bridges and schools, see Figure 1.3. The monitoring data is supposed to supplement the regular bridge inspections, and aid with the estimation of the remaining lifetime. The existing monitoring system is an excellent database for research in the field of vibration-based damage diagnosis but no damaging events have been recorded to date.

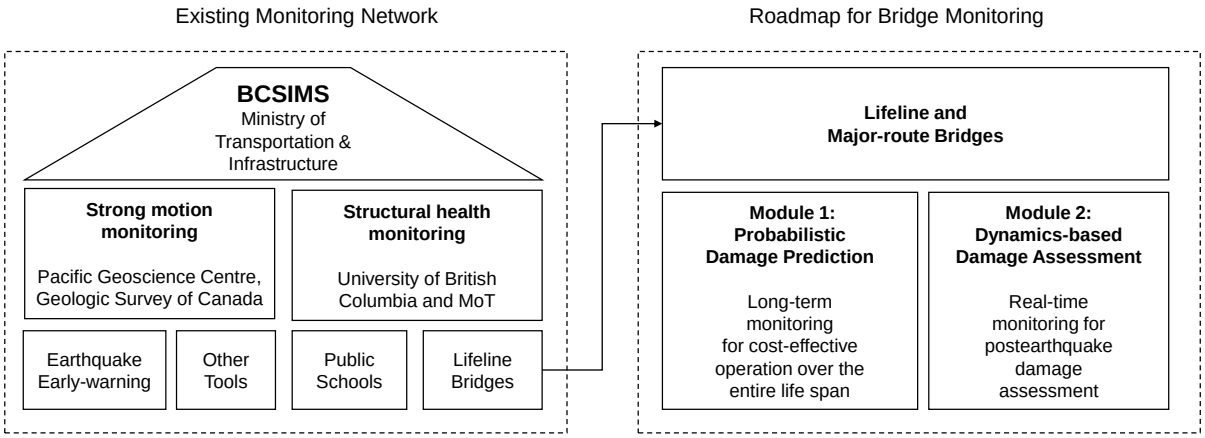

Figure 1.3: Architecture of the B.C. Smart Infrastructure Monitoring System (BCSIMS)

1.2.3 Anticipated Damage

The development of an efficient SHM system requires knowledge of probable damage scenarios during earthquakes. This section summarizes the findings from a literature review on post-earthquake damage on the five cable-stayed bridges in Japan, Taiwan, and Canada, listed in Table 1.3. All documented damage scenarios are illustrated in Fig. 1.4.

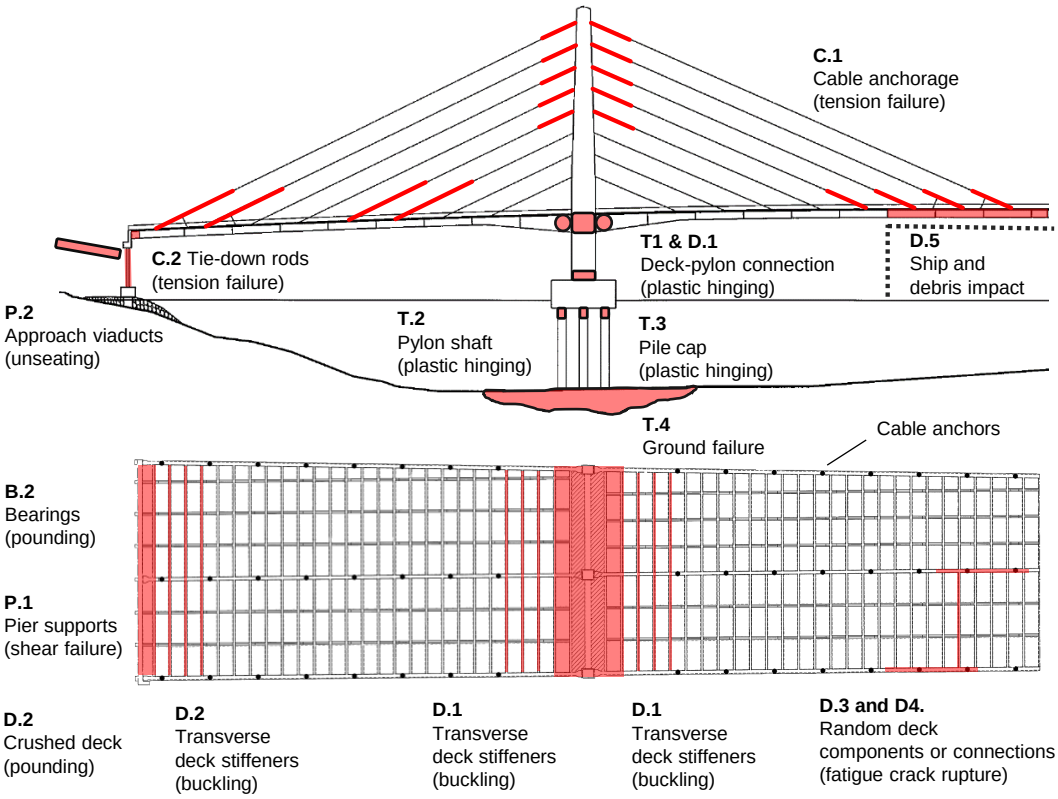

Figure 1.4: Anticipated earthquake damage on cable-stayed bridges, see Table 1.2

Component	ID	Location	Failure mechanisms	Damage symptoms	Severity*
Deck	D.1	Deck-pylon connection	Flexural hinging shear failure	Stiffness reduction, concrete spalling, yielding and buckling of reinforcement	(5)
	D.2	Deck-pier connection	Shear failure, and pounding	Buckling and cracking of transverse beams and end beams, crushing of main girders and the concrete slab in the longitudinal direction	(4)
	D.3	Main girder	Fatigue crack rupture	Stiffness reduction of main girders due to partial or complete rupture	(4)
	D.4	Girder connection	Fatigue crack rupture	Stiffness reduction of steel joints due to partial or complete rupture	(3)
	D.5	Shipping lane	Ship and debris impact	Large deformation of main girders and transverse floor beams, buckled stiffeners, concrete spalling	(5)
Deck bearings	B.1	At main pylon	Pounding	Crushed wind shoes, concrete spalling on deck and pylons	(3)
	B.2	At pier	Pounding	Crushed wind shoes	(3)
Main tower	T.1	Pylon-deck connection	Flexural hinging and shear failure	Stiffness reduction, concrete spalling, yielding and buckling of reinforcement	(5)
	T.2	Pylon shaft	Flexural hinging and shear failure	Reduced cross section due to concrete spalling	(5)
	T.3	Pile caps	Plastic hinging and cracking due to rocking or fence posting	Horizontal cracking of pile caps	(4)
	T.4	Entire tower	Ground failure due to settlements, liquefaction, landslides, etc.	Vertical pylon settlement up to 6 m, residual horizontal displacements, or rotations	(5)
Stay cables	C.1	Cable anchors	Tension failure at the main span	Cross section reduction (due to strand failure), or slacking of entire cables near anchors	(3)
	C.2	Tie-down rods at piers	Tension failure	Loss of prestress in anchor cables, and uplift of the deck from the pier support	(5)
End-span piers	P.1	Pier supports	Shear failure due to horizontal and vertical pounding	Crushing of bearings, cracking of transverse pier beams, buckling or shear failure of supporting columns	(5)
	P.2	Approach viaducts	Displacements and rotations of the pier foundations	Partial or total collapse of simply-supported approach spans (unseating)	(5)

*maximum expected damage potential expressed with respect to the performance classes defined in the Canadian highway bridge design code

Table 1.2: Anticipated earthquake damage on cable-stayed bridges, refer to Fig. 1.4

No.	Bridge	Location	Earthquake event	Magnitude	Year
1	Yokohama Bay Bridge	Japan	Tohoku Earthquake	M = 9.0	2011
2	Chi-Lu Bridge	Taiwan	Chi-Chi Earthquake	M = 7.6	1999
3	Higashi-Kobe Bridge	Japan	Kobe Earthquake	M = 6.9	1995
4	Rokko Island Bridge	Japan	Kobe Earthquake	M = 6.9	1995
5	Shipshaw Bridge	Canada	Saguenay Earthquake	M = 5.9	1988

Table 1.3: Examined cable-stayed bridges that sustained damage during earthquakes (see Table 1.2)

Table 1.2 gives details on each damage scenario shown in Fig. 1.4. It includes the failure mechanism and observed damage symptoms, and assesses the damage consequences with respect to the performance levels in the bridge design code S6-19 (2019) from Table 1.1. For example, the observed damage scenarios on stay cables are categorized into anchor failure (C.1) or failure of tie-down rods (C.2). The failure mechanism is tension failure, and observable damage symptoms include slack cables and strand failure or uplift of the deck from the pier supports, respectively. Cable-stayed bridges are redundant structural systems, so individual cable anchorage failure may lead to limited serviceability, but allow the damage to remain repairable—in other words, cable anchorage failure satisfies performance level 3 of the bridge design code (see Table 1.1). On the other hand, failure of tie-down rods, as it occurred on the Shipshaw Bridge in Canada, can lead to bridge collapse, which affects the life safety and requires a bridge replacement (Level 5 in Table 1.1). Consequently, the monitoring system should be tuned to become more sensitive to damages in local key components with Level 5 consequences on the safety and serviceability of the structure, and the sensor placement should be optimized accordingly. Another observation is that damage accumulates at stiffness discontinuities, such as cable anchors and tie-down rods, joints between different bridge components (tower, deck, foundations), and bearings. Such damage hotspots should be monitored more closely.

1.3 Methodology

1.3.1 Damage Diagnosis

Vibration-based SHM is divided into three stages: (1) the observation of the dynamic system through sensors, (2) the feature extraction, and (3) the statistical evaluation of the features. The statistical evaluation is referred to as the damage diagnosis, where damage is understood as a deterioration of structural design parameters, such as material constants (Farrar and Worden, 2012), cross-sectional values, prestressing forces (Chen and Duan, 2014), support conditions, and mass-distribution parameters (Santos et al., 2013). The primary task of damage diagnosis is to detect the presence of damage, and more advanced tasks include the narrowing down of the exact damage location (localization) and the quantification of its extent. The selected damage diagnosis method is based on the AL approach (Benveniste et al., 1987), with diagnostic capabilities including detection (Basseville et al., 2000), localization (Basseville et al., 2004), and quantification (Döhler and Mevel, 2015). It is based on a similar framework as stochastic subspace-based system identification (SSI), which has developed into a powerful algorithm for the system identification under unknown excitation since the publication of the book by van Overschee and de Moor (1995). The diagnosis method is applied in combination with the subspace-based residual, which circumvents the lengthy estimation of dynamic properties (e.g., natural frequencies), and thus, allows for an online evaluation in real-time. The measurement quantities can be accelerations, velocities, or displacements. More reasons for the choice of this method are given in Section 2.1.2.

1.3.2 Contributions

This thesis aims to build a framework to analyze the minimum diagnosable damage, i.e., the minimum detectable and localizable damage. All considerations are made based on vibration data from the undamaged structure in combination with a finite element model. This avoids empirical and structure-specific experiments, and makes the framework universally applicable to a wide range of civil and mechanical engineering structures, damage-sensitive features, and anticipated damage scenarios from Fig. 1.4. Most considerations target the performance assessment before a SHM system is installed. However, additional self-validation strategies are implemented to test the applicability of the algorithm to real structures, to verify the input parameters, and to test its performance based on non-invasive tests.

All contributions rely on the particular strength of the asymptotic local (AL) approach; it allows for a comprehensive treatment of statistical uncertainties in the damage-sensitive feature, and includes structural information from finite element (FE) models. Hence, the AL approach is not a black box algorithm but considers the physical properties of the considered structure. All contributions are listed in the following:

(1) **Minimum Detectable Damage.** The minimum detectable damage is defined as the minimum change in structural design parameters that can be reliably detected based on changes in the damage-sensitive feature. No site and structure are identical, so a structure-specific training of the damage diagnosis algorithm is required and findings from one structure cannot straightforwardly be transferred to another. Consequently, it is challenging to assess whether or not certain damages can or cannot be detected and localized before the SHM system is installed, making it hard to convince decision-makers of the benefits. Furthermore, statistical uncertainties are typically quantified through empirical approaches or rules of thumb, but they are challenging to validate. With this background, a formula is developed in this thesis that allows for the prediction of the test response to damage based on vibration measurements from the undamaged structure. When combined with a reliability concept, including the probability of false alarms (PFA) and a minimum probability of detection (POD), the minimum detectable damage can be predicted. Among other factors, the predictive framework considers the signal-to-noise ratio of the vibration measurements, and the measurement duration during testing. The prediction of the minimum detectable damage requires a FE model, but is also valid for purely data-driven tests.

(2) **Minimum Localizable Damage.** Damage localization is more complicated than damage detection. The minimum localizable damage is defined as the minimum change in a structural design parameter that can be detected and distinguished from changes in other parameters under an optimal damage localization resolution. A fundamental problem is the over-parametrization of FE models. That means that multiple structural design parameters in the model have a similar effect on the damage-sensitive feature, and, vice versa, it is challenging to identify the design parameters that have changed. The problem can be addressed by

clustering the design parameters, which corresponds to a substructuring of the finite element model into damage localization units, in which damage can be isolated. However, this thesis shows that finding the optimal substructuring arrangement is a multi-objective optimization problem: with an increasing number of substructures, the damage localization resolution increases, but the damage detectability in each substructure decreases. Moreover, an inappropriate substructure arrangement can lead to false localization alarms, which can obscure the actual damage location. The issue is addressed by expanding the predictive framework for the minimum detectable damage to damage localization. Additional considerations are made so the magnitude of false alarms can be predicted based on reference data. Ultimately, a multi-objective optimization scheme is introduced (based on Pareto optimization) to automatically find the optimal substructure arrangement as a compromise between localization resolution, damage detectability, and false alarm susceptibility.

(3) **Sensor Placement Optimization.** Damage detectability and localizability based on global structural vibrations critically depends on the sensor layout. The sensor layout determines the observability of structural modes of vibration, which carry valuable information on local design parameters. In particular, if a small number of sensors is used to monitor large structures, an optimized sensor layout ensures optimal coverage of all monitored design parameters. Many optimization criteria aim to precondition the signal and the signal-to-noise ratio. Some criteria increase the quality of the system identification with minimum uncertainty. Only a few criteria seem to optimize the damage detectability and the probability of detection. However, none of the existing criteria appear to consider the relative decrease in material strength, although this is the decisive quantity for structural design, structural health, and thus, safety. Another issue is that most sensor placement strategies optimize the sensor layout to capture the global vibration behaviour. Still, the structural safety and serviceability typically depend on the integrity of local key components, such as joints, and damage tends to accumulate at well-known hotspots, see Fig. 1.4. Therefore, a sensor placement strategy is developed in this thesis that takes as input the requested detectable damage in individual FE model components, and yields as output the corresponding optimal sensor layout. This strategy maximizes the damage detectability and localizability, and can be employed to find the optimal sensor layout as well as an appropriate number of sensors.

(4) **Monitoring Boundary Conditions.** Change in boundary conditions, i.e., a loss in pretension or support displacements, is a typical damage scenario during extreme events such as earthquakes, see Fig. 1.4. Moreover, excessive support settlements or loss of tension in prestressing tendons (due to slippage or stress corrosion) are common problems in bridge monitoring. Changes in boundary conditions have a global characteristic, as they lead to a global re-distribution of stiffness. Detecting global changes in the dynamic response measures based on global damage diagnosis methods is unproblematic, but distinguishing them from local structural changes is a challenge. In this light, an approach is put forward to calculate

the sensitivity of the damage-sensitive residual toward changes in boundary conditions. The resulting sensitivity vectors can be incorporated into the existing damage diagnosis framework of the AL approach, enabling both the localization of changes and the prediction of the minimum diagnosable changes.

(5) **Model Validation.** Bridges are vital links in primary infrastructure and damaging them for research purposes is generally not an option. Due to each structure's uniqueness, it is challenging to verify whether the theoretical assumptions are fulfilled and whether all input parameters for signal processing are set appropriately. To address the issues, this thesis proposes the application of extra masses as a non-invasive validation technique, and demonstrates the effectiveness based on a laboratory experiment on a steel beam. Moreover, another strength of the predictive framework is showcased by introducing a series of tools and quick checks to verify the input parameter choice based on numerical simulations.

1.3.3 Thesis Organization

The thesis is organized into three parts. *Part I.* includes a state-of-the-art review of global damage diagnosis methods and existing sensor placement strategies (Chapter 2). An introduction to structural dynamics from a control theory perspective is given (Chapter 3), as well as an introduction to damage diagnosis using the asymptotic local approach (Chapter 4). *Part II.* presents the theoretical contributions of this research project and is divided into the minimum detectable damage (Chapter 5), the minimum localizable damage (Chapter 6) and optimal sensor placement (Chapter 7). In addition, an approach is outlined to incorporate changes in boundary conditions into the damage diagnosis framework of the asymptotic local approach (Chapter 8). *Part III.* summarizes practical investigations. First, two case studies are presented (Chapter 9), including a laboratory steel beam and a laboratory cable-stayed bridge. Secondly, self-validation studies are summarized (Chapter 10), and ultimately, the particular strength and limitations of all methods are highlighted in the conclusions (Chapter 11).

Chapter 2

Literature Review

"If I had eight hours to chop down a tree, I'd spend the first six of them sharpening my axe."
— Abraham Lincoln

This work develops a strategy to analyze the minimum detectable damage for vibration-based structural health monitoring (SHM) and to optimize the sensor layout. Both fields are extensively researched. The review is split into two parts: the first part (Section 2.1) revisits existing damage-sensitive features and damage diagnosis methods, and gives reasons for the choice of the asymptotic local (AL) approach. Moreover, existing strategies are touched upon to diagnose changes in boundary conditions, together with previous attempts to quantify the minimum diagnosable damage. The second part (Section 2.2) reviews existing performance criteria and smart optimization algorithms to overcome the problem of combinatorial explosion in large mechanical structures.

2.1 Global Vibration-based Damage Diagnosis

The premise of vibration-based damage diagnosis is that damage alters the stiffness, mass, or damping properties of the structure. Consequently, structural changes can be inferred based on the global system response. The process of damage diagnosis is divided into data acquisition, the extraction of damage-sensitive features, and their statistical evaluation (Farrar and Worden, 2012). Depending on the method, the removal of environmental and operational variables (EOVs) on the damage-sensitive feature is considered a separate step, or integrated into the damage diagnosis method. Correspondingly, this section distinguishes between damage-sensitive features and diagnosis methods. The literature review focuses on global vibration-based SHM, as this work is motivated by the specific needs of the British Columbia Smart Infrastructure Monitoring System (BCSIMS). It is based on recent reviews by An et al. (2019) and Moughty and Casas (2017b), and preceding works by Fan and Qiao (2011), Carden and Fanning (2004), Chang et al. (2003), and Doebling et al. (1996), with a comprehensive overview in Farrar and Worden (2012).

2.1.1 Damage-sensitive Features

For an overall picture, Table 2.1 categorizes the presented damage-sensitive features, where the columns are sorted in ascending order with respect to the signal processing effort. Basic signal statistics form the first category (column 1). Farrar and Worden (2012) summarize that damage causes the peak amplitude to change, as well as the mean, the root mean, and the root mean square

Global Damage-sensitive Features					
Signal statistics	**Transient signals**	**Waveform comparisons**	**Times series models**	**Modal parameters**	**Modal parameter based**
Peak amplitude	Energy (Arias intensity)	Response data	Auto-regressive models	Resonance frequencies	Mode shape curvature
Mean, root mean, root mean square	Higher temporal moments	Covariance function	State space marices	Mode shapes	Strain energy
Variance, standard deviation	Vibration intensity	Power spectral density	Observ-ability matrix	Damping ratios	Modal flexibility
Skewness, kurtosis	Destructive potential factor	Operating deflection shapes	Kalman filter innovations	Ritz-vectors	Yuen functions
Crest factor, K-factor	Decay measures			Modal force vector	

Table 2.1: Damage-sensitive features (Farrar and Worden, 2012)

values. Mattson and Pandit (2006) argues that higher statistical moments (such as the standard deviation, skewness, and kurtosis) are more sensitive to damage than the mean or the variance. Pachaud et al. (1997) employs the crest factor and K-factor as measures of the signal's deviations from the sinusoidal response.

Transient signals form another group, including measures for energy and intensity (column 2). Smallwood (1994) discusses energy measures and higher temporal moments. Moughty and Casas (2017a) perform damage detection on the S-101 bridge using the Arias intensity, vibration intensity, cumulative absolute velocity, destructive potential factor, and others. Farrar and Worden (2012) summarize multiple measures based on the decay of vibration signals, including the 10% duration time and the Hilbert transform.

Waveform comparisons can be made in either the time-domain or frequency-domain (column 3). This includes power spectral density (PSD) as well as covariance functions, and the direct signal response to random excitation. Yin and Tang (2011) evaluate the system response to passing vehicles. Pascual et al. (1999) suggest operating deflection shapes for damage detection to avoid modal identification. Basseville et al. (2000) form a damage-sensitive residual based on the covariance matrix, and Döhler et al. (2014b) propose a similar feature that is more robust to changes in the excitation characteristics. Ultimately, Gres et al. (2017) formulate a criterion based on the

covariance function difference.

Time series models can be used as damage-sensitive features (column 4 in Table 2.1) after fitting them to the vibration record using regression techniques. For example, Fanning and Carden (2001) use the mean and the variance of the auto-regressive (AR) term as a damage-sensitive criterion. Spiridonakos and Chatzi (2015) employ non-linear AR models and minimized the simulation error. Equivalently, stochastic state space models can be employed. For example, Mehra and Peschon (1971) propose the Kalman filter innovations as damage-sensitive criteria. Swindlehust et al. (1995) use the observability as a damage-sensitive matrix for model updating. Time series-based models are suited to detect damage scenarios with non-linear characteristics and to distinguish them from linear changes due to EOVs (Figueiredo et al., 2011).

Modal parameters were among the first damage-sensitive features, and remain state-of-the-art (column 5). Adams et al. (1978) and Cawley and Adams (1979) initialize damage detection based on frequency changes. Since changes in mode shapes are less intuitive to track, Allemang and Brown (1982) propose a correlation measure, called the modal assurance criterion (MAC) for their evaluation, and Lieven and Ewins (1988) put forward a coordinate-by-coordinate MAC, called the coordinate modal assurance criterion (COMAC). Yuen (1985) combines frequencies and mode shapes into a criterion known as the Yueng function. Zouari et al. (2009) consider damping estimates, and Cao and Zimmerman (1999) use load-dependent Ritz vectors (or Lanczos vectors). Ojalvo and Pilon (1988) generate a modal force vector by confronting data-driven frequencies and mode shapes with model-based mass and stiffness matrices. While frequencies are more sensitive to damage than mode shapes (Cury and Cremona, 2012), mode shapes are less sensitive to EOVs (Deraemaeker et al., 2008) and include spatial information (An et al., 2019). Damping is non-linearly influenced by the vibration amplitude (Eyre and Tilly, 1997), and an accurate estimation often fails under unknown force inputs (Brincker and Ventura, 2015). In general, quantifying uncertainties in the modal parameters is equally as important as estimating them (Mellinger et al., 2016).

Features derived from modal parameters constitute the last category of features (column 6). Pandey et al. (1991) propose the mode shape curvature, which amplifies discontinuities in mode shapes by deriving them. Pandey and Biswas (1994) follow-up on this by introducing the modal flexibility method. Stubbs et al. (1992) employ the modal strain energy, which exhibits a higher sensitivity to local damages than modal parameters (Yam et al., 1996).

2.1.2 Damage Diagnosis Methods

The presented damage diagnosis methods are categorized into statistical pattern recognition (including supervised and unsupervised learning), finite element (FE) model updating, parametric change detection, and stochastic load vectors. The diagnosis depth is generally divided into four hierarchical steps with increasing complexity (Rytter, 1993):

- *Stage 1*: Detection
- *Stage 2*: Localization
- *Stage 3*: Quantification or classification
- *Stage 4*: Lifetime prognosis

a) Unsupervised Learning

Outlier analysis is an unsupervised learning technique. The basic idea is to assume a particular shape for the probability density function (PDF) and to detect changes that are significant in a statistical sense. In the simplest case, the distance to the mean value can be quantified through the number of standard deviations. Mahalanobis (1936) expands this idea to multivariate variables through the Mahalanobis distance (MD). Rousseeuw and van Driessen (1999) advance the MD by pairing it with the minimum covariance determinate (MCD) estimator, which reduces the influence of outliers in the training phase. Moshtagh (2005) applies the minimum volume enclosing ellipsoid (MVEE) for outlier detection. An application of the MD can be found in Worden et al. (2000), where Dervilis et al. (2014) apply all three outlier detection algorithms to the Z-24 Bridge in Switzerland under environmental influences and concludes that the MVEE performs the best, followed by the MCD, and finally, the MD.

Statistical process control is another field of unsupervised learning. The methods include several static and dynamic test statistics that are repeatedly evaluated and plotted in control charts for visualization. For example, Page (1954) introduces a uni-variate approach, the cumulative sum (CUSUM) chart. Roberts (1959) advances the tests through the exponentially weighted moving average (EWMA) chart, which dynamically adapts to the gradual changes while detecting abrupt changes. The Hotelling T^2 or Shewhart control chart is a multivariate extension of the Mahalanobis distance. Crosier (1988) and Lowry et al. (1992) put forward multivariate versions of the CUSUM and the EWMA chart. An overview of statistical control charts is given by Montgomery (2007). Kulla (2003) detects damage on the Z-24 bridge using the univariate and multivariate Shewhart charts as well as the CUSUM and EWMA charts, applied to modal parameters. Magalhães et al. (2010) apply the Shewhart chart to the natural frequencies of a long-span arch bridge. Kalman filters can also be employed for statistical process control. Kalman filters observe past measurements and predict future signals based on state space models. The difference between the predicted and the measured signals is called "innovation." Damage causes a change in the distribution properties of the innovation, so it can be inferred based on statistical hypothesis tests. Mehra and Peschon (1971) propose the idea of testing the innovation sequence for whiteness. The idea is revived by Bernal (2013), who proposes a modified whiteness test that suppresses the effect of noise changes and highlights the effect of damage, by adjusting the time lag intervals.

Multivariate statistical approaches are unsupervised learning techniques that are often applied for dimensionality reduction. Yan et al. (2005a) demonstrate how to remove correlations within data

sets using principal component analysis (PCA) and followed-up with a piece-wise linear approach to remove non-linear trends (Yan et al., 2005b). Kulla (2004) achieves similar results using factor analysis (FA). Kramer (1991) proposes non-linear PCA, known as auto-associative neural networks (AANN). Nguyen et al. (2014) employ Kernel principal component analysis (KPCA) to remove the non-linear effects. Cross et al. (2011) apply cointegration, which can also be applied without measuring the influencing variables. Multivariate statistical approaches are suitable tools for data normalization, i.e., the removal of the influence of EOVs on damage-sensitive features, without having to measure them. They have been successfully applied to the Champangshiehl Bridge in Luxembourg (Nguyen et al., 2014), the Yeongjong Grand suspension bridge in Seoul (Oh et al., 2009), the Infante D.Henrique arch bridge (Magalhães et al., 2012), and many others.

Cluster analysis is another class of unsupervised learning techniques (Sohn and Oh, 2009). Using cluster analysis, the data points are categorized into groups, and outliers can be detected regardless of the underlying distributions. Santos et al. (2015) apply cluster analysis to the Samora Machel Bridge for damage detection, and explain some shortcomings of the k-means clustering algorithm in comparison to a cloud clustering algorithm.

b) Supervised Learning

Regression analysis is a supervised learning technique. It is a suitable means to remove linear trends from data by fitting polynomial curves. Cornwell et al. (1999) employ a linear least-squares regression model. Ding and Li (2011) increase the complexity of the regression models through non-linear polynomials. Dervilis et al. (2015) apply the least trimmed square (LTS) estimator, which includes an initial screening procedure to remove erroneous data points or outliers. Application to bridge structures include the Runyang Suspension Bridge in China (Ding and Li, 2011), the Infante D. Henrique arch bridge in Portugal (Magalhães et al., 2012), the Tamar bridge in the United Kingdom, and the Z24 Bridge in Switzerland (Dervilis et al., 2015).

Artificial neural networks (ANN) constitute another group of supervised learning methods. ANN go back to Rosenblatt (1962), who developed a 3-layered network structure inspired by the architecture of the human brain (the perceptron). If a neural network exhibits more than three layers, it is counted as a "deep" learning network. Patterson and Gibson (2017) divide deep learning approach into four classes: unsupervised pretrained networks, convolutional neural networks, recurrent neural networks, and recursive neural networks. Conventional and deep learning approaches are supervised in the sense that they correlate given inputs to labelled outputs, where deep learning approaches include the feature extraction in the learning process and can be fed with raw data (Avci et al., 2021). A more recent development is the concept of transfer learning, where the findings from damaged structures are transferred to other (possibly undamaged) structures. Lee et al. (2005) apply ANN to detect mode shape changes on the Hannam Grand Bridge. Li et al. (2009b) use ANN to assesses modal parameters under varying wind and temperature conditions.

Jin et al. (2015) apply ANN to the Meriden Bridge (a composite steel girder bridge) in the U.S., and selected the weights based on a Kalman filter procedure.

Support vector machine techniques can be applied for supervised and unsupervised machine learning. The main idea of support vector machine (SVM) techniques is to separate data points through hyperplanes (straight lines in 2-D) with the largest margin possible. Applications to bridge structures include the Z24 Bridge in Switzerland Shi et al. (2016).

c) Model Updating

In FE model updating, the information from data-driven features is used to update numerical models (Friswell and Mottershead, 1995). The objective is to set up the equation of motion in modal coordinates, using the model-based mass, stiffness, and damping matrices, and the measured frequencies and mode shapes. If the model-based matrices do not reproduce the data-driven features, the system matrices or the underlying parameters are modified accordingly.

Direct updating methods directly solve for the matrix entries. If the model-based system matrices do not reproduce the measured modal parameters, a modal force vector evolves. This term can be understood as a harmonic force that is to be applied so the system matrices reproduce the measured modal parameters (Ojalvo and Pilon, 1988). The goal of matrix updating is to modify the matrix entries, so the modal force is minimized, for example, by evaluating the Euclidean norm. The methods are computationally expensive, susceptible to noise (as noise smears the stiffness changes over the whole stiffness matrix), and neglect the physical properties of the structure (Marwala, 2010). That means that system matrices may loose their symmetry, may become populated instead of banded, and nodes may loose their connectivity.

Optimal matrix updating methods employ analytical instead of numerical solutions to obtain matrices from the damaged systems (Marwala, 2010). They employ a closed-form, direct solution to compute the damaged model matrices or the perturbation matrices using Lagrange multipliers or penalty-based optimization methods (Smith and Beattie, 1991; Hemez, 1993). Baruch (1978) defines the modal force as the damage-sensitive residual, places symmetry constraints on the system matrices, and minimizes the Frobenius norm of global system matrix perturbations. Instead of minimizing the norm of the perturbation matrix, Kaouk and Zimmerman (1994) minimize the rank of the perturbation matrix, which reduces the smearing effects. Finally, Kaouk et al. (2000) extend the approach from the stiffness matrix to all dynamic system matrices, including the mass and the damping matrix. The method has been applied to the I-40 Bridge data (Simmermacher et al., 1995). However, a limitation (similar to direct model updating) is that the resulting matrices may not be physically realistic (Marwala, 2010).

Eigenstructure-assignment methods are based on control theory, where a fictitious controller is added to minimize the modal force residual. The method has been applied to a cantilever

beam (Zimmerman and Kaouk, 1992), planar truss structures (Lindner and Goff, 1993), and three-dimensional truss structures (Lim and Kashangaki, 1994). It assumes that the number of sensor locations is equal to the number of degrees of freedom (DOF) (Marwala, 2010), so it can only efficiently be applied in combination with a modal reduction technique, such as Guyan reduction, dynamic reduction, or others.

Sensitivity-based methods update the mass and stiffness matrices after evaluating the sensitivity of the error term (e.g., the modal force vector) using first-order sensitivity analysis. Hemez (1993) initially proposes the method, which evaluates the sensitivities toward structural parameters instead of system matrix entries. For this reason, it is now considered one of the most successful model updating methods based on vibration measurements (Mottershead et al., 2011). Applications to cable-stayed bridges include the Safti Link Bridge in Singapore (Brownjohn and Xia, 2000), the Kap Shui Mun Bridge (Zhang et al., 2001), the Bill Emerson Memorial Bridge in the U.S. (Zárate and Caicedo, 2008), the tower of the Runyang Bridge (Ding and Li, 2008), the Tatara Bridge in Japan (Asgari et al., 2013), and many other suspension bridges, girder bridges, and a pontoon bridge, as summarized by Petersen and Øiseth (2017).

Bayesian model updating allows one to obtain updated probabilities of system parameters (modal or structural parameters) as well as probabilistic damage measures based on system measurements. Based on the considerations in Beck and Katafygiotis (1998), Hemez and Doebling and Vanik et al. (2000) are among the first to apply probabilistic approaches to SHM. Sohn and Law (1997) and Sohn and Law (2000) compute probabilities of different damage scenarios and apply the concepts to a bridge column. Papadimitriou et al. (2001) employ the framework to obtain structural reliability updates. Beck and Au (2002) put forward an approach based on an adaptive Markov chain Monte Carlo simulation. Papadimitriou and Papadioti (2013) increase the computational efficiency by introducing component mode synthesis techniques and applied them to the simulated measurements of the Metsovo highway bridge in Greece. Kim et al. (2015) additionally consider the EOVs while applying the method for long-term monitoring of a plate-Gerber bridge. Additional applications include the Dowling Hall footbridge in the United States (Behmanesh and Moaveni, 2015), the Rivière-aux-Mulets Bridge in Canada (Sanda et al., 2017), the Saraighat truss bridge in India (Mustafa et al., 2015), and others. Bayesian-based model updating is considered the most comprehensive technique to deal with uncertainties, but it is not particularly suited to deal with epistemic uncertainty (Simoen et al., 2015).

Interval model updating is an alternate approach to uncertainty quantification. Instead of PDFs, membership functions are employed to define the uncertainties associated with the measured outputs. Zheng et al. (2020) divide the method into three categories: the interval algorithm, the vertex solution, and global optimization methods. Fang et al. (2015) apply the interval algorithm and improves it through interval response surfaces. Khodaparast et al. (2011) apply the parameter vertex method to model updating. Liu et al. (2009), Haag et al. (2010), and Erdogan and Bakir (2013) utilize approaches based on fuzzy arithmetic. Global optimization methods include but are

not limited to the genetic algorithm (Pawar and Ganguli, 2003), the particle swarm optimization (Meng et al., 2015), radial basis function neural networks (Deng et al., 2017), and Kriging methods (Khodaparast et al., 2011). Simoen et al. (2015) conclude that fuzzy model updating is better suited to handle epistemic uncertainties, and that it is computationally more efficient; however, it only allows for an assessment of worst-case uncertainties, where Bayesian approaches provide more detailed information.

Subspace fitting estimates the dynamic observability matrix in the subspace of covariance functions, and updates the model-based observability through linear regression. Swindlehust et al. (1995) initially develop the subspace fitting approach. Gautier et al. (2013) improve its accuracy, and Gautier et al. (2015) introduce a modal truncation approach to increase numerical efficiency. Moreover, Gautier et al. (2017) develop a method that quantifies the uncertainties in the data and propagates them through the system identification process to the structural parameters.

d) Parametric Change Detection

Parametric change detection has evolved from unsupervised learning methods. The distinctive feature is that the information from dynamic or structural system models is used to parametrize data-driven tests but, in contrast to FE updating, the model is not modified during the damage diagnosis, which makes the methods numerically efficient.

Kalman filter-based methods constitute the first group of parametric change detection methods. Döhler et al. (2015) introduce the perturbed innovation test, which introduces a parametric perturbation term into the Kalman filter innovations, transforming it from an unsupervised learning technique into a model-based test. The approach is extended by Döhler et al. (2017) to damage localization.

Asymptotic local methods form the second group. They assume a Gaussian distribution for the damage-sensitive feature and diagnose damage based on statistical hypothesis tests, such as the generalized likelihood ratio (GLR) and the minmax test, which are linked to system parameters through first-order sensitivity vectors. Benveniste et al. (1987) originally propose the asymptotic local approach. Inspired by the book by van Overschee and de Moor (1995), Basseville et al. (2000) reformulate the underlying concepts and pave the way for change detection in modal parameters. Basseville et al. (2004) expand the method to damage detection in model-based parameters (in FE models) and enabled damage localization. Balmès et al. (2008b) and Allahdadian et al. (2019) refine the damage localization in over-parametrized systems using a k-means clustering and hierarchical clustering approaches. Döhler et al. (2014b) reformulate the damage-sensitive feature to increase the robustness toward changes in excitation properties, and Balmès et al. (2008a) propose methods for data normalization together with Balmès et al. (2009) and Viefhues et al. (2020). Döhler et al. (2016) increase the numerical efficiency of the statistical hypothesis tests for damage detection and localization, and outline a damage quantification approach. The method has been applied for

damage detection in the S101 Bridge in Austria (Döhler et al., 2014a), the Pitt River cable-stayed bridge in Canada 2014 (Ventura et al., 2014), the Yonghe cable-stayed bridge in China 2016 (Zhou et al., 2016), and numerous laboratory experiments (Siegert et al., 2010).

e) Stochastic Load Vectors

The stochastic dynamic damage locating vector (SDDLV) method sets up the transfer matrix in the frequency domain for both the damaged and the reference state, and quantifies the difference using a discrete load vector. Bernal (2010) first proposes the SDDLV for damage detection and localization, and later expands it to damage quantification based on flexibility changes (Bernal, 2014). Marin et al. (2012) conduct further studies to quantify the uncertainties, and Marin et al. (2015) propose a more robust approach to evaluate the diagnosis results based on statistical aggregation. Bhuyan et al. (2017b) lift multiple theoretical constraints and extend the method to multiple mode sets, significantly reducing the number of required sensors. Ultimately, Bhuyan et al. (2017a) introduce a sensitivity-based approach to damage quantification. The SDDLV has successfully been applied to a laboratory model of a truss bridge (Jang et al., 2012) as well as the model of the St. Nazaire cable-stayed bridge in France (Bhuyan et al., 2018).

Method Selection

All presented damage diagnosis methods can be classified into data-driven and model-based approaches (Fan and Qiao, 2011). Model-based approaches assume that a detailed numerical model is available, where data-driven approaches depend on experimental response data or data-driven system models (e.g., AR or state space models). Unsupervised learning is a powerful data-driven approach, but it fails to provide diagnostic capability beyond detection in most cases (Farrar and Worden, 2012). Supervised learning is also data-driven and allows for an in-depth damage diagnosis; however, obtaining a sufficient amount of training data for all anticipated damaged scenarios is an unresolved challenge. On the other hand, model updating approaches exhibit multiple challenges related to the realistic modelling, the damage diagnosis in over-parametrized systems, and the computational effort. Parametric change diagnosis evaluates model-based information in the reference state, but the damage testing is based on data. This leads to a low computational burden while preserving the localization and quantification capability. The AL approach is considered a promising method to achieve the objectives of this thesis for the following reasons:

- It is applicable to a wide range of structures, damage scenarios, and damage-sensitive criteria (Basseville et al., 2000; Döhler et al., 2014b; Gres et al., 2017).
- The damage diagnosis has real-time capabilities. In particular, the subspace-based residual leads to short measurement durations, as it is formed in the time-domain and circumvents a modal system identification. The damage diagnosis itself is numerically efficient because the model is not updated.

- Parametrization is optional, meaning damage detection can also be performed without a FE model. One non-parametric test is available for data-driven damage detection and one parametric test, where the data-driven features are linked to data-driven modal parameters.
- The problem formulation is comparatively simple due to the few input parameters and because the problems of damage detection, localization, and quantification are split into individual sub-tasks.
- Individual structural parameters can be selected for monitoring. Linking the damage detection test to structural models focuses the damage diagnosis on local material properties, cross-sectional values, geometrical properties, and mass properties.
- The damage localization resolution can be adjusted. Damage localization requires additional information from FE models, which are typically over-parametrized. However, the parameters can be clustered and the user can adjust the localization resolution.
- False localization alarms are considered. The minmax localization test considers the effect that damage in some structural parameters has on others, and therefore, reduces false localization alarms.
- Uncertainties in the damage-sensitive feature are considered through a profound theoretical framework. This allows for the describing of the statistical properties of the damage diagnosis tests in both the training and the damaged state through Gaussian distributions.
- The performance can be analyzed through the probability of detection. This shows to be a promising performance measure for sensor placement optimization (Döhler et al., 2013).

More background on the discussed points from above is given in Chapter 5.

2.1.3 Changes in Boundary Conditions

Thus far, the AL method has only been used to detect and localize damage in material properties or cross-sectional values. Changes in boundary conditions (support conditions or prestressing forces) are typical damage scenarios on bridges (see Fig. 1.4). However, for localization and quantification, such damage scenarios have to be parametrized using FE models. Therefore, the following paragraphs review existing methods to parametrize changes in boundary conditions.

Teughels and de Roeck (2004) account for varying soil stiffness of the Z24 Bridge in Switzerland through translational springs. Subsequently, the calibrated model is employed for damage detection using model updating; however, the spring stiffness itself is not considered for damage detection.

Siddesha and Hegde (2017) consider support settlements and rotations where the soil reaction forces are calculated based on empirical formulas. The study is based on two-dimensional

frame structures with two and three storeys. The imposed displacement causes strains within the structure, which are detected using the flexibility method.

Elsaid and Seracino (2014) model support displacements by placing a foundation pile under the support and changing the corresponding beam length. This study aims to detect scour on bridges using the mode shape curvature and flexibility-based deflections and curvatures. The authors highlight the significance of horizontal modes of vibration for the detection of changes in support conditions.

Mottershead et al. (1996) change multiple geometric properties to accurately model boundary conditions and joints using model updating. Based on the model of a welded joint, the off-set parameters for the beam centre lines are proposed for model updating. Moreover, the length and thickness of FEs near clamped boundaries are suggested.

Gladwell and Ahmadian (1995) propose another model updating approach, which is known as the generic element method. Herein, the eigenvalues and eigenvectors of individual FE are modified in substructures near supports. Each eigenvalue can be understood as a spring coefficient for a deflection defined by the mode shapes vector, as later summarized by Mottershead et al. (2011).

Zhou and Song (2016) model changing boundary conditions using rotational springs and stress stiffening effects. The study's goal is to remove the effect of EOVs on the vibration data from a pedestrian bridge. The influence of varying support conditions (due to soil saturation of freezing) is modelled through rotational springs and the axial member forces (due to uniform temperature changes) are considered through the geometric stiffness term in the global stiffness matrix. The geometric stiffness term is also known as stress stiffening, and describes the stabilizing or destabilizing effect of axial member forces. The paper further indicates that the stiffness terms due to large deflections and large deformations (strain) are negligible during ambient vibration monitoring.

Mordini et al. (2007) present a model updating approach to parametrize a loss of cable forces based on the geometric stiffness parameters. The approach is based on a simply-supported beam model, and the application to prestressed concrete beams is showcased. It is classified as a local monitoring approach, as each cable/beam requires an individual sensor to measure transverse oscillation.

Mordini et al. (2008) apply the same approach for the model updating of cable forces in two full-scale bridges, the Lanaye Bridge and the Tulln Danube Bridge. The authors conclude that the method should be further developed, so it is universally applicable to a wide range of structures—and not just simply supported beams.

Lieven and Greening (2001) highlight the importance of prestressing forces in modal analysis modelled through the geometric stiffness term. The study is based on a simple truss structure

with prestressed diagonals. The study concludes that prestress significantly changes the dynamic behaviour.

Breccolotti et al. (2009) critically discuss the monitoring of prestressing forces. The study concludes that pretension forces should always be included for structures with external prestressing tendons. For bonded tendons, the prestressing forces should only be considered if non-linear material models are employed.

Change in support conditions can be modelled through changes in spring parameters, including translational and rotational springs, elastic bedding, and subsoil stiffness. Geometrical properties may also be used for modelling, including offset parameters of beams at joints, or the geometrical lengths or thickness of support near elements. On the other hand, the parameters of the geometric stiffness matrix appear to be appropriate for damage parametrization of changes in axial member forces.

2.1.4 Minimum Diagnosable Damage

The AL approach can detect, localize, and quantify damage; however, no universal method exists to evaluate whether anticipated damages can be detected before they occur. For that reason, previous attempts to quantify the minimum diagnosable damage are revisited in this section.

Coppolino and Rubin (1980) propose a framework to predict the minimum detectable damage for modular oil platforms based on empirical estimates for the uncertainties. The formula is based on frequency changes estimated from ambient vibrations, and applies to modular offshore oil platforms with a varying number of bays and damage scenarios in underwater trusses. It includes reliability considerations and empirical uncertainty estimates regarding the varying sea state, deck mass (due to the filling of oil tanks), maritime growth, and minor foundation changes. The resulting curves link the frequency thresholds to the number of truss members that have failed, and the number of effective bays on the platform.

Juneja et al. (1997) derive a formula to predict the minimum localizable damage based on a supervised learning approach. The approach employs input-output measurements, and the damage-sensitive features are the peak amplitudes, natural frequencies, and the flexibility matrix. Using a contrast maximization approach and average angle technique, the measured features are compared to features in the damage database, and the most likely scenarios are selected. Ultimately, detectability of damage is quantified based on the damage and the error magnitude in the measurements. For proof of concept, the method is applied to a laboratory truss structure.

Schoefs et al. (2009) focus on non-destructive testing methods and revisit reliability-based concepts to define detectability. For verification of test results, the probability of false alarms (PFA) and the probability of detection (POD) are used. The concepts are combined into what are known as receiver operating characteristics (ROC) curves. The performance of the damage diagnosis is

optimized by minimizing the PFA and maximizing the POD for a given detection threshold. This approach is applied for the non-destructive testing of coastal and maritime structures, where a threshold is set for the loss of thickness of the steel materials due to corrosion.

Afshari et al. (2009) attempt to quantify the minimum detectable fatigue crack size in Euler-Bernoulli beam models. The approach is based on frequency changes and impedance measurements. Experimental studies on a laboratory aluminum beam result in a minimum detectable frequency change of 0.27 Hz and a minimum crack size of 0.5 mm. The authors conclude that impedance measures cannot quantify damage as the damage index saturates.

Hoell and Omenzetter (2016) evaluate the minimum crack length due to disbonding in wind turbine blades. Using a genetic algorithm (GA) and the Fisher information, the optimal AR model coefficients are selected as damage-sensitive features and evaluated through the T^2-test. The numerical results indicate that a minimum crack length of 2.2% can be detected. The authors further indicate that the detectability depends on the AR coefficient subset selection, the measurement duration, the signal-to-noise ratio, and the confidence level (reliability requirements).

Cavalagli et al. (2018) study the minimum detectable damage on a masonry bell-tower due to earthquakes. Using natural frequencies as damage-sensitive features, the influence of EOVs are removed through linear regression, and damage is detected through the T^2-test. The numerical results claim that the minimum detectable frequency shift is 0.1%.

Methods to quantify the minimum detectable damage are mostly empirical, problem-specific, restricted to specific element types (such as trusses or Euler-Bernoulli beams), or based on supervised learning strategies. Reliability-based measures, such as the PFA and the POD appear to be suitable measures to assess the detectability. Finally, empirical studies imply that the reliability of the damage detection can be increased through an increased measurement duration, but no analytical relationship has been found.

2.2 Optimal Sensor Placement

This review focuses on sensor placement strategies for global vibration-based methods, and is divided into performance criteria and optimization methods.

2.2.1 Performance Criteria

Mode Visualization. If no FE model is employed, mode shapes are the only visual means to interpret the estimated modes of vibration. Hence, it is desirable to select measurement points along the edges of the structure and points that sufficiently capture the structure's deformed shape for all considered modes of vibration.

Mode Shape Amplitude. The mode shape amplitude is a measure for the signal strength. Ambient vibration testing is based on the idea that every structure tends to vibrate at their natural frequencies in the absence of driving forces. Indeed, not frequencies but mode shapes are measured through vibration sensors. Their amplitude can be measured through the mode shape summation plot (de Clerck and Avitable, 1996)

$$\mathrm{MSSP}_i = \sum_{j=1}^{N} |\Phi_{ij}| \tag{2.1}$$

where $j = [1, 2, ..., N]$ are the mode shape numbers and i is the DOF where the sensor is placed. Equivalently, the driving point residue (DPR) (Chung and Moore, 1993) can be employed

$$\mathrm{DPR}_i = \sum_{j=1}^{N} \frac{\Phi_{ij}^2}{\omega_j}, \tag{2.2}$$

where ω is the natural (circular) frequency of the j-th mode, or the eigenvalue vector product (EVP) (Larson et al., 1994)

$$\mathrm{EVP}_i = \prod_{j=1}^{N} |\Phi_{ij}|. \tag{2.3}$$

Modal Kinetic Energy. The kinetic energy is another measure for the signal-to-noise ratio (Kammer, 1991). In modal coordinates, the kinetic energy per mode is defined as

$$\mathrm{MKE}_{ij} = \Phi_{ij} \sum_{s} M_{is} \Phi_{sj} \tag{2.4}$$

where Φ_{ij} is the mode shape coordinate of mode j at location i and M_{ij} is the corresponding mass matrix entry. Unfortunately, the MKE depends on the mesh size of FE models, as DOFs in regions with a coarser mesh accumulate more mass (Papadopoulos and Garcia, 1998). It could also be assessed in power spectral density plots, where modes of vibration manifest themselves in distinct energy peaks (Brehm et al., 2013).

Modal Assurance Criterion. The modal assurance criterion is a measure for the identifiability of modes and their distinguishability (Allemang and Brown, 1982). It is defined as

$$\mathrm{MAC}_{ij} = \frac{(\boldsymbol{\Phi}_i^T \boldsymbol{\Phi}_j)^2}{(\boldsymbol{\Phi}_i^T \boldsymbol{\Phi}_i)(\boldsymbol{\Phi}_j^T \boldsymbol{\Phi}_j)}, \tag{2.5}$$

where T denotes the transpose of the vectors and i and j, are the column indices for the mode shape matrix $\boldsymbol{\Phi}$. The MAC criterion yields one if two mode shapes are identical and zero if they are orthogonal. An optimization goal is to minimize the off-diagonal terms, because if all modes are fully distinguishable, the MAC matrix is equal to the identity matrix $\mathbf{MAC} = \mathbf{I}$. Several other

criteria exist to measure the orthogonality of mode shapes, e.g., the modal scale factor, or the mass weighed MAC (Penny et al., 1994).

Singular Value Decomposition Ratio. The singular value decomposition ratio (SVDR), or condition number, is a measure for the distinguishability of modes. It is defined as

$$\text{SVDR} = \frac{\sigma_{max}}{\sigma_{min}}, \tag{2.6}$$

where σ_{max} and σ_{min} are the largest and the smallest singular values. In an ideal case, the SVDR is one, and for all other cases, it is greater than one. The SVDR is often applied to model updating problems (Friswell and Mottershead, 1995), as a low value leads to a numerically stable condition for mode shape expansion.

Fisher Information. The Fisher information matrix (FIM) quantifies the information on system parameters that is contained in data. For a random variable $\mathbf{X}$ that approximates a multivariate Gaussian distribution, it is defined as

$$\text{FIM}_{ij} = \boldsymbol{\mathcal{J}}^T \boldsymbol{\Sigma}^{-1} \boldsymbol{\mathcal{J}} \tag{2.7}$$

where $\boldsymbol{\mathcal{J}} = \frac{\partial \text{E}[\mathbf{X}]}{\partial \boldsymbol{\theta}}$ is the sensitivity of the mean vector of the observed variables towards changes in a system parameter vector $\boldsymbol{\theta}$, and $\boldsymbol{\Sigma}$ is the covariance matrix (the dispersion) of the observed variable. Various criteria can be used for optimization, e.g., the absolute magnitude of the main or off-diagonal terms, the matrix trace (the sum over the main diagonal), the determinant (Kammer, 1991), the minimum singular value of the matrix (Reynier and Abou-Kandil, 1999), or the SVDR (Kim et al., 2001). A typical SHM application is to estimate the information that a vibration signal carries on modal parameters. For example, the effective independence ratio (Kammer, 1991), aims to maximize the distinguishability between mode shapes. Other studies evaluated the Fisher information in combination with statistical damage detection tests to optimize the POD (Basseville et al., 1987; Döhler et al., 2013).

Information Entropy. The information entropy may be understood as a measure for uncertainty in estimated system parameters (Papadimitriou, 2004). It is defined as

$$IE = E_{\boldsymbol{\theta}}[-\ln p(\boldsymbol{\theta}|\mathbf{X})], \tag{2.8}$$

where $E_{\boldsymbol{\theta}}$ is the expectation operator and $\mathbf{X}$ is a random variable that contains information on the parameter vector $\boldsymbol{\theta}$. Previous applications involve the entropy of spectral density estimates (Yuen et al., 2001), the entropy of stiffness-related parameters (Papadimitriou, 2004), and the entropy of damage locations (Cantero-Chinchilla et al., 2020).

Mutual Information. The mutual information criterion is a measure for the redundancy of information within two sensor sets (Boller et al., 2009). It is defined as

$$\mathrm{MI} = \log_2 \left(\frac{P_{AB}(a_i, b_j)}{P_A(a_i) P_B(b_j)} \right), \tag{2.9}$$

where a_i and b_j are the measurements of the two sets A and B, with the corresponding PDFs $P_A(a_i)$ and $P_B(b_j)$, respectively. The term $P_{AB}(a_i, b_j)$ denotes the joint PDF between A and B. The MI is zero if the information measured through b_j and a_i are not related. An optimization goal could be to minimize the redundancy or to ensure a certain degree of redundancy, as this increases the robustness towards sensor malfunction.

Dynamic Observability. The observability is a measure for how well internal dynamic states can be inferred from sensor readings at distributed DOF. The vibration model can be observable or not, a binary condition that can be checked by evaluating the observability rank (OR) (Morari and Stephanopoulos, 1980)

$$\mathrm{OR} = \mathrm{rank}(\boldsymbol{\mathcal{O}}_{p+1}) = \begin{bmatrix} \mathbf{C}^T & (\mathbf{CA})^T & \cdots & (\mathbf{CA}^p)^T \end{bmatrix}^T. \tag{2.10}$$

where $\mathbf{A}$ and $\mathbf{C}$ are the state transition and the output matrices and p is the number of block rows. A system is observable if the observability matrix's rank is equal to the system order (Inman, 2017). The degree of observability can be quantified through the observability gramian (OG)

$$\mathrm{OG} = \sum_{k=0}^{p} (\mathbf{A}^T)^k \mathbf{C}^T \mathbf{C} \mathbf{A}^k. \tag{2.11}$$

Possible optimization goals are to maximize the minimum eigenvalue of the OG (Hać, A., & Liu, L., 1993; Ko et al., 1994; Georges, 1995), its determinant, or matrix trace (Müller and Weber, 1972). Another goal could be to achieve a balanced realization by selecting Gramians with equal values on the main diagonal (Moore, 1981). This extends the primary purpose from basic signal processing to uncertainty reduction in modal parameters, and improved FE model updating capabilities. In subspace fitting (Swindlehust et al., 1995), for example, the data-driven observability is compared to the model-based observability.

Representative Least Squares. The representative least squares method can be used in combination with an arbitrary modal identification method to improve the mathematical model of the vibrating structure, and thus, to reduce the uncertainties in the modal estimates (Li et al., 2009a). The central equation reads

$$\mathrm{RLS} = (\hat{\mathbf{q}}_i - \hat{\mathbf{q}}_{opt})^T (\hat{\mathbf{q}}_i - \hat{\mathbf{q}}_{opt}), \tag{2.12}$$

where the deviation of the mode shape coordinates $\hat{\mathbf{q}}_i$ from an optimal set $\hat{\mathbf{q}}_{opt}$ is evaluated. An optimized sensor layout may be found for a minimum RLS, as this corresponds to minimal uncer-

tainties regarding the modal parameters.

Kalman Filtering. Kalman filters (KF) are matrix operators that predict the future vibration states based on past measurements. A criterion that may be used for sensor placement optimization is the covariance of the state prediction error (Kumar and Seinfeld, 1978). The smaller the covariance, the better the approximation of the vibrating structure, and the smaller the uncertainty in the modal parameters. For methods where the characteristics of the prediction error are used as damage-sensitive criteria, e.g., the innovation whiteness test and the perturbed innovation sequence method (Bernal, 2013; Döhler et al., 2015), this optimization criteria increases the probability of detecting damage.

Kriging Prediction Error. With origins in the gold mining industry, Kriging is a geo-statistical interpolation technique that predicts response quantities and their covariances at unmeasured DOF. The mean square error depends on the sensor positions and the covariance characteristics of the wave pattern. It can be understood as a measure for the uncertainty and the spatial coverage of a mathematical model (Papadimitriou et al., 2005).

Based on the Nottingham Suspension Bridge, Meo and Zumpano (2005) compare EVP, the MKE, the EfI, the EfI-DPR, and Kriging. The mass weighed version of the effective independence (EfI-DPR) was presented as the best criterion, as it resulted in a symmetrical sensor arrangement with a convincing signal-to-noise ratio. Marano et al. (2011) confirm these findings by analyzing the optimal sensor layout on a broadcasting antenna. The paper highlights the similarity in the sensor geometry obtained through the EfI and the MKE approach. Moreover, it criticizes the EVP and DPR because of the irregular sensor layout with an unreasonable concentration of sensors at the free end of the antenna, while neglecting the mass concentration at its base. Gomes et al. (2018) perform additional case studies on free and fully clamped plates, and Li et al. (2008) analyze a ladder structure. All optimization criteria lead to distinctly different sensor layouts, and good sensor layouts are usually close to large vibration amplitudes.

To summarize, Table 2.2 categorizes all presented performance criteria with respect to their primary purpose. Many criteria aim to precondition the vibration signal by increasing the signal-to-noise ratio and quantifying the redundancy of information. Some criteria optimize the quality of the modal identification by reducing the uncertainties in modal parameters and maximizing the mode distinguishability. A few performance criteria aim to optimize the detectability of damage. None of the reviewed criteria appears to quantify the minimum detectable damage, for example, in percent of a material strength or stiffness value, although this is the decisive quantity for structural design, structural health, and thus safety.

One strategy that has shown to be efficient is to consecutively apply criteria of increasing informative value. For example, in the effective independence method, the modal kinetic energy is applied first, followed by the Fisher information (Kammer, 1991). On one hand, this guarantees that

Lvl.	Primary purpose	Secondary purpose	Criteria
1.	Signal preconditioning	Signal-to-noise ratio	# Mode shape summation plot
			# Eigenvalue vector product
			# Driving point residue
			# Modal kinetic energy
			# Observability rank
		Signal redundancy	# Mutual information
2.	Modal parameter ID	Mode differentiability	# Modal assurance criterion
			# Singular value decomposition ratio
			# Effective independence distribution
		Uncertainty reduction	# Mean square error using kriging
			# Representative least squares
			# Observability gramian
3.	Damage diagnosis	Detectability	# Fisher information
			# Kalman filter innovation
		Localizability	# Information entropy

Table 2.2: Optimization criteria categorized with respect to the primary purpose

the instrumentation can be used for several purposes. On the other hand, the sensor optimization procedure becomes more efficient, as low-level optimization criteria (on Level 1 in Table 2.2) can efficiently be calculated for a large number of sensor locations. High-level optimization criteria, such as the Fisher information, should only be evaluated for a (relatively) small number of sensor configurations, or when combined with a smart optimization method, with more information in the subsequent section.

2.2.2 Optimization Algorithms

A fundamental challenge in sensor placement optimization is the problem of combinatorial explosion. That means that the number of possible sensor locations is so large that it is infeasible to evaluate the selected performance criterion for all combinations in an exhaustive search approach, particularly if high-level criteria are used, such as the Fisher information. For a fixed number of sensors, the number of combinations is

$$N_c(r, r_{pos}) = \frac{r_{pos}!}{(r_{pos} - r)!r!} \tag{2.13}$$

where r is the number of sensors and r_{pos} is the number of possible sensor locations. For example, if 20 sensors are to be placed and the candidate locations are narrowed down to 50 using low-level criteria, the number of combinations is still $N_s = 4.71 \cdot 10^{13}$. For most performance criteria, this disqualifies the exhaustive search. However, multiple smart optimization methods exist to find a close-to-optimal solution within a reasonable time.

Deterministic optimization methods formulate an objective function based on optimization criteria, and advance the sensor layout towards minima by evaluating the gradient or Hessian matrix

(sensitivity) regarding the optimization variables (e.g., the Newton method, the steepest descent method, etc.). They may be organized into constrained and unconstrained methods, as well as linear and non-linear programming. Their suitability for smooth analytical problems with convex objective functions, i.e., problems with exactly one optimal solution, is undisputed. However, none of these conditions are given for sensor placement optimization. Moreover, the problem formulation is discrete because natural frequencies and mode shapes of large dynamic systems cannot be described analytically. It is possible to convert the problem formulation into continuous form (Sepulveda et al., 1993), but the corresponding approaches are numerically inefficient. Besides, there are issues related to local minima and convergence, which is why purely deterministic methods are rarely used (Yi and Li, 2012).

Sequential sensor placement methods iterate toward an acceptable sensor layout by systemically removing or adding a subset of sensors in each iteration step. Correspondingly, the methods are termed forward-SSP and backward-SSP. The solution may not be optimal, because it depends on the initial choice and the number of sensors that are removed at a time. Moreover, the optimal sensor location changes with a varying number of sensors, but once a sensor is removed from the set, it will not be added again. An improved version is the combined backward-forward method, which is a forward-SSP that overshoots the desired number of sensors, for example, by 10%, and then reduces the number of sensors again in a backward-SSP fashion (Li et al., 2008). Depending on the original choice, this method can lead to optimal results, while outperforming all other placement schemes if a single optimization criterion is used (Papadimitriou, 2004). However, it is not suitable for multi-objective optimization.

Genetic Algorithms (GA) mimic the natural evolution process of chromosomes by introducing random properties, such as gene mutation and crossover (Holland, 1975). Originally, the sensor configurations were understood as chromosomes that consist of multiple genes, i.e., binary strings that indicate the presence of sensors through "0" and "1" entries at certain DOF (Yao et al., 1993). The optimal solution is found by assigning a criterion-based fitness value to each chromosome. Gene mutation is implemented by randomly changing sensor locations (swapping 0 and 1); however, crossover is more challenging to implement because merging two sensor configurations changes the number of sensors. One class of methods solved this issue by introducing a partheno-GA or dual-structure encoding technique, where the mating is carried out by merely changing the order of genes (sensor location) but not their number (Kang et al., 2008; Huang et al., 2009). Another (more efficient) class of methods introduced real-float or integer numbers instead of binary encoding (Roy and Chakraborty, 2009; Chow et al., 2011; Michaelewicvz, 1994).

Nature-inspired algorithms are inspired by the social behaviour of species, where the algorithms adapt the coordinated travel paths animals take to progress toward a common goal. Combined with the appropriate optimization problem, all algorithms have the capability to outperform the genetic algorithms. This is because they combine local search techniques with coordinated global search techniques, and randomized local and global elements. This speeds up convergence, in particular

in early stages, and ensures that the local minima in the objective function can be overcome. The particle swarm optimization algorithm, which is inspired by bird flocking or fish schooling, deserves special attention due to its pioneering character and simple implementation (Eberhart and Kennedy, 1995). Each particle is assigned to a velocity vector (trajectory), which is updated as the particle moves through space. It is attracted to both local and global minima in the objective function while keeping a specified distance to other particles, and includes a randomized component. The distributed wolf method imitates the hunting and feeding behaviour of a wolf pack (Yi et al., 2016). In the searching phase, individual wolfs seek for nearby prey (local optima in the objective function) based on combined deterministic and random search criteria. In the attacking phase, they use the information provided from the alpha-wolf to progress closer to the largest prey found (global minima). In the sense of food distribution, wolfs with low search success are replaced with randomly generated new wolfs. In ant colony optimization (Overton and Worden, 2004), random ant agents search for optimal solutions while leaving behind pheromone-based information to reinforce and promote certain travel paths. Other examples are the artificial bee colony method (Scott and Worden, 2015), the firefly algorithm (Zhou et al., 2014), the micro-habitat frog leaping method (Feng and Jia, 2018), and the monkey algorithm (Yi et al., 2015).

Simulated annealing describes the process of (repeatedly) heating metals beyond their recrystallization point and cooling them down in a slow and controlled manner. Due to minimum energy principles, the crystals asymptotically move towards a highly ordered state of minimal energy, which exhibits desirable material properties. This process is imitated for sensor placement optimization (van Laarhoven and Aarts, 1987; Corana et al., 1987), but instead of thermal motion, a perturbation operator is applied to the sensor locations. Initially, the perturbation is highly random, but with an increasing number of iterations, the intensity of the perturbation gradually reduces, so the procedure converges toward the global minimum in the objective function. For each iteration step, the new sensor arrangement is accepted if it performs better than the previous one. However, to ensure that local minima in the objective function can be overcome, the algorithm has to be modified and the severity of the perturbation has to be increased at intermediate steps (corresponding to a reheating of the material). The decision of whether a heat increase is acceptable or not is based on statistic operators related to thermo-mechanics, so-called Boltzmann statistics.

2.3 Summary

This chapter summarizes the state-of-the-art in damage diagnosis methods and sensor placement strategies for global vibration monitoring. First, an overview is provided for existing damage-sensitive features (see Table 2.1). Secondly, the damage diagnosis methods are categorized into supervised learning, unsupervised learning, model updating, and parametric change detection. The review concludes that damage localization and quantification can only be achieved through model-based approaches. The asymptotic local (AL) approach is selected for the studies in the thesis due to its real-time capabilities, its diagnostic depth, its thorough treatment of uncertainties, and

its universality. Since the AL method has never been applied for change detection in boundary conditions (i.e., changes in support conditions or prestressing forces), the corresponding literature is reviewed. Damage modelling based on the geometric stiffness matrix is found to be a universal approach to parametrize changes in boundary conditions. Moreover, previous attempts to determine the minimum detectable damage are reviewed. Most existing strategies are empirical, problem-specific, or restricted to specific element types. The findings further indicate that damage detectability depends on the reliability requirements, expressed through the probability of false alarms (PFA) and the probability of detection (POD), and the measurement duration; however, no universal framework has been found to describe the relations for global vibration monitoring.

Sensor placement optimization is divided into performance criteria and optimization algorithms. To provide an overview, the performance criteria are categorized with respect to the primary purpose of the optimization (see Table 2.2). Low-level performance criteria aim to precondition the vibration signal (Level 1) by optimizing the signal-to-noise ratio and quantifying the redundancy of information. Other criteria optimize the quality of the modal system identification (Level 2), which leads to minimum uncertainties in the estimated modal parameters and maximal mode distinguishability. Advanced criteria optimize the damage detectability or localizability (Level 3), but none of the existing criteria appears to consider the relative changes in structural parameters (such as material strength values), although these are the decisive quantities for structural design, structural health, and thus, safety. Due to combinatorial explosion, an exhaustive search approach (where each possible sensor configuration is evaluated) is not applicable to sensor placement on large mechanical structures, and smart optimization algorithms have to be employed to find a close-to-optimal solution within a reasonable time. Deterministic optimization methods (based on gradients or Hessian matrices) are rarely used, due to the discrete nature of the optimization problem, but sequential sensor placement strategies offer efficient alternatives. The genetic algorithm (GA), simulated annealing, and nature-inspired algorithms (e.g., the particle swarm optimization, distributed wolf, ant colony, artificial bee colony) are particularly efficient, as they combine local search techniques with coordinated global search techniques to overcome local minima.

Chapter 3

Structural Dynamics in Control Theory

"If you change the way you look at things, the things you look at change."

— Wayne Dyer

Control theory provides mathematical models to replicate vibration measurements while avoiding numerical models of the examined structures. These models can be employed to identify modal properties (e.g., resonance frequencies, mode shapes, and damping ratios), and to detect changes in dynamic systems with known or unknown input forces. Most concepts go back to the 1950s (Kalman, 1959), but gained attention with the publication of a book in 1995 (van Overschee and de Moor, 1995) that unified the theoretical framework for mechanical systems with input-output and output-only measurements. In 2014 and 2015, two books were published that are tailored to civil engineers with no background in control theory (Rainieri and Fabbrocino, 2014; Brincker and Ventura, 2015). This chapter is written in the same spirit, starting with the Newton equation of motion. The introduced mathematical concepts are essential in order to understand the developed tools in this thesis.

Section 3.1 focuses on mechanical systems with known input forces. Basic concepts of structural dynamics, such as the free decay and impulse response function of multi-degree of freedom systems are translated into the equivalent control-theory based notations, i.e., the observability and the block Hankel matrix. Section 3.2 explains that impulse response functions can be replaced by covariance functions in block Hankel format for systems with unknown input forces, and how the block Hankel matrix can be decomposed into the observability matrix using subspace decomposition. Section 3.3 touches upon subspace-based system identification.

3.1 Input-output Systems

3.1.1 State Space Model

Linear and time-invariant (LTI) mechanical systems with N_m degrees of freedom are routinely modelled through the Newton equation of motion (Chopra, 2017)

$$\mathbf{M}\ddot{\mathbf{u}}(t) + \mathbf{C}^1\dot{\mathbf{u}}(t) + \mathbf{K}\mathbf{u}(t) = \mathbf{F} \cdot \mathbf{f}(t). \tag{3.1}$$

where $\mathbf{M}, \mathbf{C}^1, \mathbf{K} \in \mathbb{R}^{N_m \times N_m}$ are the mass, damping and stiffness matrix and $\mathbf{u}(t) \in \mathbb{R}^{N_m}$ is the displacement of the system under known external forces. The forces are split into a time-dependent part $\boldsymbol{f}(t) \in \mathbb{R}^{N_i}$, where N_i is the number of input channels, and a matrix that assigns the input channels to the corresponding degrees of freedom $\mathbf{F} \in \mathbb{R}^{N_m \times N_i}$. Since linear behaviour is assumed, any system state can be described through a state vector containing displacements and velocities $\mathbf{x}(t) = [\mathbf{u}(t)^T \ \dot{\mathbf{u}}(t)^T]^T$ (Rainieri and Fabbrocino, 2014). Equivalently, second-order derivatives in Eq. (3.1) can be substituted through the first derivative of the state vector $\dot{\mathbf{x}}(t)$ reformulating the mechanical system to

$$\begin{bmatrix} \dot{\mathbf{u}}(t) \\ \ddot{\mathbf{u}}(t) \end{bmatrix} = \begin{bmatrix} \mathbf{0} & \mathbf{I} \\ -\mathbf{M}^{-1}\mathbf{K} & -\mathbf{M}^{-1}\mathbf{C}^1 \end{bmatrix} \begin{bmatrix} \mathbf{u}(t) \\ \dot{\mathbf{u}}(t) \end{bmatrix} + \begin{bmatrix} \mathbf{0} \\ \mathbf{M}^{-1}\mathbf{F} \end{bmatrix} \mathbf{f}(t). \tag{3.2}$$

The lower half of Eq. (3.2) is the equation of motion from Eq. (3.1) solved for the accelerations $\ddot{\mathbf{u}}(t)$, and the upper half is a true statement. Eq. (3.2) can be re-written as

$$\dot{\mathbf{x}}(t) = \mathbf{A}_c\mathbf{x}(t) + \mathbf{B}_c\mathbf{f}(t), \tag{3.3}$$

where $\mathbf{A}_c \in \mathbb{R}^{n \times n}$ and $\mathbf{B}_c \in \mathbb{R}^{n \times N_i}$ are the state transition matrix and the input matrix, $\mathbf{x} \in \mathbb{R}^n$ is the state vector, and $n = 2m$ is the new system order. To include the system response measured through r sensors, a measurement equation is added. The measurement vector $\mathbf{y}(t) \in \mathbb{R}^r$ contains displacements, velocities, or accelerations superimposed with measurement noise $\mathbf{e}(t) \in \mathbb{R}^r$. It can also include different measurement quantities if selection matrices $\mathbf{L}_a, \mathbf{L}_v, \mathbf{L}_d \in \mathbb{R}^{r \times N_m}$ are defined to assign the degrees of freedom to the corresponding measurement quantity through

$$\mathbf{L}_a\ddot{\mathbf{u}}(t) + \mathbf{L}_v\dot{\mathbf{u}}(t) + \mathbf{L}_d\mathbf{u}(t) + \mathbf{e}(t) = \mathbf{y}(t). \tag{3.4}$$

After substituting the second order derivative through $\ddot{\mathbf{u}}(t)$ from Eq. (3.2), the measurement vector is re-arranged to (Rainieri and Fabbrocino, 2014)

$$\mathbf{y}(t) = \begin{bmatrix} \mathbf{L}_d - \mathbf{L}_a\mathbf{M}^{-1}\mathbf{K} & \mathbf{L}_v - \mathbf{L}_a\mathbf{M}^{-1}\mathbf{C} \end{bmatrix} \begin{bmatrix} \mathbf{u}(t) \\ \dot{\mathbf{u}}(t) \end{bmatrix} + \begin{bmatrix} \mathbf{0} \\ \mathbf{L}_a\mathbf{M}^{-1}\mathbf{F} \end{bmatrix} \mathbf{f}(t) + \mathbf{e}(t). \tag{3.5}$$

In the following, the matrix terms in the measurement vector from Eq. (3.5) are substituted,

$$\mathbf{y}(t) = \mathbf{C}_c\mathbf{x}(t) + \mathbf{D}_c\mathbf{f}(t) + \mathbf{e}(t), \tag{3.6}$$

where $\mathbf{C}_c \in \mathbb{R}^{r \times n}$ is called the output matrix and $\mathbf{D}_c \in \mathbb{R}^{r \times N_i}$ the feed-trough term. Combining the state and measurement vectors from Eq. (3.3) and (3.6) leads to the state space model (Lindquist and Picci, 2015) of the following format

$$\begin{cases} \dot{\mathbf{x}}(t) &= \mathbf{A}_c\mathbf{x}(t) + \mathbf{B}_c\mathbf{f}(t) \\ \mathbf{y}(t) &= \mathbf{C}_c\mathbf{x}(t) + \mathbf{D}_c\mathbf{f}(t) + \mathbf{e}(t). \end{cases} \tag{3.7}$$

3.1.2 Sampled System Response

Vibration measurements are only available at discrete time instants, so the state space model is to be transformed from continuous-time to discrete-time. This is achieved by assuming a zero-order hold and integrating over a time step $t = k\Delta t$. Therefore, the state space model in continuous-time from Eq. (3.7) changes to the following model in discrete-time (van Overschee and de Moor, 1995),

$$\begin{cases} \mathbf{x}_{k+1} &= \mathbf{A}\mathbf{x}_k + \mathbf{B}\mathbf{f}_k \\ \mathbf{y}_k &= \mathbf{C}\mathbf{x}_k + \mathbf{D}\mathbf{f}_k + \mathbf{e}_k, \end{cases} \tag{3.8}$$

where $\mathbf{A} = e^{\mathbf{A}_c \Delta t}$ is the state transition matrix, $\mathbf{B} = \mathbf{A}_c^{-1}(e^{\mathbf{A}_c \Delta t} - \mathbf{I})\mathbf{B}_c$ is the input matrix (Chen, 1999), and $\mathbf{C}_c = \mathbf{C}$ and $\mathbf{D} = \mathbf{D}_c$ are the output and the feed-through matrices in discrete-time. Applying the equation recursively from a known initial state $\mathbf{x}_0$ with a known input sequence leads to

$$\begin{aligned} \mathbf{x}_1 &= \mathbf{A}\mathbf{x}_0 + \mathbf{B}\mathbf{f}_0 \\ \mathbf{x}_2 &= \mathbf{A}^2\mathbf{x}_0 + \mathbf{A}\mathbf{B}\mathbf{f}_0 + \mathbf{B}\mathbf{f}_1 \\ \mathbf{x}_3 &= \mathbf{A}^3\mathbf{x}_0 + \mathbf{A}^2\mathbf{B}\mathbf{f}_0 + \mathbf{A}\mathbf{B}\mathbf{f}_1 + \mathbf{B}\mathbf{f}_2 \\ &\vdots \\ \mathbf{x}_k &= \mathbf{A}^k\mathbf{x}_0 + \sum_{i=1}^{k} \mathbf{A}^{i-1}\mathbf{B}\mathbf{u}_{k-i}. \end{aligned} \tag{3.9}$$

Equivalently, the measurements are calculated recursively by substituting the state $\mathbf{x}_k$ into the measurement equation $\mathbf{y}_k$ from Eq. (3.8) yielding (Glad and Ljung, 2000)

$$\begin{aligned} \mathbf{y}_1 &= \mathbf{C}\mathbf{A}\mathbf{x}_0 + \mathbf{C}\mathbf{B}\mathbf{f}_0 + \mathbf{D}\mathbf{f}_1 + \mathbf{e}_1 \\ \mathbf{y}_2 &= \mathbf{C}\mathbf{A}^2\mathbf{x}_0 + \mathbf{C}\mathbf{A}\mathbf{B}\mathbf{f}_0 + \mathbf{C}\mathbf{B}\mathbf{f}_1 + \mathbf{D}\mathbf{f}_2 + \mathbf{e}_2 \\ \mathbf{y}_3 &= \mathbf{C}\mathbf{A}^3\mathbf{x}_0 + \mathbf{C}\mathbf{A}^2\mathbf{B}\mathbf{f}_0 + \mathbf{C}\mathbf{A}\mathbf{B}\mathbf{f}_1 + \mathbf{C}\mathbf{B}\mathbf{f}_2 + \mathbf{D}\mathbf{F}_3 + \mathbf{e}_3 \\ &\vdots \\ \mathbf{y}_k &= \mathbf{C}\mathbf{A}^k\mathbf{x}_0 + \sum_{i=1}^{k} \mathbf{C}\mathbf{A}^{i-1}\mathbf{B}\mathbf{f}_{k-i} + \mathbf{D}\mathbf{f}_k + \mathbf{e}_k. \end{aligned} \tag{3.10}$$

These equations can be tied back to classical structural dynamics, where the first terms in Eq. (3.9) and (3.10) describe the free responses (i.e., the homogenous solution) and the remaining terms are the forced responses, i.e., the particular solution (Chen, 1999).

3.1.3 Hankel Factorization

Where the previous section reviewed how the system state and the measurements of a LTI system are recursively computed for any time instants k, this section explains how a complete vibration record

with multiple time instances $k = 1, \ldots, K$ can be modelled based on matrix-vector products. For this purpose, the concepts of *observability* and *controllability* (Kalman, 1959, 1963) are introduced and linked to the dynamic system response of a deterministic system in block Hankel matrix format.

Observability. The first term of the measurement equation from Eq. (3.10) describes the free decay of a multi-degree of freedom system to the initial state $\mathbf{x}_0$ (i.e., an initial displacement and/or velocity) in K time steps (Chen, 1999). The free decay can be captured in one matrix, the observability matrix $\boldsymbol{\mathcal{O}}_K$ through

$$\begin{bmatrix} \mathbf{y}_0 \\ \mathbf{y}_1 \\ \vdots \\ \mathbf{y}_{K-1} \end{bmatrix} = \boldsymbol{\mathcal{O}}_K \cdot \mathbf{x}_0, \qquad \text{where} \qquad \boldsymbol{\mathcal{O}}_K = \begin{bmatrix} \mathbf{C} \\ \mathbf{CA} \\ \vdots \\ \mathbf{CA}^{K-1} \end{bmatrix}. \tag{3.11}$$

Block Hankel Matrix. The second term of the measurement equation from Eq. (3.10) describes the impulse response of a multi-degree of freedom system to K unit impulses. It can be captured in one matrix, a block Hankel matrix $\boldsymbol{\mathcal{H}}$, through (Lindquist and Picci, 2015)

$$\begin{bmatrix} \mathbf{y}_0 \\ \mathbf{y}_1 \\ \vdots \\ \mathbf{y}_{K-1} \end{bmatrix} = \boldsymbol{\mathcal{H}} \cdot \begin{bmatrix} \mathbf{f}_{K-1} \\ \mathbf{f}_{K-2} \\ \vdots \\ \mathbf{f}_0 \end{bmatrix}, \quad \text{where} \quad \boldsymbol{\mathcal{H}} = \begin{bmatrix} \mathbf{CB} & \mathbf{CAB} & \iddots & \mathbf{CA}^{K-1}\mathbf{B} \\ \mathbf{CAB} & \mathbf{CA}^2\mathbf{B} & \iddots & \mathbf{CA}^{K}\mathbf{B} \\ \iddots & \iddots & \iddots & \iddots \\ \mathbf{CA}^{K-2}\mathbf{B} & \mathbf{CA}^{K-1}\mathbf{B} & \iddots & \mathbf{CA}^{2K-1}\mathbf{B} \\ \mathbf{CA}^{K-1}\mathbf{B} & \mathbf{CA}^{K}\mathbf{B} & \iddots & \mathbf{CA}^{2K-2}\mathbf{B} \end{bmatrix}. \tag{3.12}$$

It is called a "block Hankel matrix" due to its particular format, with identical blocks on the skew diagonal from the bottom left to the top right. The matrix rank is equal to the system order n for both the observability matrix and the block Hankel matrix with $\text{rank}(\boldsymbol{\mathcal{O}}_K) = \text{rank}(\boldsymbol{\mathcal{H}}) = n$.

State Controllability. The block Hankel matrix is linked to the observability matrix through the controllability matrix (Chen, 1999). The controllability transfers the system from the initial state to another state in K time steps

$$\mathbf{x}_K = \boldsymbol{\mathcal{C}}_K \begin{bmatrix} \mathbf{f}_{K-1} \\ \mathbf{f}_{K-2} \\ \vdots \\ \mathbf{f}_0 \end{bmatrix}, \qquad \text{where} \qquad \boldsymbol{\mathcal{C}}_K = \begin{bmatrix} \mathbf{B} & \mathbf{AB} & \ldots & \mathbf{A}^{K-1}\mathbf{B} \end{bmatrix}. \tag{3.13}$$

The product of the controllability from Eq. (3.13) and the observability from Eq. (3.11) yields the block Hankel matrix from Eq. (3.12), with $\boldsymbol{\mathcal{H}} = \boldsymbol{\mathcal{O}}_K \boldsymbol{\mathcal{C}}_K$. Vice versa, the block Hankel matrix

can be decomposed into the observability and controllability, for example, through singular value decomposition (van Overschee and de Moor, 1995), with more details in Section 3.3.1.

3.2 Output-only Systems

3.2.1 State Space Model

For stochastic dynamic systems, where the input $\mathbf{f}_k$ is unknown, the discrete state space model from Eq. (3.8) simplifies to (van Overschee and de Moor, 1995)

$$\begin{cases} \mathbf{x}_{k+1} &= \mathbf{A}\mathbf{x}_k + \mathbf{w}_k \\ \mathbf{y}_k &= \mathbf{C}\mathbf{x}_k + \mathbf{v}_k, \end{cases} \tag{3.14}$$

where $\mathbf{A}$ and $\mathbf{C}$ are the state transition matrix and the output matrix in discrete-time. The state noise $\mathbf{w}_k = \mathbf{B}\mathbf{f}_k$ replaces the unknown force term in the state vector and the output noise $\mathbf{v}_k = \mathbf{D}\mathbf{f}_k + \mathbf{e}_k$ replaces the force and the measurement noise. Both terms are assumed to be white noise with zero means. That means that the noise terms are assumed to be uncorrelated with the internal states, and the covariances $\mathbf{R}$ are zero,

$$\mathbf{R}_{wv} = \mathrm{E}[\mathbf{x}_k \mathbf{v}_k^T] = 0 \tag{3.15}$$

$$\mathbf{R}_{xw} = \mathrm{E}[\mathbf{x}_k \mathbf{w}_k^T] = 0. \tag{3.16}$$

The term $\mathrm{E}[\cdot]$ is the expectation operator. The excitation is assumed to be stationary, so the noise covariances remain unchanged with

$$\mathrm{E}\left[\begin{bmatrix}\mathbf{w}_p \\ \mathbf{v}_p\end{bmatrix}\begin{bmatrix}\mathbf{w}_q^T & \mathbf{v}_q^T\end{bmatrix}\right] = \begin{bmatrix}\mathbf{R}_{ww} & \mathbf{R}_{wv} \\ \mathbf{R}_{wv}^T & \mathbf{R}_{vv}\end{bmatrix}\delta_{pq}, \tag{3.17}$$

where p and q are two arbitrary time instants and δ_{pq} is the Kronecker delta, which is $\delta_{pq} = 1$ for $p = q$ and 0 otherwise. More information on the covariance follows in the next section.

3.2.2 Covariance Function

Cross-covariance functions measure the similarity of two signals and this section reviews how the auto-covariance of the measurements are linked to the dynamic system from Eq. (3.14). Another term for the cross-covariance function is the *sliding inner product*, as one signal $\mathbf{X}$ is slid along another signal $\mathbf{Y}$ by a time lag i while multiplying the two signals (Muirhead, 1982)

$$\mathbf{R}_{XY,i} = \mathrm{E}[\mathbf{X}_{k+i}\mathbf{Y}_k^T]. \tag{3.18}$$

If both signals are aligned for a certain time lag, their inner product maximizes, indicating the similarity of the two signals. Where the cross-covariance compares two different quantities $\mathbf{X}$ and

$\mathbf{Y}$, the auto-covariance compares one quantity to itself at different time instants. The system is assumed to be stationary, so the auto-covariances of the states $\mathbf{R}_{xx}$ assume the same matrix for every time instant k and zero time lag

$$\mathbf{R}_{xx} = \mathrm{E}[\mathbf{x}_k \mathbf{x}_k^T]. \tag{3.19}$$

Combining the state sequence and the measurement sequence from Eq. (3.9) and (3.10) with the assumed noise properties from Eq. (3.16), the cross-covariance between the output and the states $\mathbf{R}_{xy,1}$ at time lag $i = 1$ can be re-written as:

$$\begin{aligned}
\mathbf{R}_{xy,1} =& \mathrm{E}[\mathbf{x}_{k+1} \mathbf{y}_k^T] \\
=& \mathrm{E}[(\mathbf{A}\mathbf{x}_k + \mathbf{w}_k) \cdot (\mathbf{C}\mathbf{x}_k + \mathbf{v}_k)^T] \\
=& \mathbf{A}\mathrm{E}[\mathbf{x}_k \mathbf{x}_k^T]\mathbf{C}^T + \mathrm{E}[\mathbf{w}_k \mathbf{v}_k^T] \\
=& \mathbf{A}\mathbf{R}_{xx}\mathbf{C}^T + \mathbf{R}_{wv}.
\end{aligned} \tag{3.20}$$

So, the cross covariance $\mathbf{R}_{xy,1}$ is linked to the auto-covariance $\mathbf{R}_{xx}$ from Eq. (3.19) and the noise covariance $\mathbf{R}_{wv}$ from Eq. (3.17) (van Overschee and de Moor, 1995). The auto-covariance of the output $\mathbf{R}_{yy}$ can be re-formulated in a similar way. For a time lag of $i = 1$, it follows:

$$\begin{aligned}
\mathbf{R}_{yy,1} =& \mathrm{E}[\mathbf{y}_{k+1} \mathbf{y}_k^T] \\
=& \mathrm{E}[(\mathbf{C}\mathbf{A}\mathbf{x}_k + \mathbf{C}\mathbf{w}_k + \mathbf{v}_k)(\mathbf{C}\mathbf{x}_k + \mathbf{v}_k)^T] \\
=& \mathrm{E}[\mathbf{C}\mathbf{A}\mathbf{x}_k \mathbf{x}_k^T \mathbf{C}^T] + \mathrm{E}[\mathbf{C}\mathbf{w}_k \mathbf{v}_k^T] \\
=& \mathbf{C}\left(\mathbf{A}\mathrm{E}[\mathbf{x}_k \mathbf{x}_k^T]\mathbf{C}^T + \mathrm{E}[\mathbf{w}_k \mathbf{v}_k^T]\right) \\
=& \mathbf{C}\left(\mathbf{A}\mathbf{R}_{xx}\mathbf{C}^T + \mathbf{R}_{wv}\right) \\
=& \mathbf{C} \cdot \mathbf{R}_{xy,1}.
\end{aligned} \tag{3.21}$$

For an arbitrary time step i, the auto-covariance decomposes into

$$\mathbf{R}_i = \mathbf{R}_{yy,i} = \mathbf{C}\mathbf{A}^{i-1} \cdot \mathbf{R}_{xy,1}. \tag{3.22}$$

In other words, the auto-covariance $\mathbf{R}_{yy,i}$ of the measurements decomposes into the output matrix $\mathbf{C}$, the state transition matrix $\mathbf{A}^{i-1}$, as well as the cross-covariance between the states and the measurements $\mathbf{R}_{xy,1}$ (van Overschee and de Moor, 1995). Where the right term $\mathbf{R}_{xy,1}$ is load-dependent, the left term is characteristic for the structure. Eq. (3.22) is a fundamental expression for ambient vibration testing, as it proves that the mechanical model from Eq. (3.14) can be retrieved from random vibration data using covariance functions.

3.2.3 Hankel Factorization

To retrieve the state transition matrix and the output matrix, $\mathbf{A}$ and $\mathbf{C}$, from vibration measurements, the covariance functions are arranged in block Hankel format (van Overschee and de Moor, 1995), refer to Section 3.2.3. The indices for block rows and block columns, p and q, are the time

lag parameters for the covariance functions. The block Hankel matrix

$$\boldsymbol{\mathcal{H}}_{p+1,q} = \begin{bmatrix} \mathbf{R}_1 & \mathbf{R}_1 & \iddots & \mathbf{R}_q \\ \mathbf{R}_2 & \mathbf{R}_1 & \iddots & \mathbf{R}_{q+1} \\ \iddots & \iddots & \iddots & \iddots \\ \mathbf{R}_{p+1} & \mathbf{R}_{p+2} & \iddots & \mathbf{R}_{p+q} \end{bmatrix} = \boldsymbol{\mathcal{O}}_{p+1}\boldsymbol{\mathcal{C}}_q \tag{3.23}$$

can be interpreted as the unit impulse response matrix to white noise excitation, and decomposes into the output observability and the output controllability

$$\boldsymbol{\mathcal{O}}_{p+1} = \begin{bmatrix} \mathbf{C} \\ \mathbf{CA} \\ \vdots \\ \mathbf{CA}^{p+1} \end{bmatrix}, \qquad \text{where} \qquad \boldsymbol{\mathcal{C}}_q = \begin{bmatrix} \mathbf{R}_{xy,1} & \mathbf{AR}_{xy,1} & \cdots & \mathbf{A}^{q-1}\mathbf{R}_{xy,1} \end{bmatrix}. \tag{3.24}$$

From a mathematical point of view, the time time lag parameters p and q have to be chosen sufficiently high, so the block Hankel matrix and the observability are of full rank with the minimum condition $\min\{pr, qr\} \geq n$. Since the matrix rank is determined by the shorter matrix dimension of $\boldsymbol{\mathcal{H}}_{p+1,q}$, the time lag parameters are often set to $p + 1 = q$.

3.2.4 Practical Considerations

The assumption of white noise excitation is made to allow for a simple presentation of the theoretical derivations in this chapter. However, engineering practice has shown that the system matrices can also be retrieved if the system excitation is coloured, band-limited, or non-stationary (Benveniste and Mevel, 2007; Basseville et al., 2007), and if the measurement noise is non-white. Modelling inaccuracies of this kind may introduce spurious noise modes, which can be accounted for by increasing the system order beyond the minimum value of $n > 2N_m$. Equivalently, the selection of appropriate time lag parameters p and q is often based on user experience rather than the minimum condition from the previous section. The time lags have to be set sufficiently high, while considering the physics of the wave propagation (Rainieri and Fabbrocino, 2014), so a sufficient number of cycles of each mode of vibration is captured. Some authors proposed to set the time lag to $p = f_s/(2f_{n,1})$ based on the sampling frequency f_s and the frequency of the first mode of vibration $f_{n,1}$ (Reynders and de Roeck, 2008). This ensures that half a cycle of the fundamental mode of vibration is captured (one sinus half-wave), where all wave components of lower frequency are neglected. However, if damping estimates are not of interest, a lower value can be set and a physical interpretation is challenging, because the physical wave propagation properties also depend on structure-specific quantities, such as the distance between sensors and the speed of sound.

3.3 Stochastic System Identification

3.3.1 Subspace Decomposition

The preceding sections have shown that the block Hankel matrix from Eq. (3.23) can be interpreted as a unit impulse response matrix, and all that remains is to extract the observability (i.e., the matrix that captures the free decay), and from it, the state transition matrix and the output matrix $\mathbf{A}$ and $\mathbf{C}$. The first step is to decompose the block Hankel matrix using singular value decomposition (SVD)

$$\boldsymbol{\mathcal{H}}_{p+1,q} = \mathbf{U}\mathbf{S}\mathbf{V}^T = \begin{bmatrix}\mathbf{U}_1 & \mathbf{U}_0\end{bmatrix} \begin{bmatrix}\mathbf{S}_1 & \mathbf{0} \\ \mathbf{0} & \mathbf{0}\end{bmatrix} \begin{bmatrix}\mathbf{V}_1^T \\ \mathbf{V}_0^T\end{bmatrix} = \boldsymbol{\mathcal{O}}_{p+1}\boldsymbol{\mathcal{C}}_q, \tag{3.25}$$

where $\mathbf{U}, \mathbf{S}$ and $\mathbf{V}$ are the left singular vectors, the singular values, and the right singular vectors. Structural modes of vibration are assumed to dominate the system response over noise. Hence, the upper singular values $\mathbf{S}_1 \in \mathbb{R}^{n\times n}$ and the corresponding singular vectors $\mathbf{U}_1$ represent structural information, where the lower singular values represent noise. The observability is calculated as

$$\boldsymbol{\mathcal{O}}_{p+1} = \mathbf{U}_1\mathbf{S}_1^{-1/2} \tag{3.26}$$

and the output matrix $\mathbf{C}$ is the first block row of the observability (see Eq. 3.24). Using the shift-invariance property, which states that the state transition matrix is the component of the observability that is consistent over multiple time steps (Magalhães and Cunha, 2011),

$$\boldsymbol{\mathcal{O}}^{\uparrow}_{p+1} = \mathbf{A}\boldsymbol{\mathcal{O}}_{p+1\downarrow}, \quad \text{where} \quad \boldsymbol{\mathcal{O}}^{\uparrow}_{p+1} = \begin{bmatrix}\mathbf{C} \\ \mathbf{CA} \\ \vdots \\ \mathbf{CA}^{K-1}\end{bmatrix}, \quad \boldsymbol{\mathcal{O}}_{p+1\downarrow} = \begin{bmatrix}\mathbf{CA} \\ \mathbf{CA}^{2} \\ \vdots \\ \mathbf{CA}^{K}\end{bmatrix}, \tag{3.27}$$

the state transition matrix $\mathbf{A}$ can be approximated based on regression, with

$$\mathbf{A} = (\boldsymbol{\mathcal{O}}^{\uparrow}_{p+1})^{\dagger}\boldsymbol{\mathcal{O}}_{p+1\downarrow}. \tag{3.28}$$

3.3.2 Eigenvalue Problem

Once the system matrices $\mathbf{A}$ and $\mathbf{C}$ have been found, the way to derive modal parameters is straightforward (Brincker and Ventura, 2015). The eigenvalue problem is expressed as $\mathbf{A}\boldsymbol{\Phi} = \boldsymbol{\Phi}\boldsymbol{\Lambda}$ where $\boldsymbol{\Lambda} = \boldsymbol{\Phi}^{-1}\mathbf{A}\boldsymbol{\Phi} = \text{diag}(\lambda_1^2, \ldots, \lambda_n^2)$ is a matrix holding the eigenvalues of the system on its main diagonal, and $\boldsymbol{\Phi}$ are the eigenvectors of the states that can be transformed into the observable eigenvectors $\boldsymbol{\Psi}$ through

$$\boldsymbol{\Psi} = \mathbf{C}\boldsymbol{\Phi} = \begin{bmatrix}\boldsymbol{\Psi}_1 & \cdots & \boldsymbol{\Psi}_n\end{bmatrix}. \tag{3.29}$$

The pole λ_j of every mode of vibration j can be back-transformed into the pole μ_j of the continuous-time system, and subsequently decomposed into the corresponding natural circular frequency ω_j and damping ratio ζ_j with

$$\mu_j = \frac{\log \lambda_j}{\Delta t} = -\omega_j \zeta_j \pm \omega_j \sqrt{1-\zeta_j^2} \cdot \mathrm{i}. \tag{3.30}$$

where $\mathrm{i} = \sqrt{-1}$ is the imaginary unit. Ultimately, the poles are decomposed into natural frequencies and damping ratios

$$f_j = \frac{|\mu_j|}{2\pi} \qquad \zeta_j = -\frac{\mathrm{Re}(\mu_j)}{|\mu_j|}. \tag{3.31}$$

3.3.3 Diagonalization

Using similarity transformation, the state space model can be transformed into a new coordinate system. By defining the transformation matrix as the inverse mode shape matrix

$$\mathbf{T} = \mathbf{\Phi}^{-1}, \tag{3.32}$$

transforming the system states $\tilde{\mathbf{x}}_k = \mathbf{T}\mathbf{x}_k$, and expanding the state space model as follows,

$$\begin{cases} \mathbf{T}\mathbf{x}_{k+1} &= \mathbf{T}\mathbf{A}\mathbf{T}^{-1}\mathbf{T}\mathbf{x}_k + \mathbf{T}\mathbf{w}_k \\ \mathbf{y}_k &= \mathbf{C}\mathbf{T}^{-1}\mathbf{T}\mathbf{x}_k + \mathbf{v}_k, \end{cases} \tag{3.33}$$

the state space model is obtained in modal basis

$$\begin{cases} \tilde{\mathbf{x}}_{k+1} &= \tilde{\mathbf{A}}\tilde{\mathbf{x}}_k + \tilde{\mathbf{w}}_k \\ \mathbf{y}_k &= \tilde{\mathbf{C}}\tilde{\mathbf{x}}_k + \mathbf{v}_k. \end{cases} \tag{3.34}$$

In this case, the state transition matrix is equal to the eigenvalue matrix,

$$\begin{aligned} \mathbf{A}\mathbf{\Phi} &= \mathbf{\Phi}\mathbf{\Lambda} \\ (\mathbf{T}\mathbf{A}\mathbf{T}^{-1})\mathbf{T}\mathbf{\Phi} &= \mathbf{T}\mathbf{\Phi}\mathbf{\Lambda} \\ \tilde{\mathbf{A}} &= \mathbf{\Lambda} \end{aligned} \tag{3.35}$$

and the output matrix is the mode shape matrix.

$$\tilde{\mathbf{C}} = \mathbf{C}\mathbf{T}^{-1} = \mathbf{\Psi}. \tag{3.36}$$

The modes of vibration can be manually selected to construct the corresponding state transition matrix and the output matrix. Furthermore, the observability from Eq. (3.11) can be constructed based on modal parameters. This is used in this thesis to reduce the model order, efficiently simulate vibration data, and diagnose damage based on system matrices that are noise-free.

3.4 Summary

In this chapter, structural dynamics of multi-degree of freedom systems are interpreted from a control theory perspective. The first part explains how the Newton equation of motion can be transformed into a state space model. To do so, a measurement matrix is added with combined displacement, velocity, and acceleration records, and the second-order derivatives in the differential equation are substituted using a state vector. Moreover, fundamental concepts such as the observability matrix and the block Hankel matrix are introduced, which can be interpreted as the measured response sequence of a freely decaying multi-degree of freedom system and an impulse response function, respectively. The second part deals with stochastic state space models, where the input forces are unknown and replaced through white noise. Basic assumptions regarding the noise properties are repeated and covariance functions are introduced as a measure for the similarity of output signals. It is revisited that, when arranged in block Hankel format, the covariance functions can be interpreted as unit impulse response functions, and they can be decomposed into dynamic system matrices. The third part briefly reviews how to estimate the observability from the block Hankel matrix using singular value decomposition (SVD). Once the observability is estimated, the system matrices of the state space model can be retrieved and modal parameters (including natural frequencies, damping ratios, and mode shapes) are calculated by solving the eigenvalue problem. Ultimately, it is shown how to diagonalize the state space matrix, i.e., how to transform it into modal coordinates.

Chapter 4

Damage Diagnosis Using the Asymptotic Local Approach

"Damage increases the complexity of a structure."
— Axiom VIII of SHM
(Farrar and Worden, 2012)

This chapter is an introduction to damage diagnosis using the asymptotic local (AL) approach (Benveniste et al., 1987). For many damage-sensitive features, the vibration state of the undamaged structure can be described through well-defined (and often Gaussian) distributions, but few statements can be made about the distributions in the damaged state, which are more complex. In this sense, the statistical framework of the AL approach is special, as it allows for the distribution in the damaged state to be transformed into a Gaussian distribution, with the only difference to the training state being a shift in the mean vector. Using the example of the stochastic subspace-based residual, this chapter revisits how damage can be detected (Basseville et al., 2000), localized (Basseville et al., 2004), and quantified (Döhler and Mevel, 2015) based on global structural vibrations under random excitation. Section 4.1 recaps how damage is defined based on parameter changes in a finite element (FE) model. Section 4.2 reviews how the damage-sensitive residual is formed in the subspace of the block Hankel matrix. Moreover, the uncertainties in the estimation of the damage-sensitive residual are quantified, and its mean value is linked to structural design parameters in a FE model through sensitivity analysis. Section 4.3 and Section 4.4 explain the change detection method based on the AL approach and elaborate on how to adjust the approach for the four available damage detection and localization tests. The last section (Section 4.5) gives guidance on how to interpret the diagnosis results.

4.1 Damage Parametrization

To diagnose damage, the definition of damage must be clarified, both physically and mathematically. From an engineering perspective, structural damage is understood as a gradual or sudden degradation of design parameters, such as material constants (Worden and Dulieu-Barton, 2004; Farrar and Worden, 2012), cross-sectional values or pre-stressing forces (Chen and Duan, 2014), boundary conditions, or mass-distribution parameters (Santos et al., 2013), as all these cases alter the structure's capacity. FE models offer a convenient way to model structural damage. Nodes

and elements define the geometry of the structure and the capacity of the members depends on the assigned element dimensions and material properties. The available monitoring parameters depend on the element formulation. In theory, any subset of FE parameters can be defined as monitoring parameters, but the monitoring vector

$$\boldsymbol{\theta} = \begin{bmatrix} \theta_1 & \dots & \theta_H \end{bmatrix}^T \tag{4.1}$$

has to include all parameters that possibly undergo changes due to damage. Hence, damage is defined as a deviation of the current monitoring parameter $\boldsymbol{\theta}$ from the reference vector $\boldsymbol{\theta}^0$, so

$$\boldsymbol{\Delta\theta} = \boldsymbol{\theta} - \boldsymbol{\theta}^0. \tag{4.2}$$

Assigning different monitoring parameters to the finite elements within the same structural components can lead to an over-parametrization, meaning the effect of individual parameters cannot be distinguished from others. Later in this chapter, a clustering approach will be reviewed that combines redundant parameters (Allahdadian et al., 2019), but it is advisable to manually define substructures by assigning the same parameter θ_h to multiple FE. For example, the normal force in a cable or truss is one constant even if the cable is discretized into multiple elements.

4.2 Damage-sensitive Residual

4.2.1 Subspace-based Residual

The employed damage-sensitive residual is the subspace-based residual (Basseville et al., 2000). It is formed in the subspace of the block Hankel matrix, i.e., the output covariances $\mathbf{R}_i = E[\mathbf{y}_{k+i}\mathbf{y}_k^T]$ at different time lags $i = 1, ..., p+q$, see Section 3.2.3. Using singular value decomposition (SVD)

$$\boldsymbol{\mathcal{H}} = \begin{bmatrix} \mathbf{R}_1 & \mathbf{R}_2 & \iddots & \mathbf{R}_q \\ \mathbf{R}_2 & \mathbf{R}_3 & \iddots & \mathbf{R}_{q+1} \\ \iddots & \iddots & \iddots & \iddots \\ \mathbf{R}_{p+1} & \mathbf{R}_{p+2} & \iddots & \mathbf{R}_{p+q} \end{bmatrix} = \mathbf{U}\mathbf{S}\mathbf{V}^T = \begin{bmatrix} \mathbf{U}_1 & \mathbf{U}_0 \end{bmatrix} \begin{bmatrix} \mathbf{S}_1 & \mathbf{0} \\ \mathbf{0} & \mathbf{0} \end{bmatrix} \begin{bmatrix} \mathbf{V}_1^T \\ \mathbf{V}_0^T \end{bmatrix}, \tag{4.3}$$

the matrix is decomposed into the left singular vectors and right singular vectors, $\mathbf{U}$ and $\mathbf{V}$, as well as the singular values $\mathbf{S}$, refer to Eq. (3.25). The column space $\mathbf{U}_1 \in \mathbb{R}^{p+1 \times n}$ is limited by the system order n and it is orthogonal to the left null space $\mathbf{U}_0$. Multiplying orthogonal vector spaces yields zero $\mathbf{U}_0^T\mathbf{U}_1 = \mathbf{0}$, and consequently, all structural information is eliminated by pre-multiplying $\mathbf{U}_0$ to the block Hankel matrix it is derived from. After vectorizing the residual matrix through the column stacking operator vec$(\cdot)$, an empty column vector $\boldsymbol{\varepsilon} \in \mathbb{R}^{q(p+1)}$ is obtained,

$$\boldsymbol{\varepsilon} = \text{vec}\left(\mathbf{U}_0^T\boldsymbol{\mathcal{H}}\right) = \mathbf{0}. \tag{4.4}$$

Ultimately, a damage-sensitive residual is formed by pre-multiplying the left null space extracted from reference data to the block Hankel matrix that is evaluated based on new incoming data. In reality, however, measurement noise is present and covariance functions are calculated based on finite measurement records (Muirhead, 1982)

$$\hat{\mathbf{R}}_i = \frac{1}{N-i} \sum_{k=1}^{N-i} \mathbf{y}_{k+i} \mathbf{y}_k^T, \tag{4.5}$$

meaning they are merely estimates, as is the block Hankel matrix. As a consequence, the lower singular values in Eq. (4.3) beyond the cut-off n are close to but unequal to zero, and the subspace-based residual is subject to uncertainties (which is indicated through the hat symbol[1]).

$$\hat{\boldsymbol{\varepsilon}} = \text{vec}\left(\mathbf{U}_0^T \hat{\boldsymbol{\mathcal{H}}}\right) \tag{4.6}$$

Alternatively, the null space can be extracted from the observability matrix, because the observability is derived from the block Hankel matrix through SVD so it has the same null space, see Eq. (3.25). The observability can be constructed based on the modal parameters from operational modal analysis (OMA) or finite element analysis (FEA) which allows one to select the modes of vibration that the null space is orthogonal to, see Eq. (3.24), (3.35), and (3.36). However, estimating the null space based on the block Hankel matrix is more robust, because all signal components (including spurious noise modes) are considered and eliminated, bringing the residual closer to its theoretical properties.

4.2.2 Covariance Matrix

The aim of this section is to quantify the uncertainty of the residual from Eq. (4.6) through the covariance matrix $\boldsymbol{\Sigma}$. Uncertainties are inevitable due to stochastic loads, measurement noise, and finite sample size N. Regardless of the underlying distribution of the feature, the sample mean approximates the expected value (due to the law of large numbers), and subtracting the mean vector from the samples yields a zero mean vector $\text{E}\left[\hat{\boldsymbol{\varepsilon}} - \text{E}[\hat{\boldsymbol{\varepsilon}}]\right] = \mathbf{0}$. Moreover, the sampling distribution of output covariances approximates a multi-dimensional Gaussian distribution if the sample size is large enough (due to the central limit theorem) with theoretically $N \longrightarrow \infty$ (Hannan, 1970). Therefore, Gaussianity is not an assumption but a consequence from mechanical system properties. In the case of the residual vector, the central limit theorem (CLT) can be written as (Basseville et al., 2000)

$$\boldsymbol{\zeta} = \sqrt{N}(\hat{\boldsymbol{\varepsilon}} - \text{E}[\hat{\boldsymbol{\varepsilon}}]) \longrightarrow \mathcal{N}(\mathbf{0}, \boldsymbol{\Sigma}). \tag{4.7}$$

[1]For notational convenience, the hat symbol is dropped for all quantities that are derived from $\hat{\boldsymbol{\varepsilon}}$.

This new vector is called the *Gaussian residual* $\boldsymbol{\zeta}$ in the literature, and its covariance can be estimated as a sample covariance based on n_b data blocks with (Muirhead, 1982)

$$\boldsymbol{\Sigma} = \frac{1}{n_b - 1} \sum_{k=1}^{n_b} \boldsymbol{\zeta}_k \boldsymbol{\zeta}_k^T. \tag{4.8}$$

Where the above equations can be applied to any residual, the following considerations are specific to the stochastic subspace-based residual from Eq. (4.6). Here, the covariance depends on the covariance of the vectorized Hankel matrix

$$\boldsymbol{\Sigma}^{\boldsymbol{\mathcal{H}}} = \sqrt{N}\mathrm{vec}(\hat{\boldsymbol{\mathcal{H}}}), \tag{4.9}$$

which is approximated as a sample covariance (Döhler et al., 2014b)

$$\boldsymbol{\Sigma}^{\boldsymbol{\mathcal{H}}} = \frac{N_b}{n_b - 1} \sum_{k=1}^{n_b} \mathrm{vec}(\hat{\boldsymbol{\mathcal{H}}}^{(k)} - \hat{\boldsymbol{\mathcal{H}}})\mathrm{vec}(\hat{\boldsymbol{\mathcal{H}}}^{(k)} - \hat{\boldsymbol{\mathcal{H}}})^T. \tag{4.10}$$

The superscript (k) indicates that the block Hankel matrix $\hat{\boldsymbol{\mathcal{H}}}^{(k)}$ is estimated based on a short measurement segment of sample length N_b where $N_b \cdot n_b = N^0$. Pre-multiplying the null space $\mathbf{U}_0^T$ to the first column of the sample covariance of the block Hankel matrix leads to $\boldsymbol{\Sigma}_1 = \mathbf{U}_0^T \boldsymbol{\Sigma}_1^{\boldsymbol{\mathcal{H}}} \mathbf{U}_0$, and pre-multiplying it to the entire matrix to

$$\boldsymbol{\Sigma} = (\mathbf{I} \otimes \mathbf{U}_0^T)\boldsymbol{\Sigma}^{\boldsymbol{\mathcal{H}}}(\mathbf{I} \otimes \mathbf{U}_0), \tag{4.11}$$

where $\otimes$ is the Kronecker product.

4.2.3 Jacobian Matrix

Using sensitivity analysis, the deviation in the mean residual vector from Eq. (4.6) can be linked to changes in any system parameter, for example modal parameters or structural parameters from Eq. (4.2). Parametrization is optional but enhances the data-driven residual with physical information and is a prerequisite for damage localization. Starting with the theoretical residual from Eq. (4.4) and assuming an altered parameter vector $\boldsymbol{\theta} = \boldsymbol{\theta}^0 + \Delta\boldsymbol{\theta}$, a Taylor series expansion of $\boldsymbol{\varepsilon}(\boldsymbol{\theta})$ produces

$$\boldsymbol{\varepsilon}(\boldsymbol{\theta}) = \boldsymbol{\varepsilon}(\boldsymbol{\theta}^0) + \frac{\partial \boldsymbol{\varepsilon}}{\partial \boldsymbol{\theta}^0}(\boldsymbol{\theta} - \boldsymbol{\theta}^0) + \frac{1}{2!}(\boldsymbol{\theta} - \boldsymbol{\theta}^0)^T \frac{\partial^2 \boldsymbol{\varepsilon}}{\partial (\boldsymbol{\theta}^0)^2}(\boldsymbol{\theta} - \boldsymbol{\theta}^0) + \dots \tag{4.12}$$

with the first term being zero due to Eq. (4.4). If terms of higher-order are neglected, the equation boils down to the second term. Considering statistical variability, the Taylor series expansion still applies to the mean residual. It can be proven that terms of higher-order converge towards zero at a higher rate than the second-order term for large sample sizes $N \longrightarrow \infty$ (Benveniste et al., 1987).

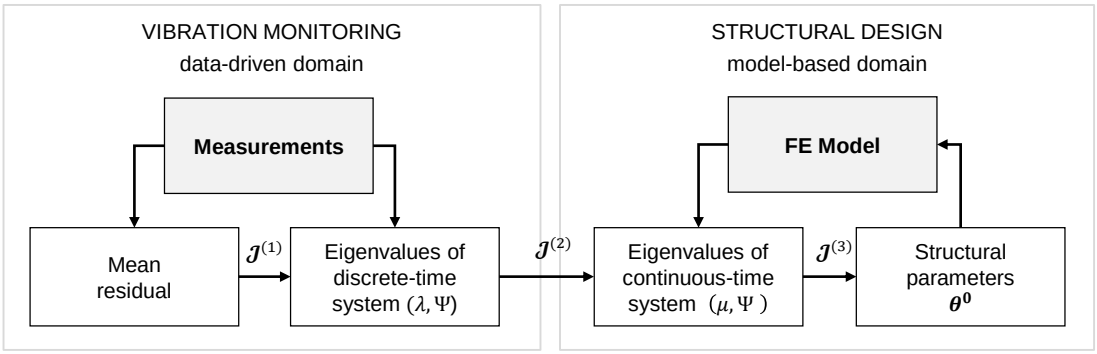

Figure 4.1: Chain of sensitivity analyses for Jacobian calculation

So, the mean residual converges toward

$$\mathrm{E}_{\boldsymbol{\theta}}[\boldsymbol{\varepsilon}(\boldsymbol{\theta})] \longrightarrow \boldsymbol{\mathcal{J}}(\boldsymbol{\theta} - \boldsymbol{\theta}^0) \tag{4.13}$$

where $\boldsymbol{\mathcal{J}} = \frac{\partial}{\partial \boldsymbol{\theta}} \mathrm{E}_{\boldsymbol{\theta}}[\boldsymbol{\varepsilon}]\big|_{\boldsymbol{\theta}=\boldsymbol{\theta}^0}$ is the first-order sensitivity matrix evaluated based on reference parameter $\boldsymbol{\theta} = \boldsymbol{\theta}^0$ and $\mathrm{E}_{\boldsymbol{\theta}}$ is the expected value of a variable calculated under system parameter $\boldsymbol{\theta}$. By setting up the sensitivity matrix, the changes in the residual are linked to changes in the parameter vector. Whereas the link between modal parameters from OMA and structural parameters of a FE model is well-documented in the literature on sensitivity-based modal updating (Heylen and Sas, 1997), the link between the data-driven residual and modal parameters is unique to stochastic subspace-based damage diagnosis.

a) Link to Operational Modal Parameters

Changes in the mean residual vector from Eq. (4.6) are linked to changes in modal parameters through the sensitivity matrix

$$\boldsymbol{\mathcal{J}}^{(1)} = \frac{\partial \mathrm{E}_{\boldsymbol{\eta}}[\boldsymbol{\varepsilon}]}{\partial \boldsymbol{\eta}}\bigg|_{\boldsymbol{\eta}=\boldsymbol{\eta}^0}, \qquad \text{where} \qquad \boldsymbol{\eta} = \begin{bmatrix} \mathrm{Re}(\mathrm{diag}(\boldsymbol{\Lambda})) \\ \mathrm{Re}(\mathrm{vec}(\boldsymbol{\Psi})) \\ \mathrm{Im}(\mathrm{diag}(\boldsymbol{\Lambda})) \\ \mathrm{Im}(\mathrm{vec}(\boldsymbol{\Psi})) \end{bmatrix}, \tag{4.14}$$

where the parameter vector $\boldsymbol{\eta}$ holds the matrices with complex conjugate mode shapes $\boldsymbol{\Psi} = [\boldsymbol{\varphi}_1, \ldots, \boldsymbol{\varphi}_{N_m}]$ and poles $\boldsymbol{\Lambda} = \mathrm{diag}(\lambda_1, \ldots, \lambda_m)$ in discrete-time and vectorized format. The modal parameters are split into real and imaginary parts, using the operator $\mathrm{Re}(\cdot)$ and $\mathrm{Im}(\cdot)$, for consistency with the following considerations. After substituting Eq. (4.6) into Eq. (4.14) and rewriting the block Hankel matrix as a product of observability and controllability,

$$\boldsymbol{\mathcal{J}}^{(1)} = \mathrm{E}\left[\frac{\partial}{\partial \boldsymbol{\eta}} \mathrm{vec}\left(\mathbf{U}_0^T \cdot \boldsymbol{\mathcal{O}}\boldsymbol{\mathcal{C}}\right)\right]\bigg|_{\boldsymbol{\eta}=\boldsymbol{\eta}^0}, \tag{4.15}$$

the derivative of the bracket term is viewed for each individual monitoring parameter η_i. An expansion according to the product rule

$$\frac{\partial}{\partial \eta_i}\left(\mathbf{U}_0^T \cdot \boldsymbol{\mathcal{O}}\boldsymbol{\mathcal{C}}\right) = \mathbf{U}_0^T \frac{\partial \boldsymbol{\mathcal{O}}}{\partial \eta_i}\bigg|_{\boldsymbol{\eta}=\boldsymbol{\eta}^0} \boldsymbol{\mathcal{C}} + \mathbf{U}_0^T \boldsymbol{\mathcal{O}} \left.\frac{\partial \boldsymbol{\mathcal{C}}}{\partial \eta_i}\right|_{\boldsymbol{\eta}=\boldsymbol{\eta}^0} \tag{4.16}$$

shows that the second term can be dropped since the observability has the same left null space as the block Hankel matrix, so $\mathbf{U}_0^T\boldsymbol{\mathcal{O}} = \mathbf{0}$, as explained at the end of Section 4.2.1. Substituting the controllability by $\boldsymbol{\mathcal{C}} = \boldsymbol{\mathcal{O}}^\dagger\boldsymbol{\mathcal{H}}$ and applying a standard calculation rule of the column stacking operator (Basseville et al., 2000)

$$\boldsymbol{\mathcal{J}}^{(1)} = \mathrm{E}\left[\mathrm{vec}\left(\mathbf{U}_0^T \cdot \frac{\partial \boldsymbol{\mathcal{O}}}{\partial \boldsymbol{\eta}}\bigg|_{\boldsymbol{\eta}=\boldsymbol{\eta}^0} \cdot \boldsymbol{\mathcal{O}}^\dagger\boldsymbol{\mathcal{H}}\right)\right] = \mathrm{E}\left(\left(\boldsymbol{\mathcal{O}}^\dagger\boldsymbol{\mathcal{H}} \otimes \mathbf{U}_0\right)^T \frac{\partial}{\partial \boldsymbol{\eta}}\mathrm{vec}(\boldsymbol{\mathcal{O}})\bigg|_{\boldsymbol{\eta}=\boldsymbol{\eta}^0}\right) \tag{4.17}$$

illustrates that the sensitivity calculation boils down to the derivative of the vectorized observability. The analytical derivative of the observability in modal basis is available (Basseville et al., 2000), but only in complex-valued format $\boldsymbol{\mathcal{O}}_c^{mod}$, indicated through the subscript c. More details on the similarity transformation of the observability into modal coordinates is given in Section 3.3.3. By re-organizing the complex-valued poles and their derivatives

$$\boldsymbol{\Lambda}_i^p = \begin{bmatrix} 1 & \lambda_i & \lambda_i^2 & \cdots & \lambda_i^p \end{bmatrix}^T, \qquad \boldsymbol{\Lambda}_i'^p = \frac{\partial}{\partial \lambda_i}\boldsymbol{\Lambda}_i^p = \begin{bmatrix} 0 & 1 & 2\lambda_i & \cdots & p\lambda_i^{p-1} \end{bmatrix}^T, \tag{4.18}$$

the derivative of the observability can be written as

$$\frac{\partial}{\partial \boldsymbol{\eta}}\mathrm{vec}(\boldsymbol{\mathcal{O}}_c^{mod}) = \left[\begin{array}{ccc|ccc} \boldsymbol{\Delta}_1'^p \otimes \boldsymbol{\varphi}_1 & & \mathbf{0} & \boldsymbol{\Delta}_1^p \otimes \mathbf{I}_r & & \mathbf{0} \\ & \ddots & & & \ddots & \\ \mathbf{0} & & \boldsymbol{\Delta}_{N_m}'^p \otimes \boldsymbol{\varphi}_{N_m} & \mathbf{0} & & \boldsymbol{\Delta}_{N_m}^p \otimes \mathbf{I}_r \end{array}\right]. \tag{4.19}$$

For consistency, a similarity transformation is applied to the state space model, leading to a real-valued observability of

$$\boldsymbol{\mathcal{O}}^{mod} = \begin{bmatrix} \mathrm{Re}(\boldsymbol{\mathcal{O}}^c) & \mathrm{Im}(\boldsymbol{\mathcal{O}}^c) \end{bmatrix}, \tag{4.20}$$

and ultimately, the real-valued derivative is obtained as (Basseville et al., 2000)

$$\frac{\partial}{\partial \boldsymbol{\eta}}\mathrm{vec}(\boldsymbol{\mathcal{O}}^{mod})\bigg|_{\boldsymbol{\eta}=\boldsymbol{\eta}^0} = \begin{bmatrix} \mathrm{Re}(\boldsymbol{\mathcal{O}}^{c'}) & -\mathrm{Im}(\boldsymbol{\mathcal{O}}^{c'}) \\ \mathrm{Im}(\boldsymbol{\mathcal{O}}^{c'}) & \mathrm{Re}(\boldsymbol{\mathcal{O}}^{c'}) \end{bmatrix} \tag{4.21}$$

and substituted into the Jacobian from Eq. (4.17). Exchanging the data-driven observability (in modal basis) with the observability constructed based on numerical modal parameters allows one to drop the expectation operator in Eq. (4.17), and alleviates all problems related to data-driven modal system identification. The last calculation steps deserve special attention because they determine the format of the final Jacobian matrix. The derivative of the observability is only available in complex-valued format and the data-driven observability in Eq. (4.17) is real-valued.

This can be remedied through a similarity transformation of the state space model, but leads to a non-intuitive arrangement of the derivatives, and, with it, the modal vector and the Jacobian matrix from Eq. (4.14).

b) Link to Structural Parameters

Changes in the mean residual can also be linked to changes in structural parameters. First, the data-driven residual is linked to modal parameters in discrete-time through the sensitivity matrix $\boldsymbol{\mathcal{J}}^{(1)}$. Secondly, modal parameters in discrete-time are linked to the modal parameters of a FE model, which are in continuous-time, through another Jacobian matrix $\boldsymbol{\mathcal{J}}^{(2)}$. Thirdly, numerical modal parameters are linked to structural parameters in the same model using $\boldsymbol{\mathcal{J}}^{(3)}$. Ultimately, all sensitivity matrices are combined into one through the chain rule

$$\boldsymbol{\mathcal{J}} = \left.\frac{\partial E_{\boldsymbol{\theta}}[\boldsymbol{\varepsilon}]}{\partial \boldsymbol{\theta}}\right|_{\boldsymbol{\theta}=\boldsymbol{\theta}^0} = \boldsymbol{\mathcal{J}}^{(1)} \cdot \boldsymbol{\mathcal{J}}^{(2)} \cdot \boldsymbol{\mathcal{J}}^{(3)} \tag{4.22}$$

as visualized in Fig. 4.1. The calculation of the first Jacobian matrix $\boldsymbol{\mathcal{J}}^{(1)}$ is explained in the previous paragraph, see Eq. (4.14). The second Jacobian matrix links the poles and mode shapes in discrete-time from Eq. (4.14) to poles and mode shapes in continuous-time $\boldsymbol{\Lambda}_c$ and $\boldsymbol{\Psi}_c$. Mode shapes are identical in both domains except that the imaginary part is missing in numerical mode shapes because classical damping is assumed, so the Jacobian entries for mode shapes default to unity or zero. However, each pole can be transformed from discrete-time into continuous-time through $\lambda_i = e^{\mu_i \Delta t}$, so the first derivative is $\partial\lambda_i/\partial\mu_i = \Delta t \lambda_i$. Ultimately, the Jacobian matrix $\boldsymbol{\mathcal{J}}^{(2)} \in \mathbb{R}^{2N_m(r+1)\times 2N_m(r+1)}$ can be assembled

$$\boldsymbol{\mathcal{J}}^{(2)} = \left.\frac{\partial \mathrm{E}_{\boldsymbol{\eta}}[\boldsymbol{\eta}]}{\partial \boldsymbol{\eta}_c}\right|_{\boldsymbol{\eta}_c=\boldsymbol{\eta}_c^0} = \left[\begin{array}{c|c|c|c} \Delta t \cdot \mathrm{Re}(\Lambda) & & -\mathrm{Im}(\Lambda) & \\ \hline & \mathbf{I} & & \mathbf{0} \\ \hline \Delta t \cdot \mathrm{Im}(\Lambda) & & \mathrm{Re}(\Lambda) & \\ \hline & \mathbf{0} & & \mathbf{I} \end{array}\right], \qquad \boldsymbol{\eta}_c = \begin{bmatrix} \mathrm{Re}(\mathrm{diag}(\boldsymbol{\Lambda}_c)) \\ \mathrm{Re}(\mathrm{vec}(\boldsymbol{\Psi}_c)) \\ \mathrm{Im}(\mathrm{diag}(\boldsymbol{\Lambda}_c)) \\ \mathrm{Im}(\mathrm{vec}(\boldsymbol{\Psi}_c)) \end{bmatrix}. \tag{4.23}$$

The third Jacobian matrix links the poles and mode shapes in continuous-time to the structural design parameters. This link could be established through finite differences, but analytical approaches are available as well, e.g., Nelson's method (Sutter et al., 1988). In this thesis, the modal approach is chosen, see (Heylen and Sas, 1997). The following equations are valid for systems with symmetric stiffness, mass and damping matrices $\mathbf{M}^T = \mathbf{M}, \mathbf{C}^{1T} = \mathbf{C}^1, \mathbf{K}^T = \mathbf{K}$, and general damping. The analytical derivative of the $i-$th eigenvalue only requires the $i-$th mode of vibration as input, where the eigenvector derivative requires all N modes of vibration of the dynamic system

in complex conjugate pairs, including non-observable modes, with

$$\begin{aligned}\frac{\partial \mu_i}{\partial \theta_h} =& -\gamma_i \boldsymbol{\Psi}_i^T \left(\mu_i^2 \frac{\partial \mathbf{M}}{\partial \theta_h} + \mu_i \frac{\partial \mathbf{C}^1}{\partial \theta_h} + \frac{\partial \mathbf{K}}{\partial \theta_h}\right) \boldsymbol{\Psi}_i, \\ \frac{\partial \boldsymbol{\Psi}_i}{\partial \theta_h} =& -\frac{1}{2}\gamma_i \boldsymbol{\Psi}_i^T \left(2\mu_i \frac{\partial \mathbf{M}}{\partial \theta_h} + \frac{\partial \mathbf{C}^1}{\partial \theta_h}\right) \boldsymbol{\Psi}_i \boldsymbol{\Psi}_i \\ &+ \sum_{r=1, r\neq i}^{2N} \left(\frac{1}{\mu_r - \mu_i} \gamma_r \boldsymbol{\Psi}_r^T \left(\mu_i^2 \frac{\partial \mathbf{M}}{\partial \theta_h} + \mu_i \frac{\partial \mathbf{C}^1}{\partial \theta_h} + \frac{\partial \mathbf{K}}{\partial \theta_h}\right) \boldsymbol{\Psi}_i \boldsymbol{\Psi}_r\right),\end{aligned} \tag{4.24}$$

but a good approximation is typically achieved after a reduced number of modes (Sutter et al., 1988). The parameter γ is a scaling factor for unit mass scaling with $\frac{1}{\gamma_i} = \boldsymbol{\Psi}_i^T [2\mu_i \mathbf{M} + \mathbf{C}^1] \boldsymbol{\Psi}_i$. In other words, the derivative of eigenvalues and eigenvectors is expressed through the derivatives of the dynamic mass, damping and stiffness matrices, $\frac{\partial}{\partial \theta_h}\mathbf{M}$, $\frac{\partial}{\partial \theta_h}\mathbf{C}^1$, $\frac{\partial}{\partial \theta_h}\mathbf{K}$. Those derivatives can either be calculated analytically or, more practically, by evaluating the finite differences

$$\frac{\partial \mathbf{K}}{\partial \theta_h} = \frac{\mathbf{K}(\theta_h^0) - \mathbf{K}(\theta_h + \Delta\theta_h)}{\Delta\theta_h}, \qquad \frac{\partial \mathbf{M}}{\partial \theta_h} = \frac{\mathbf{M}(\theta_h^0) - \mathbf{M}(\theta_h + \Delta\theta_h)}{\Delta\theta_h}. \tag{4.25}$$

This approach is compatible with the output from standard FE software, but the step size $\Delta\theta_h$ affects the accuracy of the results unless the dynamic system matrices are linear functions of the structural design parameters. Ultimately, the Jacobian $\boldsymbol{\mathcal{J}}^{(3)} \in \mathbb{R}^{2m(r+1)\times H}$ is assembled

$$\boldsymbol{\mathcal{J}}^{(3)} = \begin{bmatrix} \mathrm{Re}\left(\frac{\partial}{\partial \theta_1}\mathrm{diag}(\boldsymbol{\Lambda}_c)\right) & \cdots & \mathrm{Re}\left(\frac{\partial}{\partial \theta_H}\mathrm{diag}(\boldsymbol{\Lambda}_c)\right) \\ \mathrm{Re}\left(\frac{\partial}{\partial \theta_1}\mathrm{vec}(\boldsymbol{\Psi}_c)\right) & \cdots & \mathrm{Re}\left(\frac{\partial}{\partial \theta_H}\mathrm{vec}(\boldsymbol{\Psi}_c)\right) \\ \mathrm{Im}\left(\frac{\partial}{\partial \theta_1}\mathrm{diag}(\boldsymbol{\Lambda}_c)\right) & \cdots & \mathrm{Im}\left(\frac{\partial}{\partial \theta_H}\mathrm{diag}(\boldsymbol{\Lambda}_c)\right) \\ \mathrm{Im}\left(\frac{\partial}{\partial \theta_1}\mathrm{vec}(\boldsymbol{\Psi}_c)\right) & \cdots & \mathrm{Im}\left(\frac{\partial}{\partial \theta_H}\mathrm{vec}(\boldsymbol{\Psi}_c)\right) \end{bmatrix}. \tag{4.26}$$

Sensitivity matrices link the residual vector to user-defined monitoring parameters. Historically, data-driven modal parameter vectors $\boldsymbol{\eta}$ are used for monitoring (Basseville et al., 2000), in particular, for cases where no reliable FE model is available. However, most considerations in this thesis are based on the model-based parametrization $\boldsymbol{\theta}$ (Basseville et al., 2004). The sensitivity calculation is split into three steps, see Fig. 4.1. Where linking structural parameters to modal parameters through sensitivity vectors in the Jacobian matrices $\boldsymbol{\mathcal{J}}^{(3)}$ and $\boldsymbol{\mathcal{J}}^{(2)}$ is well-established in engineering practice, as it is an essential part of model updating, the link to data-driven residuals is unique to the stochastic subspace-based damage diagnosis through the Jacobian matrix $\boldsymbol{\mathcal{J}}^{(1)}$. The individual sensitivities $\boldsymbol{\mathcal{J}}^{(2)}$ and $\boldsymbol{\mathcal{J}}^{(3)}$ are straightforwardly computed, but the assembly in the Jacobian matrices is non-intuitive because the matrix structure is pre-determined through the derivative of the observability matrix. To aid in the interpretation, the individual Jacobian matrices are visualized in Fig. 5.5.

4.3 Statistical Decision-making

This section summarizes how the distribution of the damage-sensitive residual is transformed into a Gaussian distribution, even for vibration data from the damaged structure. Moreover, statistical tests are reviewed to decide whether the Gaussian residual is a realization of the nominal structure or the damaged structure.

4.3.1 Damage Hypothesis

During monitoring, the state of the parameter vector from Eq. (4.1) is unknown, but a hypothesis is made that it changes from its known reference state with well-defined parametrization to the damaged state with (Benveniste et al., 1987)

$$\begin{aligned} H_0 &: \ \boldsymbol{\theta} = \boldsymbol{\theta}^0 && \text{(reference state)} \\ H_1 &: \ \boldsymbol{\theta} = \boldsymbol{\theta}^0 + \boldsymbol{\delta}/\sqrt{N} && \text{(damaged state).} \end{aligned} \tag{4.27}$$

The alternative hypothesis is part of a statistical framework known as the asymptotic local approach, where the statistical change vector $\boldsymbol{\delta}$ is unknown but fixed. It implies that smaller changes are detected with increasing sample size and is consistent with the CLT for the residual

$$\boldsymbol{\zeta} = \sqrt{N}(\hat{\boldsymbol{\varepsilon}} - \mathrm{E}[\hat{\boldsymbol{\varepsilon}}]) \longrightarrow \begin{cases} \mathcal{N}(\mathbf{0}, \boldsymbol{\Sigma}) & \text{under } H_0 \\ \mathcal{N}(\boldsymbol{\mathcal{J}}\boldsymbol{\delta}, \boldsymbol{\Sigma}) & \text{under } H_1. \end{cases} \tag{4.28}$$

As explained in Section 4.2.2, the distribution of the residual vector approximates a Gaussian distribution with zero mean vector and covariance $\boldsymbol{\Sigma}$, in the reference state. In the damaged state, the mean of the residual changes from the zero vector to $\boldsymbol{\mathcal{J}}\boldsymbol{\delta}$ with

$$\boldsymbol{\delta} = \sqrt{N}(\boldsymbol{\theta} - \boldsymbol{\theta}^0). \tag{4.29}$$

The mean vector notation results from a Taylor series expansion cut off after the linear term, and multiplied by $\sqrt{N}$, compare Eq. (4.13) and (4.29). The CLT requires the covariance to be recomputed if the excitation characteristics change, but practical applications often employ the covariance from the reference state, thus assuming constant excitation characteristics. In essence, the monitoring problem simplifies to monitoring the mean vector of the Gaussian residual, and statistical hypothesis tests are applied to assess the significance of the deviation.

4.3.2 Generalized Likelihood Ratio

The generalized likelihood ratio (GLR) is a statistical hypothesis test. With the GLR, an informed decision can be made on whether the Gaussian residual computed based on incoming data is more likely to be a realization of the reference structure or the damaged structure. The starting point for the following considerations is the probability density function (PDF) of a random variable $\boldsymbol{\zeta}$

that follows a Gaussian distribution of dimension υ (Muirhead, 1982)

$$p(\boldsymbol{\zeta}) = \frac{1}{(2\pi)^{\upsilon/2}\det(\boldsymbol{\Sigma})^{1/2}} \exp\left(-\frac{1}{2}(\boldsymbol{\zeta}-\boldsymbol{\mathcal{J}}\boldsymbol{\delta})^T\boldsymbol{\Sigma}^{-1}(\boldsymbol{\zeta}-\boldsymbol{\mathcal{J}}\boldsymbol{\delta})\right). \tag{4.30}$$

The likelihood is calculated for both the null hypothesis H_0 and the alternate hypothesis H_1, where the ratio determines whether it is more likely that the variable is drawn from the PDF corresponding to the alternate hypothesis (Muirhead, 1982)

$$\mathrm{GLR}(\boldsymbol{\zeta}) = -2\log\frac{p(\boldsymbol{\zeta}|\boldsymbol{\theta}^0)}{\sup_{\boldsymbol{\theta}\in H_1} p(\boldsymbol{\zeta}|\boldsymbol{\theta})}. \tag{4.31}$$

Substituting the PDF from Eq. (4.30), the GLR unfolds to

$$\begin{aligned}\mathrm{GLR} &= \boldsymbol{\zeta}^T\boldsymbol{\Sigma}^{-1}\boldsymbol{\zeta} + \sup_{\boldsymbol{\theta}\in H_1}\left[-(\boldsymbol{\zeta}-\boldsymbol{\mathcal{J}}\boldsymbol{\delta})^T\boldsymbol{\Sigma}^{-1}(\boldsymbol{\zeta}-\boldsymbol{\mathcal{J}}\boldsymbol{\delta})\right] \\ &= \sup_{\boldsymbol{\theta}\in H_1}\left[(2\boldsymbol{\delta}^T\boldsymbol{\mathcal{J}}^T\boldsymbol{\Sigma}^{-1}\boldsymbol{\zeta} - \boldsymbol{\delta}^T\boldsymbol{\mathcal{J}}^T\boldsymbol{\Sigma}^{-1}\boldsymbol{\mathcal{J}}\boldsymbol{\delta}\right],\end{aligned} \tag{4.32}$$

where the supremum (or least upper bound) is reached for $\boldsymbol{\delta} = (\boldsymbol{\mathcal{J}}^T\boldsymbol{\Sigma}^{-1}\boldsymbol{\mathcal{J}})^{-1}\boldsymbol{\mathcal{J}}^T\boldsymbol{\Sigma}^{-1}\boldsymbol{\zeta}$. For this case, the GLR reduces to (Benveniste et al., 1987)

$$\mathrm{GLR} = \boldsymbol{\zeta}^T\boldsymbol{\Sigma}^{-1}\boldsymbol{\mathcal{J}}(\boldsymbol{\mathcal{J}}^T\boldsymbol{\Sigma}^{-1}\boldsymbol{\mathcal{J}})^{-1}\boldsymbol{\mathcal{J}}^T\boldsymbol{\Sigma}^{-1}\boldsymbol{\zeta} \tag{4.33}$$

The non-parametric GLR is a special case of the parametric GLR where the Jacobian matrix is set to unity $\boldsymbol{\mathcal{J}} = \mathbf{I}$. This means that the Gaussian residual is not linked to any parameters but monitored directly through

$$\mathrm{GLR} = \boldsymbol{\zeta}^T\boldsymbol{\Sigma}^{-1}\boldsymbol{\zeta}. \tag{4.34}$$

4.3.3 Test Distribution

This section gives insight into the statistical properties of the GLR and demonstrates that it approximates a chi-squared distribution with a well-defined number of degrees of freedom ν and non-centrality λ, with $\mathrm{GLR} \longrightarrow \chi^2(\nu,\lambda)$.

Training State. In the reference state, the Gaussian residual follows a Gaussian distribution with zero mean vector and covariance $\boldsymbol{\Sigma}$. Pre-multiplying the term $\boldsymbol{\mathcal{J}}^T\boldsymbol{\Sigma}^{-1}$

$$\boldsymbol{\zeta} \longrightarrow \mathcal{N}(\mathbf{0},\boldsymbol{\Sigma}) \tag{4.35}$$

$$\boldsymbol{\mathcal{J}}^T\boldsymbol{\Sigma}^{-1}\boldsymbol{\zeta} \longrightarrow \mathcal{N}(\mathbf{0},\boldsymbol{\mathcal{J}}^T\boldsymbol{\Sigma}^{-1}\boldsymbol{\mathcal{J}}) \tag{4.36}$$

as well as $(\boldsymbol{\mathcal{J}}^T\boldsymbol{\Sigma}^{-1}\boldsymbol{\mathcal{J}})^{-1/2}$, leads to a new vector $\mathbf{z} \in \mathbb{R}^H$ of equal size as the parameter vector from Eq. (4.1) and standard Gaussian distribution

$$\mathbf{z} = (\boldsymbol{\mathcal{J}}^T\boldsymbol{\Sigma}^{-1}\boldsymbol{\mathcal{J}})^{-1/2}\boldsymbol{\mathcal{J}}^T\boldsymbol{\Sigma}^{-1}\boldsymbol{\zeta} \longrightarrow \mathcal{N}(\mathbf{0}, \mathbf{I}), \tag{4.37}$$

and squaring up this vector yields the test statistic from Eq. (4.33).

$$t = \mathbf{z}^T\mathbf{z} = \boldsymbol{\zeta}^T\boldsymbol{\Sigma}^{-1}\boldsymbol{\mathcal{J}}(\boldsymbol{\mathcal{J}}^{\boldsymbol{T}}\boldsymbol{\Sigma}^{-\mathbf{1}}\boldsymbol{\mathcal{J}})^{-\mathbf{1}}\boldsymbol{\mathcal{J}}^T\boldsymbol{\Sigma}^{-1}\boldsymbol{\zeta} \longrightarrow \chi^2(\nu, \lambda), \tag{4.38}$$

Summing over the square of multiple zero mean and Gaussian-distributed variables through $t = \mathbf{z}^T\mathbf{z}$ results in a *central* chi-square distribution with ν degrees of freedom. The number of degrees of freedom represents the number of independent Gaussian processes that are present in the residual which, for full rank Jacobians, is equal to the number of parameters H in the parameter vector from Eq. (4.1). The PDF of the central χ^2-distribution is formally defined as (Muirhead, 1982)

$$f_{\chi^2(\nu)}(t) = \frac{x^{\nu/2-1}e^{-t/2}}{2^{\nu/2}(\nu/2-1)!}. \tag{4.39}$$

Damaged State. In the damaged state, the mean Gaussian residual is not zero but $\boldsymbol{\mathcal{J}}\boldsymbol{\delta}$, see Eq. (4.28). That means that pre-multiplying the term $\boldsymbol{\mathcal{J}}^T\boldsymbol{\Sigma}^{-1}$ not only alters the covariance but also the mean value of the Gaussian distribution, and thus, the mean value of the χ^2-distribution.

$$\begin{aligned} \boldsymbol{\zeta} &\longrightarrow \mathcal{N}(\boldsymbol{\mathcal{J}}\boldsymbol{\delta}, \boldsymbol{\Sigma}) \\ \boldsymbol{\mathcal{J}}^T\boldsymbol{\Sigma}^{-1}\boldsymbol{\zeta} &\longrightarrow \mathcal{N}(\boldsymbol{\mathcal{J}}^T\boldsymbol{\Sigma}^{-1} \cdot \boldsymbol{\mathcal{J}}\boldsymbol{\delta}, \boldsymbol{\mathcal{J}}^T\boldsymbol{\Sigma}^{-1}\boldsymbol{\mathcal{J}}). \end{aligned} \tag{4.40}$$

Correspondingly, the unit-variance vector $\mathbf{z}$ yields

$$\mathbf{z} = (\boldsymbol{\mathcal{J}}^T\boldsymbol{\Sigma}^{-1}\boldsymbol{\mathcal{J}})^{-1/2}\boldsymbol{\mathcal{J}}^T\boldsymbol{\Sigma}^{-1}\boldsymbol{\zeta} \longrightarrow \mathcal{N}((\boldsymbol{\mathcal{J}}^T\boldsymbol{\Sigma}^{-1}\boldsymbol{\mathcal{J}})^{1/2}\boldsymbol{\delta}, \mathbf{I}) \tag{4.41}$$

and squaring the vector results in

$$t = \mathbf{z}^T\mathbf{z} = \boldsymbol{\zeta}^T\boldsymbol{\Sigma}^{-1}\boldsymbol{\mathcal{J}}(\boldsymbol{\mathcal{J}}^{\boldsymbol{T}}\boldsymbol{\Sigma}^{-\mathbf{1}}\boldsymbol{\mathcal{J}})^{-\mathbf{1}}\boldsymbol{\mathcal{J}}^T\boldsymbol{\Sigma}^{-1}\boldsymbol{\zeta} \longrightarrow \chi^2(\nu, \lambda). \tag{4.42}$$

In other words, the test distribution approximates a *non-central* χ^2-distribution with a non-centrality λ, i.e., a shift in the mean value, by

$$\lambda = \mathrm{E}[\boldsymbol{\zeta}]^T \cdot \mathrm{E}[\boldsymbol{\zeta}] = ((\boldsymbol{\mathcal{J}}^T\boldsymbol{\Sigma}^{-1}\boldsymbol{\mathcal{J}})^{1/2}\boldsymbol{\delta})^T((\boldsymbol{\mathcal{J}}^T\boldsymbol{\Sigma}^{-1}\boldsymbol{\mathcal{J}})^{1/2}\boldsymbol{\delta}) = \boldsymbol{\delta}^T(\boldsymbol{\mathcal{J}}^T\boldsymbol{\Sigma}^{-1}\boldsymbol{\mathcal{J}})\boldsymbol{\delta}. \tag{4.43}$$

With respect to the central χ^2-distribution, the PDF of the non-central distribution follows (Muirhead, 1982)

$$f_{\chi^2(\nu,\lambda)}(t) = \sum_{n=0}^{\infty} e^{-\frac{\lambda}{2}} \frac{(\lambda/2)^n}{n!} f_{\chi^2(\nu+2n,0)}(t). \tag{4.44}$$

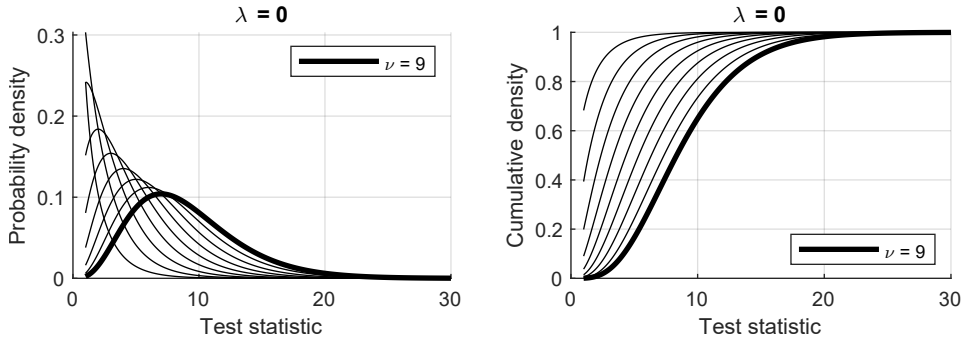

Figure 4.2: Central χ^2-distribution for a varying number of degrees of freedom $\nu \in [1, \ldots, 9]$

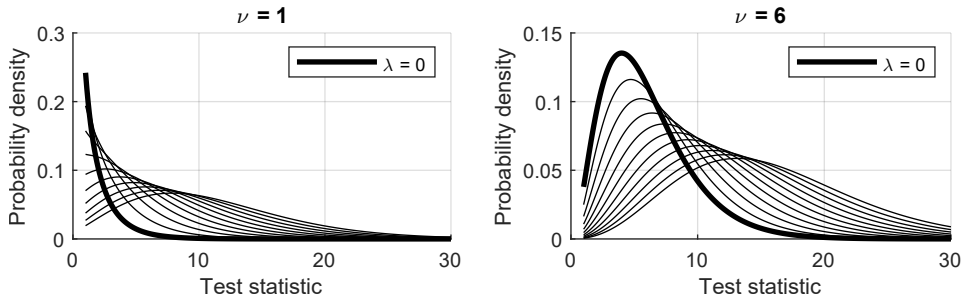

Figure 4.3: Non-central χ^2-distribution for a fixed number of degrees of freedom and varying non-centrality $\lambda \in [0, 1, \ldots, 10]$

Non-parametric Case. The non-parametric test also follows a χ^2-distribution with identical non-centrality but a different number of degrees of freedom. First, a new vector $\mathbf{z}$ with unit variance is defined by pre-multiplying $\mathbf{\Sigma}^{-1/2}$ to the residual of the damaged state, so

$$\mathbf{z} = \mathbf{\Sigma}^{-1/2}\boldsymbol{\zeta} \longrightarrow \mathcal{N}(\mathbf{\Sigma}^{-1/2} \cdot \boldsymbol{\delta}, \mathbf{I}). \tag{4.45}$$

Squaring up this vector yields the non-parametric test statistic

$$t = \mathbf{z}^T\mathbf{z} = \boldsymbol{\zeta}^T\mathbf{\Sigma}^{-1}\boldsymbol{\zeta} \longrightarrow \chi^2(k, \lambda), \tag{4.46}$$

with the non-centrality parameter

$$\lambda = \mathrm{E}[\boldsymbol{\zeta}]^T \cdot \mathrm{E}[\boldsymbol{\zeta}] = (\mathbf{\Sigma}^{-1/2}\boldsymbol{\delta})^T(\mathbf{\Sigma}^{-1/2}\boldsymbol{\delta}) = \boldsymbol{\delta}^T(\mathbf{\Sigma}^{-1})\boldsymbol{\delta} \tag{4.47}$$

and the PDF from Eq. (4.44). In summary, the GLR approximates a chi-squared distribution $\chi^2(\nu, \lambda)$. Where the number of degrees of freedom ν depends on the residual's covariance and sensitivity, see Eq. (5.4), the non-centrality depends on the damage extent, see Eq. (4.43). The non-centrality is the mean test response to damage, which is more meaningful than individual

test results because they are widely scattered. For clarity, Fig. 4.2 visualizes the PDF and the cumulative density function (CDF) of the central χ^2 distribution for varying degrees of freedom. In contrast, Fig. 4.3 plots the non-central χ^2-distribution for a fixed number of degrees of freedom and varying non-centrality.

4.3.4 Fisher Information Matrix

The Fisher information plays a key role as a scaling factor in the GLR from Eq. (4.33) as well as the non-centrality in Eq. (4.43). It is defined as (Frieden, 2004)

$$\mathbf{F} = \left(\frac{\partial \boldsymbol{\zeta}}{\partial \boldsymbol{\theta}}\right)^T \boldsymbol{\Sigma}^{-1} \left(\frac{\partial \boldsymbol{\zeta}}{\partial \boldsymbol{\theta}}\right) = \boldsymbol{\mathcal{J}}^T \boldsymbol{\Sigma}^{-1} \boldsymbol{\mathcal{J}} \tag{4.48}$$

where the informative value depends on both the residual's sensitivity and the uncertainty related to its estimation. The main diagonal values should be seen as a measure for the detectability in the corresponding monitoring parameter θ_h and the off-diagonal terms quantify how damage in a certain parameter affects the test response of other parameters.

4.4 Damage Diagnosis Tests

The GLR is applied to detect damage in Gaussian residuals and to locate the monitoring parameter that is most likely to be damaged. In total, four different tests are available, the parametric detection test, the non-parametric detection test, the direct localization test, and the minmax localization test.

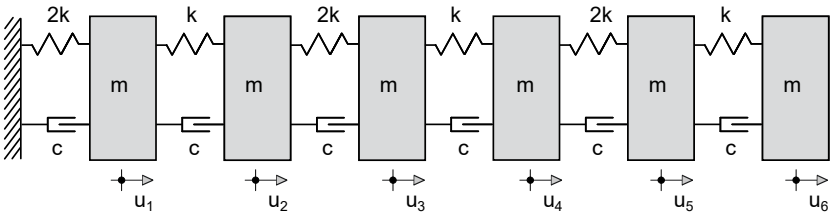

Figure 4.4: 6-DOF mass-and-spring system

For demonstration, the presented damage diagnosis tests are applied to a mass-and-spring system with six degrees of freedom, see Fig. 4.4. The mass values are $m = 1$ t and the spring stiffness is alternating with $k = 2,000$ MPa. A modal damping ratio of 2% critical damping is assumed for all modes. The natural frequencies are 2.03 Hz, 5.95 Hz, 9.28 Hz, 12.38 Hz, 15.62 Hz, and 16.96 Hz. For excitation, a white noise input signal is applied along all six degrees of freedom, and the velocities are measured at the degrees of freedom u_1, u_3, and u_5.

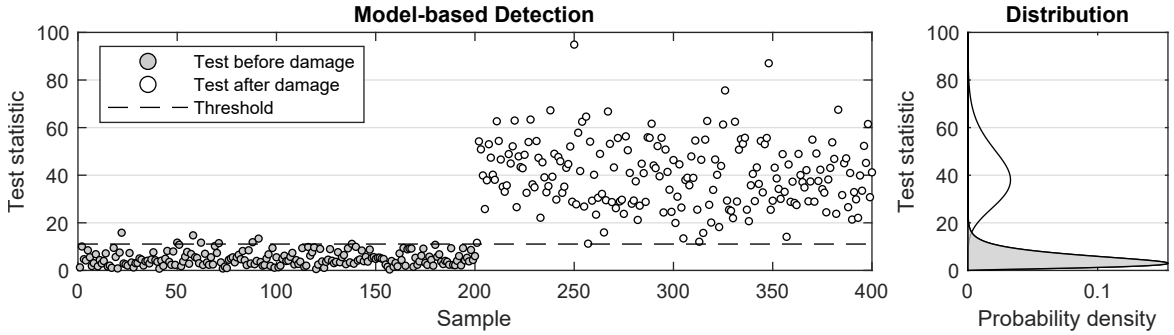

Figure 4.5: Damage detection of a 2% stiffness decrease in Spring 1

4.4.1 Parametric Detection Test

In the model-based version of the parametric detection test, structural parameters are tested for damage. The test statistic is (Basseville et al., 2000)

$$t = \boldsymbol{\zeta}^T \boldsymbol{\Sigma}^{-1} \boldsymbol{\mathcal{J}} \left(\boldsymbol{\mathcal{J}}^T \boldsymbol{\Sigma}^{-1} \boldsymbol{\mathcal{J}} \right)^{-1} \boldsymbol{\mathcal{J}}^T \boldsymbol{\Sigma}^{-1} \boldsymbol{\zeta} \longrightarrow \begin{cases} \chi^2(\nu, 0) & \text{under} \quad H_0 \\ \chi^2(\nu, \lambda) & \text{under} \quad H_1 \end{cases} \tag{4.49}$$

and approximates a χ^2-distribution with $\nu = H$ for full rank Jacobian matrices. For all detection tests, damage manifests itself in a distinct jump in the test statistic, see Fig. 4.5. The parametric detection test can also be data-driven, in which case modal parameters are tested for changes, i.e., poles and mode shapes from OMA (Basseville et al., 2004). The data-driven version is identical to Eq. (4.49) except that the Jacobian matrix is replaced with $\boldsymbol{\mathcal{J}}^{(1)}$ from Eq. (4.14)

$$t = \boldsymbol{\zeta}^T \boldsymbol{\Sigma}^{-1} \boldsymbol{\mathcal{J}}^{(1)} \left(\boldsymbol{\mathcal{J}}^{(1)T} \boldsymbol{\Sigma}^{-1} \boldsymbol{\mathcal{J}}^{(1)} \right)^{-1} \boldsymbol{\mathcal{J}}^{(1)T} \boldsymbol{\Sigma}^{-1} \boldsymbol{\zeta} \longrightarrow \begin{cases} \chi^2(\nu, 0) & \text{under} \quad H_0 \\ \chi^2(\nu, \lambda) & \text{under} \quad H_1, \end{cases} \tag{4.50}$$

which changes the number of degrees of freedom of the χ^2-distribution to $\nu = 2mr$ for full rank Jacobian matrices. Jacobian matrices that do not have a full-column rank will be discussed in Chapter 5, see Eq. (5.4).

4.4.2 Non-parametric Detection Test

The non-parametric detection test includes the Gaussian residual and the covariance, but no Jacobian matrix. It is defined as (Balmès et al., 2008b)

$$t = \boldsymbol{\zeta}^T \boldsymbol{\Sigma}^{-1} \boldsymbol{\zeta} \longrightarrow \begin{cases} \chi^2(\nu, 0) & \text{under} \quad H_0 \\ \chi^2(\nu, \lambda) & \text{under} \quad H_1. \end{cases} \tag{4.51}$$

The parametric detection test from Eq. (4.49) can be transformed into the non-parametric test by setting the Jacobian matrix to unity $\boldsymbol{\mathcal{J}} = \mathbf{I}$ (Döhler et al., 2014b). Correspondingly, the number

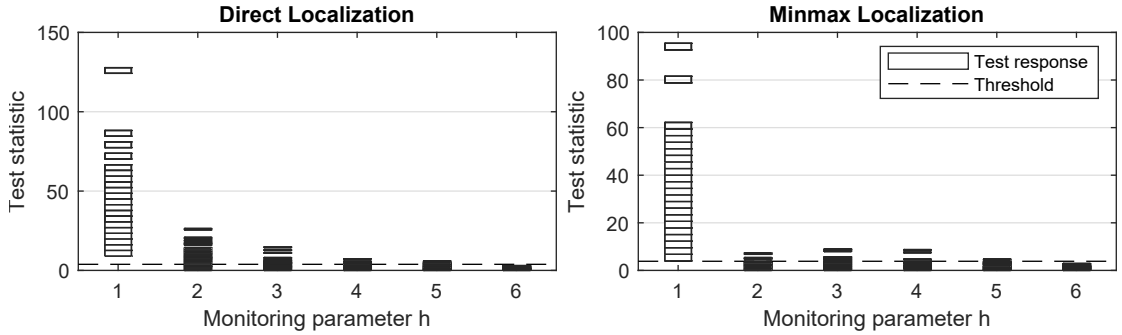

Figure 4.6: Damage localization of a 2% stiffness decrease in Spring 1

of degrees of freedom is $\nu = \operatorname{rank}\left(\boldsymbol{\Sigma}^{-1}\right)$, see Eq. (5.4). The test is purely data-driven, meaning neither a modal parametrization nor a structural parametrization is required.

4.4.3 Direct Localization Test

In the direct localization test (Basseville et al., 2004), each monitoring parameter is individually tested for damage, see Fig. 4.6. With the GLR, the alternate hypothesis H_1 is tested against the null hypothesis H_0 from Eq. (4.27) for each parameter. This assumes that damage is either restricted to one parameter $\boldsymbol{\mathcal{J}}\boldsymbol{\delta} = \boldsymbol{\mathcal{J}}_h\delta_h$ or no damage is present. The test statistic (Döhler et al., 2016)

$$t_h = \boldsymbol{\zeta}_h^T F_h^{-1}\boldsymbol{\zeta}_h \longrightarrow \begin{cases} \chi^2(1,0) & \text{under} \quad H_0 \\ \chi^2(1,\lambda) & \text{under} \quad H_1 \end{cases} \tag{4.52}$$

is identical to Eq. (4.49) except that only one column of the sensitivity matrix $\boldsymbol{\mathcal{J}}_h$ is tested

$$\boldsymbol{\zeta}_h = \boldsymbol{\mathcal{J}}_h^T\boldsymbol{\Sigma}^{-1}\boldsymbol{\zeta} \longrightarrow \mathcal{N}(F_h\delta, F_h) \tag{4.53}$$

with the Fisher information

$$F_h = \boldsymbol{\mathcal{J}}_h^T\boldsymbol{\Sigma}^{-1}\boldsymbol{\mathcal{J}}_h. \tag{4.54}$$

Consequently, the number of degrees of freedom of the test distribution is $\nu = 1$. The parameter with the greatest test response $\lambda_h = \mathrm{E}[\boldsymbol{\zeta}]^T\mathrm{E}[\boldsymbol{\zeta}] = \delta_h^2 F_h$ is likely to be the one that has changed due to damage. Unfortunately, unchanged parameters also show a response due to the off-diagonal terms of the Fisher information, see Parameter 2 in Fig. 4.6. An elegant way to diminish false localization alarms is the minmax test, which is described in the subsequent paragraph.

4.4.4 Minmax Localization Test

The minmax localization test assumes the alternate hypothesis H_1 from Eq. (4.27) for both the tested and non-tested parameters (Basseville, 1997). It evaluates how much more likely the tested partition is damaged compared to any other partition, and selects the least favourable scenario. To

implement this, the Gaussian residual is projected onto the tested parameter θ_h and the untested parameters $\boldsymbol{\theta}_{\bar{h}}$ through the corresponding sensitivity vectors

$$\boldsymbol{\zeta}_h = \boldsymbol{\mathcal{J}}_h^T \boldsymbol{\Sigma}^{-1} \boldsymbol{\zeta} \longrightarrow \mathcal{N}(F_h \delta_h, F_h) \tag{4.55}$$

$$\boldsymbol{\zeta}_{\bar{h}} = \boldsymbol{\mathcal{J}}_{\bar{h}}^T \boldsymbol{\Sigma}^{-1} \boldsymbol{\zeta} \longrightarrow \mathcal{N}(\mathbf{F}_{\bar{h}h} \delta_h, \mathbf{F}_{\bar{h}\bar{h}}), \tag{4.56}$$

and then, each partitioned residual $\boldsymbol{\zeta}_h$ is projected orthogonally to the non-tested partition $\boldsymbol{\zeta}_{\bar{h}}$,

$$\boldsymbol{\zeta}_h^* = \boldsymbol{\zeta}_h - \mathbf{F}_{h\bar{h}} \mathbf{F}_{\bar{h}\bar{h}}^{-1} \boldsymbol{\zeta}_{\bar{h}} \longrightarrow \mathcal{N}(F_h^* \delta_h, \boldsymbol{\Sigma}_h^*), \tag{4.57}$$

preserving the residual's sensitivity toward changes in the tested partition and making it blind to changes in untested partitions, with the robust Fisher information

$$F_h^* = F_h - \mathbf{F}_{h\bar{h}} \mathbf{F}_{\bar{h}\bar{h}}^{-1} \mathbf{F}_{\bar{h}h}. \tag{4.58}$$

The resulting minmax test statistic is (Döhler et al., 2016)

$$t_h^* = \boldsymbol{\zeta}_h^{*T} F_h^{*-1} \boldsymbol{\zeta}_h^* \longrightarrow \begin{cases} \chi^2(1,0) & \text{under} \quad H_0 \\ \chi^2(1,\lambda) & \text{under} \quad H_1, \end{cases} \tag{4.59}$$

is χ^2-distributed with one degree of freedom and non-centrality $\lambda_h = \delta_h^T F_h^* \delta_h$. In theory, the false localization alarms are zero, see Fig. 4.6. However, the following section gives reasons why false localization alarms are re-introduced for monitoring applications that are more complex than the considered 6-DOF system.

Parameter Substructuring

Previous consideration regarding the minmax test assumed that the Fisher information is of full rank, so the Jacobian matrix has full column rank. This is the case if the rank estimate from Eq. (5.4) yields a value that is equal to the number of monitoring parameters, and for practical applications, this means that the number of modes of vibration is high in comparison to the monitoring parameters. The problem addressed in this section is that the minmax localization test is not applicable to problems with (nearly) rank deficient Fisher information. Rank deficiency can be caused by an over-parametrization, i.e., problem formulations where multiple parameters have similar sensitivities toward the residual. Consequently, linear dependencies arise in the columns of the Jacobian matrix and a basic condition for the projection in Eq. (4.57) is violated. The problem can be remedied by removing individual parameters or combining redundant parameters in one partition and averaging the sensitivity vectors (Basseville et al., 2004). This was first done based on a k-means clustering approach (Balmès et al., 2008b), and later replaced by a hierarchical clustering (Allahdadian et al., 2019). Hierarchical clustering has several advantages, for example, convergence is guaranteed regardless of the starting point, potential issues related to local minima

are alleviated, and it is less sensitive to outliers. The hierarchical clustering approach is explained in the following. The first step is to normalize the Jacobian

$$\tilde{\boldsymbol{\mathcal{J}}} = \boldsymbol{\Sigma}^{-1/2}\boldsymbol{\mathcal{J}} = \begin{bmatrix} \tilde{\boldsymbol{\mathcal{J}}}_1 & \cdots & \tilde{\boldsymbol{\mathcal{J}}}_H \end{bmatrix} \tag{4.60}$$

so the following metrics are consistent with the damage localization test in Eq. (4.59) and the Fisher information in Eq. (4.48). Secondly, the cosine between the vectors is used to measure the dissimilarity

$$d_{ij} = 1 - \frac{\tilde{\boldsymbol{\mathcal{J}}}_i^T \tilde{\boldsymbol{\mathcal{J}}}_j}{||\tilde{\boldsymbol{\mathcal{J}}}_i|| \cdot ||\tilde{\boldsymbol{\mathcal{J}}}_j||}. \tag{4.61}$$

If the two vectors are orthogonal, the cosine is one and the dissimilarity is zero, and it is one if the two vectors are linearly dependent. At the start of the clustering algorithm, the number of clusters K equals the number of parameters H. For each iteration, the distances between all pairs of clusters are evaluated according to the complete-linkage cluster distance, defined as (Duda et al., 2012)

$$D(C_a, C_b) = \max\{d_{ij} : i \in C_a, j \in C_b\}. \tag{4.62}$$

Gradually, the two clusters with the shortest distance $d = \min\{D(C_a, C_b) : a \neq b\}$ are combined, until only one cluster is left, so $K = 1$. For each K, the cluster centres c_k is determined through averaging as

$$\mathbf{c}_k = \frac{1}{m_k} \sum_{i \in C_k} \tilde{\boldsymbol{\mathcal{J}}}_i, \tag{4.63}$$

where m_k is the number of parameters in cluster C_k and $k \in [1, \ldots, K]$ is the cluster number. Finally, the cluster centres are arranged in the clustered Jacobian

$$\tilde{\boldsymbol{\mathcal{J}}}^c = \begin{bmatrix} \mathbf{c}_1 & \cdots & \mathbf{c}_K \end{bmatrix} \tag{4.64}$$

which is of full rank and thus fulfills the requirements for the minmax test.

Option 1: Testing Clusters. One approach is to replace the original Jacobian matrix with the clustered Jacobian matrix from Eq. (4.64). In this case, the minmax test evaluates the likelihood ratio that damage is contained within one cluster while taking the least favourable result for all other clusters. In other words, the partition

$$\tilde{\boldsymbol{\mathcal{J}}}_k = \mathbf{c}_k \tag{4.65}$$

is tested while projecting it orthogonally to the sensitivity vectors

$$\tilde{\boldsymbol{\mathcal{J}}}_{\bar{k}} = \begin{bmatrix} \mathbf{c}_1 & \ldots & \mathbf{c}_{k-1} & \mathbf{c}_{k+1} & \ldots & \mathbf{c}_K \end{bmatrix}. \tag{4.66}$$

In this sense, $\boldsymbol{\mathcal{J}}_k$ and $\boldsymbol{\mathcal{J}}_{\bar{k}}$ are the tested and rejected partitions, respectively.

Option 2: Testing Parameters. Another approach is to test the original Jacobian matrix against the cluster centres in Eq. (4.64). The minmax test determines the likelihood that damage is contained in one single parameter or column of the Jacobian matrix $\boldsymbol{\mathcal{J}}_h$, while projecting the information orthogonal to the cluster centres of the clusters that do not contain the tested parameter.

$$\tilde{\boldsymbol{\mathcal{J}}}_{\bar{h}}^{c} = \begin{bmatrix} \mathbf{c}_1 & \dots & \mathbf{c}_{k(h)-1} & \mathbf{c}_{k(h)+1} & \dots & \mathbf{c}_K \end{bmatrix}. \tag{4.67}$$

That means that the monitoring parameters are tested against cluster centres. The second approach is the preferred one in this thesis because the damage location can be narrowed down.

4.5 Interpreting the Test Result

This section summarizes relevant metrics to interpret the test results. Due to the statistical nature of the method, the test statistics for damage detection and localization are scattered, and it is more reliable to evaluate test distributions instead of individuals samples. Hence, the statistical tests are repeatedly applied to different data sets in a Monte Carlo experiment, and the empirical distributions are plotted in histograms, see Fig. 4.5 and 4.6. The decisive measure is then the non-centrality, i.e., the distance between the mean values of the test distribution in the training state and the damaged state.

4.5.1 Empirical Reference Distribution

If all input parameters for the damage detection method are chosen appropriately, the histograms approximate the theoretical properties of the χ^2-distribution that are reviewed in Section 4.3.3. Vice versa, the empirical training state distribution is a an appropriate means to verify the input parameter settings. In theory, the test distribution that corresponds to an undamaged structure follow a central χ^2-distribution with the PDF in Eq. (4.39). The distribution has one variable, i.e., the number of degrees of freedom, so it can be fitted to the histogram using regression techniques. If the number of degrees of freedom of the fitted distribution is equal to the theoretical value ν from Eq. (5.4), the training state is validated. An alternate way, that avoids the use of the theoretical PDF, is to average the test responses because the mean value of the central χ^2-distribution is equal to its number of degrees of freedom. Having said that, being able to compare the shape of the theoretical distribution function to the empirical histogram is another means of validation, because an empirical distribution that is significantly wider than the theoretical function can indicate inappropriate signal processing. For the non-parametric detection test, the curve fitting plays a different role. In most cases, the singular values of the covariance matrix do not show a distinct jump and the numerical rank calculation $\nu = \text{rank}(\boldsymbol{\Sigma})$ leads to misleading results. Therefore, curve-fitting is often the only way to correctly estimate ν.

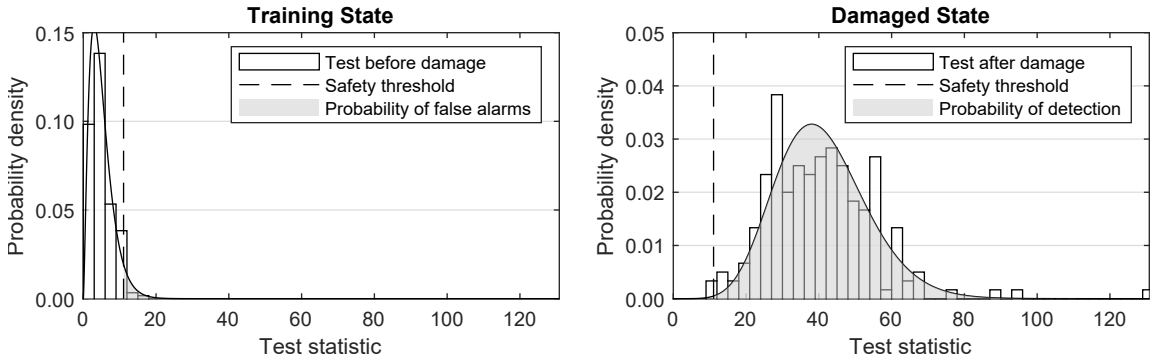

Figure 4.7: Probability of false alarms, safety threshold value, and probability of detection

4.5.2 Empirical Safety Threshold

In theory, there will always be an overlap between the distribution corresponding to the training state and damaged state, so a safety threshold is to be defined to distinguish the distributions. If a test falls beyond the safety threshold, it indicates that the structure is damaged, otherwise it is undamaged. This approach inevitability leads to false alarms, meaning the test indicates that the structure is damaged although no damage is present. Based on the acceptable probability of false alarms (PFA)

$$\alpha = P(t > t_{crit}|\boldsymbol{\theta}^0), \tag{4.68}$$

a safety threshold value is defined for the training state, see left side of Fig. 4.7. To do so, the CDF from Fig. 4.2 is evaluated by integrating over the PDF from Eq. (4.39)

$$F_{\chi^2(\nu)}(t) = \int_0^\infty f_{\chi^2(\nu)}(t)dt, \tag{4.69}$$

and the complement of the desired PFA $1-\alpha$ is plugged into the CDF together with the fitted number of degrees of freedom ν. Then, the safety threshold value can be solved for as

$$t_{crit} = F^{-1}_{\chi^2(\nu)}(1-\alpha). \tag{4.70}$$

In other words, the safety threshold is the quantile value $Q(1-\alpha)$ of the central χ^2-distribution. Typically, the PFA is set to $\alpha = 5\%$ or lower, meaning every 20th test is a false alarm. One alternative is to skip the empirical curve fitting from the previous section and use the theoretical value for the number of degrees of freedom instead. Another alternative is to discard the theoretical χ^2-distribution and simply adjust t_{crit} until the desired PFA is achieved.

4.5.3 Empirical Power of Detection

The empirical probability of detection (POD) evaluates the performance of the test. It is defined as the relative number of test samples that fall beyond the safety threshold value, see the right side

of Fig. 4.7. Where the theoretical value is POD $= P(t > t_{crit}|\boldsymbol{\theta})$, the empirical value

$$\text{POD} = \frac{1}{n_s}\sum_{k=1}^{n_s} a_k \tag{4.71}$$

can simply be evaluated by summing up the number of damage alerts a and relating them to the total number of test results n_s. To conclude this section, the damage diagnosis method is summarized in a flowchart, see Fig. 4.8. Note that a single evaluation run is sufficient in the damaged state, and a Monte Carlo simulation is only necessary if the test results are to be interpreted based on the empirical POD from Eq. (4.71).

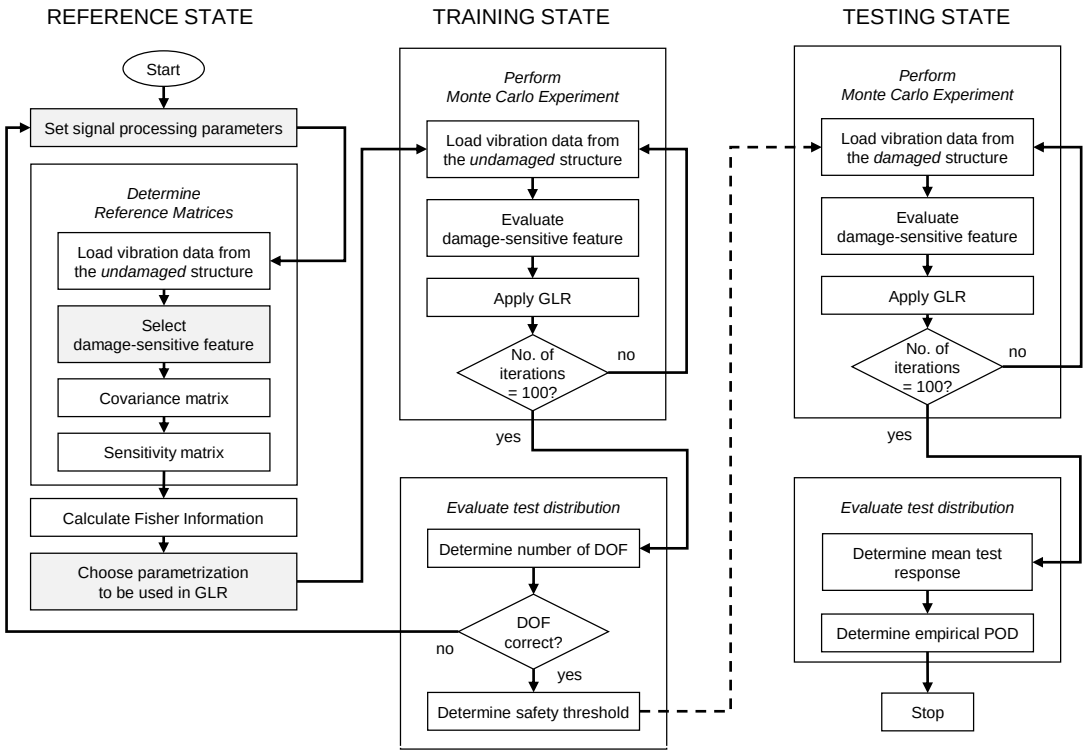

Figure 4.8: Flowchart for damage diagnosis

4.6 Summary

The asymptotic local (AL) approach is a statistical framework for vibration-based damage detection and localization. Originally, it was developed for stochastic dynamic systems, where the excitation is unknown, and applied in combination with the subspace-based residual. Having said that, the method can be applied to any damage-sensitive residual that approximates a Gaussian distribution (with well-defined covariance matrix) and can be linked to modal parameters or structural design parameters through sensitivity vectors (Jacobian matrix). What makes the presented version promising is that structural parameters are linked to a damage-sensitive residual that is formed

	Damage detection	**Damage localization**
Data-driven	Non-parametric test Parametric test (OMA-based)	
Model-based	Parametrized test (FEA-based)	
		Direct test (FEA-based) Minmax test (FEA-based)

OMA: Operational modal analysis, FEA: Finite element analysis

Table 4.1: Classifying the available damage diagnosis tests

based on covariance functions in the time domain. Since many classical damage-sensitive residuals are derived from covariance functions, the methodology presented herein is easily generalizable.

In the AL method, a decision regarding the health state of the structure is made by applying a statistical hypothesis test to the damage-sensitive feature, i.e., the generalized likelihood ratio (GLR) and the minmax test. A distinctive feature of the GLR is that the statistical properties of the test distribution are defined for both the training state and the damaged state. The Fisher information is a key element to link the damaged state to the reference state. It considers both the sensitivity of the damage-sensitive residual toward monitoring parameters as well as its uncertainty. Where each main diagonal value of the Fisher information is a measure for the detectability of damage, the off-diagonal values quantify how damage in a certain parameter affects the test response of others.

The available damage detection tests are divided into a model-based test and two data-driven tests, where the data-driven tests are either non-parametric or parametrized with respect to modal parameters, see Table 4.1. Where non-parametric damage detection is well-established and implemented in commercially available computer software, parametric damage detection and damage localization based on the AL method is a matter of ongoing research. Finite element (FE) models can be avoided during damage detection, but they are essential for damage localization. Two different damage localization tests are available, i.e., the direct localization test and the minmax localization test, see Tab. 4.1. The direct localization test directly tests each monitoring parameter for damage, but does not consider the effect that changed parameters have on the test results for unchanged parameters, which leads to false localization alarms. The minmax localization takes into account the off-diagonal values of the Fisher information and significantly reduces false alarms. If the Jacobian matrix is not of full rank, the monitoring parameters have to be clustered prior to the damage localization, which corresponds to a substructuring of the FE model into damage localization units. However, no guidance is given on how to find an appropriate number of substructures.

Part II

CONTRIBUTIONS

Chapter 5

Minimum Detectable Damage

This chapter develops a reliability-based framework to predict the minimum detectable damage based on ambient vibration data from the reference structure. The minimum detectable damage is defined as the minimum change in a structural design parameter that can be reliably detected based on changes in the damage-sensitive feature. The method is developed for statistical damage diagnosis tests based on the asymptotic local (AL) approach. It can be applied to any damage-sensitive residual $\hat{\boldsymbol{\varepsilon}}$ that approximates a Gaussian distribution with a mean value that can be linked to structural parameters through sensitivity analysis. More precisely, the damage-sensitive residual must satisfy the central limit theorem (CLT) (Benveniste et al., 1987)

$$\boldsymbol{\zeta} = \sqrt{N}(\hat{\boldsymbol{\varepsilon}} - \mathrm{E}[\hat{\boldsymbol{\varepsilon}}]) \longrightarrow \begin{cases} \mathcal{N}(\mathbf{0}, \boldsymbol{\Sigma}) & \text{(reference)} \\ \mathcal{N}(\boldsymbol{\mathcal{J}}\boldsymbol{\delta}, \boldsymbol{\Sigma}) & \text{(damaged)} \end{cases} \tag{5.1}$$

where $\boldsymbol{\Sigma}$ is the sample covariance, $\boldsymbol{\mathcal{J}}$ is the first-order sensitivity matrix that links the damage-sensitive residual $\hat{\boldsymbol{\varepsilon}}$ to structural parameters, and $\boldsymbol{\delta}$ is the statistical change vector

$$\boldsymbol{\delta} = (\boldsymbol{\theta} - \boldsymbol{\theta}^0)\sqrt{N}, \tag{5.2}$$

which is unknown, but fixed. Background information on the Gaussian residual is given in the previous chapter, which focuses on the stochastic subspace-based residual, refer to Eq. (4.28).

The chapter is organized as follows: Section 5.1 introduces a reliability-based approach to determine the minimum detectable damage based on measurement data from the reference state and sensitivities from a finite element (FE) model, and Section 5.2 provides theoretical proof that the prediction is also valid for data-driven tests. Section 5.3 addresses the numerical problems that can arise when applying the damage detection test to large mechanical systems, and the last section (Section 5.4) provides a proof of concept study using the numerical model of a steel beam.

5.1 Main Idea

A decision on whether the structure is damaged or not can be made by applying the generalized likelihood ratio (GLR) to the Gaussian residual. The definition of the test statistic from Section 4.4.1

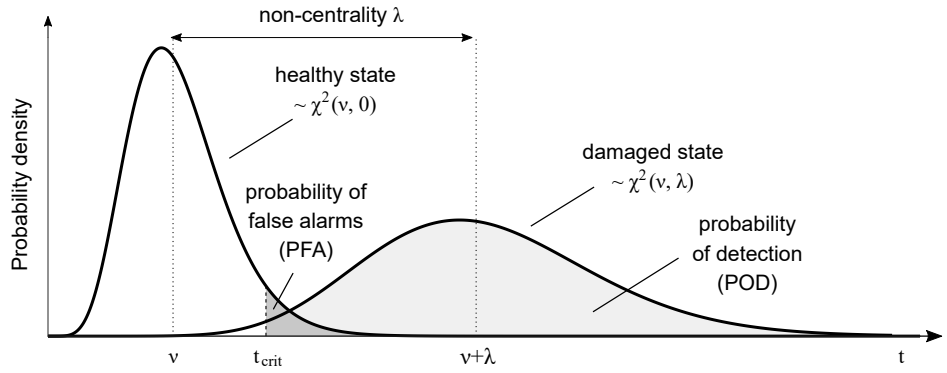

Figure 5.1: Statistical distribution of the test statistic

is repeated here for convenience (Basseville et al., 2000). The test statistic

$$t = \boldsymbol{\zeta}^T \boldsymbol{\Sigma}^{-1} \boldsymbol{\mathcal{J}} \left(\boldsymbol{\mathcal{J}}^T \boldsymbol{\Sigma}^{-1} \boldsymbol{\mathcal{J}} \right)^{-1} \boldsymbol{\mathcal{J}}^T \boldsymbol{\Sigma}^{-1} \boldsymbol{\zeta} \longrightarrow \begin{cases} \chi^2(\nu, 0) & \text{(reference)} \\ \chi^2(\nu, \lambda) & \text{(damaged)} \end{cases} \tag{5.3}$$

follows a χ^2-distribution with a number of degrees of freedom of

$$\nu = \operatorname{rank} \left(\boldsymbol{\mathcal{J}}^T \boldsymbol{\Sigma}^{-1} \boldsymbol{\mathcal{J}} \right) \tag{5.4}$$

and a non-centrality of $\lambda = \boldsymbol{\delta}^T \mathbf{F} \boldsymbol{\delta}$, where $\mathbf{F}$ is Fisher information matrix

$$\mathbf{F} = \boldsymbol{\mathcal{J}}^T \boldsymbol{\Sigma}^{-1} \boldsymbol{\mathcal{J}}. \tag{5.5}$$

The distribution of the test statistic is visualized in Fig. 5.1, including the mean value in the training state ν, the mean in the testing state $\nu + \lambda$, and the non-centrality λ, i.e., the mean test response. To clearly assign the test statistic to one distribution, a safety threshold value t_{crit} is defined, for example, based on the allowable probability of false alarms (PFA). If the test statistic is below the safety threshold for a damaged structure, it is a false-negative test result, and the complement of the false-negative rate is the probability of detection (POD).

5.1.1 Predictive Formula

In the following, the effect of a single parameter change $\Delta\theta_h = (\theta_h - \theta_h^0)$ is analyzed, while assuming no change in other parameters. Since damage is characterized by a shift in the mean vector by $\boldsymbol{\mathcal{J}}\boldsymbol{\delta}$, see Eq. (5.1), the assumption of a single parameter change is equivalent to assuming that the mean vector of the Gaussian distribution is $\mathrm{E}[\boldsymbol{\zeta}] = \boldsymbol{\mathcal{J}}_h \delta_h$ where $\boldsymbol{\mathcal{J}}_h$ is the h-th column of the Jacobian matrix and δ_h is the h-th entry of the statistical change vector $\boldsymbol{\delta}$ from Eq. (5.2) with

$$\delta_h = \sqrt{N}(\theta_h - \theta_h^0). \tag{5.6}$$

The corresponding mean test response to damage is $\lambda_h = F_{hh}\delta_h^2$, where F_{hh} is the main diagonal of the Fisher information. Substituting the change vector from Eq. (5.6) into the non-centrality results in the *predictive formula* for the mean test response

$$\lambda_h = N \cdot (\theta_h - \theta_h^0)^2 \cdot F_{hh}. \tag{5.7}$$

This formula predicts the mean test response to structural changes based on the sample size during testing N, the magnitude of the parameter changes $\Delta\theta_h$ squared, and the main diagonal value of the Fisher information matrix F_{hh}.

5.1.2 Minimum Detectability

A clear test result is obtained if the mean test response is sufficiently large, because then, the test distribution in the damaged state is well-separated from the training state with a minor overlap, as displayed in Fig. 5.1. Therefore, defining a minimum value for the non-centrality $\lambda_h = \lambda_{\min}$ is equivalent to defining a minimum reliability. Rearranging Eq. (5.7) for the minimum parameter change leads to

$$\theta_h - \theta_h^0 = \sqrt{\frac{\lambda_{\min}}{N \cdot F_{hh}}}. \tag{5.8}$$

For user-friendliness, the formula is normalized by the reference parameter $\Delta_h = (\theta_h - \theta_h^0)/\theta_h^0$ and the data length is substituted by the measurement duration during testing and the sampling frequency $N = Tf_s$. The resulting formula quantifies the *minimum detectable damage* in percent of a reference parameter.

$$\Delta_h = \frac{1}{\theta_h^0}\sqrt{\frac{\lambda_{\min}}{Tf_s \cdot F_{hh}}}[\%]. \tag{5.9}$$

The minimum detectable damage is inversely proportional to the square root of the measurement duration T, and the formula can be re-arranged to

$$T_h = \frac{1}{(\Delta\theta_h)^2}\frac{\lambda_{\min}}{f_s F_{hh}}. \tag{5.10}$$

This is the minimum measurement duration that is required to reliably detect a fixed parameter change $\Delta\theta_h = (\theta_h - \theta_h^0)$. The subscript h indicates that this is not the measurement duration for the monitoring system, but the examined monitoring parameter θ_h. The measurement duration for the structure is the maximum measurement duration over all monitoring parameters

$$T = \max_h\{T_1, \cdots, T_H\}. \tag{5.11}$$

Since the probability density function (PDF) from Fig. 5.1 is mathematically defined for both the training and the damaged state, the minimum non-centrality can be tied back to more intuitive measures such as the PFA and POD. More details on this are given in the subsequent section.

5.1.3 Reliability Concept

The minimum non-centrality quantifies the minimum required test response to damage (averaged over multiple tests), so it can be understood as a reliability index for structural health monitoring (SHM). This section lays out how the minimum non-centrality can be tied back to user-friendly measures such as the PFA and the POD.

Probability of False Alarms (PFA). The PFA is also known as the false-positive rate or the type I error, often denoted as α. It describes how often the test diagnoses a structure as damaged although no damage is present. Based on the allowable false alarm rate, a safety threshold t_{crit} can be defined as the $1-\alpha$ quantile value of the central χ^2-distribution, see Section 4.5.2. The PFA corresponds to the area under the PDF of the χ^2-distribution beyond the safety threshold value, see Fig. 5.1, and is calculated as follows

$$\text{PFA} = 1 - \int_0^{t_{\text{crit}}} f_{\chi^2(\nu,0)}(t)dt. \tag{5.12}$$

Probability of Detection (POD). The POD quantifies how often the structure is classified as healthy although damage has occurred, so it is the complement of the false-negative rate (type II error). It can be calculated by integrating over the area under the PDF of the non-central χ^2-distribution beyond the safety threshold value (see Fig. 5.1), with

$$\text{POD} = \int_{t_{\text{crit}}}^{\infty} f_{\chi^2(\nu,\lambda)}(t)dt. \tag{5.13}$$

A minimum value could be set based on the anticipated damaged consequences. For components that are critical for the safety or serviceability of the structure, the POD can be set based on the existing safety standards for SHM. For Canada and the U.S., the code-based reliability index for assessing civil engineering structures is 3.25 and 2.5. The Eurocode does not define a reliability index for assessment, but the ISO norm defines a reliability index of 4.7 (Wenzel, 2009). The reliability indices are typically used in combination with Gaussian-distributed processes, such as material strength values, but can be translated into an equivalent POD according to Table 5.1.

Minimum Non-centrality. The non-centrality is the only variable in Eq. (5.13). The number of degrees of freedom ν is known from the training state, the safety threshold t_{crit} is setup based on the allowable PFA, and the POD is set by the user based on reliability requirements. The cumulative density function (CDF) of the non-central χ^2-distribution cannot be solved for λ straightforwardly, but through numerical iteration. To determine the minimum non-centrality λ_{min}, the non-centrality λ is increased until the theoretical distribution is shifted beyond the safety threshold value and the desired POD is achieved in Eq. (5.13) for $\lambda = \lambda_{min}$.

The minimum non-centrality can be seen as a problem-specific reliability index. It is different for every monitoring application, because the number of degrees of freedom ν of the χ^2-distribution

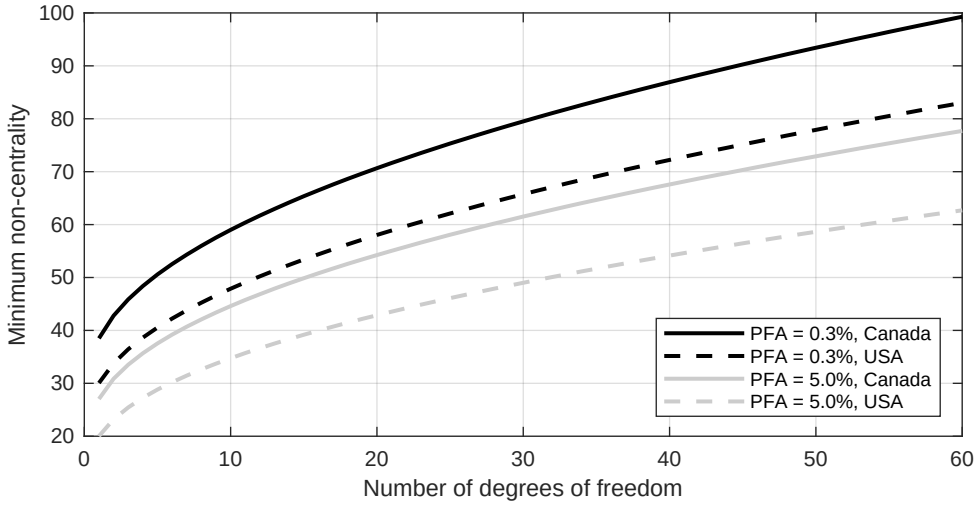

Figure 5.2: Minimum non-centrality as a code-based reliability index

varies. With increasing ν, the χ^2-distribution in the training state becomes wider, and the minimum non-centrality has to be increased to guarantee a sufficient degree of separation with the damaged state distribution. For clarity, the minimum non-centrality is plotted against the number of degrees of freedom in Fig. 5.2. In this thesis, the PFA is often set to 5% to demonstrate that the distributions overlap, but for most practical applications, a much lower value may be appropriate. The four curves in Fig. 5.2 show the reliability index for a PFA of 5% and 0.3%, and a POD of 99.94% and 99.4%, with reference to the Canadian and U.S. American design codes. It can be observed that the reliability index asymptotically increases for an increasing number of degrees of freedom.

5.1.4 Interpretation

The minimum detectable damage from Eq. (5.9) depends on the measurement duration T during testing, the sampling frequency f_s, the magnitude of the monitoring parameter $\boldsymbol{\theta}_h$, the Fisher information F_{hh}, and the reliability index λ_{min}. The Fisher information is a concise quantity that considers multiple factors at once. It includes the residual's uncertainty (covariance) and sensitivity toward structural parameters (Jacobian), see Eq. (5.5). In a broader context, the influence factors for damage detectability can be categorized as follows:

	ISO	**Canada**	**U.S.**
Reliability index	4.7	3.25	2.5
Type II Error [%]	0.0001	0.06	0.6
Probability of detection [%]	99.9999	99.94	99.4

Table 5.1: Interpreting code-based reliability indices

1. *Damage-sensitive residual and its sensitivity.* Damage sensitivity depends on the damage-related information content that is carried by the residual and the contribution of the monitoring parameter to the structure's integrity. Obviously, removing a single screw will have a different effect than removing an entire column. It also depends on the quality of the Jacobian matrix, which depends on the number of modes of vibration that are used to screen the structure for damage, as well as the number and locations of sensors.

2. *Signal-to-noise ratio.* Uncertainties due to limited data and measurement noise in the reference data are inevitable, but they are amplified in measurement records with strong noise components and weak structural signals, i.e., records with a low signal-to-noise ratio (SNR). The SNR is captured through the residual's covariance, and a high SNR leads to higher damage detectability.

3. *Measurement duration.* Uncertainties are also present in the test data, but they decrease with increasing measurement duration. The measurement duration is a powerful tuning parameter to increase the damage detectability, as the mean test response is directly proportional.

4. *Diagnosis reliability.* Setting a low PFA and a high POD may be convenient for the operator of the monitoring system because the test result is very reliable; however, this also requires the damage to be more severe for successful detection.

5. *Complexity.* The complexity of the monitoring problem depends on the number of monitoring parameter in relation to the number of modes of vibration, quantified through the rank of the Fisher information, see Eq. (5.4). A complex problem leads to a high number of degrees of freedom of the χ^2-distribution, a high minimum non-centrality, and lowered damaged detectability.

Therefore, the derived formula demonstrates that the determination of the minimum detectable damage requires an all embracing consideration of the measurement environment, the signal processing parameters, the employed damage-sensitive residual, and the reliability requirements regarding the damage detection results.

5.2 Application to Data-Driven Tests

Linking the damage-sensitive residual to structural design parameters through the Jacobian matrix is a prerequisite to physically define the minimum detectable damage.

$$\boldsymbol{\zeta} = \sqrt{N}(\hat{\boldsymbol{\varepsilon}} - \mathrm{E}[\hat{\boldsymbol{\varepsilon}}^0]) \longrightarrow \mathcal{N}(\boldsymbol{\mathcal{J}}\boldsymbol{\delta}, \boldsymbol{\Sigma}) \qquad\qquad \boldsymbol{\delta} = \sqrt{N}(\boldsymbol{\theta} - \boldsymbol{\theta}^0) \tag{5.14}$$

In many cases, however, it is desirable to perform the damage detection based on data-driven tests, without the use of a FE model. This section provides theoretical proof that the model-based prediction also holds true for data-driven tests. Two data-driven tests are available, a parametric

one and a non-parametric one. In the parametric test, the Gaussian residual is linked to data-driven modal parameters, i.e., poles and mode shapes from operational modal analysis (OMA), through the Jacobian matrix $\boldsymbol{\mathcal{J}}^{(1)}$ with

$$\boldsymbol{\zeta} = \sqrt{N}(\hat{\boldsymbol{\varepsilon}} - \mathrm{E}[\hat{\boldsymbol{\varepsilon}}^0]) \longrightarrow \mathcal{N}(\boldsymbol{\mathcal{J}}^{(1)}\boldsymbol{\delta}^{(1)}, \boldsymbol{\Sigma}), \qquad \boldsymbol{\delta}^{(1)} = \sqrt{N}(\boldsymbol{\eta} - \boldsymbol{\eta}^0). \tag{5.15}$$

The non-parametric detection test is purely data-driven, so no Jacobian matrix is required for damage diagnosis. The non-parametric test is equivalent to the parametric test where the Jacobian matrix is set to the unity matrix $\boldsymbol{\mathcal{J}}^{non} = \mathbf{I}$. Consequently, the mean vector of the Gaussian residual in the damaged state simplifies to the statistical change vector $\boldsymbol{\delta}^{non}$ with

$$\boldsymbol{\zeta} = \sqrt{N}(\hat{\boldsymbol{\varepsilon}} - \mathrm{E}[\hat{\boldsymbol{\varepsilon}}^0]) \longrightarrow \mathcal{N}(\mathbf{I}\boldsymbol{\delta}^{non}, \boldsymbol{\Sigma}), \qquad \boldsymbol{\delta}^{non} = \sqrt{N}(\hat{\boldsymbol{\varepsilon}} - \mathrm{E}[\hat{\boldsymbol{\varepsilon}}]). \tag{5.16}$$

Comparing the damaged state distribution from Eq. (5.14) and Eq. (5.15) with the distribution of the non-parametric test in Eq. (5.16) clarifies that the mean vector is expressed through different parametrizations but the same damage-sensitive residual is evaluated in every case (refer to Fig. 4.1). So, the mean of the Gaussian residual changes by the same amount, regardless of the parametrization that is used with

$$\mathrm{E}[\boldsymbol{\zeta}] = \boldsymbol{\delta}^{non} = \boldsymbol{\mathcal{J}}^{(1)}\boldsymbol{\delta}^{(1)} = \boldsymbol{\mathcal{J}}\boldsymbol{\delta}. \tag{5.17}$$

Since the mean vectors are identical, the different tests have an equal mean test response, because the non-centrality is calculated based on the mean vector. Equivalently, the test response can be expressed based on the model-based Fisher information regardless of the parametrization

$$\lambda = \mathrm{E}[\boldsymbol{\zeta}]^T\mathrm{E}[\boldsymbol{\zeta}] = \boldsymbol{\delta}^T\left(\boldsymbol{\mathcal{J}}^T\boldsymbol{\Sigma}^{-1}\boldsymbol{\mathcal{J}}\right)\boldsymbol{\delta} = \boldsymbol{\delta}^T\mathbf{F}\boldsymbol{\delta} \tag{5.18}$$

and the model-based Fisher information can be used to predict the test response of data-driven tests. Having said that, the number of degrees of freedom depends on the Jacobian matrix, see Eq. (5.4), so the reliability index λ_{min} changes for each test and, with it, the minimum detectable damage, as discussed in Section 5.1.3.

5.3 Numerical Considerations for Large Systems

This section offers a numerically efficient approach to compute the GLR from Eq. (5.3) based on a QR-decomposition with column pivoting. The presented approach is robust, even for badly conditioned sensitivity matrices with both column rank deficiency and/or row-rank deficiency. First, the matrix product $\boldsymbol{\Sigma}^{-1/2}\boldsymbol{\mathcal{J}}$ is decomposed using QR-decomposition where the sensitivity matrix is assumed to be badly degraded, i.e., column-rank deficient and row-rank deficient.

$$\mathbf{P}\left(\boldsymbol{\Sigma}^{-1/2}\boldsymbol{\mathcal{J}}\right) = \mathbf{QR} \tag{5.19}$$

The permutation matrix $\mathbf{P}$ is chosen so the main diagonal of $\mathbf{R}$ holds non-increasing values with $|r_{11}| \geq |r_{22}| \geq \dots$ Due to the rank deficiency, the equation can be reduced to

$$\boldsymbol{\Sigma}^{-1/2}\boldsymbol{\mathcal{J}} = \begin{bmatrix}\mathbf{Q}_1 & \mathbf{Q}_2\end{bmatrix} \begin{bmatrix}\mathbf{R}_{11} & \mathbf{R}_{12} \\ \mathbf{0} & \mathbf{0}\end{bmatrix} \mathbf{P}^T = \left(\mathbf{Q}_1\tilde{\mathbf{R}}\right)\mathbf{P}^T. \tag{5.20}$$

This eliminates any distortion due to rank deficiency and leaves behind the invertible matrix $\tilde{\mathbf{R}} = \begin{bmatrix}\mathbf{R}_{11} & \mathbf{R}_{12}\end{bmatrix}$ as well as the the orthonormal matrix $\mathbf{Q}_1$ with $\mathbf{Q}_1^T\mathbf{Q}_1 = \mathbf{I}$. Substituting Eq. (5.20) into the GLR from Eq. (4.49), the statistical test unfolds to

$$\begin{aligned}
t &= \boldsymbol{\zeta}^T(\boldsymbol{\Sigma}^{-1/2})^T\boldsymbol{\Sigma}^{-1/2}\boldsymbol{\mathcal{J}}\left(\boldsymbol{\mathcal{J}}^T(\boldsymbol{\Sigma}^{-1/2})^T\boldsymbol{\Sigma}^{-1/2}\boldsymbol{\mathcal{J}}\right)^\dagger \boldsymbol{\mathcal{J}}^T(\boldsymbol{\Sigma}^{-1/2})^T\boldsymbol{\Sigma}^{-1/2}\boldsymbol{\zeta} \\
&= \boldsymbol{\zeta}^T(\boldsymbol{\Sigma}^{-1/2})^T\mathbf{Q}_1\tilde{\mathbf{R}}\mathbf{P}^T\left(\mathbf{P}\tilde{\mathbf{R}}^T\mathbf{Q}_1^T\mathbf{Q}_1\tilde{\mathbf{R}}\mathbf{P}^T\right)^\dagger \mathbf{P}\tilde{\mathbf{R}}^T\mathbf{Q}_1^T\boldsymbol{\Sigma}^{-1/2}\boldsymbol{\zeta} \\
&= \boldsymbol{\zeta}^T(\boldsymbol{\Sigma}^{-1/2})^T\mathbf{Q}_1\tilde{\mathbf{R}}\mathbf{P}^T\left(\tilde{\mathbf{R}}\mathbf{P}^T\right)^\dagger\left(\mathbf{P}\tilde{\mathbf{R}}^T\right)^\dagger \mathbf{P}\tilde{\mathbf{R}}^T\mathbf{Q}_1^T\boldsymbol{\Sigma}^{-1/2}\boldsymbol{\zeta} \\
&= \boldsymbol{\zeta}^T(\boldsymbol{\Sigma}^{-1/2})^T\mathbf{Q}_1\tilde{\mathbf{R}}\mathbf{P}^T\mathbf{P}\tilde{\mathbf{R}}^\dagger(\tilde{\mathbf{R}}^T)^\dagger\mathbf{P}^T\mathbf{P}\tilde{\mathbf{R}}^T\mathbf{Q}_1^T\boldsymbol{\Sigma}^{-1/2}\boldsymbol{\zeta} \\
&= \boldsymbol{\zeta}^T(\boldsymbol{\Sigma}^{-1/2})^T\mathbf{Q}_1\cdot\mathbf{Q}_1^T\boldsymbol{\Sigma}^{-1/2}\boldsymbol{\zeta},
\end{aligned} \tag{5.21}$$

where $\dagger$ is the pseudo inverse. Using a newly defined vector $\mathbf{z} = \mathbf{Q}_1^T\boldsymbol{\Sigma}^{-1/2}\boldsymbol{\zeta}$, which describes the standard Gaussian distribution of the damage-sensitive feature as well as their relation to monitoring parameters, the global damage detection test simplifies to

$$t = \mathbf{z}^T\mathbf{z}. \tag{5.22}$$

This test can cope with sensitivity matrices that are both row-rank deficient and column-rank deficient. This is crucial because the sensitivity matrix is rank deficient for most applications. The sensitivity matrix becomes row-rank deficient if multiple residual entries exhibit similar sensitivities toward a structural parameter, which is the case in almost every application and has already been treated in the literature, see Appendix C.2 in (Döhler et al., 2014b). Column rank deficiency, on the other hand, can occur if a low number of modes is used to monitor a large number of structural parameters. Therefore, the presented test is essential when applying the statistical damage detection test to large mechanical structures.

5.4 Proof of Concept

For proof of concept, the predictive formula is validated by means of a numerical case study using MATLAB® and ANSYS®. The structure under consideration is a 4.11 m-long steel beam on pin supports. It has a hollow structural steel (HSS) cross-section with a modulus of elasticity of $E = 210,000$ MPa and a total mass of $m = 56.8$ kg. The instrumentation consists of a single vibration sensor that samples the velocity in the vertical direction, see Fig. 5.3. Damage is defined as a change in material stiffness.

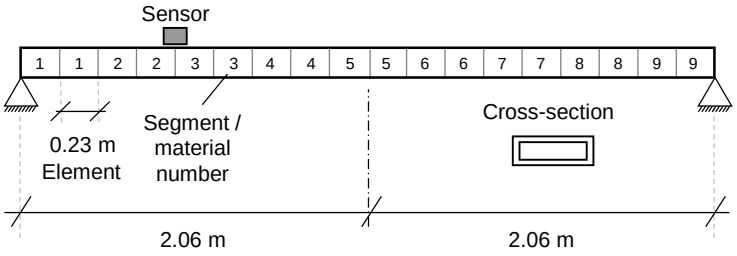

Figure 5.3: HSS beam with nine material properties and one sensor

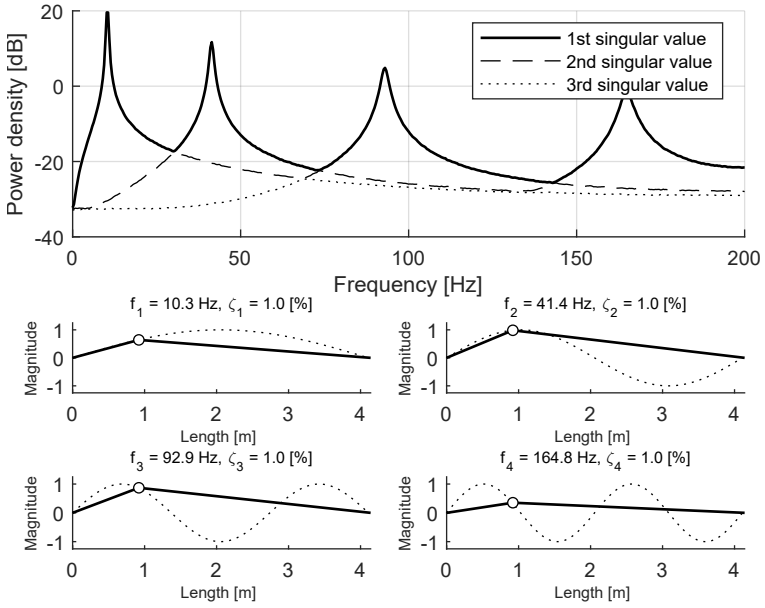

Figure 5.4: Numerical mode shapes and power spectral density of the generated signal

For modelling, the beam is discretized into 19 nodes with six degrees of freedom (DOF) at each node and 18 finite beam elements. At the supports, all degrees of freedom are restrained except the rotation about the transverse axis, reducing the degrees of freedom to 104. Damage is defined as a decrease in material stiffness, i.e., the modulus of elasticity. For simplification, two consecutive FE elements are assigned to the same material (see Fig. 5.3), reducing the number of parameters in the monitoring vector to nine

$$\boldsymbol{\theta} = \begin{bmatrix} E_1 & \dots & E_9 \end{bmatrix}. \tag{5.23}$$

The damage detection method is data-driven but a numerical model is required to calculate the analytical derivatives of structural parameters toward modal parameters, i.e., the Jacobian matrix $\boldsymbol{\mathcal{J}}^{(3)}$. The results from a numerical modal analysis are summarized in Fig. 5.4. The first four modes are considered for damage diagnosis with natural frequencies of 10.3 Hz, 41.4 Hz, 92.9 Hz, and 164.8 Hz. The figure also shows the numerical mode shapes at the single sensor location. For signal generation, a transient analysis is run while applying uniformly distributed white noise to all vertical DOF. Moreover, uniformly distributed measurement noise is added to the output signal, with a magnitude corresponding to 5% of the signal's variance. The vibration signal is first sampled

Data		Segmenting		Processing	
Measured quantity	velocity	Training segments	240	No. of sensors	r/r_0=1/1
Sampling frequency	400 Hz	Testing segments	200	Time lags	p/q=10/11
Reference data length	120 min	Samples/segment	12,000	System order	n=10
Training/testing data	100 min	Duration/segment	30 s	No. of blocks	n_b=36,000

Table 5.2: Input parameter sheet

at a high rate and later filtered and down-sampled to 400 Hz to avoid aliasing. All other input parameters for the damage diagnosis are summarized in Table 5.2. To visualize the signal-to-noise ratio, the singular values of the power spectral density matrix are plotted in Fig. 5.4 although the damage diagnosis is performed in the time domain.

To obtain the dynamic system matrices, an interface between MATLAB® and ANSYS® is created. ANSYS® takes as input the structural parameters $\boldsymbol{\theta}$, and returns the full system matrices $\mathbf{M}, \mathbf{C}^1$, and $\mathbf{K}$. Based on the *direct sensitivity method* (Heylen and Sas, 1997), MATLAB® analytically computes the derivatives of modal parameters towards structural parameters, i.e., the Jacobian $\boldsymbol{\mathcal{J}}^{(3)}$ from Sec. 4.2.3. The sensitivity matrix is set up using the poles and mode shapes of the first four modes, see Fig. 5.4, but the mode shape derivatives consider the first 30 modes.

5.4.1 Monitoring Model-based Parameters

Since this is the first application of the stochastic subspace-based damage diagnosis method in this thesis, the analysis procedure is thoroughly explained. The monitoring procedure is divided into three monitoring states: the reference state, the training state, and the testing state.

Reference State. In the reference state, all quantities are determined that define the vibration behaviour of the undamaged structure. First, the block Hankel matrix is estimated and the null space $\mathbf{U}_0$ is extracted, see Eq. (4.3). Secondly, the covariance $\boldsymbol{\Sigma}$ of the damage-sensitive residual is evaluated, see Section. (4.2.2). Using the observability in modal basis, the first sensitivity matrix is calculated $\boldsymbol{\mathcal{J}}^{(1)}$, as in Eq. (4.17). In this study, this matrix links $g = 11$ residual entries to $2N_m(r+1) = 16$ modal parameters, where N_m and r are the number of modes and number of sensors. The second Jacobian matrix has $2N_m(r+1)$ rows and columns, as it links data-driven modal parameters to numerical modal parameters. The third Jacobian matrix is available from the FE model and links $2N_m(r+1)$ modal parameters to $H = 9$ structural parameters, see Fig. 5.5. The analytical Jacobian matrices are combined to one matrix that links the Gaussian residual to structural parameters $\boldsymbol{\mathcal{J}} = \boldsymbol{\mathcal{J}}^{(1)}\boldsymbol{\mathcal{J}}^{(2)}\boldsymbol{\mathcal{J}}^{(3)}$. Ultimately, the Fisher information is calculated and the main diagonal values are extracted to assess the damage detectability, see Fig. 5.6. The measurement duration in the reference state T^0 is set so all matrices have converged, meaning it does not influence the results of the damage diagnosis.

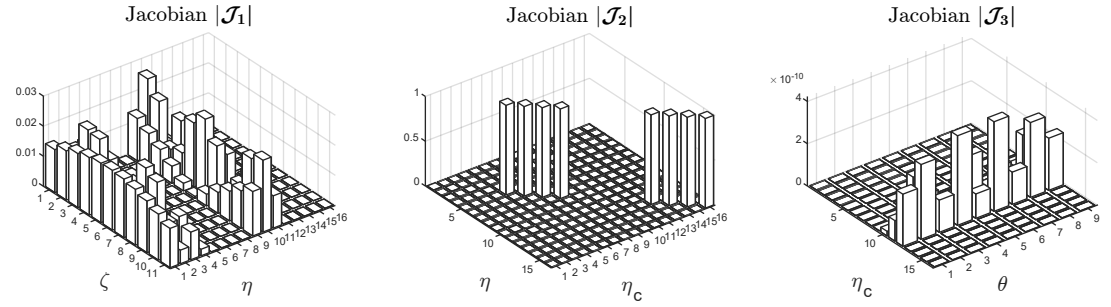

Figure 5.5: Jacobian computation through the chain rule (reference state)

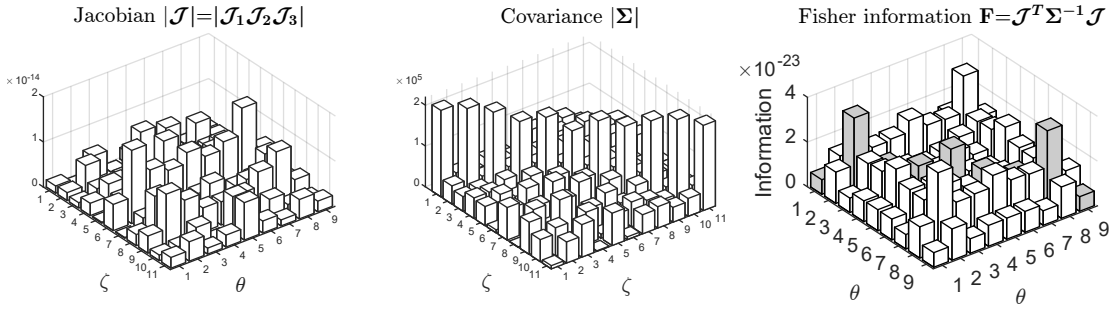

Figure 5.6: Fisher information computation (reference state)

Training State. In the training state, the distribution of the test statistic is verified, and a safety threshold value is set. For this purpose, another long data record from the undamaged structure is divided into 240 data segments of 30 s length while applying the damage detection test from Eq. (5.3) to each segment in a Monte Carlo experiment. The resulting histogram can be compared to the theoretical distribution, and a safety threshold value is set based on the allowable PFA, see Section 4.5. This is visualized in Fig. 5.7 where the empirical distribution of the test (grey histogram) is identical to the theoretical distribution with six DOF, refer to Eq. (5.4). Based on a PFA of 5%, the safety threshold is defined as the 95% quantile value, which is $t_{crit} = 14.1$. With the safety threshold t_{crit} being determined, the non-central chi-square distribution $\chi^2(\nu, \lambda_{min})$ is found by increasing the non-centrality parameter until the area under the PDF beyond the safety threshold value is equal to the acceptable POD for $\lambda = \lambda_{min}$, see Section 5.1.3. This is achieved for a minimum non-centrality of $\lambda_{min} = 31.4$. Consequently, all input parameters for the predictive formula from Eq. (5.9) are available, as the sampling frequency f_s, the measurement duration $T = 30$ s and the magnitude of the structural parameters are problem-specific constants. The minimum detectable damage is summarized in Table 5.3.

Validation State. The validation state is driven by vibration data from the damaged structure. The primary goal is to validate that the response of the damage detection test is predicted accurately, which can be done by setting the damage in one monitoring parameter to the minimum detectable damage. In that case, the empirical non-centrality is equal to the minimum non-centrality $\lambda = \lambda_{min}$ and the empirical probability of detection is equal to the required POD, in theory. The

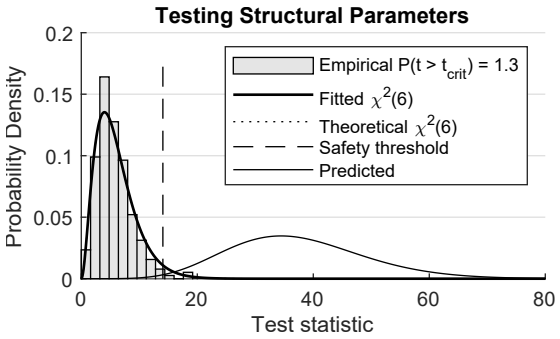

Figure 5.7: Training state

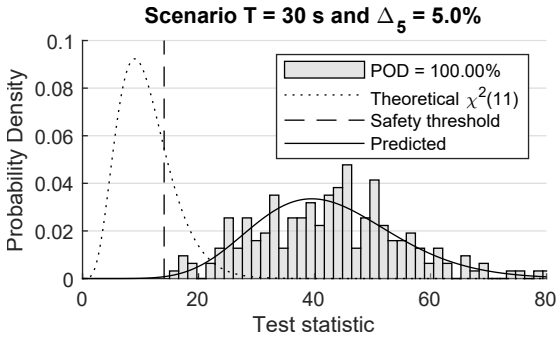

Figure 5.8: Validation state

distribution is again evaluated in a Monte Carlo experiment, meaning the vibration signal is divided into 200 data segments and the damage detection test is applied to each segment. Figure 5.8 visualizes the empirical test distribution in the damaged state, where the stiffness of beam segment 5 is reduced by the minimum detectable damage of $\Delta_5 = 5.0\%$. The mean test response appears to be equal to the theoretical test response, as the histogram fills the area under the theoretical distribution (solid black line). The POD of the Monte Carlo experiment is 100%, and thus, close to the theoretical value of 99.94%, and the predictive formula is validated. For completeness, the validation is repeated for the eight other beam segments, where the applied damaged is set to the respective minimum detectable damage from Table 5.3. The results in Fig. 5.9 confirm that the prediction is accurate for each beam segment with a POD that ranges between 99.5% and 100%.

5.4.2 Monitoring with Data-Driven Tests

This section demonstrates that the prediction of the minimum detectable damage is also valid for data-driven tests. Two data-driven tests are analyzed, i.e., the parametric test and the non-parametric test.

Study 1: Testing for Changes in Modal Parameters

In the parametric test from Eq. (4.50), the residual is linked to modal parameters so modal parameters can be tested for changes. The procedure in the reference state is identical to before, see Section 5.4.1, and the Fisher information is evaluated with respect to structural parameters. In the training state, the GLR is applied to multiple data sets from the undamaged structure, in a Monte Carlo experiment, using the Jacobian matrix with respect to modal parameters $\boldsymbol{\mathcal{J}}^{(1)}$. The

Minimum Detectable Damage [%]									
Monitoring parameter	E_1	E_2	E_3	E_4	E_5	E_6	E_7	E_8	E_9
Parameter change	9.6	4.1	6.3	6.2	5.0	6.2	6.3	4.1	9.6

Table 5.3: Minimum detectable change in the modulus of elasticity E for each beam segment

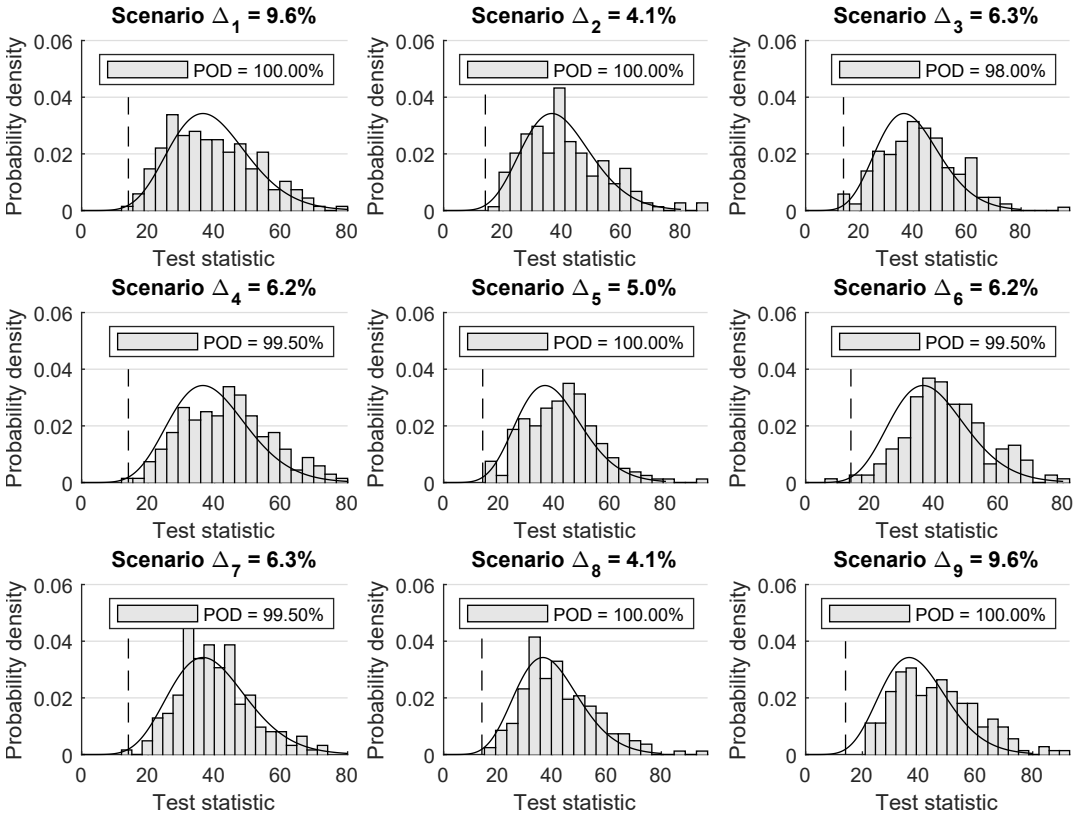

Figure 5.9: Validation state for the structural parametrization

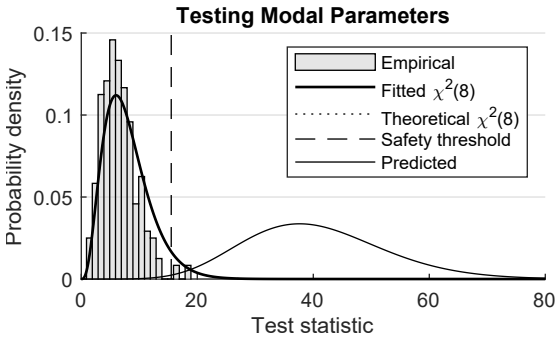

Figure 5.10: Training state

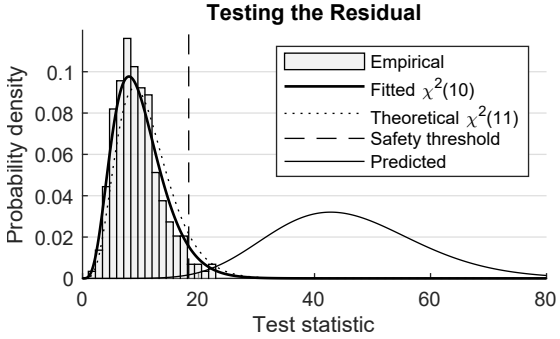

Figure 5.11: Training state

results from the Monte Carlo simulation are shown in Fig. 5.10. The empirical distribution (grey histogram) fills the area under the theoretical distribution (solid line), so the theoretical value for the number of degrees of freedom $\nu = 2mr = 8$ is verified. Since the number of degrees of freedom increases in comparison to the model-based test (where $\nu = 5$), the minimum non-centrality increases to $\lambda_{min} = 32.6$, and the resulting minimum detectable damages increase, see Table 5.4. For validation, nine different damage scenarios are simulated where the applied damaged is set to the minimum detectable damage, see Fig. 5.12. The probability of detection ranges between 99.0% and 100% for all nine cases, so the prediction of the minimum detectable damage is correct also when modal parameters are tested.

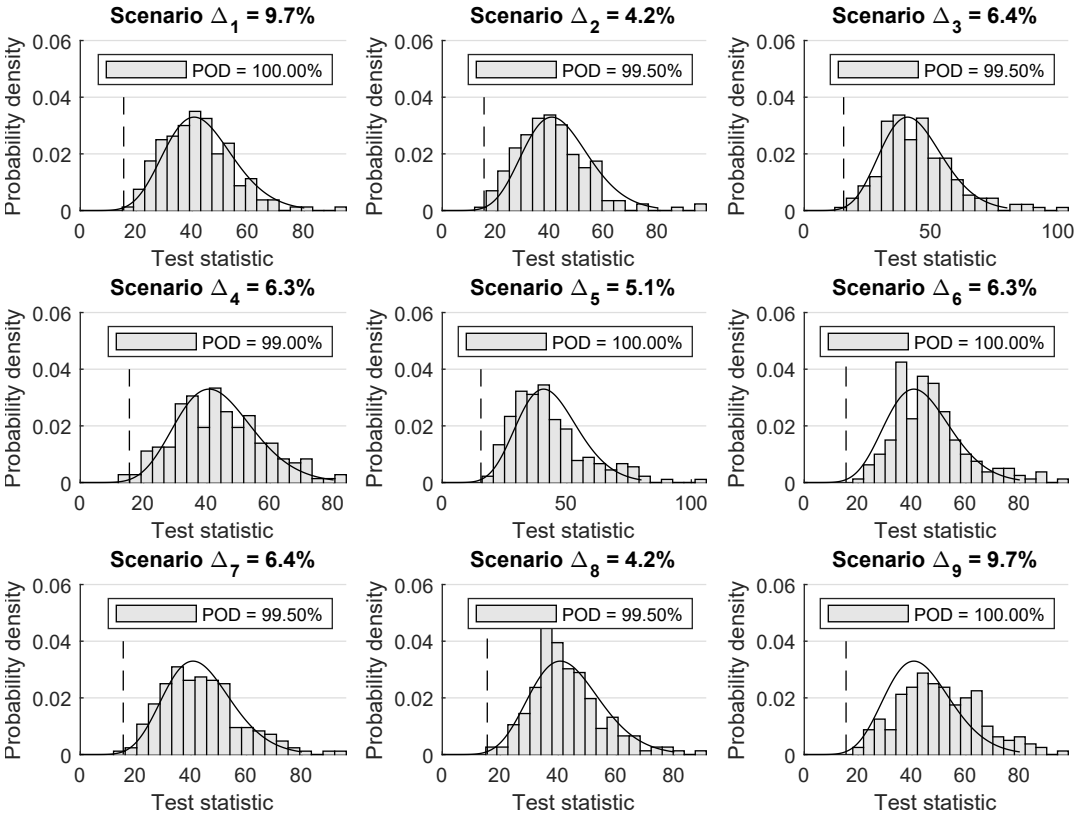

Figure 5.12: Validation state for the modal parametrization

Study 2: Testing for Changes in the Residual

In the non-parametric test, the Gaussian residual is directly tested for damage without linking it to other parameters through a Jacobian matrix. The reference state is, again, identical to the model-based test. Technically, only the covariance matrix is required for monitoring, but the prediction of the minimum detectable damage requires the model-based Fisher information. Figure 5.11 shows the training state for the non-parametric test. The empirical test distribution with a number of degrees of freedom of $\nu = 10$ is close to the theoretical one with $\nu = 11$. The corresponding minimum non-centrality is $\lambda_{min} = 34.7$, with the minimum detectable damages tabulated in Table 5.4. Ultimately, nine Monte Carlo simulations are performed, where the damage is set to the minimum detectable damage, see Fig. 5.13. The empirical POD ranges between 99.5% and 100% for all cases, so the prediction of the minimum detectable damage is accurate, even if no Jacobian matrix is used during monitoring.

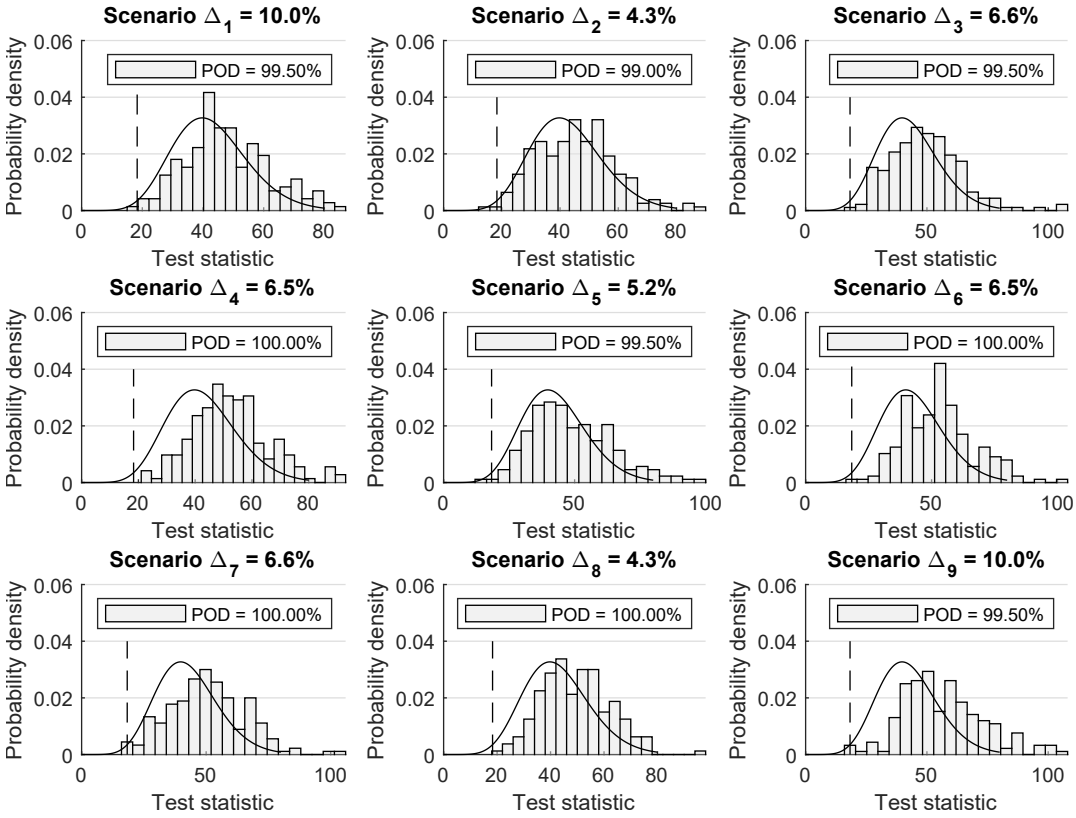

Figure 5.13: Validation state for the non-parametric test

Minimum Detectable Damage [%]									
Monitoring parameter	E_1	E_2	E_3	E_4	E_5	E_6	E_7	E_8	E_9
Model-based test	9.6	4.1	6.3	6.2	5.0	6.2	6.3	4.1	9.6
Data-driven test (parametric)	9.7	4.2	6.4	6.3	5.1	6.3	6.4	4.2	9.7
Data-driven test (non-parametric)	10.0	4.3	6.6	6.5	5.2	6.5	6.6	4.3	10.0

Table 5.4: Minimum detectable change in the modulus of elasticity E for each beam segment

For comparison, the minimum detectable damage for all model-based and data-driven detection tests are juxtaposed in Table 5.4. The results in this table clarify that the minimum detectable damage assumes higher values for data-driven tests, meaning more severe damage is necessary for a reliable detection. For example, for beam segment 5, the minimum detectable damage increases from 5.0% over 5.1% to 5.2%. This finding may be surprising at first glance, as the theoretical investigations showed that the mean test response is equal for all three damage detection tests, see Equation (5.17). However, for each test, a different number of monitoring parameters is tested, so the theoretical number of degrees of freedom of the χ^2-distribution varies, and, consequently, a different reliability index (i.e., minimum the non-centrality λ_{min}) is to be applied. The relation is visualized in Fig. 5.2.

5.5 Summary

This chapter develops a reliability-based approach to predict the minimum detectable damage for vibration monitoring using statistical tests. It demonstrates that the analysis of the minimum detectable damage requires an overarching consideration of the measurement environment, the signal processing parameters, the employed damage-sensitive residual, and the reliability requirements regarding the damage detection results. Maximum detectability is given for a high sensitivity of the damage-sensitive residual, a high signal-to-noise-ratio, a long measurement duration, and lenient requirements toward the test reliability, i.e., a high probability of false alarms (PFA) or a low probability of detection (POD).

All considerations are condensed into one concise formula, see Eq. (5.9), which relates the minimum detectable damage Δ_h to the magnitude of the monitoring parameter θ_h, the sampling frequency f_s, the measurement duration T [s], the main diagonal values of the Fisher information F_{hh}, and a reliability index λ_{min}. A reliable test result is defined by a mean test response that is sufficiently large, so the test distribution for the damaged state is well-separated from the distribution for the training state, see Fig. 5.1. Ultimately, the degree of separation is tied back to intuitive measures such as the PFA or the POD. What is more, the formula can be solved for the minimum measurement duration that is required to detect a specified damage extent.

The prediction of the minimum detectable damage requires a finite element (FE) model as well as a vibration record from the undamaged structure. However, the prediction is also valid for data-driven tests, where the damage-sensitive residual is tested directly or linked to operational modal parameters. This is shown based on theoretical investigations and a numerical case study. In conclusion, the developed formula is a helpful tool to assess the detectability of structural damage before a structural health monitoring (SHM) system is installed.

Chapter 6

Minimum Localizable Damage

This chapter proposes a method to predict the minimum localizable damage based on vibration data from the reference state and a finite element (FE) model. The minimum localizable damage is defined as the minimum change in a structural design parameter that can be detected and distinguished from changes in other parameters under an optimal damage localization resolution. Finding the minimum localizable damage means having to compromise, because with an increasing number of parameter clusters, the damage localization resolution increases, but the detectability in each cluster decreases, and the false alarm susceptibility changes. The theory is a continuation of Chapter 5, so it can be applied to any damage-sensitive residual $\hat{\boldsymbol{\varepsilon}}$ that satisfies the central limit theorem (CLT) (Benveniste et al., 1987)

$$\boldsymbol{\zeta} = \sqrt{N}(\hat{\boldsymbol{\varepsilon}} - \mathrm{E}[\hat{\boldsymbol{\varepsilon}}]) \longrightarrow \begin{cases} \mathcal{N}(\mathbf{0}, \boldsymbol{\Sigma}) & \text{(reference)} \\ \mathcal{N}(\boldsymbol{\mathcal{J}}\boldsymbol{\delta}, \boldsymbol{\Sigma}) & \text{(damaged),} \end{cases} \tag{6.1}$$

where $\boldsymbol{\Sigma}$ is the sample covariance, $\boldsymbol{\mathcal{J}}$ is the first-order sensitivity matrix that links the damage-sensitive residual $\hat{\boldsymbol{\varepsilon}}$ to structural parameters in $\boldsymbol{\theta}$, and $\boldsymbol{\delta}$ is the asymptotic change vector

$$\boldsymbol{\delta} = (\boldsymbol{\theta} - \boldsymbol{\theta}^0)\sqrt{N} \tag{6.2}$$

which is unknown, but fixed. More background information on the asymptotic change vector can be found in Chapter 4. A major difference to the studies on the minimum detectable damage from Chapter 5 is that damage localization can only be performed using model-based tests.

The chapter is organized as follows: in Section 6.1, the method to predict the minimum detectable damage is expanded to the direct localization test. In Section 6.2, the minimum localizable damage for the minmax localization test is analyzed. Both sections contain details on how to predict the test response of unchanged parameters, i.e., false localization alarms. In Section 6.3, an automated approach is developed to substructure FE parameters for optimal damage localization results, and Section 6.4 presents a numerical proof of concept study.

6.1 Direct Localization Test

The direct localization test is a straightforward expansion of the parametrized damage detection test, with the only difference being that the parameters are individually tested for damage. From a statistical standpoint, the direct localization test evaluates the likelihood ratio of the tested par-

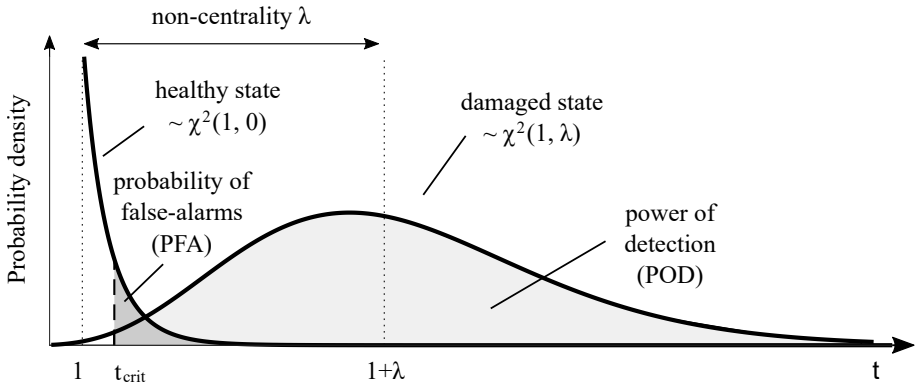

Figure 6.1: Statistical distribution of the test statistic for $\nu = 1$

titions being damaged over the likelihood of them being undamaged, while neglecting all untested parameters. In other words, the alternate hypothesis H_1 is tested against the null hypothesis H_0 for each parameter θ_h, refer to Eq. (4.27). Therefore, the prediction of the minimum localizable damage is similar to the prediction of the minimum detectable damage, at least for the parameter that has changed due to damage. A problem that remained untreated thus far is how the test responds if an unchanged parameter is tested, while one of the untested parameters has changed due to damage. This is were the off-diagonal values of the Fisher information come into play, as they characterize how changes in one parameter influence the test response of others. The influence can be considerable if changes in multiple parameters have a similar effect on the damage-sensitive residual, which is the case for large mechanical structures.

6.1.1 Damage Identifiability

Assuming that damage is restricted to one parameter, and neglecting the off diagonal values of the Fisher information, the generalized likelihood ratio (GLR) from Eq. (4.52) is rewritten in the following format

$$t_h = \zeta_h^T F_h^{-1} \zeta_h \longrightarrow \begin{cases} \chi^2(\nu, 0) & \text{(reference)} \\ \chi^2(\nu, \lambda) & \text{(damaged)} \end{cases}, \tag{6.3}$$

where $\zeta_h = \boldsymbol{\mathcal{J}}_h^T \boldsymbol{\Sigma}^{-1} \boldsymbol{\zeta}$ is the Gaussian residual projected onto the tested and damaged partition and F_h is the corresponding Fisher information

$$F_h = \boldsymbol{\mathcal{J}}_h^T \boldsymbol{\Sigma}^{-1} \boldsymbol{\mathcal{J}}_h. \tag{6.4}$$

This is the same Fisher information that is used to predict the minimum detectable damage, see Chapter 5. A major difference to damage detection is that parameters are individually tested for damage using only one sensitivity vector $\boldsymbol{\mathcal{J}}_h$ at a time, so the number of parameters of the χ^2-distribution is one, due to Eq. (5.4). The corresponding distribution is visualized in Fig. 6.1

and the predictive formula for the mean test response is

$$\lambda_h = T f_s \cdot (\theta_h - \theta_h^0)^2 \cdot F_h \tag{6.5}$$

where T and f_s are the measurement duration and sampling frequency, and $\theta_h - \theta_h^0$ is the parameter change, cf. Eq. (5.7). Based on reliability considerations, the mean test response λ_h can be fixed to a minimum value allowing for the formula to be solved for the minimum localizable damage

$$\Delta_h = \frac{1}{\theta_h^0} \sqrt{\frac{\lambda_{\min}}{T f_s \cdot F_h}} [\%]. \tag{6.6}$$

Consequently, the minimum measurement duration yields

$$T_h = \frac{1}{(\Delta\theta_h)^2} \frac{\lambda_{\min}}{f_s F_h}. \tag{6.7}$$

In preparation for the subsequent sections, the following lines elaborate on the statistical properties of the partitioned residual. As stated above, a basic assumption is that the deviation in the mean vector of the Gaussian residual is caused by a single parameter change

$$\boldsymbol{\zeta} \longrightarrow \mathcal{N}(\boldsymbol{\mathcal{J}}_h \delta_h, \boldsymbol{\Sigma}). \tag{6.8}$$

Pre-multiplying the term $\boldsymbol{\mathcal{J}}_h^T \boldsymbol{\Sigma}^{-1}$ leads to a Gaussian distribution with the following properties

$$\boldsymbol{\mathcal{J}}_h^T \boldsymbol{\Sigma}^{-1} \boldsymbol{\zeta} \longrightarrow \mathcal{N}(\boldsymbol{\mathcal{J}}_h^T \boldsymbol{\Sigma}^{-1} \boldsymbol{\mathcal{J}}_h \delta_h, \boldsymbol{\mathcal{J}}_h^T \boldsymbol{\Sigma}^{-1} \boldsymbol{\mathcal{J}}_h). \tag{6.9}$$

The operation projects the Gaussian residual onto the parameter θ_h and transforms the distribution so it exhibits a mean vector of $F_h \delta_h$ and a covariance of F_h.

$$\zeta_h \longrightarrow \mathcal{N}(F_h \delta_h, F_h) \tag{6.10}$$

Projecting the residual onto individual parameters can also be used to analyze the test response in parameters that have not changed due to damage, but more on this follows in the next section.

6.1.2 False Localization Alarms

A false localization alarm is a significant test response of a parameter due to damage-related changes in another parameter. False localization alarms are inherent to the direct localization test, because the off-diagonal terms of the Fisher information matrix are ignored. Having said that, this section illustrates that the magnitude of these false alarms can also be predicted for the direct localization test, using vibration data from the reference state.

The starting point is the Gaussian residual vector from Eq. (6.1), so $\boldsymbol{\zeta} \longrightarrow \mathcal{N}(\boldsymbol{\mathcal{J}}\boldsymbol{\delta}, \boldsymbol{\Sigma})$. In the following, the parameter that has changed due to damage is denoted as θ_h, where the unchanged

parameters are $\theta_{\bar{h}}$. Its mean value is a superposition of the response of the unchanged parameter and false alarms $\boldsymbol{\mathcal{J}}\boldsymbol{\delta} = \boldsymbol{\mathcal{J}}_h\delta_h + \boldsymbol{\mathcal{J}}_{\bar{h}}\boldsymbol{\delta}_{\bar{h}}$. Pre-multiplying $\boldsymbol{\mathcal{J}}_h^T\boldsymbol{\Sigma}^{-1}\boldsymbol{\zeta}$ and $(\boldsymbol{\mathcal{J}}_h^T\boldsymbol{\Sigma}^{-1}\boldsymbol{\mathcal{J}}_h)^{-1/2}$ to the residual yields a new vector $\mathbf{z}$ with unit variance

$$\begin{aligned} \boldsymbol{\zeta} &\longrightarrow \mathcal{N}(\boldsymbol{\mathcal{J}}_h\delta_h + \boldsymbol{\mathcal{J}}_{\bar{h}}\boldsymbol{\delta}_{\bar{h}}, \boldsymbol{\Sigma}) \\ \boldsymbol{\mathcal{J}}_h^T\boldsymbol{\Sigma}^{-1}\boldsymbol{\zeta} &\longrightarrow \mathcal{N}(F_{hh}\delta_h + \mathbf{F}_{h\bar{h}}\boldsymbol{\delta}_{\bar{h}}, F_{hh}) \\ \mathbf{z} = (\boldsymbol{\mathcal{J}}_h^T\boldsymbol{\Sigma}^{-1}\boldsymbol{\mathcal{J}}_h)^{-1/2}\boldsymbol{\mathcal{J}}_h^T\boldsymbol{\Sigma}^{-1}\boldsymbol{\zeta} &\longrightarrow \mathcal{N}(F_{hh}^{1/2}\delta_h + F_{hh}^{-1/2}\mathbf{F}_{h\bar{h}}\boldsymbol{\delta}_{\bar{h}}, \mathbf{I}). \end{aligned} \tag{6.11}$$

Squaring this vector yields the test statistic from Eq. (6.3) with $t_h = \mathbf{z}^T\mathbf{z}$, so the non-centrality decomposes into (Döhler et al., 2016)

$$\lambda_h = E[\boldsymbol{\zeta}]^T \cdot E[\boldsymbol{\zeta}] = \boldsymbol{\delta}_h^T F_{hh}\boldsymbol{\delta}_h + 2\boldsymbol{\delta}_h^T\mathbf{F}_{h\bar{h}}\boldsymbol{\delta}_{\bar{h}} + \boldsymbol{\delta}_{\bar{h}}^T(\mathbf{F}_{\bar{h}h}F_{hh}^{-1}\mathbf{F}_{h\bar{h}})\boldsymbol{\delta}_{\bar{h}}. \tag{6.12}$$

If an unaltered parameter θ_h is tested for changes but another, untested parameter $\theta_{h'}$ has actually changed due to damage, the mean test response is equal to the last term, so

$$\lambda_{h,h'} = \boldsymbol{\delta}_{\bar{h}}^T(\mathbf{F}_{\bar{h}h}F_{hh}^{-1}\mathbf{F}_{h\bar{h}})\boldsymbol{\delta}_{\bar{h}}. \tag{6.13}$$

Assuming that damage is limited to a single untested parameter $\theta_{h'}$, while all other parameters are undamaged (including the tested one), and taking advantage of the symmetry of the Fisher information with $F_{h'h} = F_{hh'}$, the non-centrality for the tested parameter simplifies to

$$\lambda_{h,h'} = \delta_{h'}^2(F_{hh}^{-1}F_{h'h}^2). \tag{6.14}$$

The bracket term is interpreted as the Fisher information for the test response of a tested but unaltered parameter

$$F_{h,h'} = F_{hh}^{-1}F_{h'h}^2, \tag{6.15}$$

i.e., false localization alarms. That means that the mean test response of parameters that have not changed due to damage $\theta_{\bar{h}}$ can be predicted through the formula from Eq. (6.5) - (6.7) after substituting $F_h = F_{h,h'}$.

6.1.3 Reliability Despite False Localization Alarms

The minimum non-centrality λ_{min} is a reliability index that can be determined based on acceptable probability of false alarms (PFA) and probability of detection (POD), see Section 5.1.3. In contrast to damage detection, the number of degrees of freedom ν of the χ^2-distribution is lower for damage localization ($\nu = 1$), and a lower ν generally leads to a higher damage detectability, see Fig. 5.2. However, the PFA is also higher because false alarms can occur in any monitoring parameter θ_h with $h = 1, 2, \ldots, H$. The global PFA is equivalent to the probability that at least one false test occurs, with

$$\mathrm{PFA} = 1 - (1 - \mathrm{PFA}_h)^H. \tag{6.16}$$

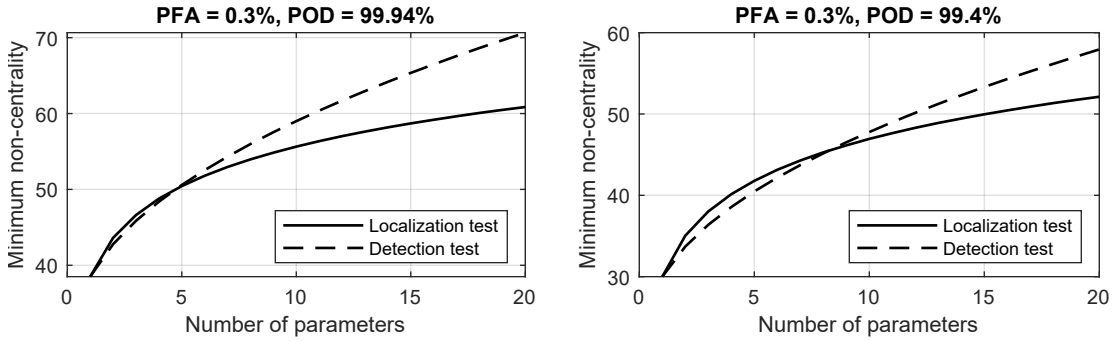

Figure 6.2: Comparing the minimum non-centrality for damage detection and localization

Equivalently, the probability of false negative results increases, so the minimum POD has to be decreased to

$$\mathrm{POD} = (\mathrm{POD}_h)^H. \tag{6.17}$$

Considering the updated PFA and the updated POD from Eq. (6.16) and (6.17), a fair comparison between the damage detection and localization tests can be made. Figure 6.2 plots the minimum non-centrality for damage detection tests for a PFA of 0.3% and a POD of 99.94% and 99.4%, with respect to the Canadian and U.S. American reliability requirements. For the two cases, the damage detection test is more sensitive than the damage localization test if the number of monitoring parameters exceeds $H = 5$ (Canada) and $H = 8$ (U.S.).

6.2 Minmax Localization Test

The minmax localization tests parameters individually for damages but it additionally considers the possibility that damage might also have occurred in untested parameters. Mathematically, it tests the alternate hypothesis H_1 for the tested partition against the least favourable H_1 in untested partitions, see Eq. (4.27). To implement this, a mathematical operation is employed that could be interpreted geometrically as an orthogonal projection. The projection considers the off-diagonal terms of the Fisher information and reduces false localization alarms; however, it introduces bias if the problem is over-parametrized, i.e., if changes in multiple structural parameters have a similar effect on the damage-sensitive feature or vice versa. To remedy this, a hierarchical clustering approach is applied that combines redundant sensitivity vectors. Clustering monitoring parameters is equivalent to substructuring the FE model into units in which damage can be isolated. Regardless of the clustering, the parameters can still individually be tested for damage. This leads to a higher damage localization resolution but may also cause false localization alarms if the cluster centres are not representative of the included parameters, see Section 4.4.4.

6.2.1 Damage Identifiability

This section explains how to derive the modified Fisher information F_h to predict the mean test response of the minmax localization test. Testing the likelihood of parameters θ_h being damaged against the likelihood of cluster centres $\mathbf{c}_k$ being damaged leads to a notational challenge, in particular, because the cluster centres $\mathbf{c}_k$ are already normalized and the parameters are not, see Eq. (4.60). The tested partition is indicated through the subscript h and the corresponding sensitivity vector is $\boldsymbol{\mathcal{J}}_h$. The untested partition is indicated through the subscript $\bar{h}$, it includes the sensitivity vectors of all cluster centres $k = 1, 2, \ldots, K$ except the one that contains the tested parameter, denoted as $k(h)$. The corresponding sensitivity vectors are

$$\tilde{\boldsymbol{\mathcal{J}}}^c_{\bar{h}} = \begin{bmatrix} \mathbf{c}_1 & \ldots & \mathbf{c}_{k(h)-1} & \mathbf{c}_{k(h)+1} & \ldots & \mathbf{c}_K \end{bmatrix}, \tag{6.18}$$

where the cluster centres are averaged sensitivity vectors $\mathbf{c}_k = 1/m_k \sum_{i \in C_k} \tilde{\boldsymbol{\mathcal{J}}}_i$. Since the clustered sensitivity vectors are normalized $\tilde{\boldsymbol{\mathcal{J}}} = \boldsymbol{\Sigma}^{-1/2}\boldsymbol{\mathcal{J}}$, the Fisher information is now

$$\mathbf{F} = \begin{bmatrix} F_h & \mathbf{F}^c_{h\bar{h}} \\ \mathbf{F}^c_{\bar{h}h} & \mathbf{F}^c_{\bar{h}\bar{h}} \end{bmatrix} = \begin{bmatrix} \boldsymbol{\mathcal{J}}_h^T \boldsymbol{\Sigma}^{-1} \boldsymbol{\mathcal{J}}_h & \boldsymbol{\mathcal{J}}_h^T \boldsymbol{\Sigma}^{-1/2} \tilde{\boldsymbol{\mathcal{J}}}^c_{\bar{h}} \\ \tilde{\boldsymbol{\mathcal{J}}}^{cT}_{\bar{h}} \boldsymbol{\Sigma}^{-1/2} \boldsymbol{\mathcal{J}}_h & \tilde{\boldsymbol{\mathcal{J}}}^{cT}_{\bar{h}} \tilde{\boldsymbol{\mathcal{J}}}^c_{\bar{h}} \end{bmatrix}. \tag{6.19}$$

Assuming that damage is restricted to one parameter, the Gaussian residual is projected onto the tested parameter by pre-multiplying it by $\boldsymbol{\mathcal{J}}_h^T \boldsymbol{\Sigma}^{-1}$. The distribution of the tested residual is characterized as follows:

$$\begin{aligned} \boldsymbol{\zeta} &\longrightarrow \mathcal{N}(\boldsymbol{\mathcal{J}}_h \delta_h, \boldsymbol{\Sigma}) \\ \boldsymbol{\mathcal{J}}_h^T \boldsymbol{\Sigma}^{-1} \boldsymbol{\zeta} &\longrightarrow \mathcal{N}(\boldsymbol{\mathcal{J}}_h^T \boldsymbol{\Sigma}^{-1} \boldsymbol{\mathcal{J}}_h \delta_h, \boldsymbol{\mathcal{J}}_h^T \boldsymbol{\Sigma}^{-1} \boldsymbol{\mathcal{J}}_h) \\ \zeta_h &\longrightarrow \mathcal{N}(F_h \delta_h, F_h). \end{aligned} \tag{6.20}$$

Secondly, the Gaussian residual is projected onto the untested partition. The distribution of the rejected partition exhibits the following properties:

$$\begin{aligned} \boldsymbol{\zeta} &\longrightarrow \mathcal{N}(\boldsymbol{\mathcal{J}}_h \delta_h, \boldsymbol{\Sigma}) \\ \tilde{\boldsymbol{\mathcal{J}}}^{cT}_{\bar{h}} \boldsymbol{\Sigma}^{-1/2} \boldsymbol{\zeta} &\longrightarrow \mathcal{N}(\tilde{\boldsymbol{\mathcal{J}}}^{cT}_{\bar{h}} \boldsymbol{\Sigma}^{-1/2} \boldsymbol{\mathcal{J}}_h \delta_h, \tilde{\boldsymbol{\mathcal{J}}}^{cT}_{\bar{h}} \tilde{\boldsymbol{\mathcal{J}}}^c_{\bar{h}}) \\ \boldsymbol{\zeta}^c_{\bar{h}} &\longrightarrow \mathcal{N}(\mathbf{F}^c_{\bar{h}h} \delta_h, \mathbf{F}^c_{\bar{h}\bar{h}}). \end{aligned} \tag{6.21}$$

Next the Gaussian residual is reduced to the information content of the tested partition. The following operation

$$\zeta^*_h = \zeta_h - \mathbf{F}^c_{h\bar{h}} \mathbf{F}^{c-1}_{\bar{h}\bar{h}} \boldsymbol{\zeta}^c_{\bar{h}} \longrightarrow \mathcal{N}(F^{c*}_h \delta_h, \boldsymbol{\Sigma}^*_{h,h}) \tag{6.22}$$

makes the tested residual blind to changes in the untested partition and can be interpreted geometrically as a projection orthogonal to the sensitivity vectors of the cluster centres. The corresponding

robust Fisher information is

$$F_h^{c*} = F_h - \mathbf{F}^c_{h\bar{h}} \mathbf{F}^{c-1}_{\bar{h}\bar{h}} \mathbf{F}^c_{\bar{h}h}. \tag{6.23}$$

Having derived the Fisher information, the mean test response of the minmax test can be predicted by substituting F_h through F_h^{c*} in the formulas from Eq. (6.5) - (6.7). As an alternative, the cluster centres could be defined as the tested partition. This may lead to a more convenient notation, but reduces the quality of the damage localization.

6.2.2 False Localization Alarms

For the minmax test, a false localization alarm is defined as a significant response of the test for a parameter that is not within the same cluster as the parameter that has changed due to damage. Originally, the minmax test was designed so false alarms could be diminished. However, false alarms might be cause if the cluster centres are too similar or if they misrepresent some parameters. As a consequence, the projection does not fully eliminate the effect that changes in the rejected partition have on the tested partition. However, this section explains how to predict the Fisher information related to false alarms.

For consistency, the tested parameter is denoted as θ_h, and the parameter that has changed due to damage as $\theta_{h'}$. First, the Gaussian residual is projected onto θ_h by pre-multiplying $\boldsymbol{\mathcal{J}}_h^T \boldsymbol{\Sigma}^{-1}$:

$$\boldsymbol{\zeta} \longrightarrow \mathcal{N}(\boldsymbol{\mathcal{J}}_{h'} \delta_{h'}, \boldsymbol{\Sigma}) \tag{6.24}$$

$$\boldsymbol{\mathcal{J}}_h^T \boldsymbol{\Sigma}^{-1} \boldsymbol{\zeta} \longrightarrow \mathcal{N}(\boldsymbol{\mathcal{J}}_h^T \boldsymbol{\Sigma}^{-1} \boldsymbol{\mathcal{J}}_{h'} \delta_{h'}, \boldsymbol{\mathcal{J}}_h^T \boldsymbol{\Sigma}^{-1} \boldsymbol{\mathcal{J}}_h) \tag{6.25}$$

$$\boldsymbol{\zeta}_{h,h'} \longrightarrow \mathcal{N}(\mathbf{F}_{hh'} \delta_{h'}, F_h). \tag{6.26}$$

Secondly, the Gaussian residual is projected onto the rejected partition, i.e., the cluster centres $\tilde{\boldsymbol{\mathcal{J}}}^c$ which are already normalized, see Eq. (4.60):

$$\boldsymbol{\zeta} \longrightarrow \mathcal{N}(\boldsymbol{\mathcal{J}}_{h'} \delta_{h'}, \boldsymbol{\Sigma}) \tag{6.27}$$

$$\tilde{\boldsymbol{\mathcal{J}}}^{c\,T}_{\bar{h}} \boldsymbol{\Sigma}^{-1/2} \boldsymbol{\zeta} \longrightarrow \mathcal{N}(\tilde{\boldsymbol{\mathcal{J}}}^{c\,T}_{\bar{h}} \boldsymbol{\Sigma}^{-1/2} \boldsymbol{\mathcal{J}}_{h'} \delta_{h'}, \tilde{\boldsymbol{\mathcal{J}}}^{c\,T}_{\bar{h}} \tilde{\boldsymbol{\mathcal{J}}}^c_{\bar{h}}) \tag{6.28}$$

$$\boldsymbol{\zeta}^c_{\bar{h},h'} \longrightarrow \mathcal{N}(\mathbf{F}^c_{\bar{h}h'} \delta_{h'}, \mathbf{F}^c_{\bar{h}\bar{h}}). \tag{6.29}$$

Thirdly, an orthogonal projection is applied to project the information of the tested partition orthogonally to the rejected cluster centres. The resulting expression is a robust Gaussian residual $\boldsymbol{\zeta}^*_h$ that is sensitive to changes in the tested parameter θ_h and blind to changes in untested clusters $\boldsymbol{\theta}_{\bar{h}}$. The robust residual approximates the following distribution

$$\boldsymbol{\zeta}^*_{h,h'} = \boldsymbol{\zeta}_{h,h'} - \mathbf{F}^c_{h\bar{h}} \mathbf{F}^{c-1}_{\bar{h}\bar{h}} \boldsymbol{\zeta}^c_{\bar{h},h'} \longrightarrow \mathcal{N}(F^{*c}_{h,h'} \delta'_{h'}, \boldsymbol{\Sigma}^*_{h,h'}) \tag{6.30}$$

and the robust Fisher information is

$$F^{*c}_{h,h'} = F_{hh'} - \mathbf{F}^{c}_{h\bar{h}}\mathbf{F}^{c-1}_{\bar{h}\bar{h}}\mathbf{F}^{c}_{\bar{h}h'}. \tag{6.31}$$

By substituting $F_h = F^{*c}_{h,h'}$, the test response of the false localization alarms can be predicted using the same formulas as before, see Eq. (6.5) - (6.7).

6.2.3 Non-centrality Ratio

In this section, a metric is developed to predict false localization alarms for the minmax localization test, i.e., the theoretical non-centrality ratio (NCR). The main idea is to calculate the Fisher information for a tested but unaltered parameter $F^{*c}_{h,h'}$ (Section 6.2.2) and to translate it into a non-centrality (a mean test response) according to Eq. (6.5). Secondly, the Fisher information is calculated for the parameter that has changed due to damage (Section 6.2.1) and translated into a non-centrality. Ultimately, the non-centrality of the unaltered parameter is put into relation to the non-centrality of the altered parameter, which yields the relative mean test response of unaltered parameters (false localization alarms), with

$$\mathrm{NCR} = \frac{\lambda_{h,h'}}{\lambda_{h,h}} = \frac{F^{*c}_{h,h'}}{F^{c*}_{h}}. \tag{6.32}$$

If the parameters are clustered appropriately, meaning if the cluster centres are representative of the included parameters, the NCR is zero as no false alarms occur. For inappropriate clusters, the response is between zero and one, where a value of one means that the false localization alarm is of the same magnitude as the mean test response for the parameter that has actually changed due to damage. If the NCR is close to a value of one or beyond, identifying the parameter that has changed is not possible. Interestingly, the magnitude of the parameter change $\boldsymbol{\theta} - \boldsymbol{\theta}^0$ cancels out, meaning the NCR does not depend on the damage extent, and the false alarm susceptibility can be predicted based on vibration data from the reference state.

The implementation of the non-centrality ratio is straighforward: for each damage scenario i, the Gaussian residual $\boldsymbol{\zeta}(i) \longrightarrow \mathcal{N}(\boldsymbol{\mathcal{J}}\boldsymbol{\delta}, \boldsymbol{\Sigma})$ with $\boldsymbol{\delta} = (\boldsymbol{\theta} - \boldsymbol{\theta}^0)\sqrt{N}$ is replaced by a Dirac delta function with $\delta_i(i) = 1$ and zero otherswise, as the magnitude of the damage is not important. Subsequently, the minmax localization test is evaluated for all parameters and the test response is divided by the test response of parameter i—the one that is actually damaged.

6.3 Optimal Damage Localization

The minmax localization test is a promising method for high-resolution damage localization, with fewer false localization alarms as the direct localization test. A disadvantage is that the clustering approach critically depends on one user input parameter, i.e., the minimum dendrogram distance d from Eq. (4.61) that specifies how many substructures are considered. For visualization, the

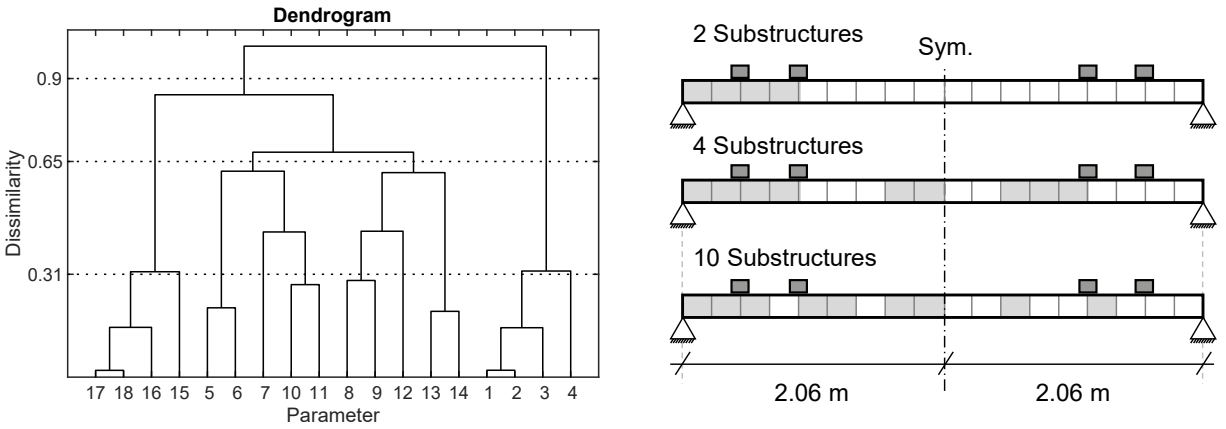

(a) Cluster tree with three cut-off values

(b) Corresponding substructures

Figure 6.3: Visualizing the hierarchical clustering

dendrogram (or cluster tree) for damage localization of a pin supported beam is plotted in Fig. 6.3. Cutting the cluster tree off at $d = 0.9$ (on the left side) leads to two parameter clusters, so damage can be isolated in one of the two substructures (on right side). Choosing a lower cut-off value of 0.65 or 0.31 leads to four or 10 substructures, so the damage localization resolution significantly increases. However, the previous sections demonstrated that a lower cut-off value affects the damage detectability in each parameter cluster and the number and severity of false alarms. Therefore, finding the optimal cluster setting is a multi-objective optimization problem. This section explains how to weigh the three criteria by defining lower and upper bounds, and how to find the optimal solution based on Pareto optimization.

6.3.1 Localization Resolution

The first optimization criterion is the damage localization resolution. It can be defined as the number of substructures, as each substructure is individually tested for damage. The higher the number of substructures, the higher the damage localization resolution. When formulated as a minimization problem, the first objective functions reads

$$f_1(K) = \frac{K - K_b}{K_g - K_b}, \tag{6.33}$$

where K is the number of substructures and K_b and K_g is the lower and upper bound. The subscripts b and g indicate a bad and a good number of substructures, respectively. Since damage localization with a single substructure is meaningless, the lower bound for the number of substructures should be set to $K_b \geq 2$. The upper limit could be set to the maximum number of distinguishable substructures, defined through the matrix rank $K_g = \text{rank}(\boldsymbol{\mathcal{J}}^T \boldsymbol{\Sigma}^{-1} \boldsymbol{\mathcal{J}})$. An alternate way to define the damage resolution is to count the maximum number of parameters within one substructure. This would avoid the formation of large substructures that include a majority of monitoring parameters, and promote an equal damage localization resolution across the entire

structure.

6.3.2 Damage Identifiability

The second optimization criterion is the minimum detectable damage, which is calculated based on Eq. (6.6). The normalization by the magnitude of the reference parameter θ_h^0 leads to minimum detectable damage in percent, and allows one to define a hard upper bound of $K_b = 100\%$, where the lower bound could be set to $K_g = 0\%$. Hence, the weighed objective function is given as

$$f_2(K) = \frac{\Delta_{\max}(K) - \Delta_g}{\Delta_b - \Delta_g}, \tag{6.34}$$

where $\Delta_{\max}(K) = \max\{\Delta_1(K), ..., \Delta_H(K)\}$ is the largest value for the minimum detectable damage over all monitoring parameters. If the proposed lower and upper bounds are used, the objective function reduces to $f_{2,a}(K) = \Delta_{\max}(K)$. Alternatively, the damage localizability could be defined based on the minimum measurement duration. This would require the measurement duration to be updated after the substructuring. More information on how to use the measurement duration as a measure for the damage detectability is given in Chapter 8.

6.3.3 False-Alarms Susceptibility

The third optimization criterion is the false alarm susceptibility. It is quantified based on the non-centrality ratio of the parameters that have not changed. There are numerous ways to define an objective function based on the NCR. The proposed one is to count the number of scenarios N_{sc} in which the maximum NCR exceeds a threshold value of, for example, $\text{NCR}_{crit} = 0.5$, for parameters that have not changed due to damage. This means that false localization alarms with a magnitude lower than 50% are tolerable. The weighed objective function can be expressed as

$$f_3(K) = \frac{N_{sc}(K) - N_g}{N_b - N_g}, \tag{6.35}$$

where N_b and N_g are user-defined parameters to define the worst and best cases. The total number of damage scenarios equals the number of monitoring parameters, so the upper bound could be set to $N_b = H$, and the lower bound to $N_g = 0$. Having said that, it might be desirable to further diminish false alarms by setting stricter upper bounds. An alternate way to formulate the objective function is based on so called *blind spots*. A blind spot is defined as a parameter with a false alarm response that exceeds the response of the parameter that has actually changed due to damage, so the damage location cannot be found. Even if blind spots are not used as optimization criterion, they could still be employed as a knock-out criterion, meaning cluster configurations with blinds spots are discarded.

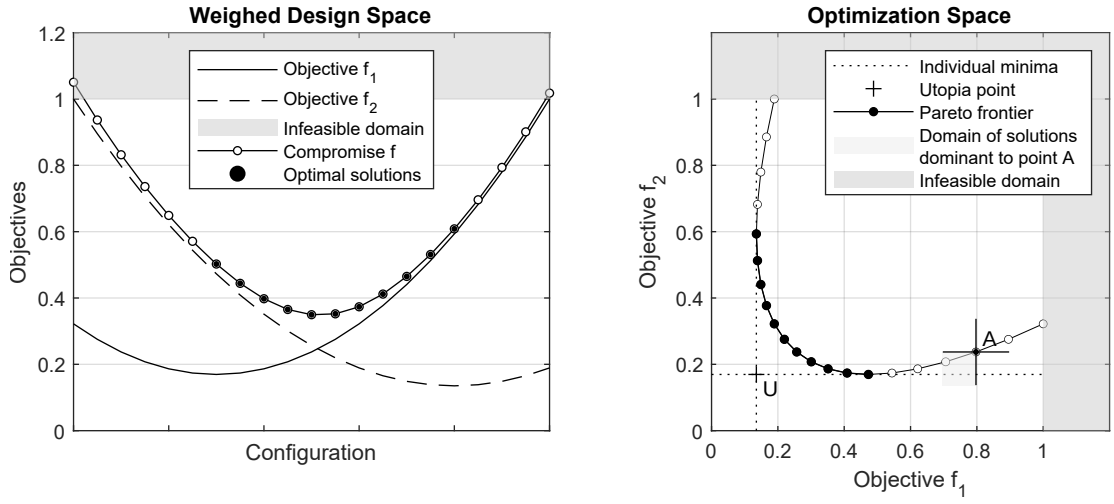

Figure 6.4: Multi-objective optimization with two objective functions

6.3.4 Optimal Compromise

After scaling the three performance criteria through lower and upper bounds, they are considered equal, as damage detectability is equally as important as localization resolution, and the resolution becomes meaningless if the false alarms exceed the actual test response. They all depend on the dendrogram distance d and the associated number of clusters K in the clustering approach. The lower the cut-off value d_{trim} is chosen, the higher the damage localization resolution K, and the smaller the detectability in each substructure. The localization resolution and the minimum detectable damage are conflicting, as with an increasing number of substructures, the detectability Δ decreases inevitably. This is because the orthogonal projection from Eq. (6.23) is to be performed with respect to more cluster centres, which reduces the information content on tested parameters. Where neither the detectability nor the localizability can be improved without degrading the other objective function, it is possible to simultaneously reduce the number of false alarms and one other objective. However, the false alarm susceptibility seems to be uncorrelated to the localization resolution and detectability, so it should be considered as a separate objective function.

Dealing with conflicting objective functions of equal importance is known as *Pareto optimization* (Censor, 1977; Deb, 2001) with the basic concepts being visualized in Fig. 6.4. On the left side, two scaled objective functions are plotted in what is called the weighed *design space*. On the right side, the *space of objective functions* is shown where the objective function values are plotted against each other after rejecting infeasible solutions with objective functions greater than one. To assess the quality of a particular solution (Point A), a cross hair is drawn on top of it where all solutions in the lower left quadrant are said to be dominant to A. Non-dominated solutions typically form a front, also known as the *Pareto frontier*, which connects the two optimum points of the individual objective functions. Each point on the Pareto frontier is an optimal solution. To allow for a fair comparison, the utopia point U, i.e., the imaginary projection of the optimal points of all objective functions, should be the origin of the coordinate system. This is achieved

by defining appropriate bounds when weighing the objective functions. The concepts can easily be expanded to optimization with three or more objective functions, but the plots are less intuitive.

In the particular case of finding the optimal parameter clustering, all possible solutions are available and the decision-making can be done a posteriori. Multiple approaches are available to select one solution on the Pareto frontier. The most straightforward one is to select the point with the minimum distance to the origin, as this point optimizes all objective functions simultaneously. Using the Euclidean distance in a three-dimensional design space, the minimization problem is formally defined as

$$\begin{aligned} \min_{K} \quad & f = \sqrt{f_1(K)^2 + f_2(K)^2 + f_3(K)^2} \\ \text{s.t.} \quad & f_1(K) \leq 1, f_2(K) \leq 1, f_3(K) \leq 1. \end{aligned} \tag{6.36}$$

where f is also referred to as the compromise function that is subject to (s.t.) the inequality conditions from Eq. (6.36). Additional information on more advanced multi-objective optimization algorithms is given in the next chapter, see Section 7.3.2.

6.4 Proof of Concept

For proof of concept, the minimum localizable damage is analyzed for the hollow structural steel (HSS) beam. Both the structure and the diagnosis procedure have already been described in detail in Section 5.4. Damage is defined as a change in the modulus of elasticity, and since nine material are assigned to the beam, the parameter vector for monitoring is $\boldsymbol{\theta} = [E_1, \ldots, E_9]$. The main difference to the previous case study is that the number of sensors is increased to four, as shown in Fig. 6.5, and the number of modes of vibration, which are considered in the calculation of the Jacobian matrix, is increased to six to allow for a higher localization resolution, see Fig. 6.6. For conciseness, all input parameters for the damage diagnosis are summarized in Table 6.1. The section is organized in the same fashion as the chapter, elaborating on the direct localization test first, followed by the minmax localization test, and finally, the minmax approach including automated susbtructuring.

6.4.1 Direct Localization Test

In this first study, the test response of the direct localization test is predicted for parameters that have changed and others that have not changed due to damage. The damage diagnosis is divided

Data		**Segmenting**		**Processing**	
Measured quantity	velocity	Training segments	240	No. of sensors	r/r_0=4/4
Sampling frequency	850 Hz	Testing segments	200	Time lags	p/q=4/5
Reference data length	120 min	Samples/segment	12,000	System order	n=14
Training/testing data	100 min	Duration/segment	30 s	No. of blocks	n_b=72,000

Table 6.1: Input parameter sheet

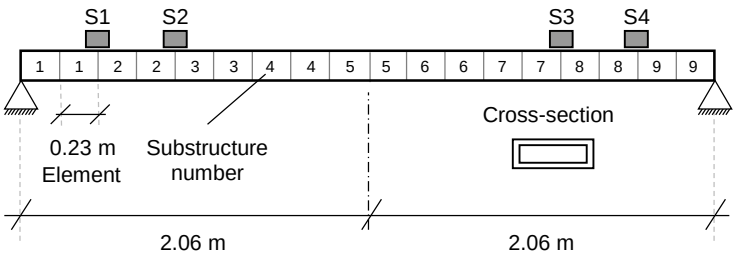

Figure 6.5: Numerical HSS beam with nine materials and four sensors

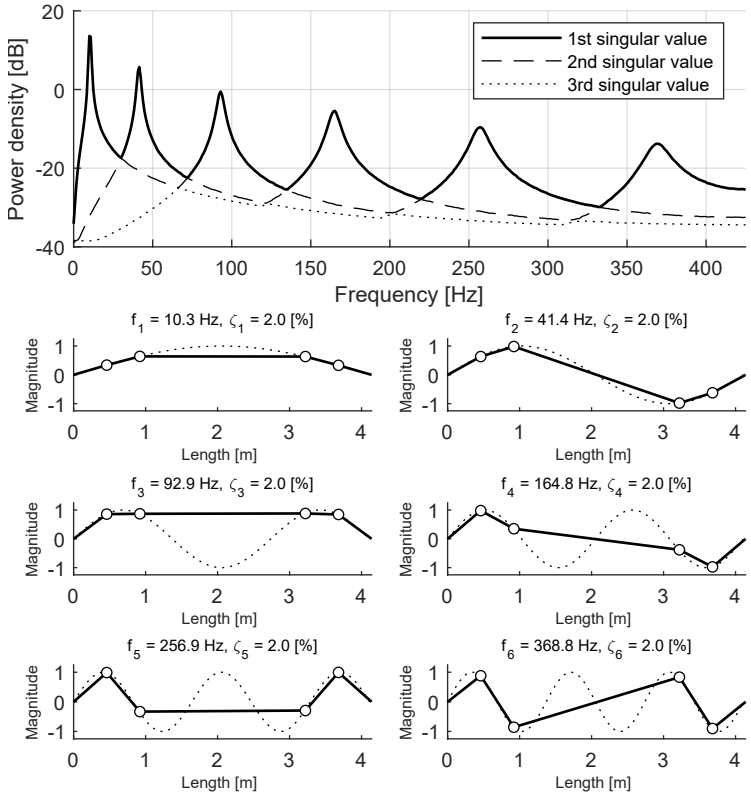

Figure 6.6: Numerical mode shapes and power spectral density of the generated signal

into three states: the reference state, the training state, and the validation state.

Reference State. In the reference state, one long vibration record is generated based on the system matrices from the undamaged structure. Next, the reference matrices are set up, including the null space, the covariance, and the Jacobian matrix. At the end of the reference state, the Fisher information is calculated, with a visualization on the left side of Fig. 6.7.

Training State. For the sake of variety, no Monte Carlo simulation is performed in the training state. Instead, the theoretical value for the number of degrees of freedom of the χ^2-distribution is used, i.e., $\nu = 1$. Based on reliability consideration, including a PFA of 5% and a POD of 99.994%, the safety threshold is set to $t_{crit} = 3.84$ and the minimum non-centrality is fixed to $\lambda_{min} = 20$,

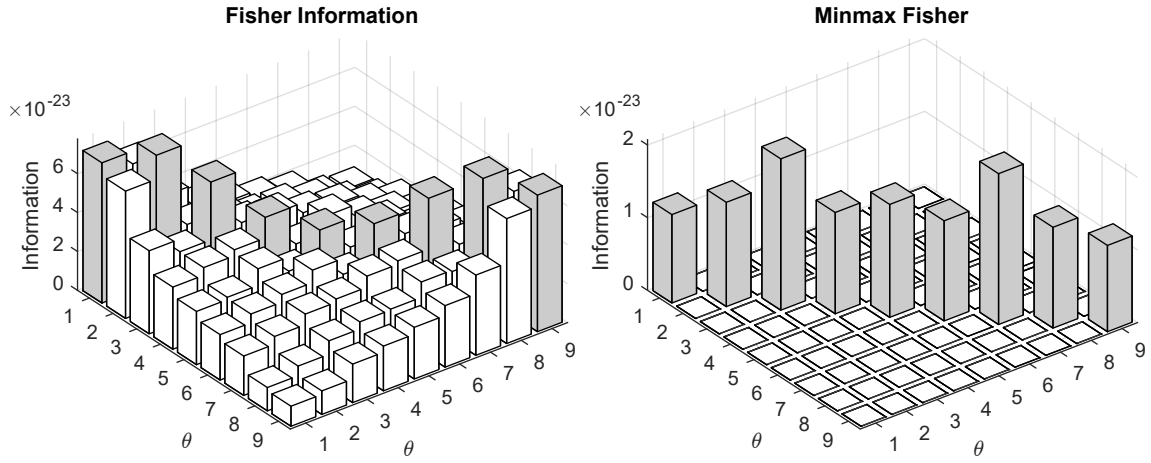

Figure 6.7: Fisher information for the direct test (left) and the minmax test (right)

see Section 5.1.3. At the end of the training phase, the minimum localizable damage is predicted based on Eq. (6.6). Using the Fisher information from Eq. (6.4) and Eq. (6.15), the response is predicted for altered and unaltered parameters.

Validation State. To validate the predictions, an additional vibration record is generated for each monitoring parameter while setting the damage to the minimum localizable damage. For each of the nine damage scenarios, the record is split up into 200 data segments of 30 s length, and the direct localization test from Eq. (6.3) is applied to each data segment. The validation state for a 2.1% damage at the centre beam segment is visualized in Fig. 6.8a. For each data segment, the damage localization test yields nine test statistics, one for each monitoring parameter. The results can be displayed in nine 3-D histograms (left plot), but the most meaningful way to display the histograms is from above in combination with their mean values (right plot). It can be observed that the parameter θ_5 shows the greatest response with a POD of 100%, which is close to the theoretical value of 99.994%, meaning the prediction of the minimum localizable damage for the direct localization test is accurate.

Figure 6.8a also allows for an analysis of false localization alarms. The damage location is clear as the parameter that has changed due to damage exhibits the greatest mean test response, but the mean test responses of all other parameters are also beyond the safety threshold value, which makes the results from the direct localization test less meaningful. The predicted false alarm magnitude is visualized through the black stairstep graph. It is calculated by evaluating the modified Fisher information from Eq. (6.15) for each parameter, plugging it into the predictive formula from Eq. (6.5), and adding the mean value of the training distribution, which is $\nu = 1$. The predicted mean values are close to the empirical mean values, so the prediction of the false alarms is successful. For completeness, the validation of the false alarms and the actual test response is repeated for the remaining eight monitoring parameters, see Fig. 6.9b. The results from this numerical case study demonstrate that the behaviour of the direct localization test is fully

predictable, for both parameters that have changed and parameters that have not changed due to damage.

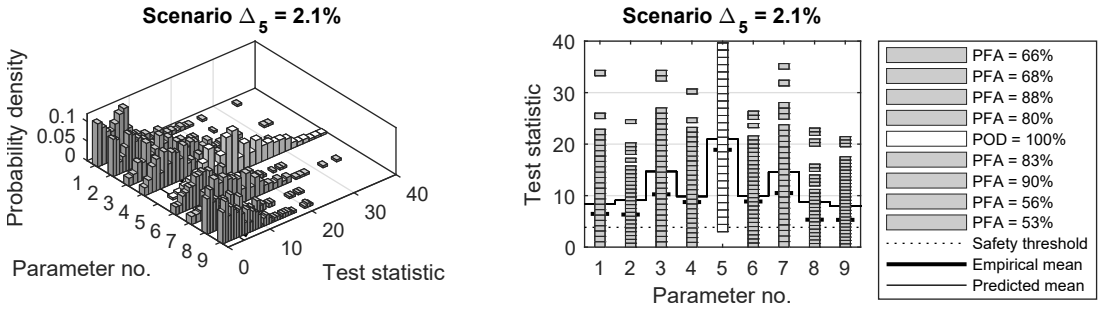

(a) 3-D histograms (left) and top view (right) for damage scenario 5

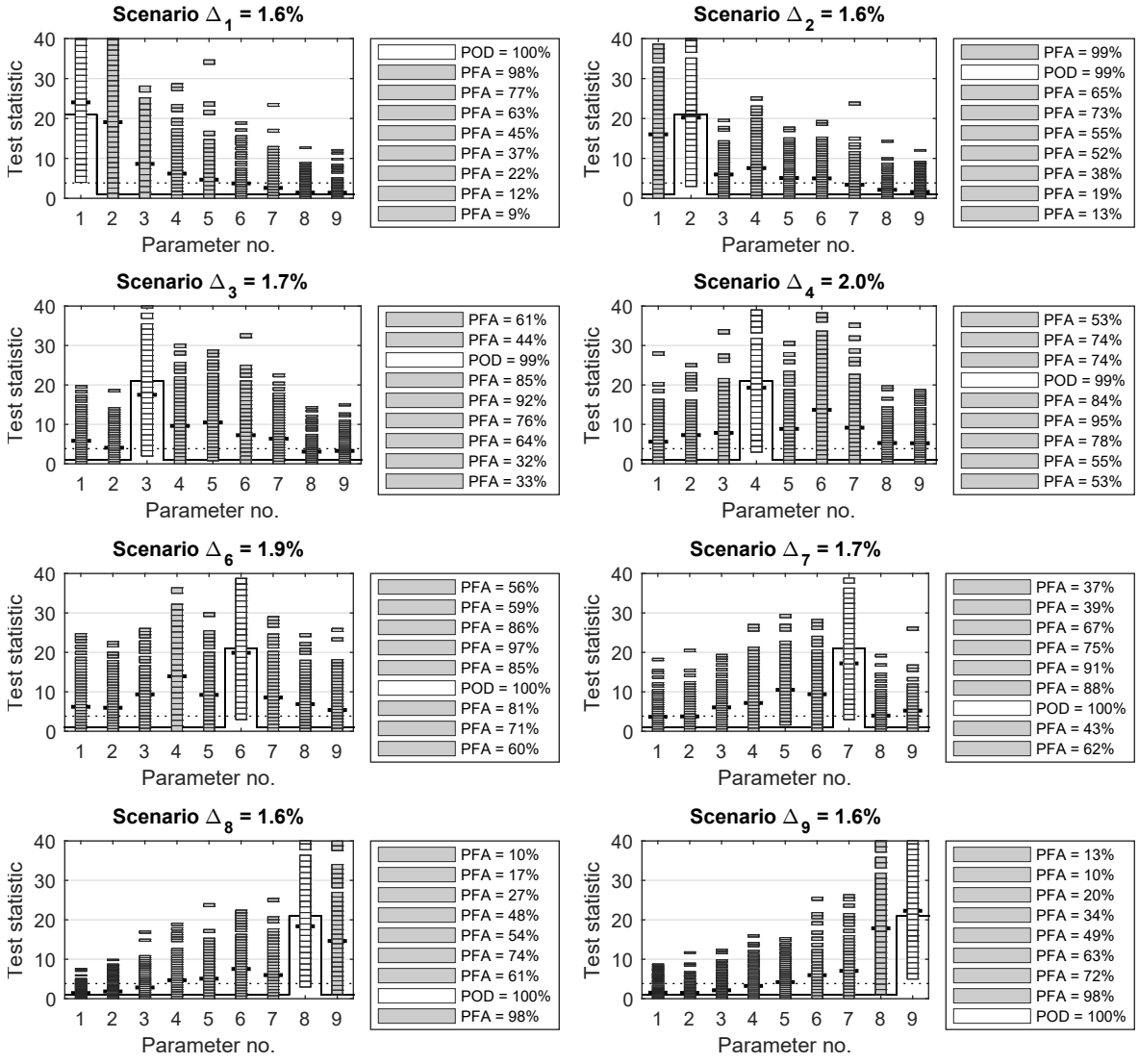

(b) Top view for all other scenarios

Figure 6.8: Validation of the prediction for the direct localization test

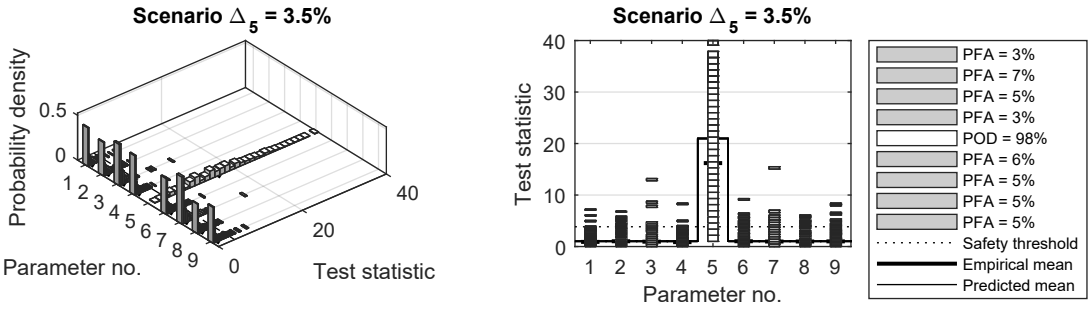

(a) 3-D histograms (left) and top view (right) for damage scenario 5

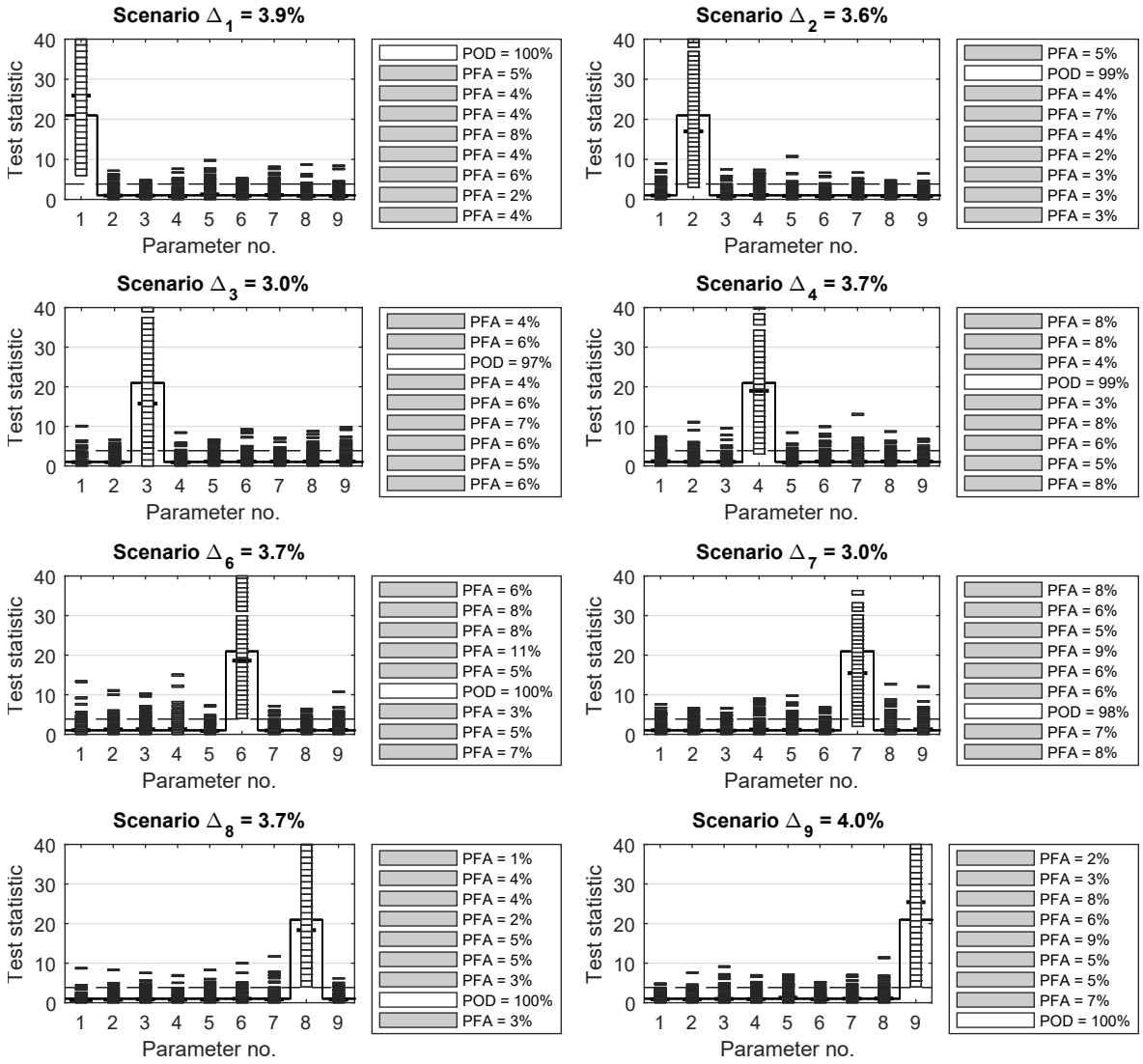

(b) Top view for all other scenarios

Figure 6.9: Validation of the prediction for the minmax localization test

6.4.2 Minmax Localization Test

In this second study, the test response of the minmax localization test is predicted and validated. The analysis is setup in the same way as for the direct localization test, meaning the sensitivity is calculated toward nine structural components with the material constants $\boldsymbol{\theta} = [E_1 \ \dots \ E_9]$. It is important to note that the components are defined manually by assigning two consecutive beam elements to the same material, so no clustering is applied. The Fisher information is calculated based on Eq. (6.23) for every parameter, and by looking at the visualization on the right side of Fig. 6.7, it can be appreciated that the off-diagonal terms are zero, due to the orthogonal projection from Eq. (6.22). The validation procedure of the minimum detectable damages for the minmax test is visualized in Fig. 6.9. The POD ranges between 97% and 100% for all nine components. Moreover, the damage localization results are significantly improved in comparison to the direct localization test (cf. Fig. 6.8) and the false alarms are indeed zero. This encouraging result is the reason why all following considerations regarding the optimal damage localization are based on the minmax localization test.

6.4.3 Optimal Damage Localization

Clustering monitoring parameters and substructuring the FE model is important to obtain an accurate damage localization result. In the previous studies in this chapter, the HSS is substructured manually by assigning the same material properties to two subsequent FE. The obtained damage localization results are encouraging, mainly because the applied damage affected the entire segment as assumed during the computation of the minimum detectable damage; however the substructuring is certainly too coarse to identify small and local damages. The approach in this section is to assign a separate material to each of the 18 FE, as shown in the top plot of Fig. 6.10, and subsequently re-combine materials in an optimal way through hierarchical clustering. The optimal solution is assessed with respect to the three developed optimization criteria, i.e., the damage detectability, the localization resolution, and the false alarms susceptibility. False alarms are introduced because each monitoring parameter (not cluster) is tested for damage.

All three objective functions for an optimal substructuring are summarized in one plot, see Fig. 6.11. The first objective function f_1 (dashed line) is the damage localization resolution, refer to Section 6.3.1. For a single substructure, the localization test transitions into the parametric detection test, and the objective is within the infeasible domain $f_1 > 1$. With an increasing number of substructures, the first objective function linearly decreases until it reaches its optimum at $K = \text{rank}(\boldsymbol{\mathcal{J}}^T \boldsymbol{\Sigma}^{-1} \boldsymbol{\mathcal{J}}) = 13$. The second objective f_2 is the detectability in each parameter (solid black line), where the maximum value among all monitoring parameters is the decisive one, i.e., $\Delta_{max} = \max(\Delta_1, \cdots, \Delta_{18})$. The detectability gradually decreases up to a cluster number of $K = 11$ where the objective function shows a distinct jump. Beyond this point, the minimum detectable damage in some parameters exceeds 100%, and the objective function moves into the infeasible domain with $f_2 > 1$. The third objective function f_3 quantifies the number of false alarm

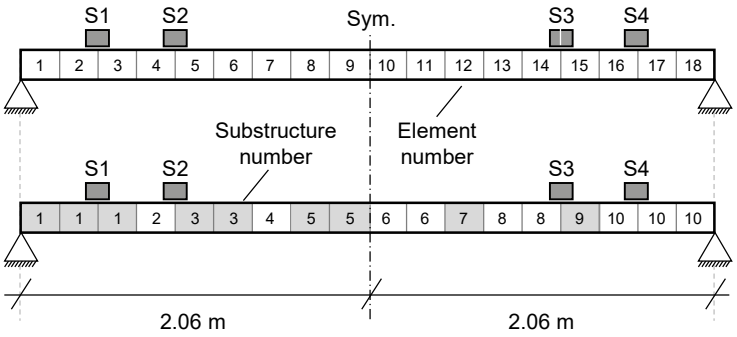

Figure 6.10: Original model (top) and substructured model (bottom)

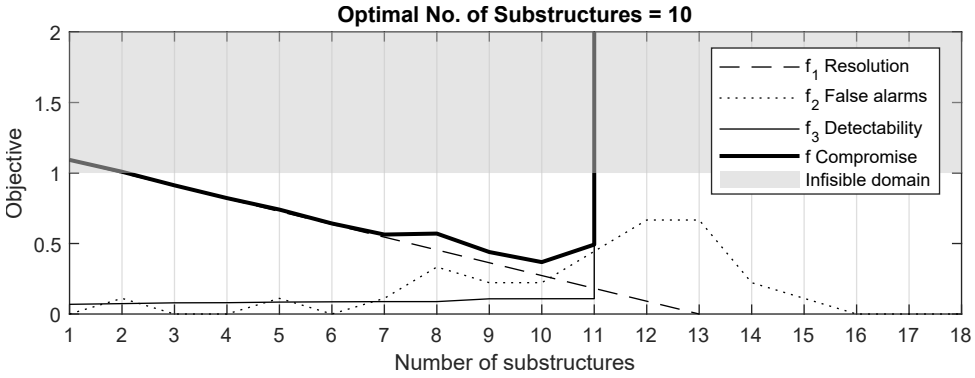

Figure 6.11: Objective functions for automated substructuring

scenarios (dotted line). The function is less intuitive; however, a significant increase is noticed if more than seven clusters are used, and for cluster configurations with 12 and 13 clusters, the false alarms are the most pronounced. The plot also shows the compromise functions (thick solid line), which is the Euclidean distance of all weighed objective functions, compare Eq. (6.36). An optimal compromise between damage resolution, detectability, and false alarms is reached for a configuration with $K = 10$ clusters. The corresponding substructure arrangement is visualized in the bottom plot of Fig. 6.10. The largest clusters are found near the supports and at midspan, possibly because of the low vibration amplitudes of multiple modes of vibration at these points.

For completeness, the prediction of the mininum localizable damage and the false alarm magnitude is repeated for the optimal substructure arrangement, see Fig. 6.12. The validation state includes 18 Monte Carlo simulations, as each of the 18 FE can individually be tested for damage. The POD ranges between 92% and 100%, so the prediction of the minimum localizable damage is correct. Parameters that are within the same cluster typically show a similar response to damage, but the parameter that has actually changed due to damage exhibits the greatest response, as seen in Scenario Δ_3 in Fig. 6.12. False alarms, i.e., a significant response of a parameter outside of the cluster in which damage has occurred, are minimized and can be predicted well. Another observation is that the damage detectability decreases with an increasing number of substructures. The difference between Fig. 6.12 and Fig. 6.9 is that 18 parameters are tested instead of nine, and the minimum localizable damage in the first beam segment decreases from $\Delta_1 = 3.9\%$ to $\Delta_1 = 12\%$

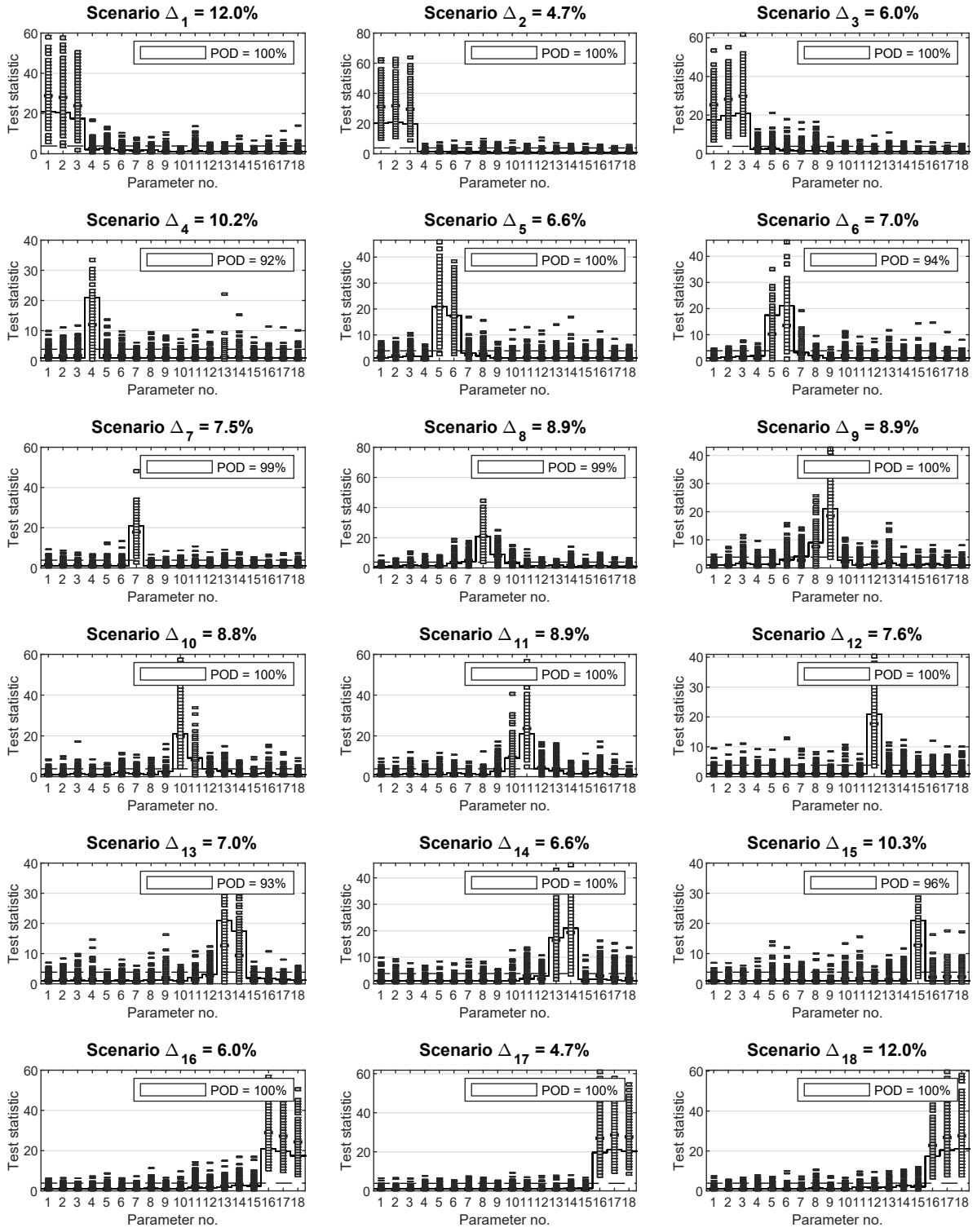

Figure 6.12: Validation of the automated substructuring approach

and $\Delta_2 = 4.7\%$, as the segment is split into two. This validates the automated substructuring approach and concludes the proof of concept study.

6.5 Summary

This chapter expands the theoretical investigations regarding the minimum detectable damage to damage localization. Damage localization is more challenging, as the statistical tests are applied to each individual monitoring parameter in the finite element (FE) model and changes in one parameter due to damage can cause a response in unchanged parameters, so-called false localization alarms. Based on the off-diagonal terms of the Fisher information, a framework is devised that predicts both the test response of altered parameters as well as the magnitude of false localization alarms, using vibration data from the undamaged structure. When combined with reliability considerations, this framework allows one to predict the minimum localizable damage and the minimum measurement duration for the direct localization test.

Subsequently, all considerations are applied to predict the minimum identifiable damage for the minmax localization test. As outlined in previous sections, the minmax localization test significantly reduces false localization alarms, but it critically depends on a user-defined input parameter, which determines the number of substructures in which damage can be isolated. This chapter demonstrates that finding the optimal substructure arrangement is a multi-objective optimization problem: with an increasing number of substructures, the localization resolution increases, but the damage identifiability in each substructure decreases, and the number of false alarms changes. Since the minimum identifiable damage and the false alarm magnitude can be predicted based on vibration data from the undamaged structure, an approach is put forward (based on Pareto optimization) to weigh the optimization criteria (by defining appropriate lower and upper bounds) and to automatically find a suitable substructure arrangement as the optimal compromise between the three objective functions.

Chapter 7

Sensor Placement Optimization

This chapter proposes a criterion for sensor placement optimization and combines it with a state-of-the-art genetic algorithm (GA) to efficiently find a close-to-optimal solution in a large pool of possible sensor combinations. Most of the existing criteria aim to pre-condition the signal and to improve the quality of the modal identification, but a reliable modal identification does not guarantee a reliable damage diagnosis. Another issue is that most sensor placement strategies optimize the sensor layout on a global vibration level, but the structural safety and serviceability typically depend on the integrity of local components, such as joints, and damage tends to accumulate at well-known hotspots, see Fig. 1.4. With this knowledge, a sensor placement strategy is developed that takes as input the requested detectable damage in individual finite element (FE) model components, and yields as output an optimal sensor layout. The primary purpose of the optimization is to maximize the damage detectability and localizability, and to align the objectives of vibration analysis with structural design requirements.

The methodology is developed for damage-sensitive residuals $\hat{\boldsymbol{\varepsilon}}$ that approximate a Gaussian distribution with well-defined uncertainty (covariance $\boldsymbol{\Sigma}$) and a mean vector that can be linked to changes in structural design parameters $\boldsymbol{\theta}$ through a first-order sensitivity matrix (Jacobian $\boldsymbol{\mathcal{J}}$). Such residuals satisfy the central limit theorem (CLT)

$$\boldsymbol{\zeta} = \sqrt{N}(\hat{\boldsymbol{\varepsilon}} - \mathrm{E}[\hat{\boldsymbol{\varepsilon}}]) \longrightarrow \begin{cases} \mathcal{N}(\mathbf{0}, \boldsymbol{\Sigma}) & \text{(reference)} \\ \mathcal{N}(\boldsymbol{\mathcal{J}}\boldsymbol{\delta}, \boldsymbol{\Sigma}) & \text{(damaged),} \end{cases} \tag{7.1}$$

which is based on a statistical framework called the asymptotic local (AL) approach (Benveniste et al., 1987), with the statistical change vector

$$\boldsymbol{\delta} = (\boldsymbol{\theta} - \boldsymbol{\theta}^0)\sqrt{N}. \tag{7.2}$$

The chapter is organized as follows: Section 7.1 proposes the measurement duration as a performance criterion to optimize damage detectability. It outlines how to determine the optimal sensor layout as well as an appropriate number of sensors. Section 7.2 develops a sensor placement strategy for damage localization. In Section 7.3, the performance criteria are combined with a single-objective and multi-objective GA, and the last section presents a proof of concept study on a numerical steel beam as well as on a numerical cable-stayed bridge.

7.1 Optimizing the Detectability

In the framework of the AL approach, a decision on whether the structure is damaged or not is made by applying the generalized likelihood ratio (GLR) to the Gaussian residual $\boldsymbol{\zeta}$ (Basseville et al., 2000)

$$t = \boldsymbol{\zeta}^T \boldsymbol{\Sigma}^{-1} \boldsymbol{\mathcal{J}} \left(\boldsymbol{\mathcal{J}}^T \boldsymbol{\Sigma}^{-1} \boldsymbol{\mathcal{J}} \right)^{-1} \boldsymbol{\mathcal{J}}^T \boldsymbol{\Sigma}^{-1} \boldsymbol{\zeta} \longrightarrow \begin{cases} \chi^2(\nu, 0) & \text{(reference)} \\ \chi^2(\nu, \lambda) & \text{(damaged).} \end{cases} \tag{7.3}$$

This test statistic follows a χ^2-distribution with $\nu = \text{rank}(\boldsymbol{\mathcal{J}}^T \boldsymbol{\Sigma}^{-1} \boldsymbol{\mathcal{J}})$ number of degrees of freedom and a non-centrality, i.e., a mean test response, of $\lambda = \boldsymbol{\delta}^T \mathbf{F} \boldsymbol{\delta}$, where $\mathbf{F}$ is the Fisher information matrix

$$\mathbf{F} = \boldsymbol{\mathcal{J}}^T \boldsymbol{\Sigma}^{-1} \boldsymbol{\mathcal{J}}. \tag{7.4}$$

The Fisher information is a measure for damage detectability, defined as the sensitivity of the damage-sensitive residual toward structural parameters (Jacobian $\boldsymbol{\mathcal{J}}$) scaled by the uncertainties in its estimation (covariance $\boldsymbol{\Sigma}$). The magnitude of the Fisher information depends on the information content of the damage-sensitive residual and the contribution of the monitoring parameter to the structure's integrity, see Section 5.1.4. Moreover, it depends on the sensor layout and the number of sensors, which is addressed in this chapter.

7.1.1 Minimum Measurement Duration

The mean test response to damage can be quantified through $\lambda_h = \delta^2 F_{hh}$ if it is assumed that changes are restricted to one parameter. Considering the definition of the statistical change vector $\delta_h = (\theta_h - \theta_h^0)\sqrt{N}$, the mean test response to damage can be predicted based on vibration data from the reference state through

$$\lambda_h = N \cdot (\theta_h - \theta_h^0)^2 \cdot F_{hh}. \tag{7.5}$$

After replacing the sample size by the product of the measurement duration and the sampling frequency $N = T_h f_s$, Eq. (7.5) can be solved for the minimum measurement duration that is required to detect a prescribed parameter change successfully

$$T_h = \frac{1}{(\Delta\theta_h)^2} \frac{\lambda}{f_s F_{hh}}. \tag{7.6}$$

The measurement duration depends on the desired mean test response λ, the sampling frequency f_s, the magnitude of the parameter change $\Delta\theta_h$ squared, and the main diagonal value of the Fisher information F_{hh}, see Eq. (7.4). An efficient sensor configuration leads to a high Fisher information and a short measurement duration. Consequently, the measurement duration from Eq. (7.6) can be employed as a performance criterion for sensor placement optimization, provided both the mean

test response λ and the parameter change $\Delta\theta_h$ are predefined by the user.

- *Relative parameter change* $\Delta\theta_h$*.* The relative parameter change is a tuning parameter for the damage diagnosis. It enables the user to select a design parameter θ_h in a FE model and to define the minimum change Δ_h in this parameter that has to be sensed by the damage diagnosis method. This feature is pivotal for global damage diagnosis based on a small number of modes and a sparse sensor layout: irrelevant parameter changes in the global structure can be neglected, and the sensor placement can be tuned to become more sensitive to damage hotspots or changes in local components, which are critical for the safety or serviceability of the structure.

- *Minimum non-centrality* λ_{min}*.* Fixing the mean test response to a minimum value $\lambda = \lambda_{min}$ is equivalent to requiring a minimum damage detectability. So, it can be interpreted as a reliability index and fixed based on the acceptable probability of false alarms (PFA) and probability of detection (POD), see Section 5.1.3.

7.1.2 Performance Criterion

This section explains how to calculate the performance criterion based on one vibration record from the reference structure. The record $\mathbf{Y}$ contains N^0 samples, r_{pos} possible sensors locations, and is typically generated based on numerical simulations, as it is challenging to capture the vibrations at all possible sensor positions simultaneously.

$$\mathbf{Y}(\theta_0) = \begin{bmatrix} y_{1,1} & \cdots & y_{1,r_{pos}} \\ \vdots & \vdots & \vdots \\ y_{N^0,1} & \cdots & y_{N^0,r_{pos}} \end{bmatrix} \tag{7.7}$$

To examine a specific sensor layout with r sensors, the corresponding columns are extracted from the measurement matrix in Eq. (7.7). Subsequently, the statistical properties of the damage-sensitive residual are evaluated (covariance matrix $\mathbf{\Sigma}$), together with the sensitivity of the mean vector toward structural design parameters (Jacobian $\boldsymbol{\mathcal{J}}$), and ultimately, the Fisher information and the measurement duration T_h are calculated for each monitoring parameter according to Eq. (7.4) and Eq. (7.6). The decisive measurement duration is the maximum measurement duration over all parameters, so

$$T(c, r) = \max_h \{T_1, \cdots, T_H\}. \tag{7.8}$$

The indices clarify that the maximum measurement duration depends on both the sensor coordinates c and the number of sensors r.

7.1.3 Optimal Sensor Layout

For a fixed number of sensors, the number of possible configurations is

$$N_c(r, r_{pos}) = \frac{r_{pos}!}{(r_{pos} - r)!r!}. \tag{7.9}$$

One way to find the optimal sensor configuration is the exhaustive search (ES) or brute force method, meaning the performance criterion from the previous section is calculated for each combination. That means that the corresponding columns are extracted from the measurement matrix in Eq. (7.7) to re-calculate the covariance, the Jacobian matrix, the Fisher information, and ultimately, the measurement duration. Finally, the optimal sensor layout is the one with the highest damage detectability, i.e., the shortest measurement duration

$$T_{opt}(r) = \min_c \{T(c, r)\}. \tag{7.10}$$

When formulated as a minimization problem, the objective function formally reads

$$\begin{aligned} \min_c \quad & f_1(c) = \frac{T(c, r)}{T_{thres}} \\ \text{s.t.} \quad & f_1 \leq 1. \end{aligned} \tag{7.11}$$

Normalizing the measurement duration through an upper bound T_{thres} and constraining the optimization to values below $f_1 \leq 1$ is an efficient way to remove unsuitable sensor layouts, to normalize the criterion (so it can be compared to other criteria), and to find an appropriate number of sensors.

7.1.4 Appropriate Number of Sensors

The preceding section showed that, for a fixed number of sensors, the most efficient sensor layout can be determined as the one with the lowest optimal measurement duration. A convenient way to decide on an appropriate number of sensors is to calculate the optimal measurement duration T_{opt} for a varying number of sensors $r = 1, \ldots, r_{pos}$, and to plot T_{opt} over r. This plot is called the performance curve, see Fig. 7.8 on page 114. With an increasing number of sensors, the slope gradually decreases, so adding additional sensors hardly improves the damage detectability. The elbow point, where the curve begins to flatten, is an indicator for an appropriate number of sensors. Alternatively, the first best sensor configuration could be chosen that exhibits a measurement duration below the maximum allowable measurement duration T_{thres} with

$$T_{opt} < T_{thres}. \tag{7.12}$$

Using the objective function from Eq. (7.11), the optimization problem for finding the optimal number of sensors can be expressed as

$$\begin{aligned} \min_{r} \quad & f(r) = 1 - \min_{c} f_1(c) \\ \text{s.t.} \quad & 0 \leq f \leq 1 \end{aligned} \tag{7.13}$$

7.2 Optimizing the Localizability

This section develops a sensor placement strategy for damage localization. Using the minmax localization test, a decision can be made on the monitoring parameter that is most likely to be damaged. The minmax test statistic is evaluated for each parameter θ_h and defined as

$$t_h = \zeta_h^{*T} F_h^{c*-1} \zeta_h^* \longrightarrow \begin{cases} \chi^2(\nu, 0) & \text{(reference)} \\ \chi^2(\nu, \lambda) & \text{(damaged),} \end{cases} \tag{7.14}$$

with the robust residual $\zeta_h^* = \zeta_h - \mathbf{F}_{h\bar{h}}^c \mathbf{F}_{\bar{h}\bar{h}}^{c-1} \boldsymbol{\zeta}_{\bar{h}}^c$ and the corresponding Fisher information

$$F_h^{c*} = F_h - \mathbf{F}_{h\bar{h}}^c \mathbf{F}_{\bar{h}\bar{h}}^{c-1} \mathbf{F}_{\bar{h}h}^c, \qquad \begin{bmatrix} F_h & \mathbf{F}_{h\bar{h}}^c \\ \mathbf{F}_{\bar{h}h}^c & \mathbf{F}_{\bar{h}\bar{h}}^c \end{bmatrix} = \begin{bmatrix} \boldsymbol{\mathcal{J}}_h^T \boldsymbol{\Sigma}^{-1} \boldsymbol{\mathcal{J}}_h & \boldsymbol{\mathcal{J}}_h^T \boldsymbol{\Sigma}^{-1/2} \tilde{\boldsymbol{\mathcal{J}}}_{\bar{h}}^c \\ \tilde{\boldsymbol{\mathcal{J}}}_{\bar{h}}^{cT} \boldsymbol{\Sigma}^{-1/2} \boldsymbol{\mathcal{J}}_h & \tilde{\boldsymbol{\mathcal{J}}}_{\bar{h}}^{cT} \tilde{\boldsymbol{\mathcal{J}}}_{\bar{h}}^c \end{bmatrix}. \tag{7.15}$$

The minimum measurement duration is an intuitive performance criterion to find the optimal sensor layout for damage detection tests. It can be calculated for damage localization tests as well, but optimizing the damage localization is a multi-objective optimization problem (see Chapter 6). With increasing damage localization resolution, the damage detectability decreases and the number of false alarms changes. Moreover, a larger pool of solutions is available, because the monitoring parameter must be clustered and there are as many cluster configurations as there are monitoring parameters for each sensor layout. Instead of one, three criteria have to be considered, and they have to be calculated multiple times for each sensor configuration.

7.2.1 Performance Criteria

This section summarizes the three criteria to optimize the sensor layout for damage localization using the minmax test. Moreover, the objective functions are weighed by defining lower and upper bounds. The approach is similar to the one described in Section 6.3.

Localization Resolution. The first objective function is the damage localization resolution. It is quantified through the number of clusters K in which damage can be isolated. The objective is defined as

$$f_2(K) = \frac{K - K_b}{K_g - K_b} \tag{7.16}$$

where $K_b = 2$ and $K_g = \operatorname{rank}(\boldsymbol{\mathcal{J}}^T \boldsymbol{\Sigma}^{-1} \boldsymbol{\mathcal{J}})$ are the lower and upper bounds.

Damage Identifiability. The second objective function is the identifiability of damage. For each monitoring parameter, the damage identifiability is quantified through the minimum identifiable damage

$$\Delta_h = \frac{1}{\theta_h^0}\sqrt{\frac{\lambda_{\min}}{Tf_s \cdot F_h}}[\%], \tag{7.17}$$

with the minmax Fisher information $F_h = F_h^{c*}$ from Eq. (7.15). First, the minimum identifiable damage is evaluated for all monitoring parameters, and then, it is divided by the desired detectable damage $\boldsymbol{\Delta_b}$. The decisive parameter is the one with the highest ratio and the corresponding objective function is

$$f_3(K) = \max_h \left(\frac{\Delta_h(K) - \Delta_{g,h}}{\Delta_{b,h} - \Delta_{g,h}} \right) \tag{7.18}$$

This makes the input vector $\boldsymbol{\Delta_b}$ a powerful tool to tune the sensor layout so it becomes more sensitive to user-defined components in the FE model. In theory, a lower bound for the minimum identifiable damage $\boldsymbol{\Delta_g}$ could be defined as well; however, this quantity defaults to a zero vector.

False Alarms. The third objective function is the false alarm susceptibility. False alarms are quantified by evaluating the non-centrality ratio (NCR) from Eq. (6.32) and counting the number of scenarios N_{sc} in which false alarms are expected to occur. The objective function is

$$f_4(K) = \frac{N_{sc}(K) - N_g}{N_b - N_g}, \tag{7.19}$$

where the lower and upper bounds can be set to $N_g = 0$ and $N_b = H$, with H being the number of monitoring parameters. To further decrease false alarms, the upper bound could be set to a fraction of the number of monitoring parameters, e.g., $N_b = 0.5 \cdot H$.

7.2.2 Optimal Compromise

Since the objective functions are already weighed through the definition of lower and upper bounds, a compromise function can be set up as the Euclidean distance in the three-dimensional objective space. To optimize the damage localization, the objective functions from Eq. (7.16) - (7.19) are combined, that is, the localization resolution, the damage identifiability, and the false alarm susceptibility.

$$\begin{aligned} \min_K \quad & f = \sqrt{f_2(K)^2 + f_3(K)^2 + f_4(K)^2} \\ \text{s.t.} \quad & f_2(K) \leq 1, f_3(K) \leq 1, f_4(K) \leq 1 \end{aligned} \tag{7.20}$$

To optimize the damage localization and damage detection at the same time, a fourth objective

function is added, i.e., the damage detectability from Eq. (7.11).

$$\begin{aligned} \min_{K} \quad & f = \sqrt{f_1(K)^2 + f_2(K)^2 + f_3(K)^2 + f_4(K)^2} \\ \text{s.t.} \quad & f_1(K) \leq 1, f_2(K) \leq 1, f_3(K) \leq 1, f_4(K) \leq 1 \end{aligned} \tag{7.21}$$

As an alternative to the compromise function, a population-based optimization method can be employed that is capable of handling multiple objective functions simultaneously, e.g., the multi-objective GA that is described in the subsequent section.

7.3 Implementing a Genetic Algorithm

A problem that has already been encountered in the literature review is the problem of combinatorial explosion, see Eq. (7.9). The problem is that, even for a low number of possible sensor locations, the number of possible sensor combinations is excessively large, making it infeasible to evaluate the objective functions for each combination c in an exhaustive search (ES) approach. In this thesis, the problem is overcome by employing the genetic algorithm (GA) that is pre-implemented in the Global Optimization Toolbox in MATLAB® (Messac, 2015), and modified through custom functions for generating, modifying, and merging sensor layouts.

7.3.1 Single-objective Optimization

Single-objective optimization means that one objective function is considered, e.g., the objective function from Eq. (7.11) or the compromise function from Eq. (7.20) or (7.21). GAs are inspired by the natural evolution process based on Darwin's survival of the fittest principle. In this context, the objective function is referred to as the *fitness* function, a single sensor layout is an *individual* that consists of multiple genes (i.e., sensor numbers), and a *population* is an array of individuals. In this work, the genes are encoded as integer sensor numbers, and each individual is a vector that includes r entries, where r is the number of sensors, see Fig. 7.1. Evolution takes place over multiple *generations*, where the parent population contributes its genes to its children through cross-over, mutation, and elitism, with more information in the subsequent paragraph. A basic assumption for successful evolution is a diverse gene pool, where *diversity* is defined as the average distance between the fitness of individuals within one population.

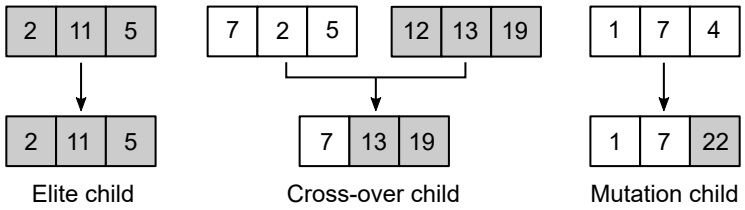

Figure 7.1: Elements of reproduction of the GA with integer sensor encoding and $r = 3$ sensors

Cross-over. Cross-over describes the merging of two sensor layouts, where each vector entry is randomly selected from one of the two parents, see Fig. 7.1. Only parents with comparatively good fitness values are chosen for cross-over, where individuals can be selected more than once as parents. The custom cross-over function includes a restraint that does not allow for multiple sensors to be placed at the same locations, comparable to a sudden death condition. A crucial input parameter is the cross-over fraction, which defines the number of children within a population, not including elite children, that are generated through cross-over.

Mutation. Mutation children are generated through the random permutation of individual genes in a single parent, see Fig. 7.1. Mutation is an important stochastic element to maintain diversity within the population and avoid premature convergence (Deb, 2001). For efficiency, the custom mutation function is implemented so the mutation rate linearly decreases, meaning the number of perturbed sensor numbers is high initially, but with increasing number of iterations (i.e., generations), the intensity of the perturbation gradually reduces, so the procedure converges toward the global minimum in the objective function. This implementation combines the positive aspects from another optimization method, called simulated annealing, with more information in Section 2.2.1. To guarantee unique genes, the mutation function also includes a sudden death condition.

Elitism. Elite parents are particularly fit individuals that automatically survive to the next generation without genetic modification, comparable to a cloned child, see Fig. 7.1. Elitism is a non-stochastic element that ensures that the found optimal solution cannot be lost. Elites can be selected as parents for cross-over, and multiple identical elites are possible. A crucial input parameter is the elite count, i.e., the fraction of parents within the population that become elite members. For the sake of diversity, this fraction should be kept low, so the population is not dominated by elite members (Deb, 2001).

A flowchart of the algorithm is depicted in Fig. 7.2. The optimization is based on a single vibration record and launches with a random initial population. For each generation, the fitness of each individual is calculated and scaled using the lower and upper bounds. Based on the elite count, the fittest individuals are passed on to the next generation without modification, and a cross-over fraction determines the number of cross-over and mutation children. The selection of parents for cross-over is made in a tournament selection (Yang and Soh, 1997), meaning a user-defined number of individuals (e.g., two individuals) are randomly selected in the current population, and only the fitter one is allowed to reproduce. The algorithm terminates if one of the following stopping criteria is met: a maximum number of generations is exceeded, a maximum computation time is exceeded, or the optimal solution has not improved (by more than a specified tolerance value) over a certain period of time or number of generations. Additional stopping criteria are documented in the referenced literature (Deb, 2001).

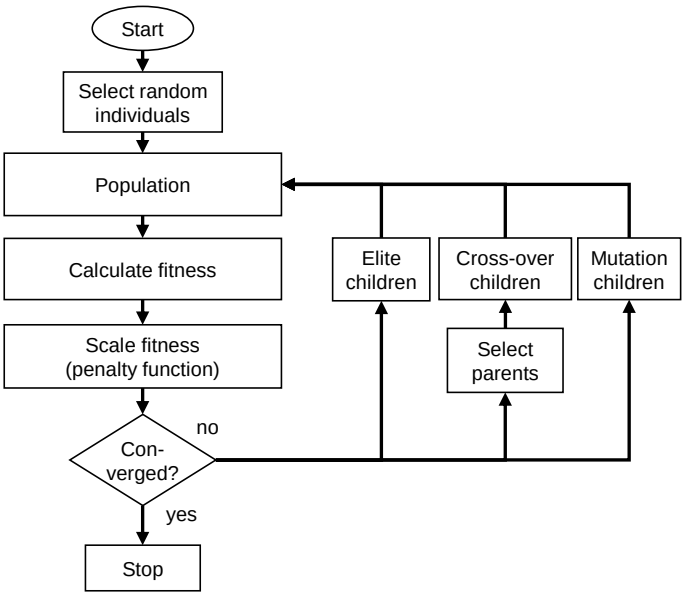

Figure 7.2: Flowchart for the genetic algorithm with a single objective

7.3.2 Multi-objective Optimization

There are numerous variants of the GA that are capable of handling multiple objective functions at the same time, with a good example being the 2nd generation of the non-dominated sorting genetic algorithm (NSGA-II) (Deb, 2001) that is pre-implemented in MATLAB®. In previous sections, a compromise function is employed to find the elite solutions in a multi-objective optimization space. The compromise function favours sensor layouts that minimize all three objectives simultaneously. However, a more meaningful way to present the pool of optimal solutions is the visualization of the entire Pareto frontier, as all solutions on the Pareto frontier are optimal or non-dominated solutions. The primary goal of the NSGA-II is to advance the Pareto frontier as a whole toward better solutions while keeping a maximum distance between the different points, i.e., a diverse population.

The element of mutation and cross-over are implemented in a similar way as for the single-criterion GA, but the concept of elite members is re-defined. All solutions on the Pareto frontier are considered optimal, and no objective functions can be improved without degrading another, see Section 6.3.4 and Fig. 6.4. Therefore, all solutions on the Pareto frontier are considered elite members, and to classify solutions that are not on it, different ranks are assigned: Rank 1 individuals are not dominated by any other solutions, so they are on the Pareto frontier. Rank 2 individuals are only dominated by solutions on the Pareto frontier, and so forth, see Fig. 7.3. To maintain diversity, only a certain fraction of rank 1 members are kept, i.e., the Pareto fraction. Figure 7.3 also shows that, in each iteration step, the population is extended first through mutation and cross-over children, so parents and children coexist. Subsequently, the individuals in the extended population are ranked, and the population is reduced to its original size. In other words, parents

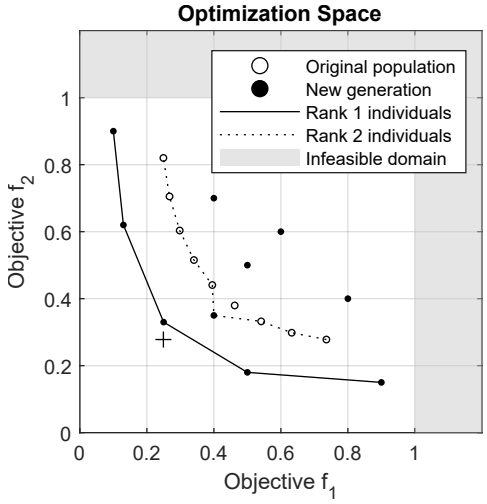

Figure 7.3: Evolution of sensor layouts in the multi-objective GA

can survive on to the next generation without modification, even if they are not elite members. For completeness, two more concepts have to be introduced, i.e., the crowding distance and the spread.

Crowding Distance. The crowding distance measures the distance between adjacent individuals of the same rank, in all dimension of the optimization space (Deb, 2001). It is calculated through

$$distance(i) = \sum_{k} x(k, i+1) - x(k, i-1) \tag{7.22}$$

where k is the dimension of the optimization space, x is the distance, and $i+1$ and $i-1$ are the closest neighbours of individual i. The crowding distance is an appropriate tie-breaker when two individuals have the same rank, as solutions with greater distance are favoured. To keep the Pareto frontier wide, the distance of individuals at extreme points is set to infinity.

Spread. The spread is a measure of the convergence, as it measures the movement of the Pareto set (Deb, 2001). Spread is defined as

$$spread = (\mu + \sigma)/(\mu + Qd) \tag{7.23}$$

where Q and d are the number of points on the Pareto frontier with finite distance and the distance among them, respectively, and σ is the standard deviation of their crowding distance. The variable μ is the distance between the current minimum points on the Pareto front to previous runs, summed over all objective functions. The spread is small when the points on the Pareto frontier are spread evenly (small σ), and when the extreme objective function values do not change much (small μ). The spread is an excellent stopping criterion.

7.4 Proof of Concept

For proof of concept, the sensor placement optimization strategy for damage detection is applied to a hollow structural steel (HSS) beam similar to the one from Sections 5.4 and 6.4. The primary goal is to find the optimal sensor layout and the corresponding measurement duration, so a damage extent of 5% can be reliably detected in any beam segment. Damage is defined as a decrease in the modulus of elasticity with the monitoring parameter $\boldsymbol{\theta} = [E_1, \ldots, E_9]$ and $E_i = 210,000$ MPa. The eight possible sensor locations P1 - P8 are visualized in Fig. 7.4, where the vibration data is recorded in the vertical direction. For conciseness, all modal parameters are summarized in Fig. 7.5, and the input parameters for the damage diagnosis are summarized in Table 7.3.

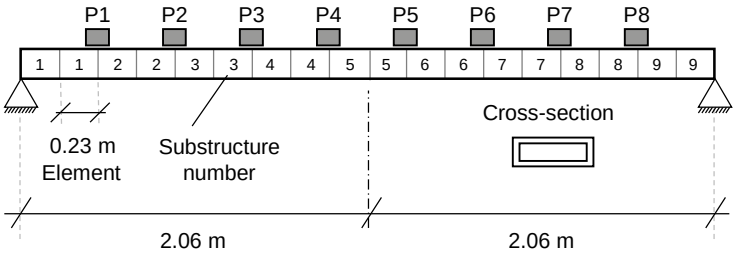

Figure 7.4: Numerical HSS beam including the possible sensor locations P1 - P8

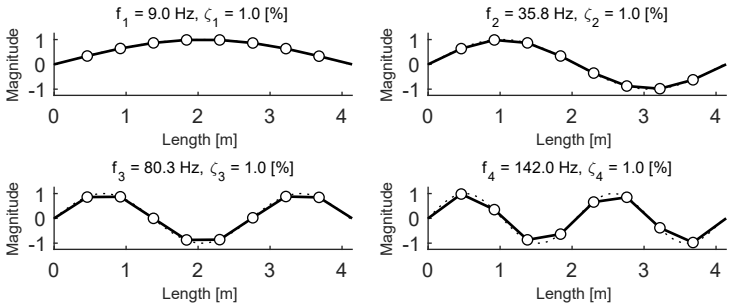

Figure 7.5: Numerical mode shapes

7.4.1 Optimizing the Detectability

Study 1: Exhaustive Search

Measurement Duration. This section explains how the measurement duration is estimated for a fixed sensor configuration, for instance, a single sensor at location P2 from Fig. 7.4. First, the Fisher information is calculated based on a long vibration record from the reference structure, see Section 5.4. Secondly, the reliability index is determined to $\lambda_{min} = 33.7$ based on an acceptable PFA of 5% and a POD of 99.4%. The sampling frequency f_s is fixed to 360 Hz and each monitoring parameter has a magnitude of $\theta_h = 210,000$ MPa. Using Eq. (7.6), the main diagonal value of the Fisher information is translated into a measurement duration T_h for each beam segment, with the results being visualized in Fig. 7.6a. The minimum measurement duration is the longest near the

Data		Segmenting		Processing	
Measured quantity	velocity	Training segments	100	No. of sensors	varying
Sampling frequency	360 Hz	Testing segments	100	Time lags	varying
Reference data length	60 min	Samples/segment	T.B.D.	System order	n=20
Training/testing data	T.B.D.	Duration/segment	T.B.D.	No. of blocks	n_b=20,000

Table 7.1: Input parameter sheet

pin-supports, with a maximum measurement duration of $T_1 = 101$ s. For comparison, the results for a second sensor configuration with two sensors at position P1 and P8 are summarized in Fig. 7.6b. It can be appreciated that increasing the number of sensors from one to two reduces the decisive measurement duration by a factor of 1.8 to $T = 56$ s.

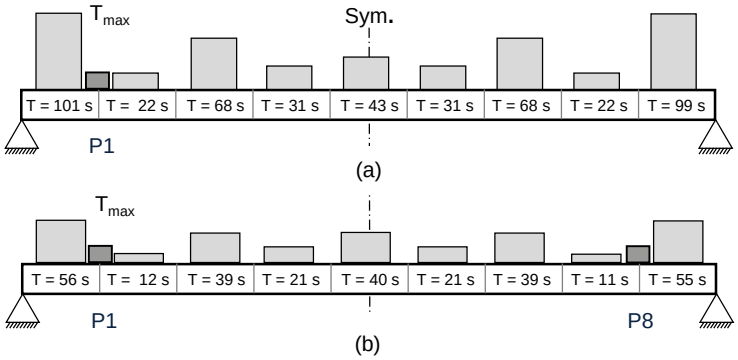

Figure 7.6: Minimum measurement duration T_h for (a) one sensor at position P2, and (b) two sensors at P1 and P8

Optimal Sensor Layout. Following this train of thought, the decisive measurement duration $T_{opt}(r = 1)$ is evaluated for all sensor layouts with one sensor, and the results are summarized in an evaluation chart, see Fig. 7.7. Position P1 and P8 occur to be the optimal sensor locations, with a minimum measurement duration of $T = 101$ s. In contrast, configuration C(3) and C(6) appear to be the least favourable sensor configurations with sensors at P3 and P6 and a measurement duration of $T_{max} = 280$ s. The sensor locations coincide with the zero-vibration points of Mode 3, see Fig. 7.5. Since Mode 3 is non-observable, it does not contribute to the Fisher information, and reduced information results in a prolonged measurement duration. For multiple reasons, non-observable modes have to be removed from the analysis (but more details on this follow in Section 10.2.3). For the sake of comparison, the optimization is repeated for sensor configurations with two sensors, see Fig. 7.9. Configuration C(3,6) exhibits the longest measurement duration as the sensors are placed at P6 and P3, i.e., the zero-vibration points of Mode 3. The optimal sensor configuration is C(1,8), with a measurement duration of $T = 56$ s. The sensor layouts that correspond to the optimal measurement durations for one and two sensors are visualized in Fig. 7.6.

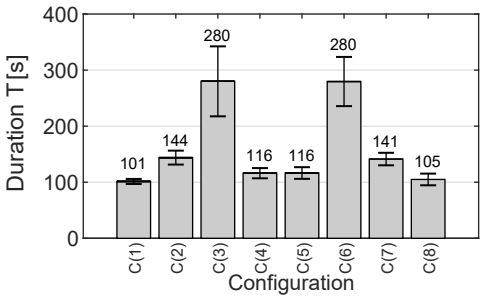

Figure 7.7: Measurement durations $T(c, r = 1)$ and standard deviations

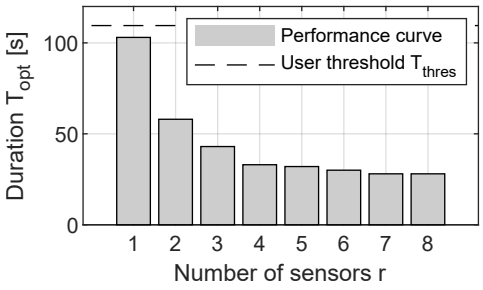

Figure 7.8: Optimal measurement time $T_{opt}(c)$ for a varying number of sensors

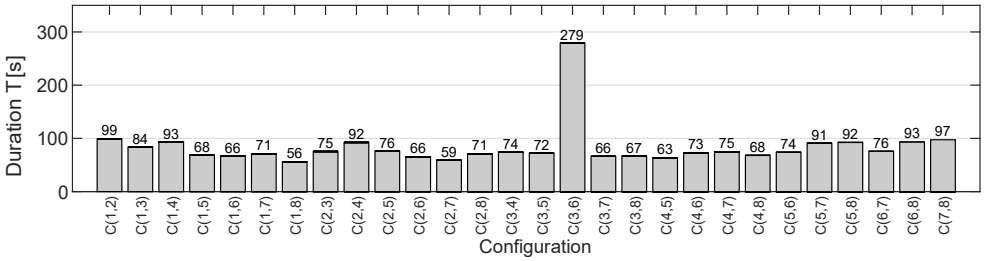

Figure 7.9: Measurement durations $T(c, r = 2)$

Appropriate Number of Sensors. An appropriate number of sensors leads to an optimal measurement duration T_{opt} that is shorter than the maximum allowable measurement duration T_{thres}. The main idea is to gradually increase the number of sensors from $r = 1$ to $r = 8$ while evaluating the optimal sensor configuration, as explained in the previous sections. Plotting the optimal measurement duration over the corresponding number of sensors is a particularly intuitive way to understand the effect that an added sensor has on the performance of the damage detection method, and to decide on an appropriate number of sensors, see Fig. 7.8. This plot is also referred to as the performance curve. In this study, the maximum allowable measurement duration is set to 110 s, and the sensor layout with one sensor is chosen for monitoring.

Validating the Optimal Solution. The last step of the sensor placement strategy is to validate the optimal sensor layout. This is done through a damage diagnosis based on simulated vibration data from the damaged state. In total, nine validation runs are performed (one for each monitoring parameter), while the applied damage is set to the requested minimum detectable damage of 5%, and the measurement duration is set to the optimal measurement duration $T_{opt} = 101$ s. The mean test response is greater than the minimum non-centrality for all cases, with $\lambda > \lambda_{min}$, except the beam element near the support. This was the decisive element that led to a measurement duration of 101 s, so the mean test response is equal to the theoretical one, see Fig. 7.10.

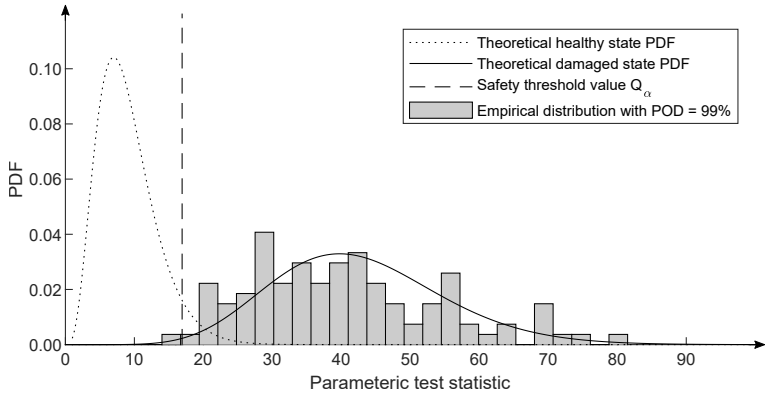

Figure 7.10: Test distribution for a 5% stiffness decrease in stiffness parameter E_1

Study 2: Genetic Algorithm

In the previous study, the maximum number of possible sensor combinations was $N_c = 70$ for the case where four sensors are to be placed at eight locations, see Eq. (7.9). If the number of candidate locations is increased to $r_{tot} = 24$, with a tri-axial sensor instead of uni-axial sensor at each location (as visualized in Fig. 7.11), and the number of sensors is set to $r = 3$, the number of possible combinations increases to $N_c = 2,024$. This is an appropriate case study to demonstrate the efficiency of the GA, as the problem is small enough for the exhaustive search (ES) method to cope with it and big enough for the GA to become efficient. Moreover, only modes of vibration in the vertical direction are considered, so the optimal sensor positions are expected to be at vertical degrees of freedom as well.

First, the ES method is applied, and the layouts are ranked with respect to the measurement duration. The optimal performance is achieved for a sensor placement at positions P6, P9, and P24 in Fig. 7.11.

Secondly, the GA is launched while assigning the final rank (from the ES) to the elite members of each generation. For example, if an elite member contains the optimum sensor configuration from the ES, it is tagged with a rank of one, where the least favourable solution has a rank of 2,024. This way, it is possible to trace how long it takes for the GA to find the optimal solution with a rank of one. The population size is set to 20 and the number of generations to 20. The elite count is set to 25%, meaning the best five configurations survive to the next generation without modification. The cross-over fraction is 25%, so a quarter of all children (other than elite children) are made up of cross-over children, and the others are mutation children. The results are summarized in the convergence chart in Fig. 7.12. The genetic algorithm finds the global minimum within five generations, so $5 \cdot 20 = 100$ calculations of the objective function. That means the computation is sped up by a factor of $2,024/100 \approx 20$ in comparison to the ES. A close-to-optimal solution with a rank of 10 is already found within four generations and 80 calculation steps. In conclusion, the genetic algorithm outperforms the exhaustive search even for small combinatorial problems and efficiently finds an appropriate sensor layout.

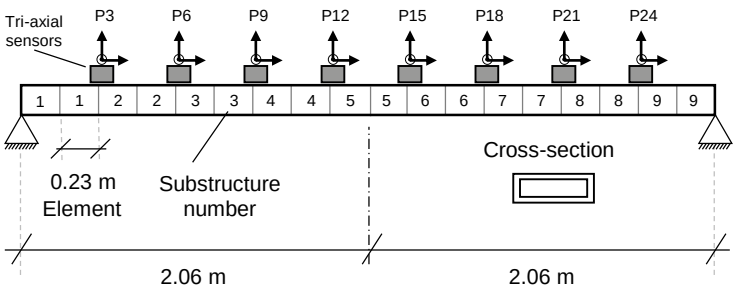

Figure 7.11: HSS beam including the possible sensor locations P1 - P24

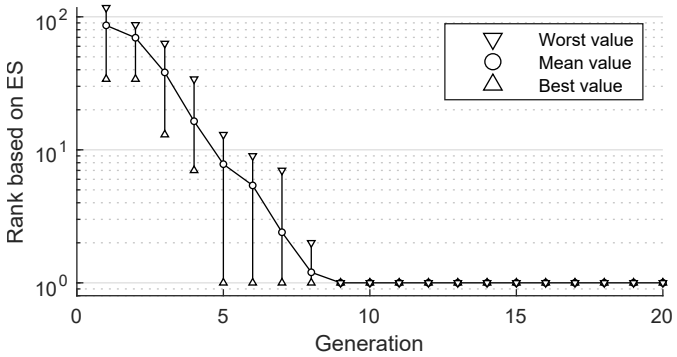

Figure 7.12: Convergence chart for the genetic algorithm, showing the rank of elite members with respect to their ranking after an exhaustive search (ES)

7.4.2 Optimizing the Localizability

In this section, the sensor placement strategy for damage localization is applied to a schematic 2-D model of a cable-stayed bridge, with two sensors and six possible sensor locations, see Fig. 7.13. The objective is to highlight the particular strengths of the placement strategy, i.e., the capability to tune the sensor layout to become more sensitive to damage hotspots at inaccessible locations.

Experimental Setup

Bridge Description. The structure is inspired by the Shipshaw Bridge in Canada. The deck of the bridge model is split into six beam elements, each 10 m in length, with a fixed support on the left side, no connection to the tower, and a roller support on the right side, see Fig. 7.13. The single tower starts 5 m below deck and rises 10 m over it. Two steel hangers suspend the deck where the forces are redirected over the tower into the backstay hanger, and finally into the tie-down anchor at the fixed support.

Finite Element Model. Based on the model, the vibration record is generated, and the model-based sensitivity matrix is calculated with numerical modal parameters. The FE model is built through custom code in MATLAB®, and three different cross-sections and materials are assigned to the tower, the deck, and the hangers, see Table 7.2. All elements are modelled as Bernoulli beams

No.	Description	Height [m]	Width [m]	E-Modulus [MN/m^2]	Mass density [kg/m^3]
1	Deck	0.40	0.20	210,000	7,800
2	Tower	1.00	1.00	30,000	2,500
3	Hanger	0.03	0.03	110,000	7,800

Table 7.2: Finite element specifications

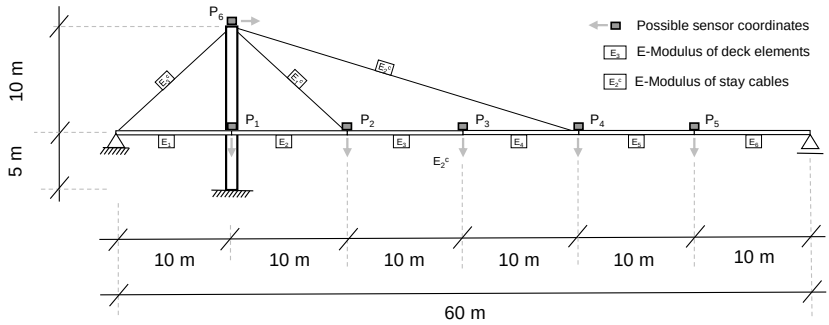

Figure 7.13: Schematic bridge with six possible sensor locations P1 - P6

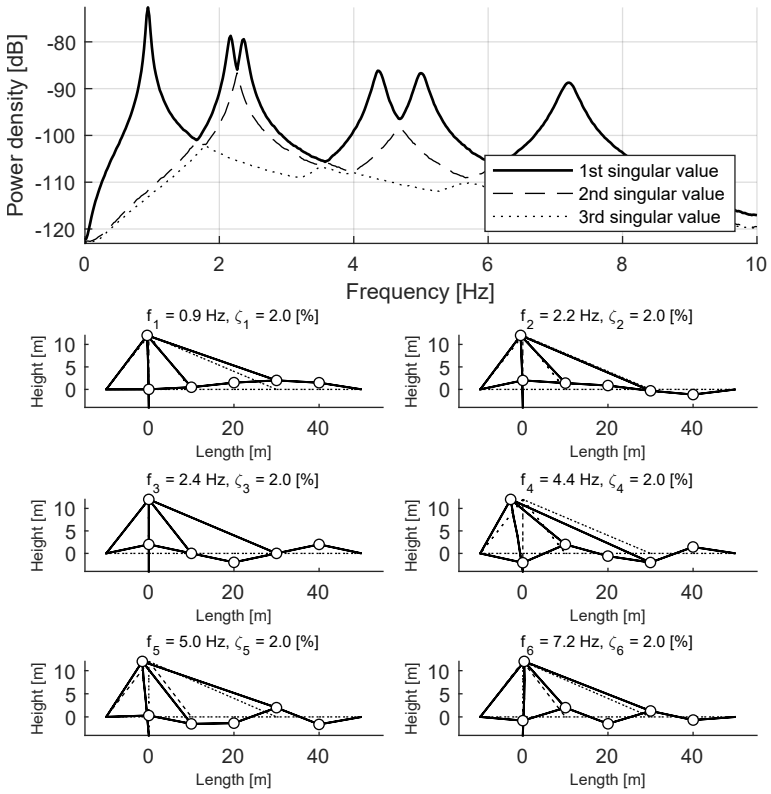

Figure 7.14: Modes of vibration

Data		Segmenting		Processsing	
Measured quantity	velocity	Training segments	100	No. of sensors	r/r_0=2/2
Sampling frequency	20 Hz	Testing segments	100	Time lags	p/q=8/9
Reference data length	1,800 min	Samples/segment	18,000	System order	n=16
Training/testing data	1,800 min	Duration/segment	15 min	No. of blocks	n_b=2,000

Table 7.3: Input parameter sheet

with consistent mass matrices and rigid connections at all joints (but the tower is not connected to the deck). For simplicity, the cable hangers are used instead of cables, which have tensile and compressional stiffness. For conciseness, the results from numerical modal analysis are summarized in Fig. 7.14, including the natural frequencies, the assumed damping ratios, and the mode shapes. Damage is defined as a stiffness reduction in any of the six deck components or the hangers. The respective modulus of elasticity is $E_i = 210{,}000$ MPa and $E_i^c = 110.000$ MPa with the monitoring vector

$$\boldsymbol{\theta} = \begin{bmatrix} E_1 & E_2 & E_3 & E_4 & E_5 & E_6 & E_1^c & E_2^c & E_3^c \end{bmatrix}^T.$$

Instrumentation. In total, six uni-axial sensors are considered, five on the deck and one on top of the tower, see Fig. 7.13. The velocity records are simulated with a sampling frequency of 128 Hz and subsequently down-sampled to 20 Hz. For transparency, the power spectral density (PSD) of the output signal is depicted in Fig. 7.13 although the damage diagnosis is performed in the time domain. The reliability requirements toward the test results are defined based on a PFA of 5% and a POD of 99.4%. All other input parameters for the damage diagnosis are summarized in Table 7.3 with a measurement duration of $T = 15$ min during damage testing.

Study 1: Balanced Layout

This study aims to find the optimal sensor layout for damage localization with two sensors. The main input parameter is the upper bound for the minimum detectable damage $\boldsymbol{\Delta}_b$ in each structural component. Using a "balanced layout" means to set the same upper bound (for example 50%) for all monitored components including the deck and the hangers, leading to

$$\boldsymbol{\Delta}_b = \begin{bmatrix} 0.5 & 0.5 & 0.5 & 0.5 & 0.5 & 0.5 & 0.5 & 0.5 & 0.5 \end{bmatrix}^T. \tag{7.24}$$

Other input parameters include the upper bound for the magnitude of false alarms, which is set to 10%, as well as the worst number of false alarm scenarios in relation to the total number of damage scenarios, which is set to 50%. Ultimately, the default values for the lower and upper bounds for the number of clusters K are used, i.e., $K_b = 2$ and $K_g = \text{rank}(\boldsymbol{\mathcal{J}}^T \boldsymbol{\Sigma}^{-1} \boldsymbol{\mathcal{J}})$.

In total, there are 15 possible sensor combinations to place two sensors at six candidate locations. Every layout has nine possible cluster configurations, expanding the pool of possible solutions from 15 to 135. After removing the infeasible layouts, 96 solutions remain, with 11 solutions that are

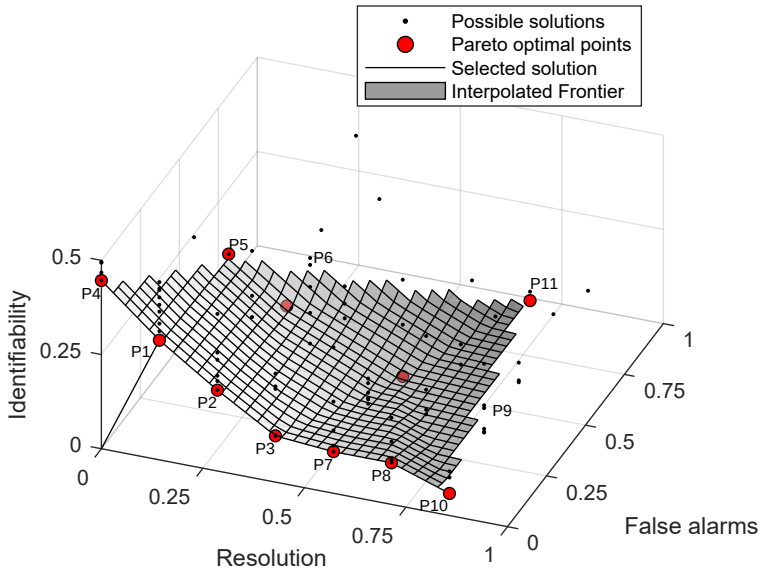

Figure 7.15: Feasible optimization space with 11 Pareto optimal solutions

	Damage Identifiability Δ [%]										**K**	$\mathbf{N}_{sc}$	**Score**
	Δ_1	Δ_2	Δ_3	Δ_4	Δ_5	Δ_6	Δ_7	Δ_8	Δ_9	Δ_{mean}			
P1	7.1	10.7	15.9	13.3	9.4	7.1	5.1	10.1	12.6	10.1	8	0	0.35
P2	4.2	5.9	5.6	6.8	10.7	5.9	2.4	2.4	2.6	5.2	7	0	0.36
P3	4.0	5.9	4.7	5.3	6.1	3.4	2.3	2.2	2.6	4.1	6	0	0.45
P4	18.8	18.4	22.3	19.8	15.7	18.2	5.2	6.8	10.7	15.1	9	0	0.45
P5	10.7	14.4	15.0	15.3	11.5	13.8	2.8	4.7	6.8	10.6	8	2	0.56
P6	8.3	8.3	7.9	9.5	9.9	5.8	3.2	4.7	6.6	7.1	7	2	0.56
P7	3.4	4.4	5.5	4.2	3.6	3.0	2.5	3.5	4.8	3.9	5	0	0.58
P8	3.3	4.1	5.5	4.1	3.6	2.9	1.9	3.2	3.8	3.6	4	0	0.72
P9	1.9	2.5	2.2	3.5	1.8	1.5	1.4	2.5	3.0	2.3	5	2	0.73
P10	1.3	2.0	1.9	2.9	1.3	1.2	1.3	2.4	2.9	1.9	3	0	0.86
P11	1.7	2.1	1.9	3.1	1.8	1.5	1.3	2.4	2.9	2.1	4	4	1.14

Δ_i : = detectable damage, K := no. of substructures, N_{sc} := no. of false alarm scenarios

Table 7.4: Pareto optimal points P1 - P11 with unscaled objective functions

not dominated by any other solution. These non-dominated solutions form a three-dimensional surface, called the Pareto frontier. The Pareto optimal points are highlighted in Fig. 7.15, and the underlying objective functions are listed in Table 7.4. In the automated version, the optimal solution is selected as the one with the shortest distance to the origin, as this exhibits the optimal compromise between damage localization resolution, identifiability, and false alarms. However, plotting the entire Pareto front in the presented format gives the user the chance to hand-pick the preferred solution. For example, the second-best solution P2 exhibits $K = 7$ clusters instead of $K = 8$, but a considerably higher damage identifiability with a maximum identifiable damage

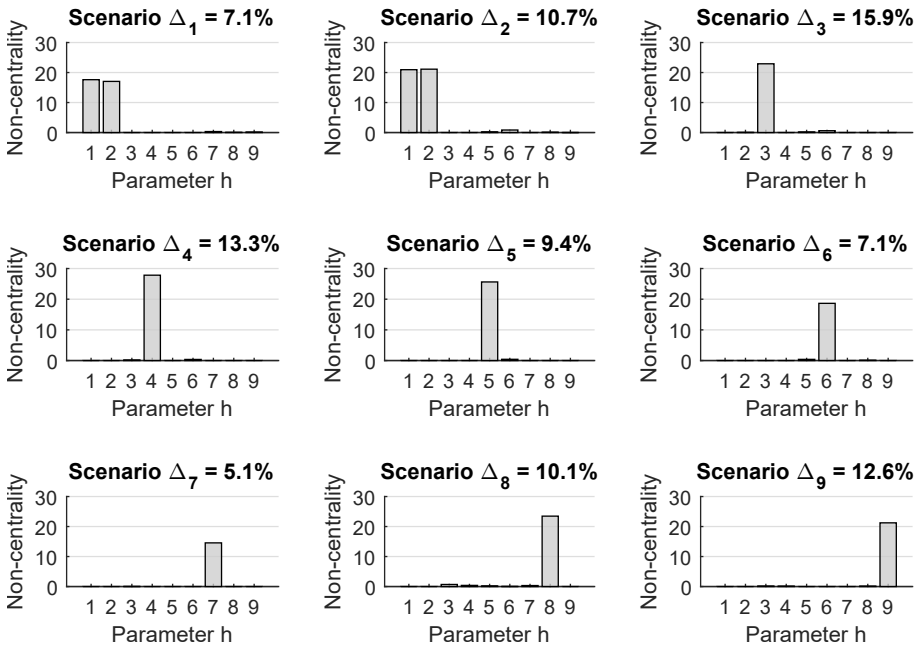

Figure 7.16: Empirically validating the mean test response to the minimum detectable damages

of 10.7% instead of 15.9%. On average, the minimum detectable damage increased from 10.1% to 5.2%, where the number of false alarms remains unchanged. Now, the user can make the final decision on whether to put emphasis on damage identifiability or localization resolution. In this case study, point P1 is chosen, leading to an optimal sensor layout with sensors at P3 and P5, see left side of Fig. 7.17. The benefit of the implemented multi-objective GA is that the results can be presented in the same fashion.

To complete the sensor placement optimization, the optimal solution has to be validated. For this purpose, nine damage diagnosis runs are performed, where the damage in each monitoring parameter 1 - 9 is set to the minimum identifiable damage. Figure 7.16 shows the mean test responses which, in all cases, are close to $\lambda = 20$. This is consistent with the theoretical value of $\lambda_{min} = 19.98$, which corresponds to a PFA of 5% and a POD of 99.4%, so the test response is predicted correctly and the validation is completed.

Study 2: Tuned Layout for Hanger Monitoring

The sensor placement is now tuned to become particularly sensitive to stiffness decreases in the hangers, by reducing the upper bound of the minimum detectable damages from 50% to 10%.

$$\boldsymbol{\Delta}_b = \begin{bmatrix} 0.5 & 0.5 & 0.5 & 0.5 & 0.5 & 0.5 & 0.1 & 0.1 & 0.1 \end{bmatrix}^T \tag{7.25}$$

As a consequence, the optimal sensor layout changes. Instead of placing the sensors on the deck at P3 and P5, the optimization algorithm suggests placing them at P3 and P6, at the top of the tower. Moreover, the response of the minmax localization test to damage in hangers increases, while

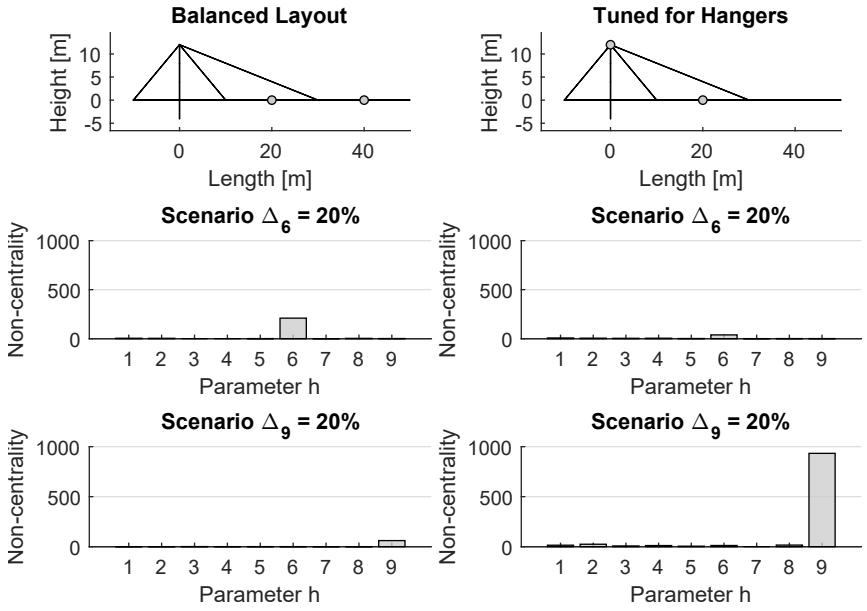

Figure 7.17: Test response to damage in a deck element (Parameter 6) and a hanger (Parameter 9) for balanced and tuned sensor layouts

damage in the deck components leads to less pronounced responses. For example, for Parameter 9, i.e., the backstay hanger, the mean test response to a 20% damage increases from 60 to 933, and the test response to damage in Parameter 6 (the 6th deck component) decreases from 209 to 38. In other words, the sensor layout can straightforwardly be tuned to become more sensitive to user-defined components.

7.5 Summary

This chapter develops a sensor placement strategy with the primary goal of optimizing the detectability of damage. It proposes the measurement duration as a performance criterion for sensor placement optimization, and demonstrates how it can be combined with a (state-of-the-art) genetic algorithm (GA) to efficiently find the optimal sensor layout for large structures. The performance criterion is intuitive, as it takes as input the required minimum detectable damage and yields the corresponding measurement duration. Since the minimum detectable damage can be defined differently for each structural component, it is possible to tune the sensor layout to become more sensitive to changes in structural parameters that are decisive for the safety or serviceability of the structure, as well as damage hotspots. The measurement duration appears to reduce with an increasing number of sensors, so a decision on an appropriate number of sensors can be made by defining an upper bound for the measurement duration. For the analysis, vibration data from the undamaged structure is required and a finite element model for the computation of the model-based sensitivity. In the second part, the sensor placement strategy is extended to damage localization, with the primary goal of maximizing the localizability of damage. As explained in the previous chapter,

optimal localizability is a compromise, as with an increasing number of substructures, the damage localization resolution increases, but the identifiability of damage in each parameter decreases, and the number of false alarms changes. Ultimately, the 2nd generation of the non-dominated sorting genetic algorithm (NSGA-II) is employed to solve the multi-objective optimization problem and determine an optimal set of solutions when the number of possible sensor combinations is excessively large.

Chapter 8

Monitoring Boundary Conditions

This chapter puts forward an approach to detect and localize changes in the force (also called natural) boundary conditions and displacement (also called essential) boundary conditions. All previous studies involving the asymptotic local (AL) approach consider changes in the material properties or cross-sectional values, but changes in boundary conditions have not been included into the diagnostic framework. Having said that, being able to diagnose changes in boundary conditions is relevant for post-earthquake damage assessment on bridges, and makes the predictive framework more universal. A classical modelling approach would be to parametrize damage as a change in local stiffness elements such as support springs or elastic bedding. However, local support stiffness changes may be challenging to distinguish from stiffness changes in adjacent structural elements and, in general, may not be a suitable way to consider the physics of the problem. Changes in boundary conditions are local phenomena, but they lead to global geometry changes, a global redistribution of mass and stiffness, and stabilizing or destabilizing effects. Following this train of thought, an approach is introduced in this chapter that is based on the global geometric stiffness matrix (stress stiffening). Consequently, the boundary condition parameters can be included in the parameter vector $\boldsymbol{\theta}$ and the sensitivities can be incorporated into the damage detection and localization framework of the AL approach, which ultimately allows for a prediction of the minimum change in boundary conditions.

The chapter is organized as follows: Section 8.1 reviews how changing boundary conditions are modelled in finite element (FE) software, i.e., by updating the geometry and introducing a geometric stiffness matrix that considers the stabilizing or de-stabilizing effects. Section 8.2 proposes two approaches to link the stiffness changes to changes in the modal parameters using the modal approach (Heylen and Sas, 1997). Ultimately, two case studies are presented in Section 8.3 for proof of concept including a prestressing tendon and a cable-stayed bridge.

8.1 Effect on System Matrices

Axial member forces and imposed deformations, intended or accidental, alter the initial condition of structures. The effect that such initial conditions have on the vibration behaviour can be modelled through an altered stiffness matrix (Bathe, 2014). If non-linear effects are considered, i.e., changes in the structure's geometry due to large displacements, rotations, or strains, the mass matrix changes as well. The goal of this section is to show how the altered stiffness and mass matrix $\mathbf{K}^*$ and $\mathbf{M}^*$ are calculated for changing boundary conditions, so the modal parameters, including

poles $\mathbf{\Omega} = \text{diag}(\lambda_1^2, \ldots, \lambda_m^2)$ and mode shapes $\mathbf{\Psi}$, can be obtained by solving the classical eigenvalue problem for proportionally damped mechanical systems

$$(\mathbf{K}^* - \mathbf{\Omega}\mathbf{M}^*)\,\mathbf{\Psi} = \mathbf{0}. \tag{8.1}$$

8.1.1 Linear Analysis (Stress Stiffening)

The starting point is the Newton equation of motion for a mechanical system with m degrees of freedom, in global coordinates, and neglecting damping. The equation includes the assembled mass and the stiffness matrices $\mathbf{M}, \mathbf{K} \in \mathbb{R}^{m \times m}$, as well as the displacement of the structure $\mathbf{u} \in \mathbb{R}^m$ and the nodal force vector $\mathbf{f} \in \mathbb{R}^m$, which only includes internal reaction forces, i.e., prestress.

$$\mathbf{M}\ddot{\mathbf{u}} + \mathbf{K}\mathbf{u} = \mathbf{f} \tag{8.2}$$

The degrees of freedom include the free degrees of freedom $\mathbf{u}_a$ and the fixed degrees of freedom $\mathbf{u}_b$ at the supports, so the total displacement vector is $\mathbf{u} = [\mathbf{u}_a^T, \mathbf{u}_b^T]^T$. Equivalently, the matrix equation can be re-formulated to (Bathe, 2014)

$$\begin{bmatrix} \mathbf{M}_{aa} & \mathbf{M}_{ab} \\ \mathbf{M}_{ba} & \mathbf{M}_{bb} \end{bmatrix} \begin{bmatrix} \ddot{\mathbf{u}}_a \\ \ddot{\mathbf{u}}_b \end{bmatrix} + \begin{bmatrix} \mathbf{K}_{aa} & \mathbf{K}_{ab} \\ \mathbf{K}_{ba} & \mathbf{K}_{bb} \end{bmatrix} \begin{bmatrix} \mathbf{u}_a \\ \mathbf{u}_b \end{bmatrix} = \begin{bmatrix} \mathbf{f}_a \\ \mathbf{f}_b \end{bmatrix}, \tag{8.3}$$

where $\mathbf{M}_{aa}$, $\mathbf{K}_{aa}$ are the components of the mass and stiffness matrices at the free degrees of freedom, which characterized the dynamic behaviour, see Eq. (8.1). Assuming a measurable, static support displacement $\mathbf{u}_b$ has occurred, i.e., the accelerations are zero at the supports with $\ddot{\mathbf{u}}_b = \mathbf{0}$, the first line can be re-formulated to $\mathbf{M}_{aa}\ddot{\mathbf{u}}_a + \mathbf{K}_{aa}\mathbf{u}_a = \mathbf{f}_a - \mathbf{K}_{ab}\mathbf{u}_b$. In other words, the effect of a permanent support deformation $\mathbf{u}_b$ on the system matrices is modelled through an equivalent force vector $-\mathbf{K}_{ab}\mathbf{u}_b$ at the free degrees of freedom (Bathe, 2014), which is added to the existing forces

$$\tilde{\mathbf{f}}_a = \mathbf{f}_a - \mathbf{K}_{ab}\mathbf{u}_b. \tag{8.4}$$

The internal forces due to imposed displacements and pre-stressing forces lead to *stress stiffening*. The stress stiffening describes the stabilizing or de-stabilizing effect that axial member forces have on the system. For example, if a tension force is applied to a single member, it tries to straighten it and counteract any lateral deformation. The effect can be considered through a *geometric stiffness* matrix (Przemieniecki, 1968) that is added to the *elastic stiffness* matrix to obtain the total stiffness

$$\mathbf{K}^* = \mathbf{K}_{el} + \mathbf{K}_{geo}(\tilde{\mathbf{f}}_a). \tag{8.5}$$

Due to the assumption of linear system behaviour, the geometric stiffness is proportional to support displacements $\mathbf{u}_b$ and changes in the prestressing forces $\mathbf{f}_a$, see Eq. (8.4). The mass matrix, on the other hand, remains unchanged with $\mathbf{M}^* = \mathbf{M}_{aa}$ because the geometry does not change. The dynamic behaviour of the pre-tensioned system can be characterized through Eq. (8.1).

8.1.2 Non-linear Analysis (Large Displacements)

Changing boundary conditions violate the condition for linear finite element analysis (Bathe, 2014). They lead to geometry changes that are not infinitesimally small (large displacements), so the mass and stiffness matrix may have to be updated to $\mathbf{M}^*, \mathbf{K}^*$ using the new element lengths. Moreover, the dynamic system cannot be solved straightforwardly because the stiffness matrix or, more precisely, the geometric stiffness matrix from Eq. (8.4) is a function of the system displacements, with $\mathbf{u}_a = \mathbf{K}_{aa}(\mathbf{u}_a)^{-1}\tilde{\mathbf{f}}_a$. A classic approach to solve for non-linear displacements is the Newton-Raphson method (Bathe, 2014). Herein, the external force is applied incrementally using a scaling factor α. In each iteration step i, a residual force vector

$$\mathbf{f}_{res} = \mathbf{f}_{int,i} - \mathbf{f}_{ext,i} \tag{8.6}$$

is set up as the difference between the external force $\mathbf{f}_{ext,i} = \alpha_i \tilde{\mathbf{f}}_a$ and internal forces $\mathbf{f}_{int,i} = \mathbf{K}_{aa}^{*-1}\mathbf{u}_{a,i}^*$ (which is zero at the beginning of the iteration), where

$$\mathbf{K}_{aa,i}^* = -\frac{\partial \mathbf{f}_{res}}{\partial \mathbf{u}_{a,i}} \tag{8.7}$$

is the tangent stiffness matrix. Next, the incremental displacement vector is solved for

$$\mathbf{\Delta u}_{a,i} = \mathbf{K}_{aa,i}^{*-1} \cdot \mathbf{f}_{res} \tag{8.8}$$

and the residual force vector from Eq. (8.6) is recalculated based on the total system displacement $\mathbf{u}_{a,i}^* = \mathbf{u}_{a,i-1}^* + \mathbf{\Delta u}_{a,i}$. The calculation steps from Eq. (8.6) to (8.8) are repeated until equilibrium is achieved, meaning until the Euclidean vector norm of the force residual $\varepsilon_f = ||\mathbf{f}_{res}||$ falls below a user threshold value of, for example, 10^{-16}. While the damage event as such is a non-linear process, the dynamic behaviour before and after it is assumed to be linear and time-invariant (LTI), with the updated system matrices $\mathbf{M}^*$ and $\mathbf{K}^*$ and the characteristic equation from Eq. (8.1). If the force is applied in one load step $\alpha = 1$, and the resulting force residual remains under the specified threshold without further iteration, a non-linear calculation was not necessary. More details on how the updated geometry changes the dynamic system matrices are given in Example 8.1.

Example 8.1. This example shows the effect that axial prestress has on a 2-D Bernoulli beam element. Figure 8.1 shows the undeformed beam in local coordinates with internal pretension force T. The material constants E and ρ are the modulus of elasticity and the mass density, and the cross-sectional parameters A and I are the area and the moment of inertia. The corresponding

mass matrix is (Chopra, 2017)

$$\mathbf{M}^l = \frac{\rho AL}{420}\begin{bmatrix} 140 & 0 & 0 & 70 & 0 & 0 \\ & 156 & 22L & 0 & 54 & -13L \\ & & 4L^2 & 0 & 13L & -3L^2 \\ & & & 140 & 0 & 0 \\ & sym. & & & 156 & -22L \\ & & & & & 4L^2 \end{bmatrix}, \tag{8.9}$$

where the total stiffness matrix is split into an elastic stiffness and a geometric stiffness $\mathbf{K}^l = \mathbf{K}^l_{el} + \mathbf{K}^l_{geo}$ with (Paultre, 2011)

$$\mathbf{K}^l_{el} = E\begin{bmatrix} \frac{A}{L} & 0 & 0 & -\frac{A}{L} & 0 & 0 \\ & \frac{12I}{L^3} & -\frac{6I}{L^2} & 0 & -\frac{12I}{L^3} & -\frac{6I}{L^2} \\ & & \frac{4I}{L} & 0 & \frac{6I}{L^2} & \frac{2I}{L} \\ & & & \frac{A}{L} & 0 & 0 \\ & sym. & & & \frac{12I}{L^3} & -\frac{6I}{L^2} \\ & & & & & \frac{4I}{L} \end{bmatrix}, \quad \mathbf{K}^l_{geo} = \frac{T}{L}\begin{bmatrix} 0 & 0 & 0 & 0 & 0 & 0 \\ & \frac{6}{5} & -\frac{L}{10} & 0 & -\frac{6}{5} & \frac{-L}{10} \\ & & \frac{2L^2}{15} & 0 & \frac{L}{10} & -\frac{L^2}{30} \\ & & & 0 & 0 & 0 \\ & sym. & & & \frac{6}{5} & \frac{L}{10} \\ & & & & & \frac{2L^2}{15} \end{bmatrix}, \tag{8.10}$$

where $T = EA \cdot \varepsilon$ is the axial tension force, $\varepsilon = (\Delta L/L)$ is the axial strain, and $\Delta L = u^l_4 - u^l_1$ is the axial elongation due to the axial beam end displacement u^l_4 and u^l_1 in local coordinates, see Fig. 8.1. On close inspection of the matrix entries of the geometric stiffness $\mathbf{K}^l_{geo}$, it can be understood that the axial tension force counteracts any lateral deformation of the beam due to beam end displacements u^l_2 and u^l_5 or rotations u^l_3 and u^l_6. The stiffness entries are proportional to the tension force, and thus, the displacements u^l_1 and u^l_4. Moreover, all three matrices ($\mathbf{K}^l_{el}$, $\mathbf{K}^l_{geo}$, and $\mathbf{M}^l$) non-linearly depend on the elongation ΔL, so non-linearities are introduced if the system geometry is updated.

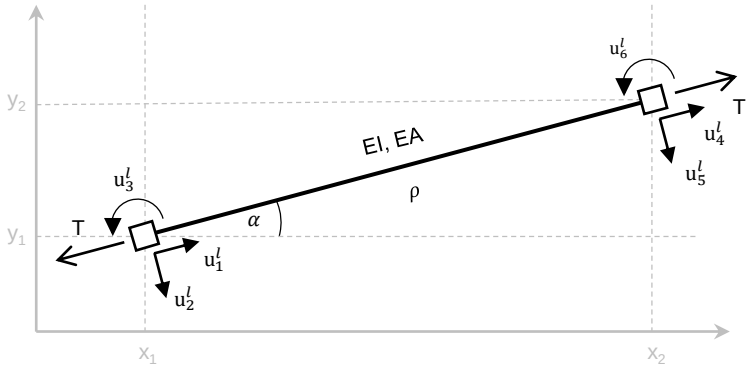

Figure 8.1: 2-D Bernoulli beam in local coordinates (undeformed)

8.2 Sensitivity Calculation

The stochastic subspace-based damage diagnosis method is data-driven, but a FE model is required to calculate the sensitivity (Jacobian $\boldsymbol{\mathcal{J}}$) that links the damage-sensitive residual to structural parameters, such as support displacements or prestressing forces with the monitoring vector

$$\boldsymbol{\theta} = \begin{bmatrix} \mathbf{f}_a \\ \mathbf{u}_b \end{bmatrix}. \tag{8.11}$$

The Jacobian computation is split into three parts: first, changes in the damage-sensitive residual are linked to data-driven modal parameters through $\boldsymbol{\mathcal{J}}^{(1)}$. Secondly, changes in data-driven modal parameters are linked to numerical modal parameters through $\boldsymbol{\mathcal{J}}^{(2)}$, and ultimately, the numerical modal parameters are linked to structural parameters through $\boldsymbol{\mathcal{J}}^{(3)}$, see Section 4.2.3. This section puts forward two approaches to modify the Jacobian matrix $\boldsymbol{\mathcal{J}}^{(3)}$ so changes in boundary conditions can be detected and localized in the same manner as other parameter changes.

8.2.1 Neglecting Geometry Changes

A simplified approach to calculate the sensitivities of poles and mode shapes to changes in boundary conditions is to consider the stress stiffening effect on the geometric stiffness matrix $\mathbf{K}_{geo}$ from Eq. (8.5), and to neglect geometry changes of the structure. To be able to monitor the system with and without initial forces, the stiffness matrix is assumed to change from its reference state $\mathbf{K}_{geo}(\theta_h^0)$ to the altered state $\mathbf{K}_{geo}(\theta_h^0 + \Delta\theta_h)$. The corresponding sensitivities can be calculated analytically using the direct sensitivity method (Heylen and Sas, 1997)

$$\begin{aligned} \frac{\partial \mu_i}{\partial \theta_h} &= -\gamma_i \boldsymbol{\Psi}_i^T \left(\mathbf{K}'_{geo,h}\right) \boldsymbol{\Psi}_i, \\ \frac{\partial \boldsymbol{\Psi}_i}{\partial \theta_h} &= \sum_{r=1, r\neq i}^{2N} \frac{1}{\mu_r - \mu_i} \gamma_r \boldsymbol{\Psi}_r^T \left(\mathbf{K}'_{geo,h}\right) \boldsymbol{\Psi}_i \boldsymbol{\Psi}_r, \end{aligned} \tag{8.12}$$

where $1/\gamma_i = \boldsymbol{\Psi}_i^T [2\mu_i \mathbf{M} + \mathbf{C}^1] \boldsymbol{\Psi}_i$ is a scaling factor for unit mass scaling and $\mathbf{K}'_{geo,h}$ is the derivative of the geometric stiffness matrix with respect to a single change $\Delta\theta_h$. Since the geometric stiffness matrix is a linear function of the axial forces (caused by a change in the boundary conditions), the derivative of the stiffness matrix can be calculated based on finite differences

$$\mathbf{K}'_{geo,h} = \frac{\mathbf{K}_{geo}(\theta_h^0 + \Delta\theta_h) - \mathbf{K}_{geo}(\theta_h^0)}{\Delta\theta_h} \tag{8.13}$$

without loss in accuracy. This approach is justified for structures where the effect of geometry changes is negligible.

8.2.2 Considering Geometry Changes

For applications, where the geometry changes cannot be neglected, the change in the boundary conditions causes non-linear changes in both the global stiffness and the mass matrix from Eq. (8.2), see Example 8.1. Consequently, the derivatives can be approximated through (Heylen and Sas, 1997)

$$\begin{aligned}\frac{\partial \mu_i}{\partial \theta_h} &= -\gamma_i \boldsymbol{\Psi}_i^T \left(\mu_i^2 \mathbf{M}_h' + \mathbf{K}_h'\right) \boldsymbol{\Psi}_i, \\ \frac{\partial \boldsymbol{\Psi}_i}{\partial \theta_h} &= -\frac{1}{2}\gamma_i \boldsymbol{\Psi}_i^T \left(2\mu_i \mathbf{M}_h'\right) \boldsymbol{\Psi}_i \boldsymbol{\Psi}_i \\ &\quad + \sum_{r=1, r\neq i}^{2N} \frac{1}{\mu_r - \mu_i} \gamma_r \boldsymbol{\Psi}_r^T \left(\mu_i^2 \mathbf{M}_h' + \mathbf{K}_h'\right) \boldsymbol{\Psi}_i \boldsymbol{\Psi}_r,\end{aligned} \tag{8.14}$$

where $1/\gamma_i = \boldsymbol{\Psi}_i^T [2\mu_i \mathbf{M} + \mathbf{C}^1] \boldsymbol{\Psi}_i$ is a scaling factor for unit mass scaling and $\mathbf{M}_h'$ and $\mathbf{K}_h'$ are the first derivatives of the mass matrix and the stiffness matrix with respect to a change in the boundary conditions $\Delta\theta_h$ with the finite differences

$$\mathbf{M}_h' = \frac{\mathbf{M}(\theta_h^0 + \Delta\theta_h) - \mathbf{M}(\theta_h^0)}{\Delta\theta_h}, \qquad \mathbf{K}_h' = \frac{\mathbf{K}(\theta_h^0 + \Delta\theta_h) - \mathbf{K}(\theta_h^0)}{\Delta\theta_h}. \tag{8.15}$$

The accuracy now depends on the change magnitude $\Delta\theta_h$, because the derivatives of the mass and stiffness matrix non-linearly depend on the element length. The advantage of both approaches is that they are compatible with the output from standard FE software, where the stiffness matrix can be exported but the analytical derivatives are not available.

8.2.3 Discussion

The first approach to calculating the sensitivities is obviously an approximation, because geometry changes are neglected, see Section 8.2.1. However, the second approach from Section 8.2.2 is also an approximation that is accurate if the change magnitude is chosen sufficiently small. For academic purposes and simple structures, it might be tempting to replace the finite differences from Eq. (8.15) with the analytical derivatives of the mass and stiffness matrix $\mathbf{M}_h' = \frac{\partial}{\partial \theta_h}\mathbf{M}(\theta_h)$ and $\mathbf{K}_h' = \frac{\partial}{\partial \theta_h}\mathbf{K}(\theta_h)$. A major problem with this, however, is that the coordinate transformation, which takes the mass and stiffness matrices from the local to the global coordinate system, also depends on the displacements in $\mathbf{u}$. This complicates the analytical derivatives to an extent that makes the computation unreasonable.

8.3 Proof of Concept

For proof of concept, two numerical case studies are presented in the following, showcasing that changes in the support conditions and in prestressing forces can be detected and localized.

8.3.1 Pre-stressing Tendon

The first case study is a 35 m long metal string clamped on both sides, see Fig. 8.2. This could be a cable or prestressing tendon. It exhibits a circular solid cross-section with a modulus of elasticity of $E = 160,000$ MPa and a mass density of $\rho = 7,800\ kg/m^3$. Using custom-made FE code, the string is modelled in MATLAB® and divided into eight nodes with six degrees of freedom at each node and seven three-dimensional Bernoulli beam elements. Damage is defined as a support displacement on the right side of the tendon or a decrease in the material stiffness in any element with the monitoring vector

$$\boldsymbol{\theta} = \begin{bmatrix} \mathrm{E}_1 & E_2 & E_3 & E_4 & E_5 & E_6 & E_7 & u \end{bmatrix}^T. \tag{8.16}$$

The placement of the three uni-axial sensors is visualized in Fig. 8.2, sampling velocity data in vertical direction at a frequency of 150 Hz. The numerical modal analysis is summarized in Fig. 8.3, including natural frequencies, mode shapes, and damping ratios. The power spectral density (PSD) is shown as well, although it is not used for the subsequent damage diagnosis. For the sensitivity computation, all observable modes of vibration are used. The reliability requirements are based on a probability of false alarms (PFA) of 5% and a probability of detection (POD) of 99.4% (refer to Section 5.1.3). For conciseness, all other input parameters are summarized in Table 8.1. As shown in the table, the measurement duration during testing is set to 10 s.

Study 1: Support Displacement (Neglecting Geometry Changes)

In the first study, the sensitivity is computed based on the stress stiffening effect on the stiffness matrix, see Section 8.2.1, and geometry changes are neglected. The objective is to validate the Jacobian approximation by predicting the minimum localizable damage for the minmax localization test and verifying it through Monte Carlo simulations.

As explained in Section 5.4.1, the damage diagnosis procedure is divided into three states, i.e., the reference state, the training state, and the validation state. At the end of the training state, the minimum localizable damage is predicted based on vibration data from the reference structure. Following the method introduced in Chapter 6, the minimum localizable support displacement is predicted to be $\Delta\theta_8 = 6.9\ cm$. For conciseness, only the validation state is summarized here, where vibration data is generated after displacing the support by the minimum localizable amount. The

Data		**Segmenting**		**Processing**	
Measured quantity	velocity	Training segments	100	No. of sensors	r/r_0=3/3
Sampling frequency	150 Hz	Testing segments	100	Time lags	p/q=6/7
Reference data length	16.7 min	Samples/segment	1,500	System order	n=16
Training/testing data	16.7 min	Duration/segment	10 s	No. of blocks	n_b=2,000

Table 8.1: Input parameter sheet

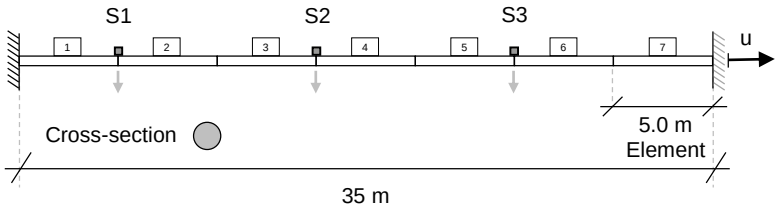

Figure 8.2: Metal string with sensors S1 - S3 and support displacements u

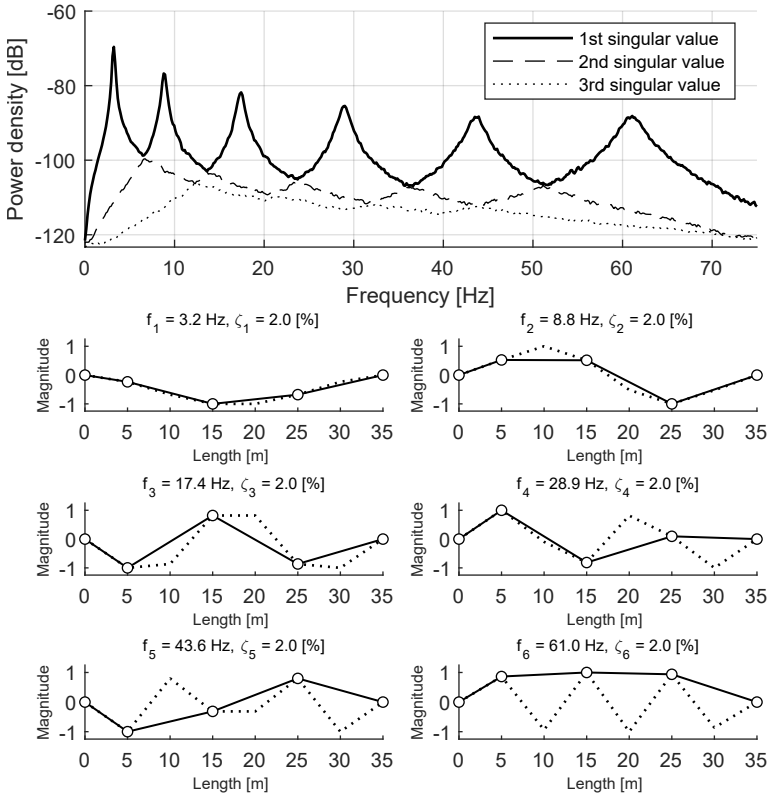

Figure 8.3: Numerical mode shapes and power spectral density of the generated signal

record is split up into 100 data segments of 10 s length, and the minmax localization test is applied to each segment in a Monte Carlo experiment, with the empirical test distributions being visualized in Fig. 8.4. The support displacement can be localized, as the test distribution for parameter θ_8 exceeds the safety threshold value and other parameters $\theta_1 - \theta_7$ do not show a significant test response. The mean value of the empirical distribution is close to the predicted one (solid black lines) and the empirical probability of detection is 99%, which is close to the theoretical value of 99.4%. In other words, a support displacement can be distinguished from other damage scenarios, and the sensitivity calculation presented in this chapter leads to an accurate prediction of the minimum localizable damage.

To investigate the limitations of the sensitivity approximation, the predictions based on the Jacobian matrix are compared to the actual behaviour of the structure. The Jacobian $\boldsymbol{\mathcal{J}}^{(3)}$ links

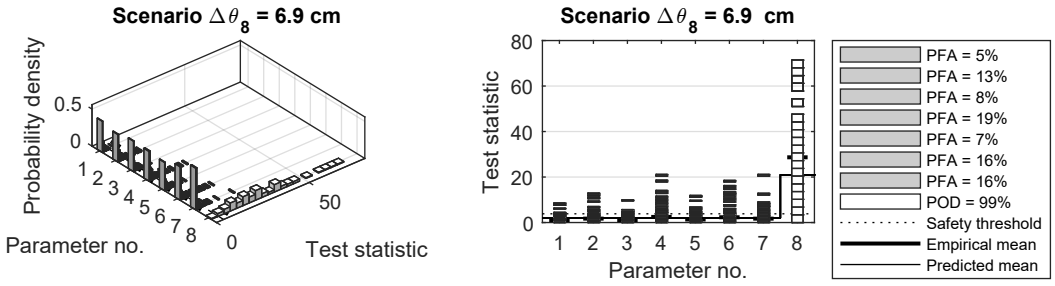

Figure 8.4: Validation of the prediction for the minmax localization test

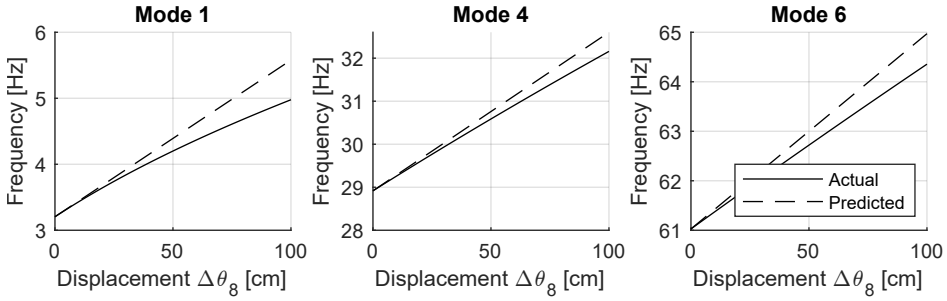

Figure 8.5: Validating the Jacobian approximation

changes in structural parameters to changes in modal parameters, so modal parameter changes can be approximated if the parameter changes are known through $\boldsymbol{\eta} = \boldsymbol{\mathcal{J}}^{(3)}\boldsymbol{\theta}$ (refer to Section 10.4.1). A suitable way to visualize the approximation is to re-combine the entries in the modal vector $\boldsymbol{\eta}$ that correspond to the poles of the system, and to derive the corresponding natural frequencies. Figure 8.5 shows the change of the natural frequencies of Mode 1, 4, and 6 over a support settlement $\Delta\theta_8$. Up to a support displacement of 20 cm, the Jacobian appears to yield an accurate approximation. Beyond 20 cm damage localization is still possible, but the prediction becomes inaccurate. This study suffices to prove that the Jacobian matrix is correct. More information on the limitation of the entire Jacobian matrix $\boldsymbol{\mathcal{J}} = \boldsymbol{\mathcal{J}}^{(1)}\boldsymbol{\mathcal{J}}^{(2)}\boldsymbol{\mathcal{J}}^{(3)}$ is given in Section 10.4.

Study 2: Support Displacement (Considering Geometry Changes)

In the second study, the sensitivity is computed based on the changes in the mass and stiffness matrices, see Section 8.2.2, while considering geometry changes. This approach is more sophisticated, but the prediction of the minimum localizable damage for the minmax localization test is identical with $\Delta\theta_8 = 6.9$ cm, see Fig. 8.6. The probability of detection is 98%, so the prediction of the minimum localizable damage is accurate. Comparing the approximated frequencies to the actually measured frequencies over an increasing support displacement reveals that the Jacobian becomes inaccurate for displacement of more than 20 cm, see Fig. 8.7. Consequently, the approach is not more accurate than for the simplified approach from the previous section that neglected geometry changes for the considered structure.

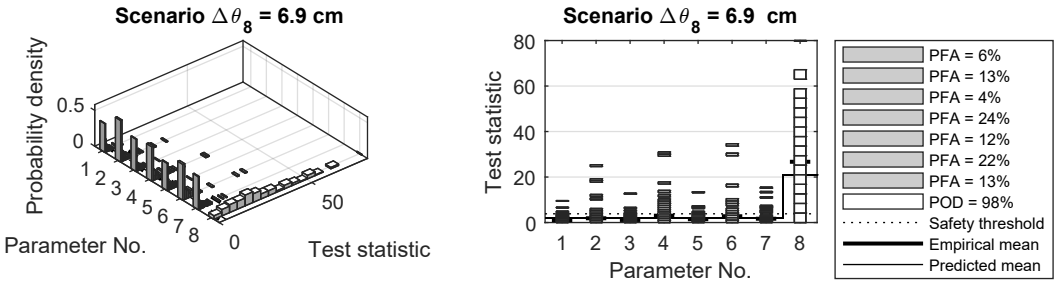

Figure 8.6: Validation of the prediction for the minmax localization test

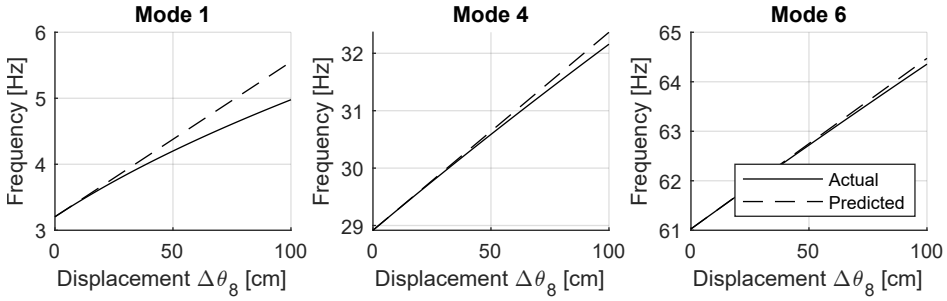

Figure 8.7: Validating the Jacobian approximation

Study 3: Loss in Pretension

The third study assumes that the structure is pretensioned through an initial displacement of $u_0 = 10$ cm, and the goal is to localize a loss in pretension due to a relaxation of the support. The minmax localization test is applied for damage localization and the sensitivity is calculated considering geometry changes, see Section 8.2.2. The initial support displacement leads to an axial tension force of 898 kN and increases the geometric stiffness, quantified through the natural frequencies, which increase to 3.4 Hz, 9.2 Hz, 17.7 Hz, 29.3 Hz, 44.0 Hz, and 61.4 Hz, cf. Fig. 8.3. Using the same diagnosis procedure, the algorithm is now trained based on the pretensioned structure, and the minimum detectable support displacement is predicted to be $\Delta\theta_8 = -7.4$ cm. Then, the support is relaxed by 7.4 cm and a Monte Carlo damage diagnosis is run. The validation plot in Figure 8.8 shows that the support displacement can be localized with a POD of 98%, so the Jacobian calculation is validated. Another way to pretension the tendon is to directly define a pretension force, but this is demonstrated in the following section for a cable-stayed bridge.

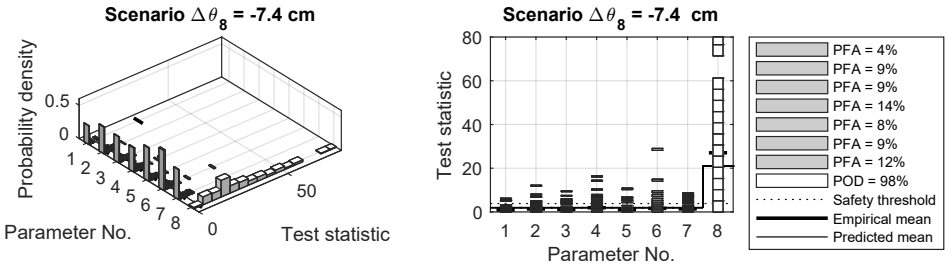

Figure 8.8: Validation of the prediction for the minmax localization test

8.3.2 Cable-stayed Bridge

The second proof of concept study is a schematic 2-D model of a cable-stayed bridge, see Fig. 8.9. The design is inspired by the Shipshaw Bridge in Canada, which attracted the attention of the engineering community, as a tie-down anchor ruptured during the 1988 Saguenay earthquake and remained undiscovered for three years (Filiatrault et al., 1993). The objective of this study is to show that an uplift of the support can be localized for cable-stayed bridges. Other considered damage scenarios include a rotation of the tower foundation, and a loss in pretension in one of three cables. The experimental setup has already been described in Section 7.4.2. However, in contrast to previous studies, the cables are now pretensioned with 300 kN each. Moreover, different input parameter are used for signal processing (see Table 8.2).

Study 1: Support Settlements

In the first analysis, damage is defined as a abutment settlement at the tie-down rod or a rotation of the tower foundation. To prove that damage can be detected and distinguished from other damage scenarios, the material stiffness of the six deck elements are also defined as monitoring parameters. Hence, the monitoring vector is defined as

$$\boldsymbol{\theta} = \begin{bmatrix} E_1 & E_2 & E_3 & E_4 & E_5 & E_6 & u & \varphi \end{bmatrix}^T. \tag{8.17}$$

As explained in Section 5.4.1 and Chapter 6, the algorithm is trained based on vibration data from the reference structure, and the minimum localizable support settlement and tower tilt are predicted to be 2.0 cm and 0.2°. To validate the predictions, two different validation runs are performed. In the first one, the abutment settlement is set to the minimum detectable value of $\theta_7 = 2.0$ cm, so internal stresses build up. Subsequently, 100 data segments of 300 s length are generated in the damaged state, while applying the minmax localization test to each segment. The resulting distributions of the test statistic for each monitoring parameter, plotted on the left side of Fig. 8.11, show that the settlement can be localized. Since the distribution mean value is close to the predicted mean value, and the empirical POD of 99% is close to the theoretical one of 99.94%, the prediction based on the sensitivity matrix is accurate. Repeating the validation for a tower tilt of $\theta_8 = 0.2°$, which corresponds to a lateral displacement on top of the tower by 5.24 cm, yields similar results with a mean value close to the predicted one and a POD of 99%, see right plot in Fig. 8.11.

Data		**Segmenting**		**Processsing**	
Measured quantity	velocity	Training segments	100	No. of sensors	r/r_0=6/6
Sampling frequency	20 Hz	Testing segments	100	Time lags	p/q=3/4
Reference data length	500 min	Samples/segment	6,000	System order	n=16
Training/testing data	500 min	Duration/segment	5 min	No. of blocks	n_b=2,000

Table 8.2: Input parameter sheet

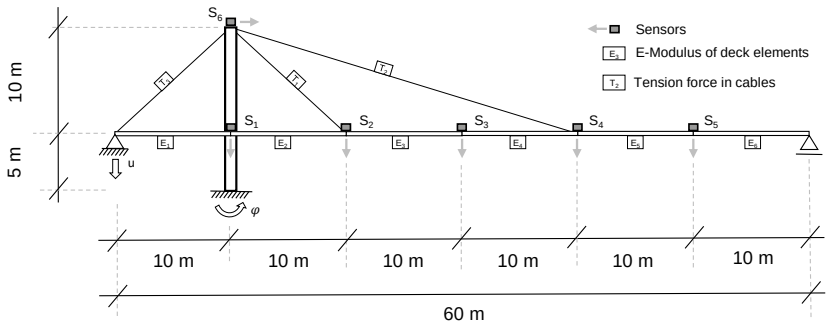

Figure 8.9: Schematic cable stayed bridge with six sensors

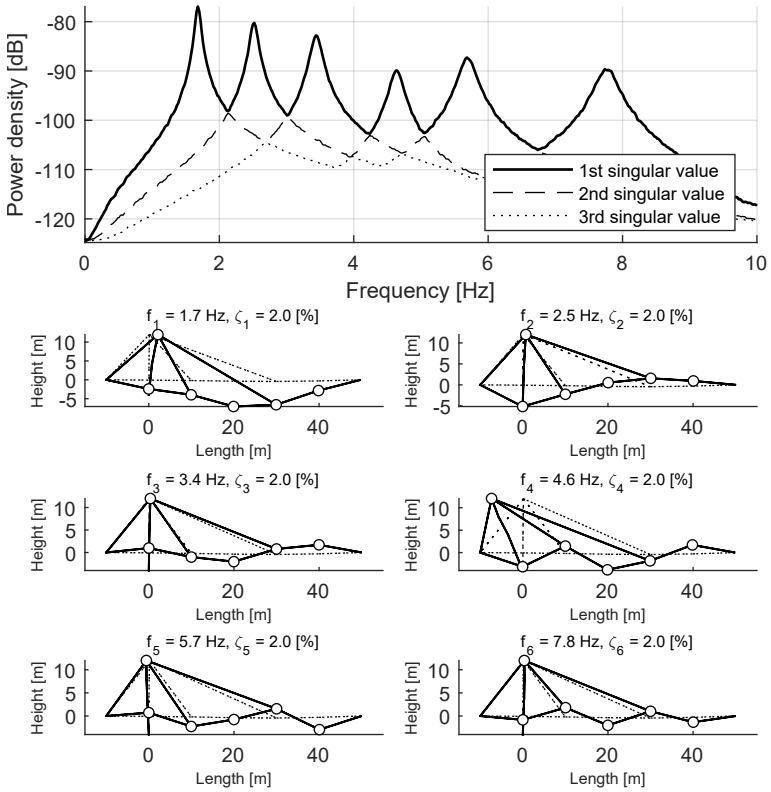

Figure 8.10: Modes of vibration

Ultimately, the limitations of the Jacobian matrix $\boldsymbol{\mathcal{J}}^{(3)}$ are visualized by plotting the natural frequencies of Mode 4, 5, and 6 over the displacement θ_7 and the rotation θ_8, respectively, see Fig. 8.12. The other modes are not plotted because their mode numbers within the FE model changes. This plot clarifies that the prestressed system behaves non-linearly; however, the predicted values for the support displacements and rotation are small enough, so a linearization is justifiable, in particular, if the goal is to detect and localize small changes.

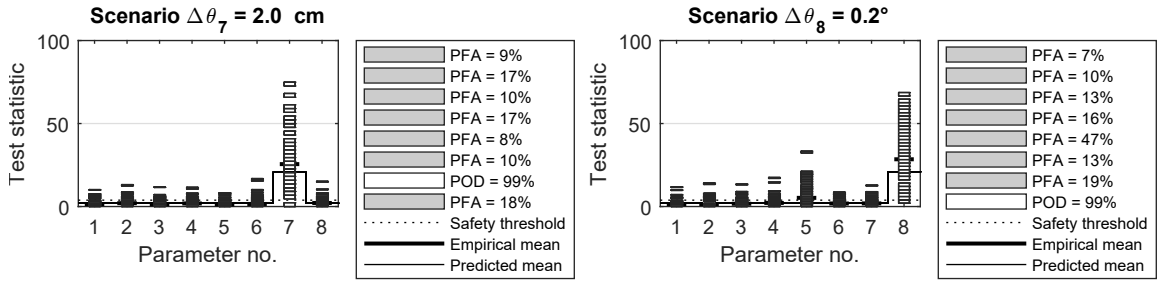

Figure 8.11: Localization of abutment settlement (left) and tower tilt (right)

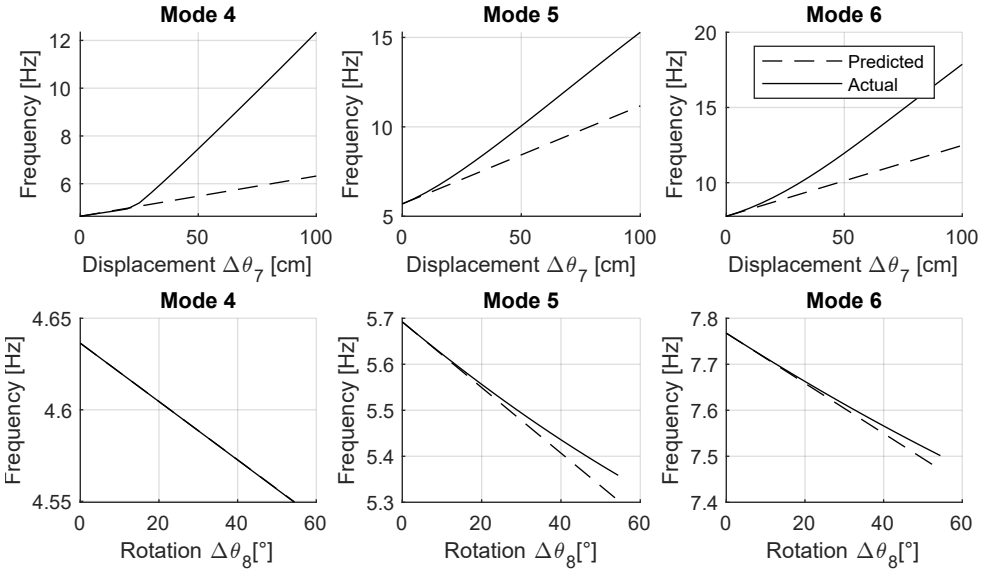

Figure 8.12: Validating the Jacobian approximation

Study 2: Loss of Cable Prestress

In this second analysis, damage is defined as a loss in pretension in one of the three cables T_1, T_2, or T_3, see Fig. 8.9, or any of the stiffness values of the deck. Therefore, the parameter vector for monitoring is re-defined as

$$\boldsymbol{\theta} = \begin{bmatrix} E_1 & E_2 & E_3 & E_4 & E_5 & E_6 & T_1 & T_2 & T_3 \end{bmatrix}^T, \tag{8.18}$$

where the initial cable prestress is 300 kN. Based on the automated substructuring approach, the structure is divided into eight substructures where the monitoring parameters T2 and T3 are combined into one cluster. Subsequently, the minimum localizable damage is predicted to be $\Delta\theta_7 = 34.3\%$, $\Delta\theta_8 = 4.9\%$, and $\Delta\theta_9 = 11.5\%$. The three validation runs are summarized in Fig. 8.13. The predicted mean values of the damaged state test distributions are close to the theoretical ones with PODs of 97%, 100%, and 100%. This concludes the proof of concept studies.

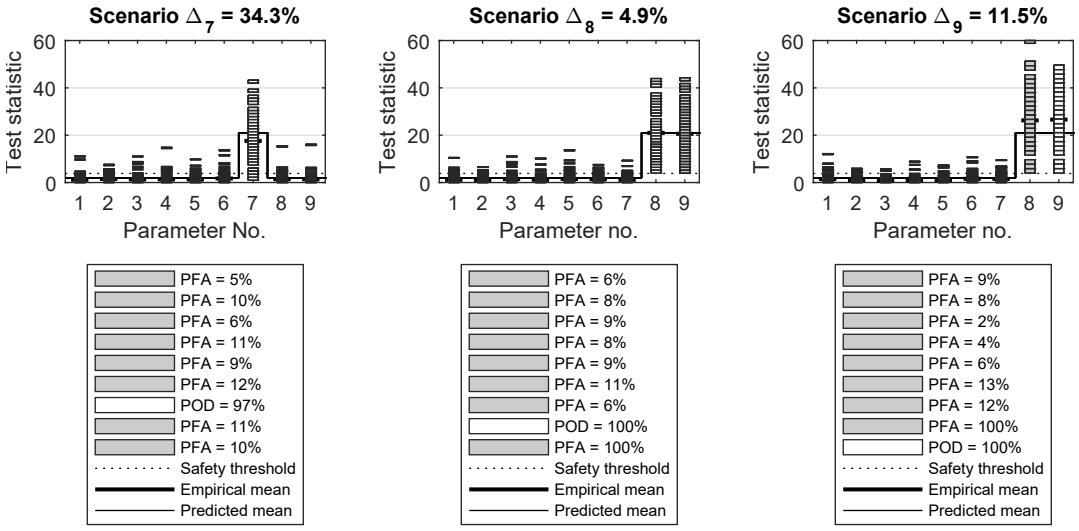

Figure 8.13: Localization of a loss in pretension in cables T_1, T_2, and T_3

8.4 Summary

This chapter develops a method to monitor support deformations and changes in prestressing forces based on the geometric stiffness matrix, i.e., the stabilizing or destabilizing effect that large deformations have on the stiffness of the structure. The method can be incorporated into the framework of the asymptotic local (AL) approach, meaning it is possible to detect and localize support displacements and to predict the minimum detectable or localizable damage as explained in the preceding chapters. The main difference is that the Jacobian matrix, which links modal parameters to structural design parameters, is modified. For proof of concept, the method is applied to a prestressing tendon and a schematic model of a cable-stayed bridge. The localization results confirm that, although the support displacements change the stiffness in the entire structural system, they can be distinguished from local structural changes, e.g., a degradation of material properties of individual structural components. The results are encouraging, as the prediction of the minimum localizable damage appears to be sufficiently accurate despite the first-order approximation for small changes in the boundary conditions.

Part III

APPLICATIONS

Chapter 9

Experimental Case Studies

This chapter presents two case studies, including a laboratory steel beam on pin supports and a laboratory model of the St. Nazaire Bridge in France. The primary goal is to apply the statistical tests for damage detection and localization and to prove that the prediction of the test response and false alarms is accurate and robust, even for real structures in noisy vibration environments.

Acquiring real damage-corrupted data is a major challenge of damage detection and localization research, in particular for bridge health monitoring. Bridges are vital links in primary infrastructure and damaging them for research purposes can only be justified after exceeding their life expectancy. One approach to remedying this problem is to build laboratory prototypes, such as the model of the St. Nazaire Bridge, and to perform validation studies for anticipated damage scenarios (see Section 9.2). However, no bridge and no site are identical, and training the algorithm is a structure-specific task, so findings from one study cannot straightforwardly be transferred to another. Another avenue of research is to develop non-destructive validation methods, for example, based on extra masses (Mottershead, 2001; Kim and Bartkowicz, 2001; Papatheou et al., 2010). The application of non-structural masses modifies the dynamic properties of the structure, so they can be sensed by the damage diagnosis module. This way, it can be verified whether the theoretical assumptions are fulfilled and whether all input parameters for signal processing are set appropriately, without having to damage the structure. This second approach is taken for the case study with the hollow structural steel (HSS) beam (see Section 9.1).

9.1 HSS Beam (104 DOF)

The main objective of this study is to confirm that the prediction of the minimum diagnosable damage is valid for real structures in noisy measurement environments. The case study is subdivided into four objectives:

- *Objective 1*: Demonstrate that the prediction of the minimum diagnosable damage is valid for real data and both the model-based and data-driven detection tests (Section 9.1.2)
- *Objective 2*: Confirm that the prediction for the minimum localizable damage is correct and that false alarms can be predicted as well (Section 9.1.3)
- *Objective 3*: Validate that the sensor layout with the strongest test response has the shortest predicted measurement duration (Section 9.1.4)

- *Objective 4*: Define damage as a change in mass and show that the application of extra masses is a suitable, non-invasive validation technique to verify that the algorithm has been implemented correctly

9.1.1 Experimental Setup

Beam Description. The specimen is a 4.11 m laboratory steel beam with a HSS cross-section, HSS 152×51×4.78 mm (6 x 2 x 3/16 inches), a modulus of elasticity of $E = 210{,}000$ MPa, and a total measured mass of $m = 56.8$ kg. The beam is supported by two pin supports and bent about the weak axis, see Fig. 9.1 and 9.2. This laboratory beam is identical to the numerical beam that is used for the proof of concept studies in all chapters.

Instrumentation and Signal Processing. The beam is instrumented with one shaker and eight vibration sensors. The shaker has a total mass of 3.6 kg and a moving mass of 360 g. It is placed on top of beam segment 2, injecting white noise signals vertically into the beam, see Fig. 9.2. The eight sensors are equally spaced at 46 cm, with a weight of 1.28 kg each. Wireless seismic sensors (Tromino Tromographs) are used, and synchronized through radio communication. The sensor choice allows for different data quantities to be analyzed, as each sensor module records accelerometers, high-gain velocimeters, and low-gain velocimeters in all three dimensions. Having said that, only vertical acceleration measurements are considered in this study. They are originally sampled at 512 Hz and later down-sampled to 330 Hz using a linear interpolation method (Akima H., 1970). Furthermore, a high-pass filter is applied to attenuate signal components below 4 Hz. Additional signal processing parameters are summarized in Table 9.1.

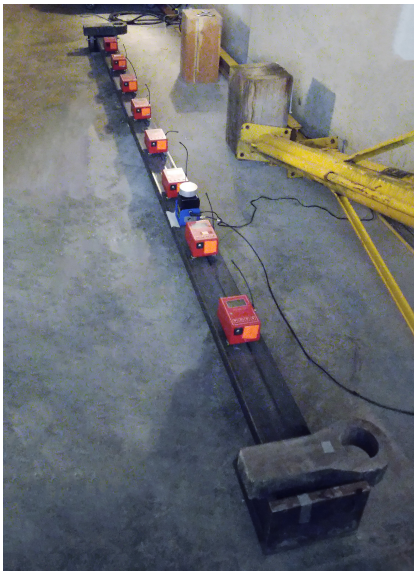

(a) Instrumentation

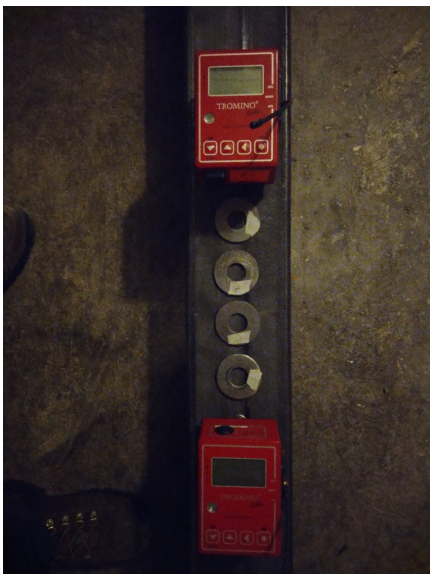

(b) Extra mass on Segment 5

Figure 9.1: Laboratory HSS steel beam on pin supports

Damage Scenarios. Structural damage is defined as a change in mass, and during the experiment, the mass of individual beam segments is increased by 5% for damage detection studies, and 10% for damage localization studies by adding extra masses, see Fig. 9.1b. The two examined damage scenarios are an extra mass at midspan (Segment 5) and an extra mass close to the support (Segment 8), see Fig. 9.9. To validate whether the predictions are accurate, the damage is set to the applied damage and the measurement time T is adjusted, so the empirical test response is equal to the predicted one, and the empirical probability of detection (POD) is identical to the theoretical one that is used for predicting the measurement duration.

Finite Element Model. The damage diagnosis test is data-driven, but a finite element model is required to parametrize damage and to calculate the sensitivity matrix (Jacobian $\boldsymbol{\mathcal{J}}^{(3)}$) of the damage-sensitive residual toward mass changes in the beam. Using ANSYS®, the beam is discretized into 19 nodes with six degrees of freedom (DOF) at each node, and 18 finite beam elements (BEAM188 with linear shape functions). At the supports, all DOF are restrained except the rotation about the transverse bolt, reducing the number of degrees of freedom to 104. Nine components are defined by assigning the same material to two consecutive beam elements. Since damage is defined as a change in mass, the monitoring vector is

$$\boldsymbol{\theta} = \begin{bmatrix} m_1 & \dots & m_9 \end{bmatrix}^T. \tag{9.1}$$

To link changes in structural masses to the damage-sensitive residual, the structural masses have to be linked to changes in modal parameters first. The considered modal parameters are the poles and mode shapes of the first four modes of vibration at the sensor locations P1, P2, P7, and P8, which are visualized in Fig. 9.4, and all other modes are disregarded. The damping ratio is set to 1.0% critical damping for simplicity. The finite element (FE) model also considers the weight of the instrumentation as point loads.

9.1.2 Detecting Mass Changes

Study 1: Model-based Detection

In the first study, the parametric version of the damage detection test from Eq. (4.49) is applied, where the damage-sensitive residual is linked to model-based masses in the monitoring vector from Eq. (9.1) through the Jacobian matrix $\boldsymbol{\mathcal{J}}$. As usual, the damage diagnosis procedure is split into three states: the reference state, the training state, and the validation state.

Reference State. In the reference state, all matrices are set up based on a 110 min long vibration record measured on the undamaged structure. First, the block Hankel matrix is computed and the null space is extracted. This requires the definition of the time lag parameters $p = 12$ and $q = 13$, as well as the system order $n = 16$. Using singular value decomposition (SVD), the block Hankel matrix is decomposed into its subspace, and the left null space is extracted, with the

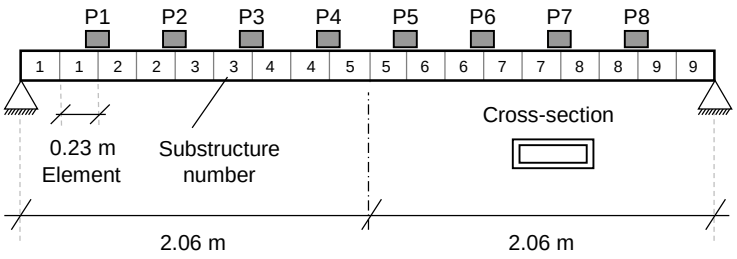

Figure 9.2: Numerical HSS beam with eight sensor locations P1 - P8

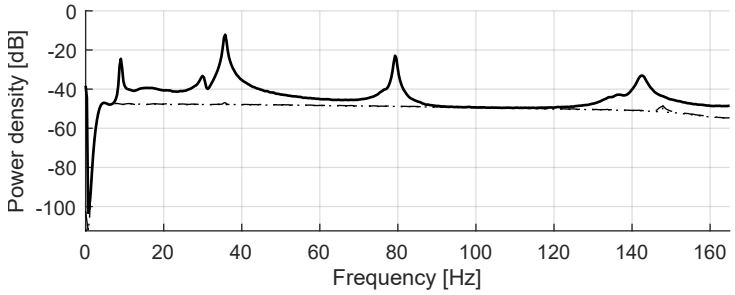

Figure 9.3: Experimental power spectral density from eight sensors

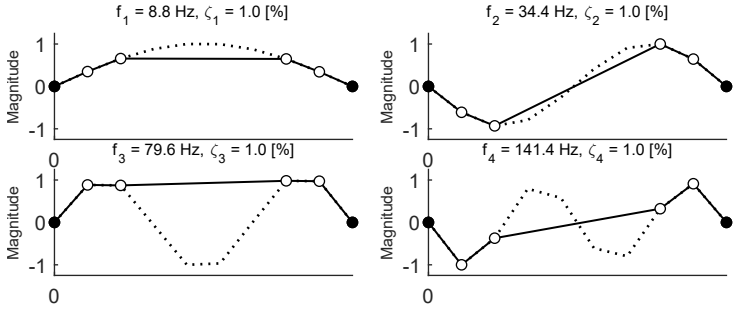

Figure 9.4: Numerical modal analysis with four sensors at P1, P2, P7, and P8

singular values being visualized in Fig. 9.5. The first eight singular values correspond to structural information followed by a clear jump that indicates the transition to noise modes. Ultimately, the covariance matrix and the sensitivity matrix are computed and combined to the Fisher information, see Fig. 9.7. The structure's geometry is symmetrical, and so is the Jacobian matrix. However, the main diagonal values of the Fisher information are not symmetrical because of the varying excitation characteristics along the beam (the shaker is placed on one side), which is considered through the covariance matrix. This clarifies that the Fisher information considers the signal-to-noise ratio.

Training State. The training is based on vibration data from the reference structure. For brevity, the workflow is visualized in Fig. 9.8 and summarized in the following list:

- *Step 1:* Fix the measurement duration to a sufficiently large value. Divide the record into 100 data sets, apply the damage detection test to each segment in a Monte Carlo experiment, and plot the histogram of the test distribution.

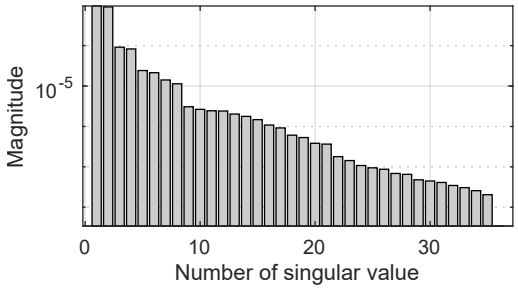

Figure 9.5: Block Hankel singular values

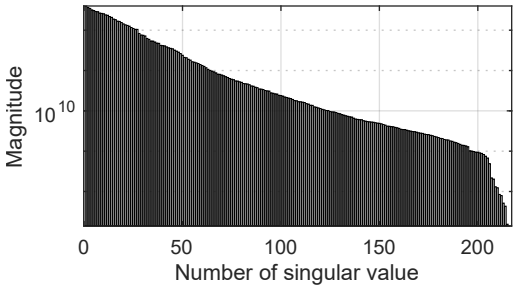

Figure 9.6: Covariance singular values

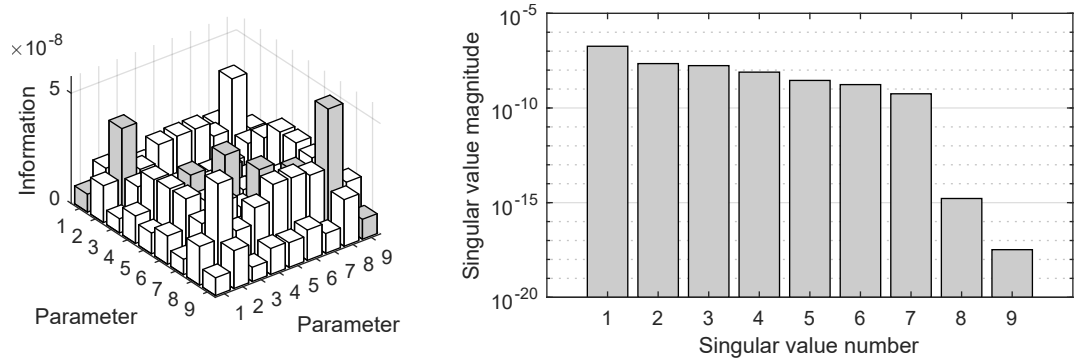

Figure 9.7: Fisher information matrix and its singular values

- *Step 2:* Fit a central χ^2-distribution to the histogram to verify that the number of degrees of freedom of the training distribution is equal to the theoretical value of $\nu = \text{rank}(\boldsymbol{\mathcal{J}}^T \boldsymbol{\Sigma}^{-1} \boldsymbol{\mathcal{J}})$, see Eq. (5.4). Based on the fitted distribution and an acceptable probability of false alarms (PFA), set the safety threshold value.

- *Step 3:* Determine the reliability index λ_{min} by increasing the non-centrality of the χ^2-distribution until the area under the probability density function (PDF) and beyond the safety threshold is equal to the desired POD for $\lambda = \lambda_{min}$. Set the damage in the considered parameter to the applied 5% damage, and calculate the corresponding minimum measurement duration T_h. Use this measurement duration for the entire structure, and continue with the validation state.

Data		**Segmenting**		**Processing**	
Measured quantity	acceleration	Training segments	100	No. of sensors	r/r_0=4/4
Sampling frequency	330 Hz	Testing segments	100	Time lags	varying
Reference data length	110 min	Samples/segment	varying	System order	varying
Training/testing data	varying	Duration/segment	varying	No. of blocks	varying

Table 9.1: Input parameter sheet for detection

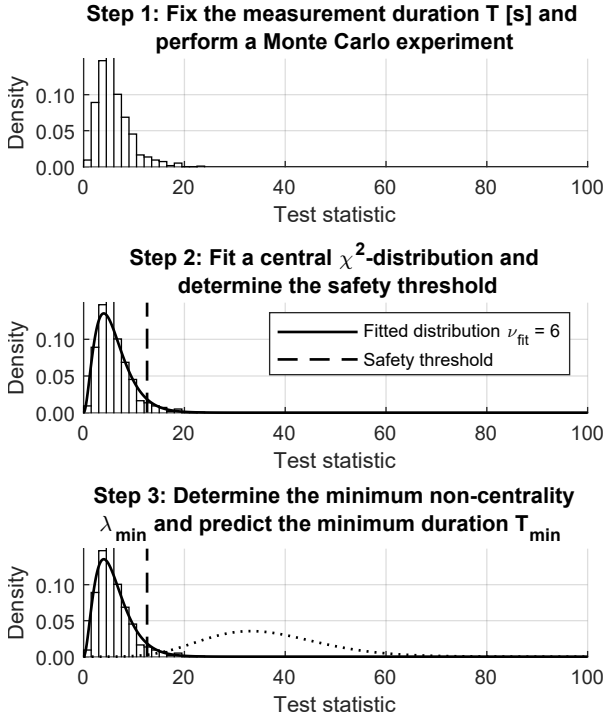

Figure 9.8: Training procedure to determine the minimum measurement duration

Validation State. The validation state is based on vibration data from the damaged structure, recorded after the extra mass of 5% is applied. Again, the vibration record is divided into 100 segments while applying the damage detection test to each segment in a Monte Carlo experiment. Finally, the number of data points beyond the safety threshold is counted and put into relation to the number of data segments—this yields the empirical POD which should be close to the required POD of 99.4% from the prediction.

The entire monitoring procedure, including training and testing, can be summarized in one plot that visualizes the test distribution in the training and damaged states, see Fig. 9.10. The top plot of Fig. 9.10a shows the empirical distributions for the model-based detection test, with an extra mass at beam segment 8. The three decisive quantities are the number of degrees of freedom, the measurement duration, and the empirical POD, which are analyzed separately in the following.

- Fitting the χ^2-distribution to the histogram results in a number of degrees of freedom of six, which is close to the theoretical value of $\nu = \text{rank}(\boldsymbol{\mathcal{J}}^T\boldsymbol{\Sigma}^{-1}\boldsymbol{\mathcal{J}}) = 7$. Both numbers are smaller than the number of monitoring parameters, so the sensitivity matrix (the Jacobian $\boldsymbol{\mathcal{J}}$) is not of full rank, see Fig. 9.7. This demonstrates that column-rank deficiency is a common problem, even for simple monitoring tasks such as the HSS beam, and highlights the importance of the numerical considerations for rank-deficient Jacobian matrices (from Section 5.3).

- The measurement duration to detect a 5% mass increase is $T = 7$ s. Such a short duration is uncommon for ambient vibration tests and only feasible because the damage detection test

circumvents a data-driven modal analysis. The information on modal parameters is included in the sensitivity matrix, which is set up in the reference state. For statistical evaluation of the test performance (and an accurate approximation of the POD), the test is applied to 100 data segments, increasing the measurement duration of the entire data set to about 12 min. However, this is only necessary for validation purposes.

- The empirical POD of 94% is close to the theoretical value of 99.4%, so the test distribution in the damaged state approximates the theoretical χ^2-distribution. Considering the inaccuracies due to sampling a χ^2-distribution and possible modelling issues, the validation is considered successful.

The top plot of Fig. 9.10b shows the validation for the damage scenario with an extra mass at beam segment 5 (at midspan).

- With an empirical POD of 95%, the prediction of the minimum detectable damage can be confirmed. That means that the prediction is accurate for multiple beam segments along the beam.

- However, a longer measurement duration of $T = 13$ s is required to detect a 5% mass change in Parameter 5 compared to Parameter 8. This is due to a lower Fisher information value F_{55} compared to F_{88} (see Fig. 9.7) and showcases that the main diagonal of the Fisher information is a measure for the detectability of damage. Moreover, it shows that the measurement duration is an appropriate tuning parameter to increase the test response to damage in parameters with low damage detectability.

- The number of degrees of freedom of the χ^2-distribution is close with $\nu = 7$ instead of $\nu = 6$ despite the longer measurement duration. Therefore, an increased measurement does not alter the test distribution in the training state of the model-based test. This verifies the statistical properties of the parametric test distribution and confirms that the number of degrees of freedom is an application-specific quantity that describes the complexity of the problem. This completes the validation of the model-based damage detection test.

Study 2: Data-driven Tests

In the second study, the minimum measurement duration is predicted for data-driven tests. Two data-driven tests are available, namely, the non-parametric test from Eq. (4.51) and a parametric one from Eq. (4.50), where the damage-sensitive residual is linked to modal parameters. Regardless of the employed damage detection test, the Fisher information is calculated based on the FE model, as this is required to physically define (or parametrize) damage. Although the same Fisher information is used for the prediction, the damage detectability changes because the number of degrees of freedom of the χ^2-distributions depends on the number of monitoring parameters, which is different for each test.

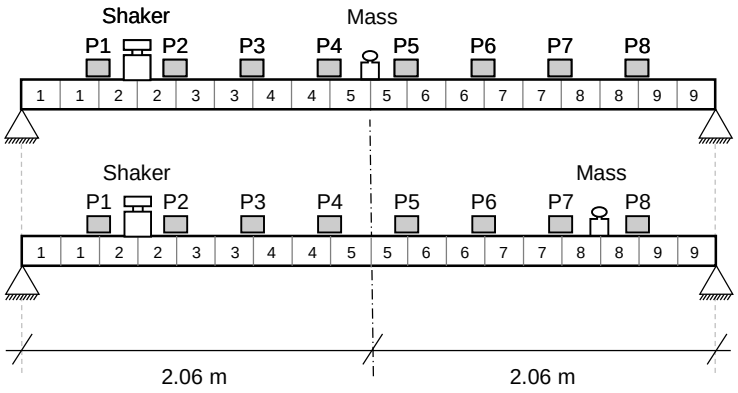

Figure 9.9: Damage scenarios with extra masses

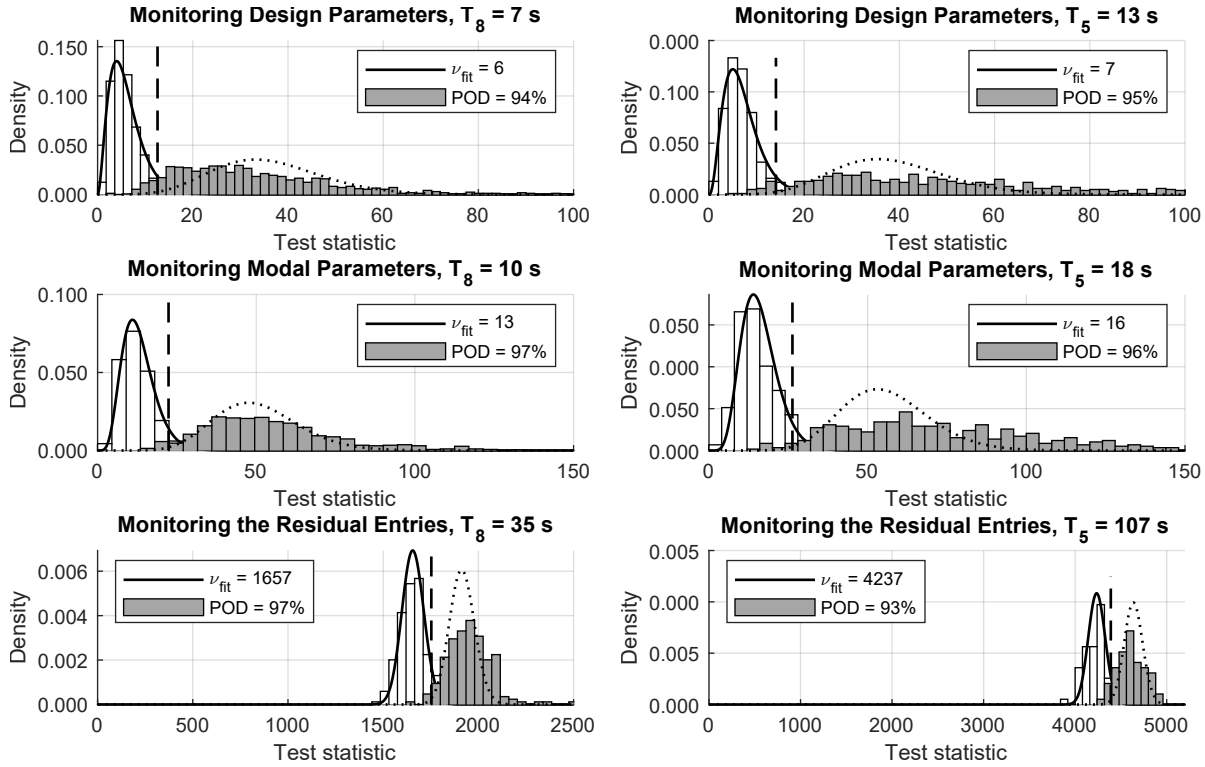

(a) Extra mass on Segment 8

(b) Extra mass on Segment 5

Figure 9.10: Validating the prediction for the damage detection tests

a) Validating the Parametric Test. This section focuses on the data-driven detection test that is linked to modal parameters. The training and validation state is shown in the same figure as for the model-based test, where the first analysis is performed for the damage scenario with an extra mass on beam segment 8 (centre plot of Fig. 9.10a).

- The number of degrees of freedom of the fitted χ^2-distribution is $\nu = 13$, which is higher than for the model-based test ($\nu = 6$) due to the increased complexity of the monitoring problem. Complexity is defined through a higher number of monitoring parameters in relation to the

number of modes of vibration (see Section 5.1.4). At the same time, it is lower than the number of vectorized modal parameters ($H = 2N_m(r+1) = 40$), so the sensitivity matrix (the Jacobian $\boldsymbol{\mathcal{J}}^{(1)}$) is also column-rank deficient.

- The POD is not affected by the complexity of the monitoring task, because the developed reliability index considers the number of degrees of freedom. An increased number of degrees of freedom leads to an increase in the minimum non-centrality λ_{min}. Consequently, an equally reliable test performance can be achieved for data-driven tests with a POD of 97%.

- An increased reliability index (non-centrality λ_{min}) leads to a decreased damage detectability compared to the model-based tests. This is indicated through a longer measurement duration T_8 (10 s vs. 7 s). The finding that the data-driven test has a lower detectability is specific to this structure, because the number of structural parameters is lower than the number of modal parameters.

For completeness, the validation procedure is repeated for the damage scenario with an extra mass on top of beam segment 5 (centre plot in Fig. 9.10b). The number of degrees of freedom is $\nu = 16$, the measurement duration is $T_5 = 18$ s, and the empirical POD is 96%. The measurement duration is longer because of the smaller Fisher information F_{55} compared to F_{88}, and the number of degrees of freedom attains the same value, even for a longer measurement duration. These results confirm that the predictions of the minimum detectable damages based on a FE model are also valid for the data-driven test using modal parameters (see Section 5.2).

b) Validating the Non-parametric Test. Now, the prediction for the non-parametric damage detection test is validated starting with the damage scenario with a 5% extra mass on beam element 8 (bottom plot of Fig. 9.10a).

- The number of degrees of freedom of the χ^2-distribution is $\nu = 1{,}657$. This value is significantly larger than for the parametric test using modal or structural parameters, so the monitoring problem is more complex. However, this value is also higher than the dimension of the covariance matrix (see Fig. 9.6), which is inconsistent with the theory, and indicates that the test distribution of the non-parametric test based on real vibration data can be biased. Since it is the only test that does not employ a sensitivity matrix, it can be concluded that parametrization enhances the robustness with respect to measurement noise. The sensitivity matrix can be understood as a transformation matrix that projects the mathematical problem onto a lower-dimensional space. From this perspective, it is recommended that one choose the parametric detection test over the non-parametric one, whenever possible.

- Due to the high complexity, the damage detectability is lower than for any other damage detection test, with a measurement duration of $T_8 = 35$ s.

- Despite the biased training state distribution, the empirical POD is 97%. This value is almost identical to the other damage detection tests (with 97% and 94%) and close to the theoretical

value of 99.4%. The results highlight the importance of the empirical curve-fitting developed in this thesis. Where for the parametric damage detection tests, the theoretical value could have been chosen, with $\nu = \text{rank}(\boldsymbol{\mathcal{J}}^T \boldsymbol{\Sigma}^{-1} \boldsymbol{\mathcal{J}})$, the prediction of the non-parametric test is only possible after empirically evaluating the number of degrees of freedom of the χ^2-distribution. The bias appears to equally affect the test distribution in the training and damaged states, so the prediction of the minimum detectable damage is accurate.

For the damage scenario with a 5% extra mass on beam segment 5 (bottom plot in Fig. 9.10b), a longer measurement duration of $T_5 = 107\ s$ is required. Moreover, the number of degrees of freedom increases ($\nu = 4,237$) indicating that the test distribution is affected by the measurement duration, which is inconsistent with the theory. However, the model-based prediction based on the empirical ν and the model-based Fisher information results in a POD of 93%, so the prediction is still accurate.

Conclusions

The damage detectability varies across the structure, and the model-based Fisher information is a measure for the detectability of damage (see Section 5.1.1). Based on reliability considerations, the Fisher information can be translated into a minimum measurement duration for each component, making the measurement duration an equivalent measure for detectability (Section 5.1.2). The test distributions of the damage detection tests approximate χ^2-distributions with a problem-specific number of degrees of freedom. This confirms the underlying assumptions of the reliability concept (Section 5.1.3). The predictive framework is valid for real structures and robust toward noisy measurement environments. The prediction of the minimum detectable damages are valid for model-based and data-driven tests, meaning the FE model is required for the prediction of the minimum detectable damage but not in the active monitoring phase (see Section 5.2). This widens the field of application, and makes the approach more universal. Parametrization is optional, but enhances the robustness towards noise effects. In this sense, the model-based test is the most robust, if the number of monitoring parameters is lower than the number of modal parameters. If data-driven tests are to be employed, the parametric version is to be chosen over the non-parametric one for robustness. Even for simple monitoring problems, the sensitivity matrix may be column-rank deficient, underlining the importance of the numerical considerations (from Section 5.3).

9.1.3 Localizing Mass Changes

Identifying the entry in the monitoring parameter that has changed (damage localization) is more challenging than damage detection, because damage in one parameter affects the test response of others, which leads to false localization alarms. The developed framework can predict the test response of parameters that have changed due to the damage and false localization alarms, and this section showcases that the predictions are also valid for real structures in noisy measurement environments.

Damage localization tests are evaluated parameter-wise, so each diagnosis run yields as many test statistics as there are monitoring parameters. For statistical evaluation of the test distributions, the localization tests are applied to 100 data sets in a Monte Carlos simulation, and only the distributions' mean values are plotted. Figure 9.14 summarizes the training state (top plot) together with the two validation states (centre plot and bottom plot) for an extra mass at Segment 5 and 8. For each damage scenario and localization, the measurement duration was adjusted so a 10% extra mass causes a mean test response that is equal to the minimum non-centrality $\lambda = \lambda_{min}$. The plots visualize the safety threshold value (dashed line), the empirical mean test response (grey bars), and the predicted test response (plus signs). Detailed descriptions for the direct localization test and the minmax localization test follow in the subsequent paragraphs.

Study 1: Direct Localization Test

First, the direct localization test is applied, see Fig. 9.14a. In the training state (top plot of Fig. 9.14a), all distributions approximate a mean value of one (grey bars). This confirms the theoretical investigations (plus signs); in theory, the mean value of a central χ^2-distribution is equal to the number of degrees of freedom, which is one if parameters are individually tested for damage.

For damage scenario $\Delta_5 = 10\%$ (centre plot of Fig. 9.14a), the minimum measurement duration is $T_5 = 7$ s. It appears that the test response of the unchanged parameter (grey bar at Parameter 5) is close to the predicted value (plus sign at Parameter 5). Since the direct localization test does not consider the off-diagonal terms of the Fisher information, false alarms occur at all unchanged parameters, which diminishes the meaningfulness of the damage localization. However, using the predictive framework, the magnitude of false alarms can be analyzed. As shown in the plot, the predicted mean test responses (plus signs) are close to the empirical mean test responses (grey bars) for all parameters that have not changed due to damage. This confirms the developed theoretical investigations for the minimum localizable damage (Section 6.1.1) and the false alarm predictions (Section 6.1.2).

For damage scenario $\Delta_8 = 10\%$ (bottom plot of Fig. 9.14a), the measurement duration is significantly shorter with $T_8 = 3.0$ s. This is because the Fisher information value F_{88} is higher than F_{55} (see Fig. 9.7), making it a measure for the localizability of damage. The predictions of the test response to a 10% mass increase are correct for all Parameters except θ_5, where an inexplicable deviation is noticed.

Study 2: Minmax Localization Test

In a second study, the minmax localization test is applied. The objective is to validate the automated substructuring approach as well as the prediction of the minimum localizable damage and false localization alarms.

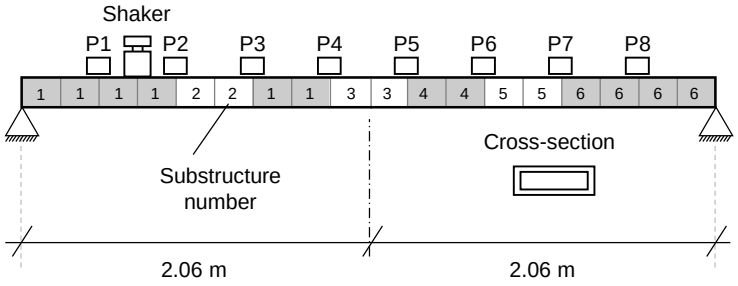

Figure 9.11: Optimal substructure arrangement for $K = 6$ clusters

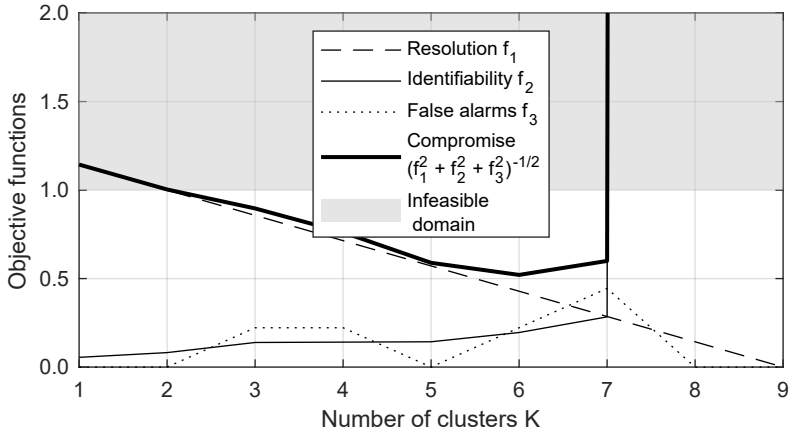

Figure 9.12: Automated parameter clustering

First, the monitoring parameters are clustered using the automated substructuring approach (from Section 6.3), with the optimization procedure being summarized in Fig. 9.12. With an increasing number of clusters, the damage localization resolution increases, as the objective function f_1 linearly decreases. Parameter clusters with one cluster are infeasible and the maximal cluster number is $K = 9$. An increasing number of clusters reduces the damage identifiability in each parameter (objective f_2), with a distinct jump into the infeasible domain for configuration with more than seven clusters. This abrupt change can be tied back to the Fisher information from Fig. 9.7; due to the small main diagonal value for support-near parameters (Parameter 1 and 9), it is challenging to localize damage in those parameters. This is also indicated by the eighth and ninth singular values of the Fisher information, which are significantly smaller, see Fig. 9.7. The number of false alarm scenarios (objective f_3) is maximal for the cluster arrangement with seven clusters, changing the optimal compromise (thick black line) from seven to $K = 6$ clusters. The corresponding substructure arrangement is visualized in Fig. 9.11.

The clustered sensitivity matrix is handed over to the minmax localization test to predict the minimum localizable damage and the false localization alarms. The results are summarized in Fig. 9.14b. In the training state (top plot), the empirical test response approximates a mean value of one (grey bars) for all parameters. This confirms the theoretical investigations regarding the statistical distribution of the minmax test.

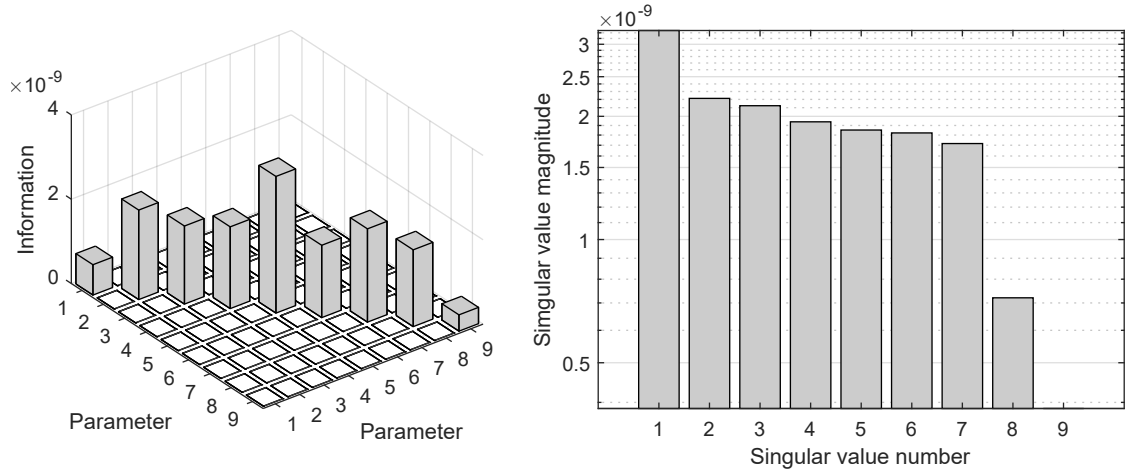

Figure 9.13: Minmax Fisher information with six clusters $K = 6$ and its singular values

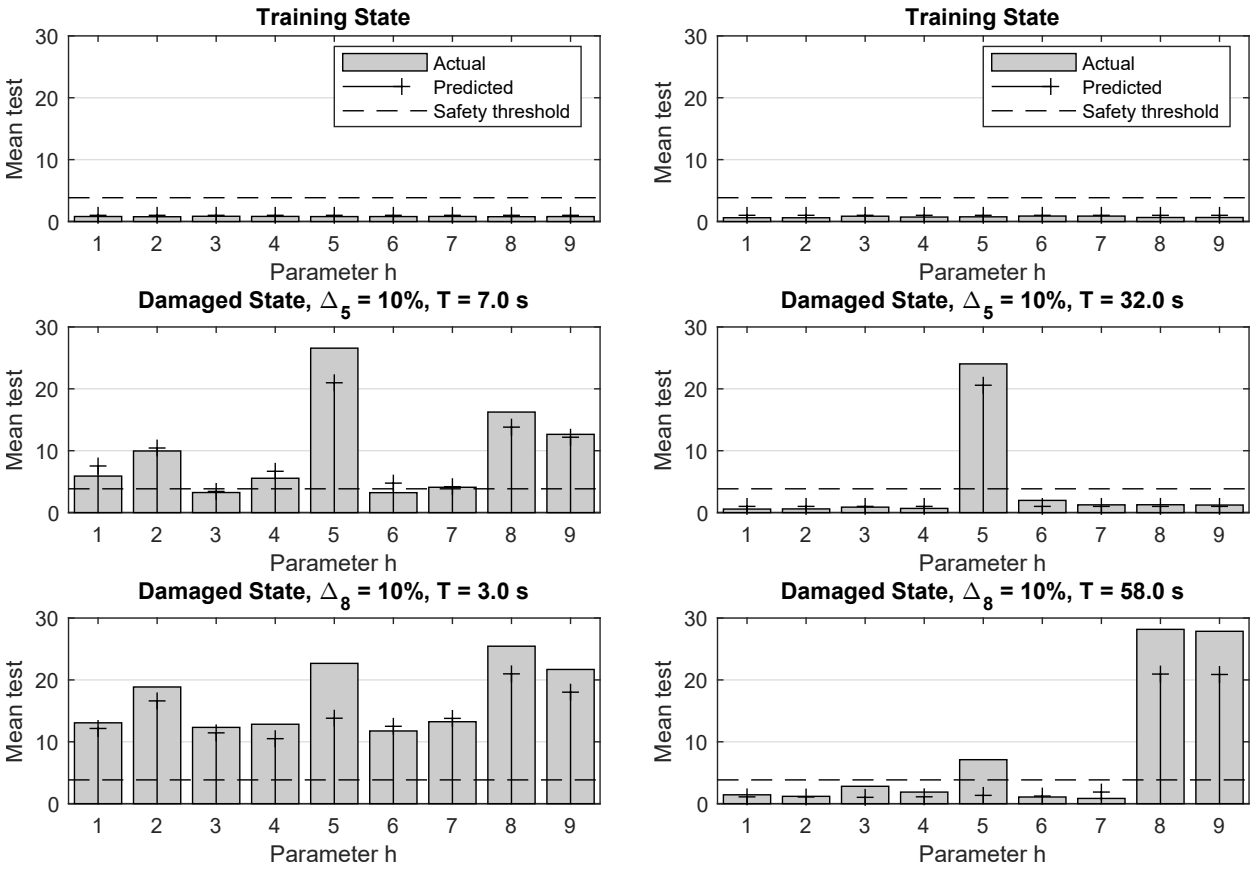

(a) Direct test

(b) Minmax test

Figure 9.14: Damage localization

For damage scenario $\Delta_5 = 10\%$ (centre plot), the minimum measurement duration is calculated to $T = 32$ s, and the empirical mean test response (grey bars) is almost identical to the predicted response (plus sign) for the changed parameters. Furthermore, the minmax localization test con-

siders the off-diagonal terms of the Fisher information, which causes all false localization alarms to disappear. This is reflected in both the empirically measured and predicted values.

For damage scenario $\Delta_8 = 10\%$ (bottom plot), the empirical mean test response for Parameter 8 (grey bar) is close to the predicted one (plus sign), so the prediction for the minmax localization test is considered accurate. Since Parameters 8 and 9 are in the same cluster, the test response of Parameter 9 is not a false alarm; however, Parameter 5 shows a false localization alarm that is slightly more pronounced than anticipated (this was also the case for the direct localization test). Nonetheless, the laboratory test shows that the magnitude of the minmax localization test can be predicted (see Section 6.2), as well as the false alarm magnitude (see Section 6.2.2), which confirms the theoretical investigations. Moreover, damage scenario $\Delta_8 = 10\%$ demonstrates the diagnostic capabilities of the minmax localization test. Where the direct localization test could not reliably localize the damage location due to significant false alarms (Fig. 9.14a), the minmax localization test leads to clear results with almost no false alarms (Fig. 9.14b). However, a low false alarm rate and increased damage localization resolution come at the cost of reduced identifiability. This is shown through a long measurement duration of $T_8 = 58$ s. In contrast to all other tests, the measurement duration for scenario $\Delta_8 = 10\%$ is longer than for $\Delta_5 = 10\%$, because the minmax test utilizes the robust Fisher information from Fig. 9.13, and the main diagonal value F_{88} is smaller than F_{55}. This concludes the validation of the minmax localization test. The results verify all findings regarding the optimal damage localizability (see Section 6.3).

Conclusions

The results from this section verified all theoretical investigations regarding the minimum localizable damage (Chapter 6) based on real vibration measurements on the laboratory HSS beam in a noisy measurement environment. Using the direct localization test, this section shows that the model-based Fisher information is a measure for the localizability of damage (Section 6.1.1), and that the behaviour of the damage localization test can be fully predicted for both the parameters that have changed due to damage and parameters that have not, i.e., false localization alarms (see Section 6.1.2). For damage localization, the empirical number of degrees of freedom of the statistical distributions is one, which resonates with the theoretical investigations and leads to a high damage detectability in combination with short measurement durations. The minimum measurement duration to localize a 10% damage based on the direct localization test is 3.0 s. Such short measurement durations are possible because the FE model is not updated during testing. Having said that, the diagnosis results from the direct localization test are unusable for some damage scenarios due to significant false alarm magnitudes. Using the minmax localization test, false alarms can be eliminated and the mean test response can be predicted for changed parameters (see Section 6.2), unchanged parameters in the same clusters, and false localization alarms (see Section 6.2.2). The detectability for the minmax localization test is significantly lower than for the direct localization test with measurement durations up to 58 s to detect a 10% mass damage.

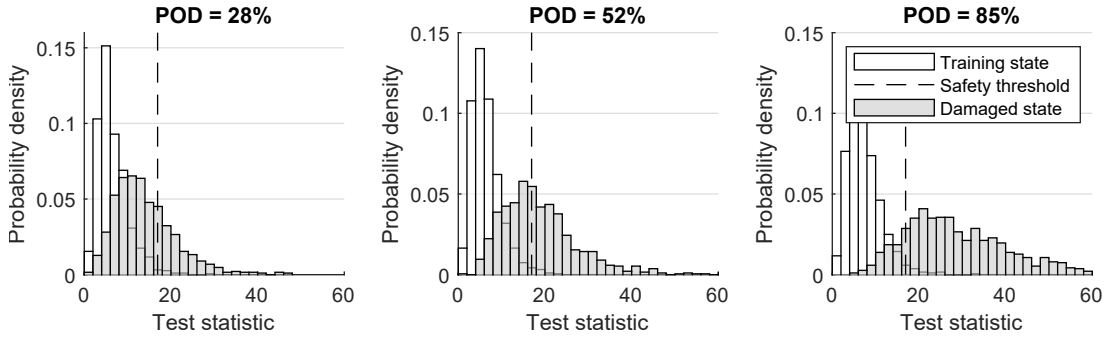

Figure 9.15: Probability of detection for sensor configurations with rank 70, 36 and 1

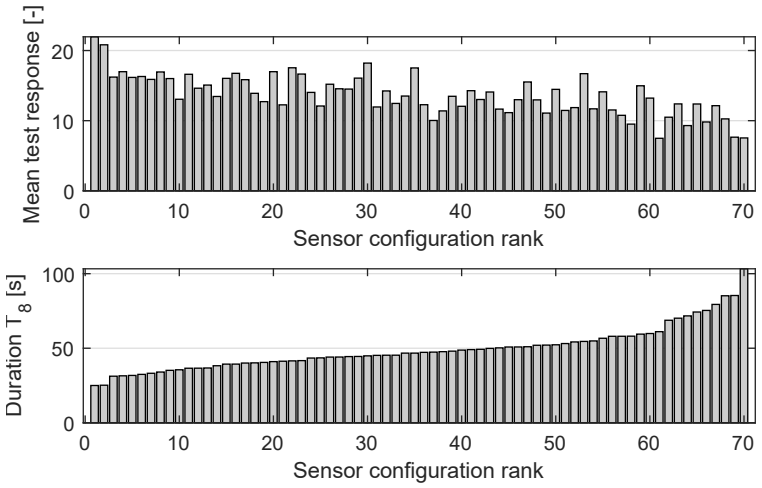

Figure 9.16: Ranking all 70 configurations with $r = 4$ sensors

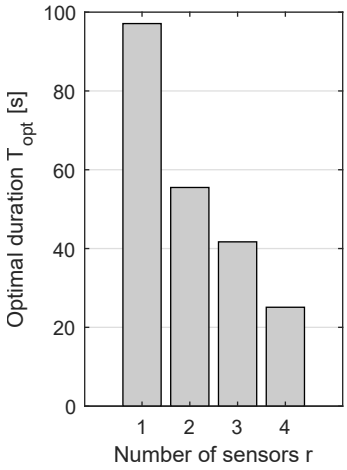

Figure 9.17: Performance curve

This justifies all research efforts for the automated substructuring approach, which finds the optimal compromise between a high damage localization resolution, high detectability, and a low false alarm rate (see Section 6.3) .

9.1.4 Optimizing the Sensor Placement

The main idea of the sensor placement optimization scheme is to use the main diagonal of the Fisher information as a measure for the detectability of damage, and to translate it into the minimum measurement duration to detect a certain damage amount in different structural components. This section sets out to verify the assertion empirically using real vibration data from the HSS beam.

The validation is performed for the model-based damage detection test. The main idea is to evaluate the mean test response for each sensor configuration for a fixed measurement duration of T = 7 s and a fixed damage extent $\Delta_8 = 5\%$. To evaluate whether the predicted minimum measurement duration is a measure for the detectability of damage, it is calculated for each sensor configuration through

$$T_8 = \frac{1}{(\Delta\theta_8)^2} \frac{\lambda_{min}}{f_s F_{88}}. \tag{9.2}$$

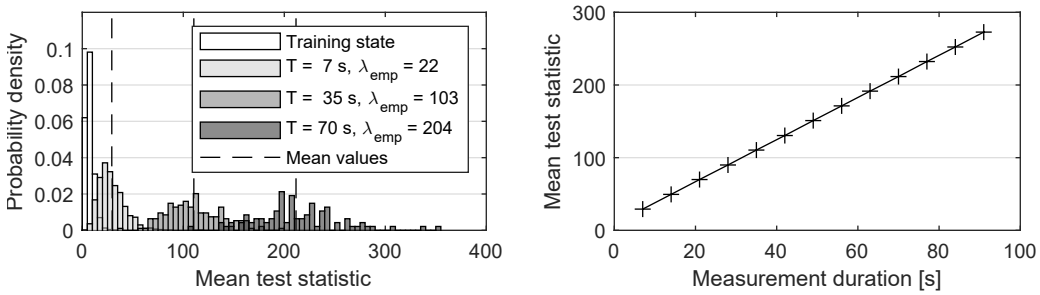

Figure 9.18: Relation between the mean test response and the measurement duration

Figure 9.16 compares the predicted measurement duration to the mean test response, where the sensor configurations are ranked according to T_8 in both subplots. A shorter minimum measurement duration is equivalent with a more pronounced mean test response, which validates the theoretical investigations. For clarity, the best solution is plotted on the right side of Fig. 9.15 together with the solution number 36 and 70. As expected, an improved sensor layout leads to a significantly higher POD. This proves that the minimum measurement duration is a measure for the detectability of damage and a suitable performance criterion for sensor placement optimization. Optimal performance can be achieved for a sensor layout with four sensors at the positions [1, 4, 5, 7], followed by the second best layout with sensors at [2, 4, 5, 7]. The lowest detectability was achieved if the sensors are placed at the positions [1, 2, 3, 6]. The vibration measurements at these positions carry the least information on the health state of the beam, most likely because positions P3 and P6 are vibrational nodes of Mode 3, see Fig. 9.4.

Next, the optimal measurement duration is calculated for 1 - 4 sensors, see Fig. 9.17. It appears that the measurement duration decreases with an increasing number of sensors, where the measurement duration for the optimal layout with four vibration sensors is 3.9-times shorter than for the optimal layout with a single sensor. This demonstrates that the measurement duration is a helpful means to compare sensor layouts with a varying number of sensors, and to decide on an appropriate number of sensors.

Ultimately, the optimal sensor configuration with four sensors is selected, and the mean test response is plotted over a varying measurement duration, see Fig. 9.18. Increasing the measurement duration by a factor of ten (from 7 s to 70 s) causes a mean test response that is ten times stronger (left plot). Plotting the mean test response over the corresponding measurement duration (right plot) leads to a straight line. Consequently, the mean test response λ is proportional to the measurement duration T with $\lambda = (\Delta\theta_h^2 F_{hh} f_s) \cdot T$. This further validates the predictive formula for the minimum detectable damage, and concludes the case study of the HSS steel beam.

9.2 St. Nazaire Bridge Model (1,002 DOF)

The primary purpose of the second case study is to apply the stochastic subspace-based damage diagnosis method to a scaled-down model of a cable-stayed bridge with the following objectives:

- *Objective 1*: Based on real data from a laboratory experiment, show that the complete failure of cable pair 19 can be detected and localized (Section 9.2.2)
- *Objective 2*: Based on simulated vibration data, demonstrate that the predictive framework is valid for larger mechanical structures by predicting the mean test response (Section 9.2.3)

9.2.1 Experimental Setup

Bridge Description. The specimen is a scaled-down laboratory model of the St. Nazaire cable-stayed bridge in France (scale 1:200), designed by the Department of Civil and Mechanical Engineering at the University in Nantes (Cadoret et al., 2020), see Fig. 9.19. The specimen models the cable-supported section of the bridge with a total length of 3.6 m. The structure is split into the main span and two side spans with a length of 2.02 m and 79 cm, respectively. To mimic the dynamic behaviour of the real bridge, the prototype exhibits higher density materials conforming to the similitude requirements. The bridge deck is a steel box girder, continuous over all three spans, with a width of 7.5 cm. The cross-section is composed of foam (with a density of 51 kg/m^3 and a stiffness of 74 MPa) encased by a trapezoidal steel sheet with a thickness of 0.1 mm. The piers at the cable end spans are made of aluminum, topped up with an H-shaped pier cap made of steel. The two A-shaped towers, also made of aluminum, rise 33 cm over the steel deck, where the two aluminum posts of each tower are connected at the top through a steel sheet that includes fixtures for stay cables. Each tower sits on top of a monolithic tower pier that models two vertical pillars (on top of which the tower rests), a transverse beam, and a solid piece that expands to the foundations. The 72 steel cables, with a diameter of 0.38 mm, connect the upper part of the tower to the deck and form two cable planes in fan-arrangement. More details on the cross-sectional values are given in the modelling section and Table 9.2.

Instrumentation and Signal Processing. The instrumentation consists of one shaker and 10 uni-axial vibration sensors. The shaker—a converted speaker with an attached stinger—is placed under the deck and vertically connected to the deck near cable pair P32, see Fig. 9.21. The piezoelectric accelerometers (0.8 gm) with a sensitivity of 100 mV/g (PCB of reference ICP) are aligned in the vertical direction and glued to the centre line of the deck at the positions shown in Fig. 9.21. While white noise is vertically injected into the bridge, a two-minute acceleration record is sampled at a rate of f_s= 4,800 Hz and later down-sampled to 340 Hz. Furthermore, a low-pass filter is applied before re-sampling the records to avoid aliasing, but no high-pass filter is used. However, the signal components around 80.5 Hz are removed in all records, using an orthogonal projection method (Greś et al., 2021), in order to reduce the observable modes of vibration to the

six modes used in the sensitivity matrix. More information on this is given in the section on the FE model. In between the measurements, all sensors are removed and re-attached for the subsequent run.

Finite Element Model. The subspace-based damage diagnosis method is data-driven, but a FE model is required to parametrize damage, to calculate the sensitivities of the damage-sensitive residual toward structural design parameters, and to generate vibration data for preliminary validation studies. The FE model was provided by the Department for Civil and Mechanical Engineering in Nantes, see Fig. 9.21. It is designed in MATLAB® using custom-code for 3-D beam and truss elements. The continuous deck is discretized into 51 nodes and 50 beam elements with identical cross-sections and material properties over all three spans (see Group 1 in Table 9.2). The piers are

Figure 9.19: St. Nazaire Bridge (Janberg, 2020)

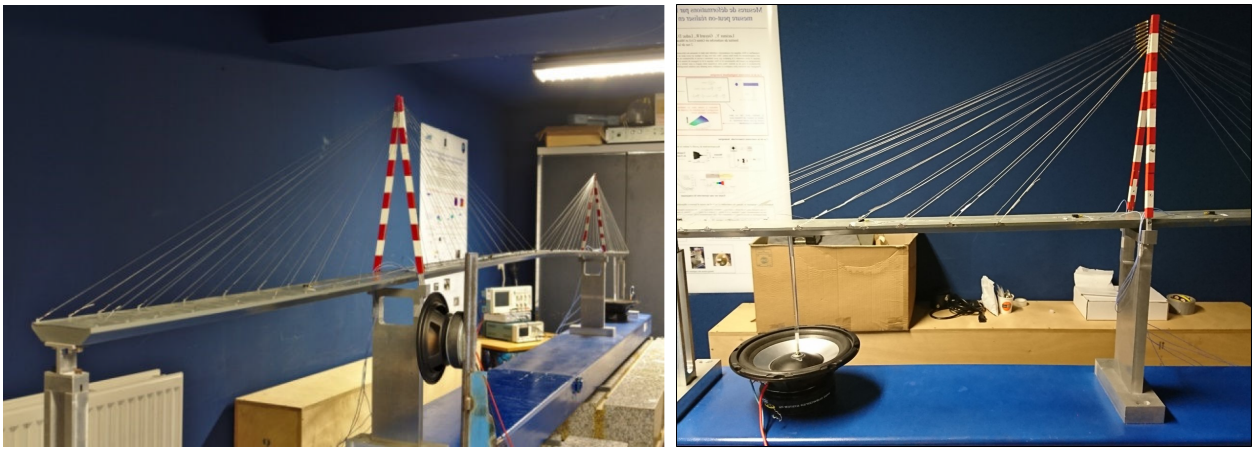

(a) Laboratory model (1:200) (b) Shaker point excitation

Figure 9.20: Experimental setup for the St. Nazaire Bridge

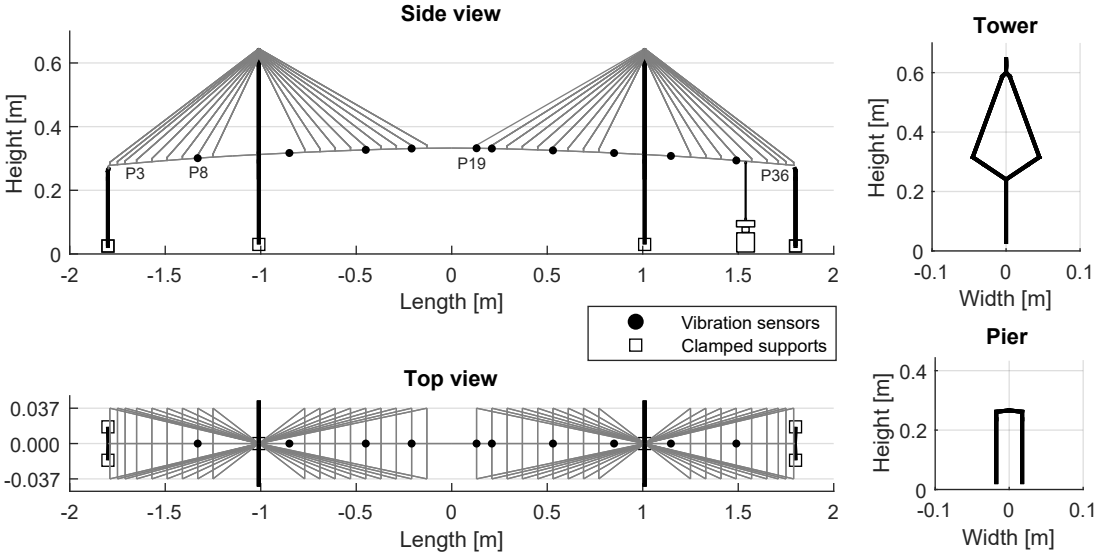

Figure 9.21: Finite element model of the St. Nazaire Bridge in MATLAB®

No.	Type	Density $[\frac{kg}{m^3}]$	E $[\frac{MN}{m^2}]$	G $[\frac{MN}{m^2}]$	A $[m^2]$	I_y $[m^4]$	I_z $[m^4]$	J $[m^4]$
1	Deck	37,000	210,000	81,000	2.0E-05	2.1E-08	1.8E-09	2.3E-08
2	Pier	2,700	69,000	27,000	2.0E-04	1.7E-09	6.7E-09	8.3E-09
3	Pier	7,800	210,000	81,000	2.4E-04	8.0E-09	2.9E-09	1.1E-08
4	Pylon	2,700	69,000	27,000	1.8E-03	1.2E-06	6.0E-08	1.3E-06
5	Pylon	2,700	69,000	27,000	9.0E-04	1.5E-07	3.0E-08	1.8E-07
6	Pylon	2,700	69,000	27,000	9.0E-04	1.5E-07	3.0E-08	1.8E-07
7	Pylon	2,700	69,000	27,000	2.4E-05	3.2E-11	7.2E-11	1.0E-10
8	Pylon	2,700	69,000	27,000	2.4E-05	3.2E-11	7.2E-11	1.0E-10
9	Pylon	7,800	210,000	81,000	2.4E-05	3.2E-11	7.2E-11	1.0E-10
10	Links	100	1.0E+10	5.0E+9	6.3E-08	3.3E-16	3.3E-16	6.5E-16
11	Links	100	1.0E+10	5.0E+9	6.3E-08	3.3E-16	3.3E-16	6.5E-16
12	Cables	7,800	210,000		7.7E-03			

Table 9.2: Finite element specifications

split into pier pillars (Group 2) and pier caps (Group 3) and the pylons are split into six groups: the piers (Group 4), the V-shaped pier caps (Group 5 and 6), the A-shaped towers (Group 7 and 8), and the vertical cable anchor elements (Group 9) made of metal. Group 10 are link elements at the top of the A-shaped towers that link the steel components to the aluminum component. Group 11 are link elements that connect the deck beam to stay cables and piers. The stay cables (Group 12) are the only elements that are modelled as trusses. In total, the model exhibits 1,038 degrees of freedom. All six degrees of freedom at the two tower foundations and the four pier foundations are fixed, reducing the number of unrestrained degrees of freedom to 1,002.

a) Model Calibration. The considered natural frequencies and mode shapes of the MATLAB®

model are summarized in Fig. 9.22. The damping matrix is set up based on a damping ratio of 1% critical damping for each mode. In addition, the numerical model exhibits a repeated mode at 80.5 Hz (which is also observable in the vibration data); however, these two modes are excluded from the analysis and removed during signal preprocessing to avoid numerical issues in the sensitivity computation, see Fig. 9.23. For calibration, the modal parameters are compared to a FE model in Abaqus, as well as the result from operational modal analysis (OMA), considering the first 17 modes of vibration (Cadoret et al., 2020). Table 9.3 summarizes the natural frequencies and damping ratios of the considered six modes from OMA. The mode shape of Mode 2 is similar to Mode 3, but it exhibits no bending components in the towers and a more pronounced longitudinal movement of the deck. This may cause the higher damping ratio of 3.36% as it interacts with the piers at the end spans.

b) Damage Parametrization. Damage is defined as a change in the cross-section A of the cables. The same monitoring parameters are assigned to the cables on both sides of the deck, reducing the number of parameters from 72 to 36 with the monitoring vector

$$\boldsymbol{\theta} = \begin{bmatrix} A_1 & \dots & A_{36} \end{bmatrix}. \tag{9.3}$$

During the laboratory experiment, cable pair P19 is removed, which corresponds to a damage of $\Delta_{19} = 100\%$. The stiffness contribution of three-dimensional truss elements is a linear function of the cross-section A, the modulus of elasticity E, and the cable length L, meaning a change

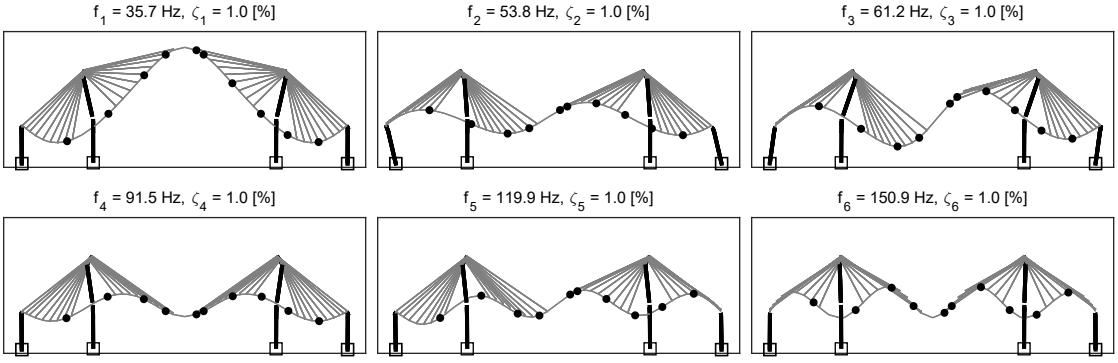

Figure 9.22: First six modes of vibration in the vertical direction (FE Model)

Operational Modal Analysis						
Mode number	1	2	3	4	5	6
Frequency [Hz]	35.7	53.8	61.2	91.5	119.9	150.9
Damping ratio [%]	1.03	3.36	1.12	1.94	1.39	1.13

Table 9.3: Operational modal analysis results (covariance-driven SSI)

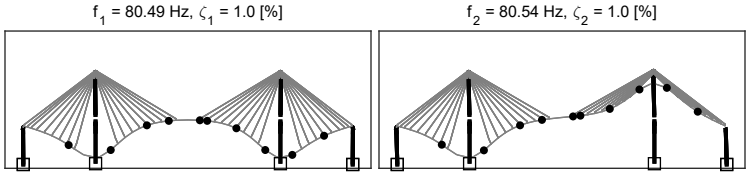

Figure 9.23: Repeated mode at about 80.5 Hz

linearization through the Jacobian matrix does not introduce bias.

$$\mathbf{K}_{el}^{l} = EA/L \begin{bmatrix} 1 & -1 \\ -1 & 1 \end{bmatrix} \tag{9.4}$$

c) Sensitivity Computation. The Jacobian matrix, which links the data-driven residual to structural design parameters, is split into three parts, where the sensitivity of poles and mode shapes toward structural parameters (i.e., Jacobian $\boldsymbol{\mathcal{J}}^{(3)}$) is model-based. For its computation, the first six modes of vibration are considered, see Fig. 9.22. The natural frequencies of the two modes at 80.5 Hz are almost identical, which causes numerical issues in the derivative of the poles and mode shapes, see Fig. 9.23. Hence, they are not included in the Jacobian matrix and removed from the measured vibration records. The pole derivatives are computed analytically (using the modal approach), and so are the mode shape derivatives. For the mode shape computation, the first 30 modes of vibration are included.

d) Vibration Generation. For vibration generation, the mechanical system matrices $\mathbf{K}$ and $\mathbf{M}$ are extracted from the model, the modal damping matrix $\mathbf{C}^1$ is set up based on an assumed value of 1% critical damping for each mode, and transformed into a state space model in modal coordinates. This allows for the individual modes of vibration to be selected that contribute to the vibration record. Subsequently, a white noise input signal is applied to the vertical degrees of freedom of the deck beam, a transient analysis is run, and the output at the sensor locations is stored after superimposing it with uniformly distributed measurement noise with a magnitude corresponding to 5% of the output variance.

Data		**Segmenting**		**Processsing**	
Measured quantity	acceleration	Training segments	6	No. of sensors	r/r_0=10/10
Sampling frequency	340 Hz	Testing segments	6	Time lags	p/q=4/5
Reference data length	120 s	Samples/segment	6,800	System order	n=12
Training/testing data	120 s	Duration/segment	20 s	Block length	N_b= 10

Table 9.4: Input parameter sheet

9.2.2 Localization Cable Failure

Based on the vibration data from the reference state, the block Hankel matrix is computed with its singular values shown on the left side of Fig. 9.26. A distinct drop is noticed after the 12th singular value, so the system order is set to $n = 12$, with the minimum time lag parameters $p + 1 = q = 5$. Moreover, the null space is extracted and the sample covariance of the damage-sensitive residual is estimated based on a block length that approximates one cycle of the fundamental mode of vibration, i.e., $N_b = 10$. Ultimately, the sensitivity is calculated, i.e., the Jacobian $\boldsymbol{\mathcal{J}}^{(3)}$; however, the Jacobian matrix occurs to be column-rank deficient, meaning it has to be clustered prior to damage localization using the minmax localization test.

Automated Substructuring. Clustering the Jacobian matrix corresponds to a creation of substructures in the FE model, in which damage can be isolated. Finding the optimal substructure arrangement is a multi-objective optimization problem, with the optimization criteria being the localization resolution (i.e., the number of clusters), the damage identifiability, and the false alarm susceptibility (see Chapter 6). The maximum number of substructures is dictated by the rank of the Fisher information, which is six in this case, as the singular values exhibit a clear jump after the sixth singular value, as shown on the right side of Fig. 9.26. The minimum identifiable damage, on the other hand, appears to be below 100%, even for a high number of clusters. This can be seen in Fig. 9.24, where objective function f_1 (the damage detectability) jumps into the infeasible domain after 27 clusters. This figure also summarizes the other optimization criteria (resolution and false alarms). The optimal compromise function is found for five or six clusters, as the compromise function attains a global minimum, where the configuration with six clusters is chosen. The substructure arrangement is symmetrical, meaning the damage localization test will likely not be able to identify the semi-harp in which damage has occurred.

Damage Localization. The applied statistical tests for damage localization are the direct localization test and the minmax localization test, and the input parameters for the damage diagnosis are summarized in Table 9.4 with a short measurement duration of 20 s. The decisive measure for interpreting the damage diagnosis results is the non-centrality, i.e., the distance between the mean values of the test distribution in the training and the damage state, which is plotted in Fig. 9.25. The direct test (top plot) indicates that the cable pairs P17 - P20 are the most likely to be damaged, but false alarms occur close to the damaged cable pair and at remote cable pairs P9 and P28. The minmax test manages to narrow down the damage localization to parameter P18 and P19 with insignificant false alarms. Although not shown here, it could be proven that the magnitude of the test response is proportional to the measurement duration, which complies with the predictive framework.

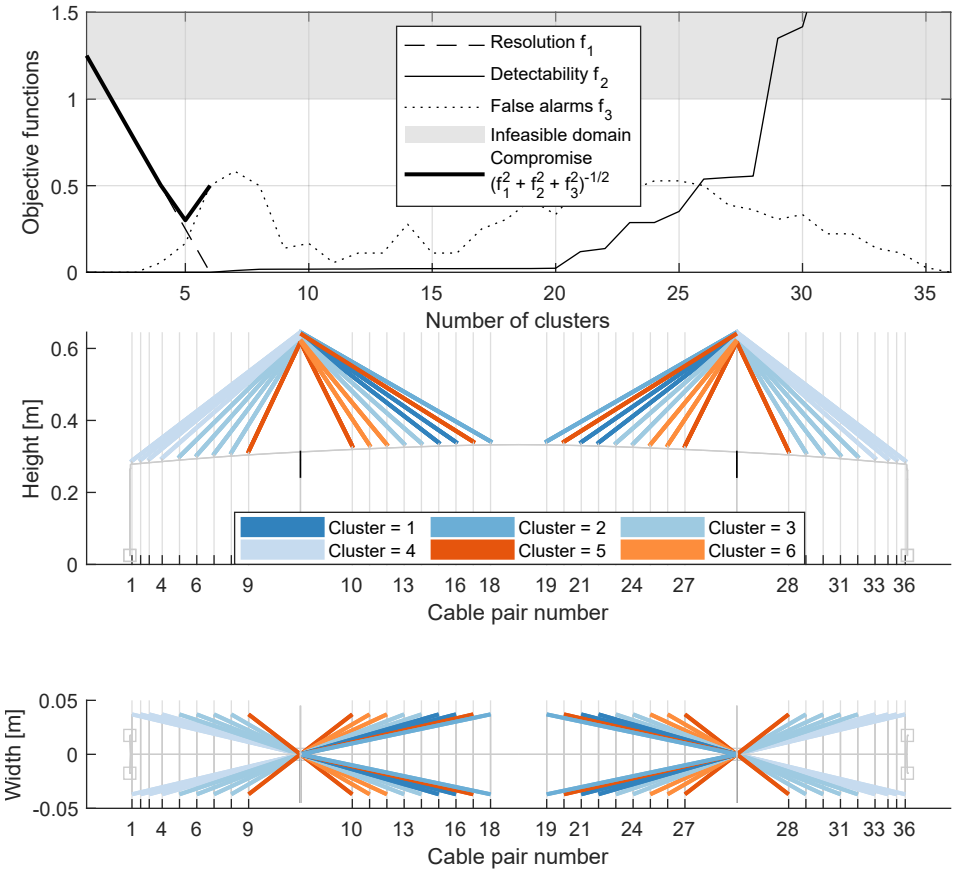

Figure 9.24: Automated clustering of cable cross-section parameters

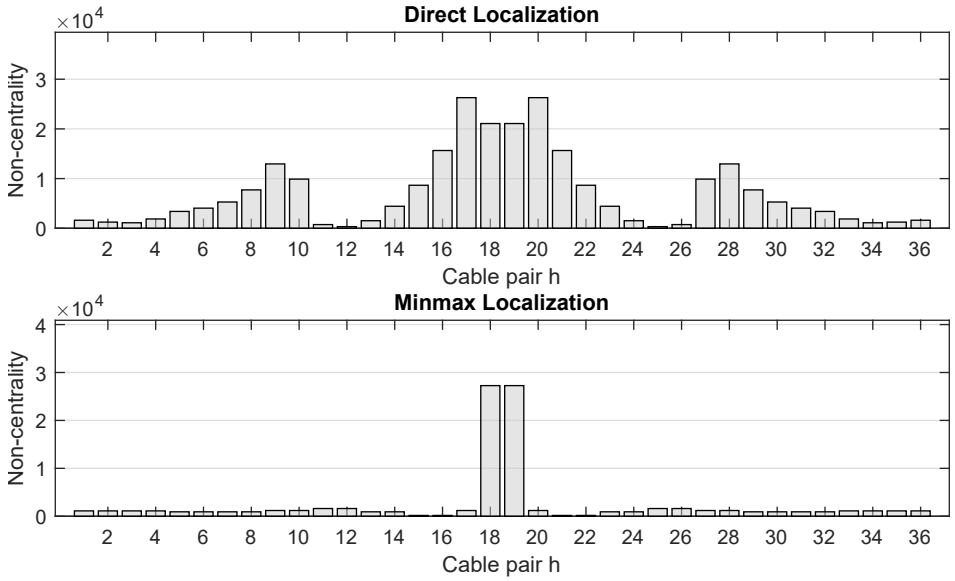

Figure 9.25: Non-centrality of the minmax localization test for damage scenario P19

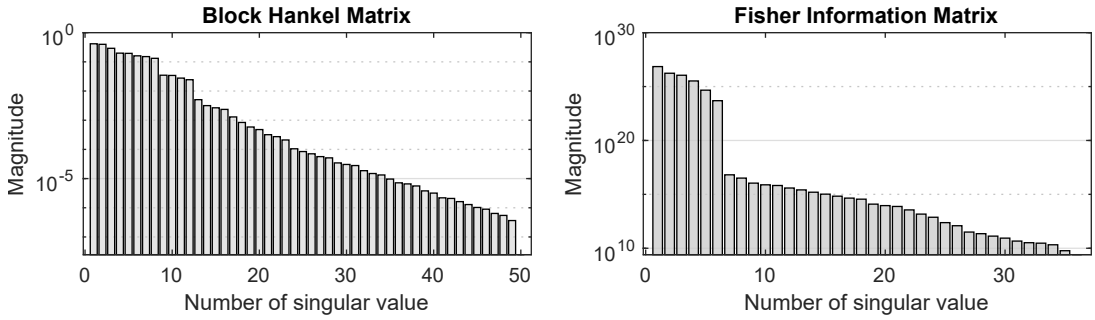

Figure 9.26: Singular values of the Block Hankel matrix and the Fisher information

9.2.3 Additional Numerical Studies

The studies in this section are based on simulated vibration data. The damage diagnosis is performed based on the same input parameters, see Table 9.4 except that the measurement duration in the reference state is increased from 2 min to 30 min.

In previous studies with real data, the upper bound for the number of clusters was set to $K_g = 6$ because the rank of the Fisher information showed a distinct jump, see right side of Fig. 9.26. For simulated data, the automated substructuring approach would yield a similar plot as in Fig. 9.24 (so the plots are not repeated). However, this time, the number of substructures is manually set to $K = 18$. This was done to study why the objective functions f_1 remained within the feasible domain up to a cluster number of $K = 27$, meaning the minimum identifiable damage was below 100%. The resulting substructuring arrangement is symmetrical and assigns each cable pair within one cable fan to a separate cluster, see Fig. 9.27.

For validation of the predictive framework, the mean test response to 50% damage in each cable is predicted together with the corresponding false alarms. Subsequently, the damage is applied to the bridge model and the empirical mean test response is measured. Figure 9.28 shows the results for damage in cable pair P3. It appears that the predicted non-centrality (plus sign) is close to the measured non-centrality for the damaged cable pair P3, as well as for all undamaged monitoring parameters (bar plot), so false alarms are also predicted correctly. The white bars mark the damaged cable pair as well as other parameters within the same cluster. For completeness, the validation is repeated for all 36 possible damage scenarios with the results shown in Fig. 9.29. This plot showcases that the relative magnitude of false alarms can be predicted accurately for all scenarios. For some components with particularly high or low test responses (e.g., Parameter 9 or 16, respectively) minor discrepancies can be observed between the absolute values of the predicted and the measured mean test responses, but this result is considered sufficiently accurate. In other words, the predictive framework is valid even for large mechanical systems such as the modelled cable-stayed bridge.

At the beginning of this study, the number of substructures was set to a value that exceeded the numerical rank of the Fisher information matrix. However, the predictions of the mean test

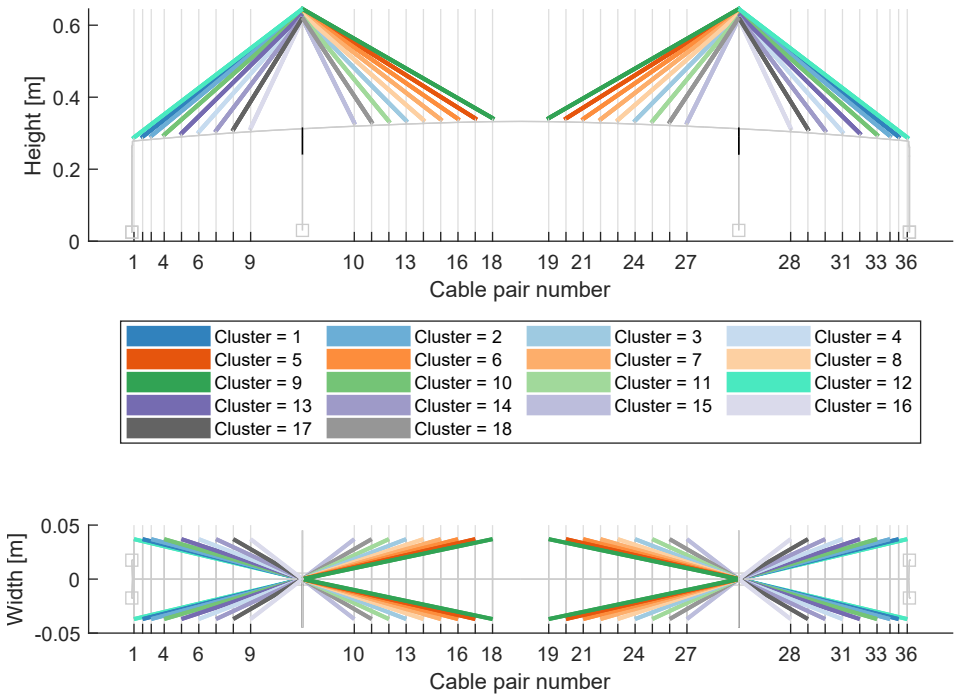

Figure 9.27: Substructure arrangement for 20 parameter clusters

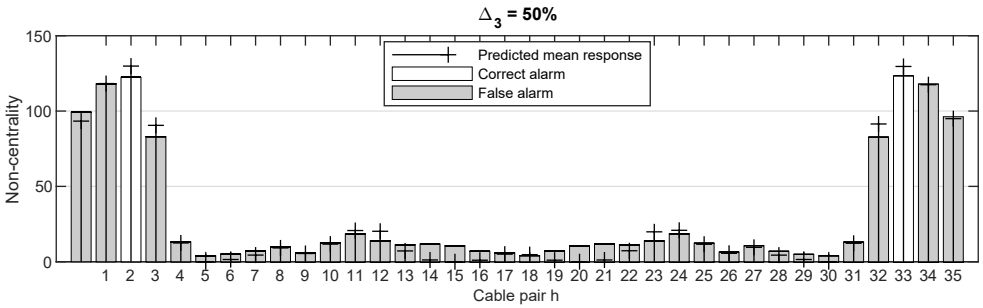

Figure 9.28: Comparing the predicted and the measured non-centrality for $\Delta_3 = 50\%$

responses are still correct, meaning the numerical rank calculation might have been incorrect. A possible explanation is that the jump in the singular values of the Fisher information was misinterpreted as the matrix rank, although it describes the transition of the eigenvalues corresponding to the six pole derivatives to the mode shape derivatives in the Jacobian matrix. On close inspection of Fig. 9.26, the singular values appear to decrease more rapidly in magnitude after the 26th singular value, which may be the true matrix rank. Indeed, removing the eigenvector derivatives from the sensitivity matrix results in an unambiguous matrix rank of six. On the other hand, removing the eigenvector derivatives leads to gradually decreasing singular values. The contribution of the mode shape derivatives appears to be less pronounced. To conclude, the rank computation can be misleading and should always be verified (e.g., by looking at the singular value of the Fisher information matrix). This concludes the case study of the St. Nazaire Bridge model.

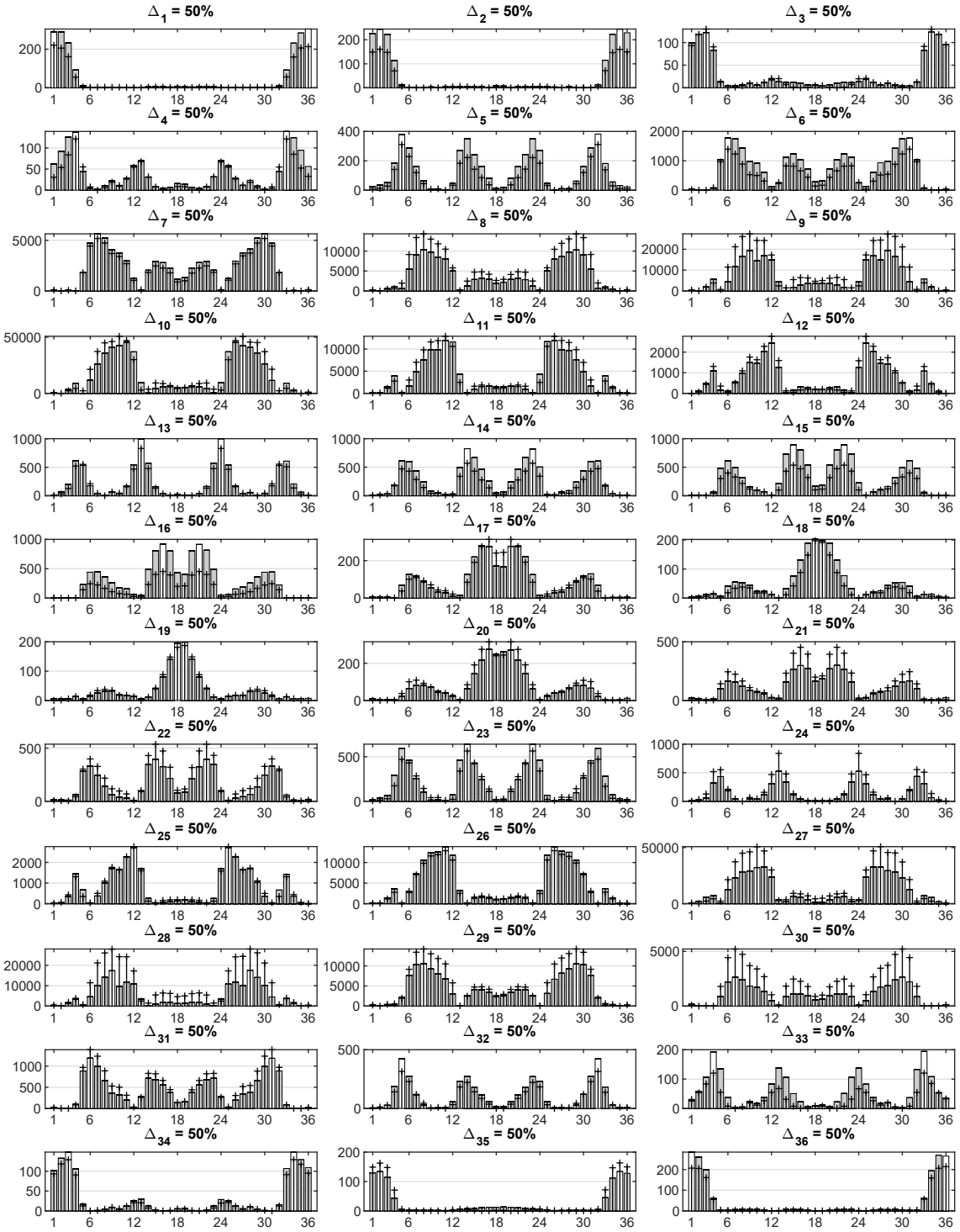

Figure 9.29: Validation state for all 36 damage scenarios

9.3 Summary

This chapter presents two case studies, a laboratory steel beam on pin supports and a laboratory cable-stayed bridge. Based on the hollow structural steel (HSS) steel beam, it is demonstrated

that the prediction of the minimum detectable damage is correct for both model-based and data-driven tests. The prediction is also verified for damage localization tests, with the result that the test response for changed and unchanged parameters (false localization alarms) can be predicted correctly. Moreover, it is shown that the sensor configuration with the shortest measurement duration exhibits the strongest test response to damage, which verifies the approach to sensor placement optimization. Ultimately, damage is simulated by applying extra masses to the beam. The results show that the application of extra masses is a suitable, non-destructive validation method for applications where damaging the structure is not an option.

Applying the tests to the St. Nazaire cable-stayed bridge model showed that a complete failure of a cable pair near midspan can be detected and localized with a measurement duration below 20 s. In-depth studies based on simulated data verified that the prediction of the mean test response to cable failure is accurate, even for large mechanical systems.

Chapter 10

Model Validation

"Basic research is what I'm doing when I don't know what I'm doing."

— Wernher von Braun

In this chapter, another strength of the developed framework becomes apparent: the predictive formula is a suitable tool for model validation studies. A great example is the verification of the input parameters. If all parameters for signal acquisition, signal processing, and damage diagnosis are set appropriately, the prediction of the minimum detectable damage and measurement duration is accurate. This allows deep insights into the effects that individual input parameters have. Since none of the previous studies on stochastic subspace-based damage diagnosis included a systematic validation of the input parameters, a separate chapter is dedicated to this matter.

The chapter is organized as follows: Section 10.1 briefly summarizes the case study, which is referred to throughout all parameter studies. Section 10.2 gives several examples that explain the effect of the main input parameters, including the time lags p and q, the system order n, the number of modes N_m, and the number of data segments for the evaluation of the empirical test distribution N_{seg}. Section 10.3 elaborates on the lower bound for the measurement duration in the reference state and testing state, and Section 10.4 proposes tools to validate the small damage assumption. All findings are summarized in Table 10.4 on page 188, which also gives an overview over all studies in this chapter.

10.1 Case Study

For demonstration purposes, all methods in this chapter are applied to the same case study that was employed in previous chapters. The 4.11 m long simulated steel beam has a hollow structural steel (HSS) cross-section, HSS 152×51×4.78 mm (6 x 2 x 3/16 inches), a modulus of elasticity of $E = 210{,}000$ MPa, and a mass density of $\rho = 7,850$ kg/m^3. The beam is supported by two pin supports and bent about the weak axis. For excitation, white noise is injected at all vertical degrees of freedom, where the system velocities are sampled in the vertical direction at the two sensor locations marked in Fig. 10.1. Damage is defined as a change in stiffness.

The applied test is the model-based detection test (from Section 4.4.1), as it is comparatively simple but allows for the study of all input parameters that have not been discussed in detail in

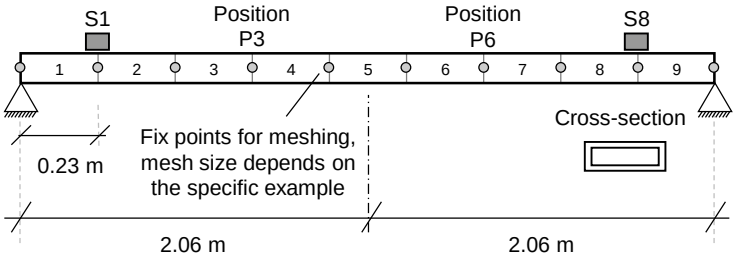

Figure 10.1: Numerical HSS beam with nine materials and two sensors

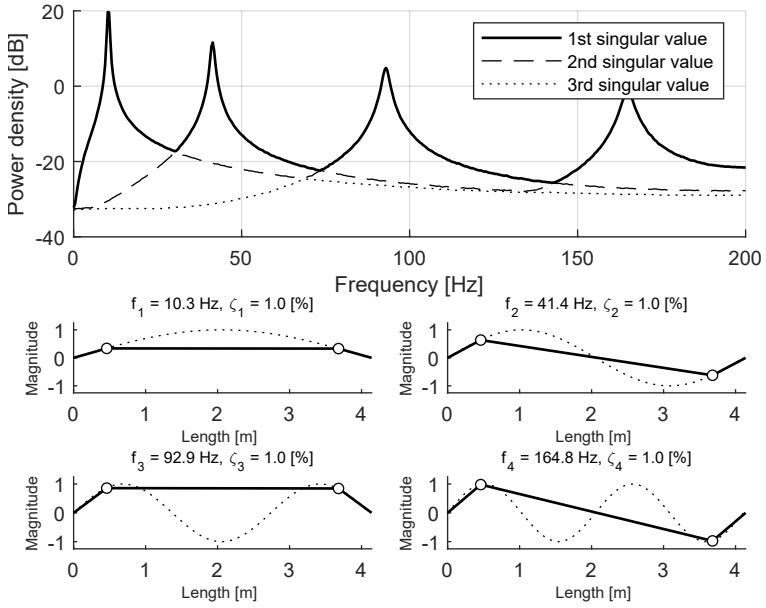

Figure 10.2: Numerical modal analysis

the preceding sections. The test statistic

$$t = \boldsymbol{\zeta}^T \boldsymbol{\Sigma}^{-1} \boldsymbol{\mathcal{J}} \left(\boldsymbol{\mathcal{J}}^T \boldsymbol{\Sigma}^{-1} \boldsymbol{\mathcal{J}} \right)^{-1} \boldsymbol{\mathcal{J}}^T \boldsymbol{\Sigma}^{-1} \boldsymbol{\zeta} \longrightarrow \begin{cases} \chi^2(\nu, 0) & \text{under} \quad H_0 \\ \chi^2(\nu, \lambda) & \text{under} \quad H_1 \end{cases} \tag{10.1}$$

follows a χ^2-distribution with ν degrees of freedom and non-centrality parameter λ. The damage diagnosis test is data-driven, but a finite element (FE) model is required to calculate the sensitivity matrix (Jacobian $\boldsymbol{\mathcal{J}}$) of the damage-sensitive residual $\boldsymbol{\zeta}$ toward changes in the stiffness of the beam. Using ANSYS®, the beam is discretized into 19 nodes with six degrees of freedom (DOF) at each node, and nine line elements to connect the nodes. At the supports, all DOF are restrained except a rotation about the transverse bolt. The line division for meshing is a variable that can be adjusted to refine the mesh size arbitrarily; however, if the examples give no information on the mesh and monitoring parameters, the beam is divided into 18 FE elements and nine materials, so $H = 9$.

Data		Segmenting		Processing	
Measured quantity	velocity	Training segments	100	No. of sensors	r/r_0=2/2
Sampling frequency	400 Hz	Testing segments	100	Time lags	p/q=7/8
Reference data length	120 min	Samples/segment	4,000	System order	$n = 12$
Training/testing data	16.7 min	Duration/segment	10 s	No. of blocks	N_b=57,599

Table 10.1: Default input parameters

Damage is defined as a change in stiffness, so the monitoring vector is

$$\boldsymbol{\theta} = \begin{bmatrix} E_1 & \dots & E_H \end{bmatrix}^T. \tag{10.2}$$

To link changes in the monitoring parameters to the damage-sensitive residual, the monitoring parameters have to be linked to changes in modal parameters first (through the sensitivity matrix $\boldsymbol{\mathcal{J}}^{(3)}$). The considered modal parameters are the poles and mode shapes of the first four modes of vibration, which are visualized in Fig. 10.2. The damping ratio is set to 1.0 % critical damping for simplicity.

The diagnosis is split into three states: the reference state, the training state, and the validation state. In the reference state, all matrices for the damage diagnosis are calculated based on vibration data from the undamaged structure, with the Fisher information matrix as the final result. In the training state, the distribution of the test statistic from Eq. (10.2) is verified by comparing it to its theoretical distribution with $\nu = \text{rank}(\boldsymbol{\mathcal{J}}^T \boldsymbol{\Sigma}^{-1} \boldsymbol{\mathcal{J}})$, and a safety threshold value is set up based on the allowable probability of false alarms (PFA) of 5%. Moreover, the minimum non-centrality λ_{min} and the minimum detectable damage Δ_h are predicted for each monitoring parameter, based on an acceptable probability of detection (POD) of 99.94%. The formula for the minimum detectability is repeated here for convenience:

$$\Delta_h = \frac{1}{\theta_h} \sqrt{\frac{\lambda_{min}}{N F_{hh}}}. \tag{10.3}$$

In the validation state, the change in one monitoring parameter is set to the minimum detectable damage to confirm that the empirical test response coincides with the prediction. A key quantity is the non-centrality ratio (NCR); it describes the ratio of the empirical non-centrality, i.e., the shift in the mean value of the empirical distributions $\lambda = \text{E}[\chi^2(\nu, \lambda)] - \text{E}[\chi^2(\nu)]$, over the minimum non-centrality λ_{min}, with

$$\text{NCR} = \frac{\lambda}{\lambda_{min}}. \tag{10.4}$$

If the prediction of the minimum detectable damage is accurate, the NCR is 100%, and a lower NCR indicates that the predicted minimum damage is underestimated.

10.2 Main Input Parameters

10.2.1 Time Lags

The time lag parameters p and q for the block Hankel matrix determine how accurate and how redundant the dynamic system model is. Where p is the recursion parameter for the observability, which captures the number of observed time steps of a freely decaying system, q is the shift parameter for the evaluation of the covariance functions in between different sensor positions (refer to Chapter 3). The time lags obey the mathematical minimum condition of $pr > n$ and $qr > n$ to guarantee that the block Hankel matrix captures all modes of vibration and that the left null space exists. Since the rank is limited by the shorter matrix dimension, a symmetrical block Hankel matrix is sought, with $p + 1 = q$. However, the following examples show that the time lag parameters also influence the damage detectability.

Example 10.1. Effect of Changing Time Lags
The goal of this example is to evaluate the relation between the minimum detectable damage and the time lag parameters. During the analysis, the system order is fixed to $n = 12$ and the time lag parameters p and q are varied separately, see Fig. 10.3. The first observation is that the accuracy of the prediction is not affected by p and q, as the NCR remains equal for all runs. Another observation is that increasing the time lag parameter p leads to higher damage detectability, where q appears to have no influence on the results of the HSS beam. Increasing the time lag parameters from the minimum value of $p = 7$ to $p = 29$ decreases the minimum detectable damage by 12.8%, from 7.56% to 6.59%, and the minimum measurement duration by 24.0%, from 5.71 s to 4.34 s. Slightly increasing the time lags over the minimum value can be beneficial; however, the damage detectability appears to converge quickly, and little improvement can be achieved with heavy computational burden. Increasing the time lags increases the dimensions of the block Hankel matrix and all derived quantities, including the Gaussian residual, the covariance matrix, and the Jacobian matrix. In the literature on subspace-based system identification (Reynders and de Roeck, 2008), a suggestion is put forward to set the time lag parameter sufficiently high, so one sinus half-wave of the fundamental mode of vibration is captured, and all long-term effects are excluded. This approach is not recommended for subspace-based damage diagnosis, as the measurement duration further increases beyond this point, but could aid with the physical interpretation. The premise is to keep the time lag parameter as high as necessary but as low as possible.

Since the time lags affect the measurement duration, the issue of finding an appropriate setting is of paramount importance for sensor placement optimization, where the measurement duration is employed as a performance criterion. The main issue arises when sensor configurations with varying number of sensors are compared. With an increasing number of sensors r and fixed system order n, the time lag parameter p can be reduced without violating the minimum requirement $pr > n$. Setting the time lag parameters based on the minimum examined number of sensors and keeping it constant throughout the analysis is not recommended. This leads to unfeasibly long computation times of an already expensive objective function. The proposed approach is to set the time lags

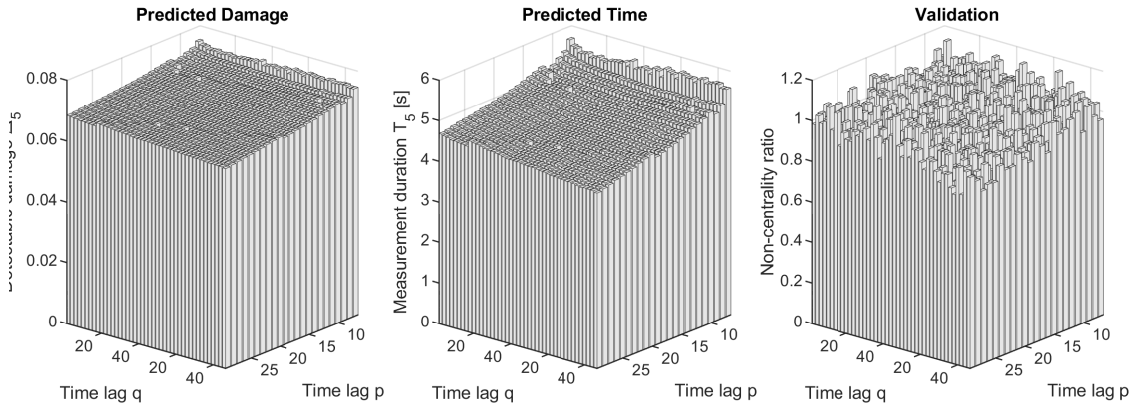

Figure 10.3: Effect of changing time lags

to the minimum values during the numerical optimization procedure, and to perform a parameter study on the time lag parameter only for the optimal sensor layout, and vibration data from the real structure.

10.2.2 System Order

The system order n defines the number of eigenvectors in the block Hankel matrix which the left null space is orthogonal to. For damage diagnosis, it can be set significantly lower than for stochastic system identification. The system order should be set based on the number of physical modes of vibration N_m that are observable in the considered frequency band. Since modes of vibration are contained as complex conjugate vector pairs, a theoretical lower bound is given by the condition $n = 2N_m$; however, an over-determination is recommended to accommodate for stable non-structural modes (Example 10.2) and to reduce the uncertainties in the null space (Example 10.3). Setting the system order to low may manifest itself in a shift of the test statistic towards higher values for the training and the damaged state probability density function (PDF).

Example 10.2. Noisy Measurement Environments
This example shows that noisy measurement environments require a higher system order. The objective is to gradually increase the noise contamination and to study the effect on the minimum detectable damage and the non-centrality ratio for a varying system order n. The noise contamination is measured in percent of the output variance and, for the sake of example, the power spectral density (PSD) for the cases with noise contamination of 5% and 55% are shown in the top plots of Fig. 10.4. The same figure visualizes that the minimum detectable damage increases with increasing noise contamination (bottom left plot), in particular, if the system order is set to the minimum value of $n = 2N_m = 8$. However, the effect can be compensated by increasing the system order n. The bottom right plot shows the NCR which should be equal to one for all cases for the prediction to be accurate. Having said that, increasing noise contamination causes the NCR to exceed 100% unless the system order is set sufficiently high. To summarize, an over-determined

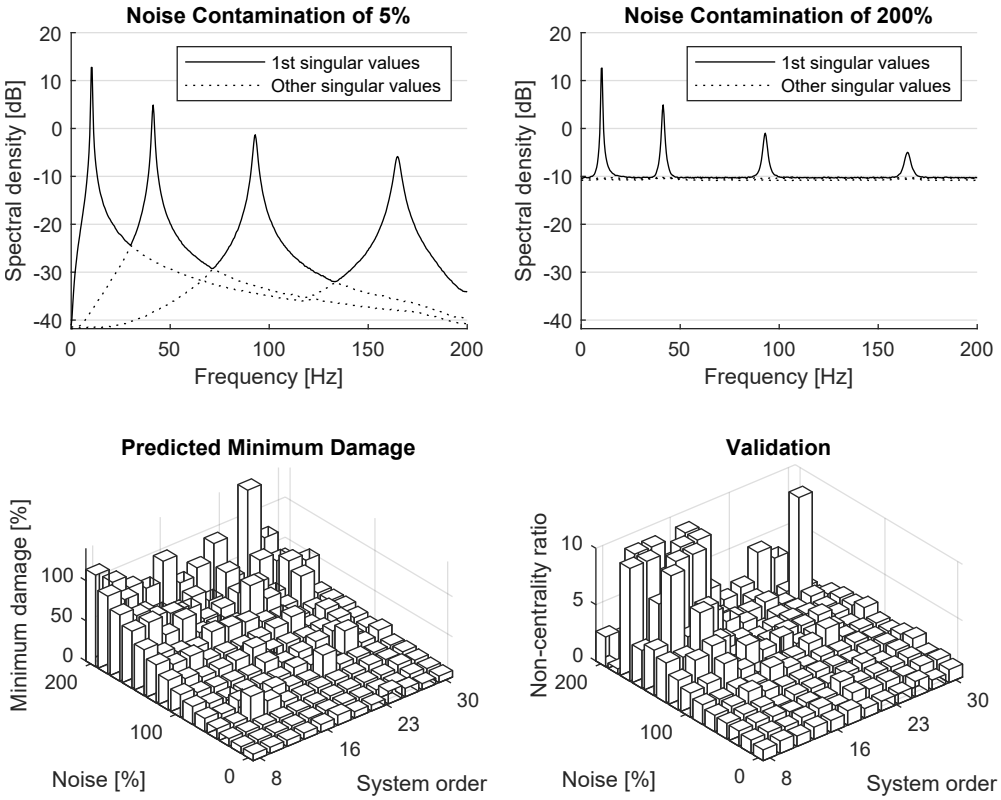

Figure 10.4: Minimum detectable damage and non-centrality ratio for increasing noise contamination. The noise is in percent of the output variance

system order makes it possible to achieve an accurate prediction with high detectability despite an extreme noise contamination.

Example 10.3. Subspace Angles

This example gives reasons for why the system order should be over-determined, even in noise-free measurement environments. The challenge in the estimation of the left null space is the estimation uncertainty, which may impair the orthogonality condition for a low model order. This uncertainty is due to measurement noise and due to the unknown excitation. The recommended way to set up the damage-sensitive residual is to extract the left null space from the block Hankel matrix in the reference state and to pre-multiply it to the block Hankel matrix of incoming data in the testing state. This assumes that the column space of the block Hankel matrix, which contains the structural modes of vibration, is orthogonal to the left null space, with a subspace angle of zero. Due to a variation in the dynamic system model, the subspaces may deviate from zero. The effect becomes apparent when the subspace angle between the Hankel column space and the observability is evaluated, where the observability is constructed in modal coordinates based on the modes of vibration from the FE model, which eliminates uncertainties (see Section 3.3.3). A small subspace angle indicates that the subspaces are nearly linearly dependent, which is to be expected because the observability can be derived from the block Hankel matrix. Figure 10.5 plots the subspace angle

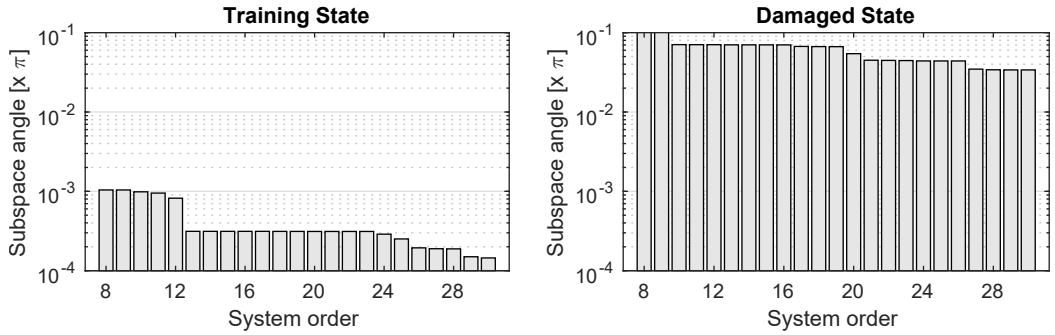

Figure 10.5: Subspace angles between the FEA-based observability and the data-driven column space of the block Hankel matrix

over the system order n. In the damaged state (right plot), the subspace angles are unequal to zero, as the structural health state has changed, so the column space of the block Hankel matrix is not linearly dependent on the columns space of the observability from the reference state. However, a deviation from zero can also be noticed in the reference state (left plot) with a discernible drop after a system order of $n = 12$. That means that the uncertainty in the covariance computation (which causes linear dependencies) can be compensated by increasing the model order over the minimum value of $n = 2N_m = 8$.

10.2.3 Mode Selection

The sensitivity matrix should contain all observable modes of vibration. If the frequency band is widened, and more modes are included in the damage diagnosis, the sensitivity toward structural parameter changes, and the damage detectability increases, in most cases. A minimum number of modes of vibration is required if the Jacobian has to be of full column-rank. In particular for damage localization, the minimum number of modes of vibration is decisive, because it affects the maximum localization resolution. The next three examples help to understand the effect that the number of modes of vibration has on the damage detectability.

Example 10.4. Understanding the Fisher Information
The Fisher information matrix is a measure for the detectability of damage in each monitoring parameter. In Fig. 10.6, the Fisher information is plotted using only the first mode of vibration (top left). The plot also shows the Fisher information using the first two modes (top right), as well as the first three and four modes (bottom plots). The sampling frequency is kept constant, and a modal reduction technique is applied during the vibration generation, so only the considered modes are present in the data and the sensitivity matrix. For demonstration, the beam is split into 54 parameters, and the excitation source is placed on one quarter of the beam. The first two cases with one and two modes (top row) clarify that the Fisher information represents superposed mode shapes. The last two cases with three and four modes (bottom row) further indicate that a higher excitation magnitude leads to an increased Fisher information. Ultimately, the absolute magnitude of the Fisher information increases with an increasing number of modes. To summarize,

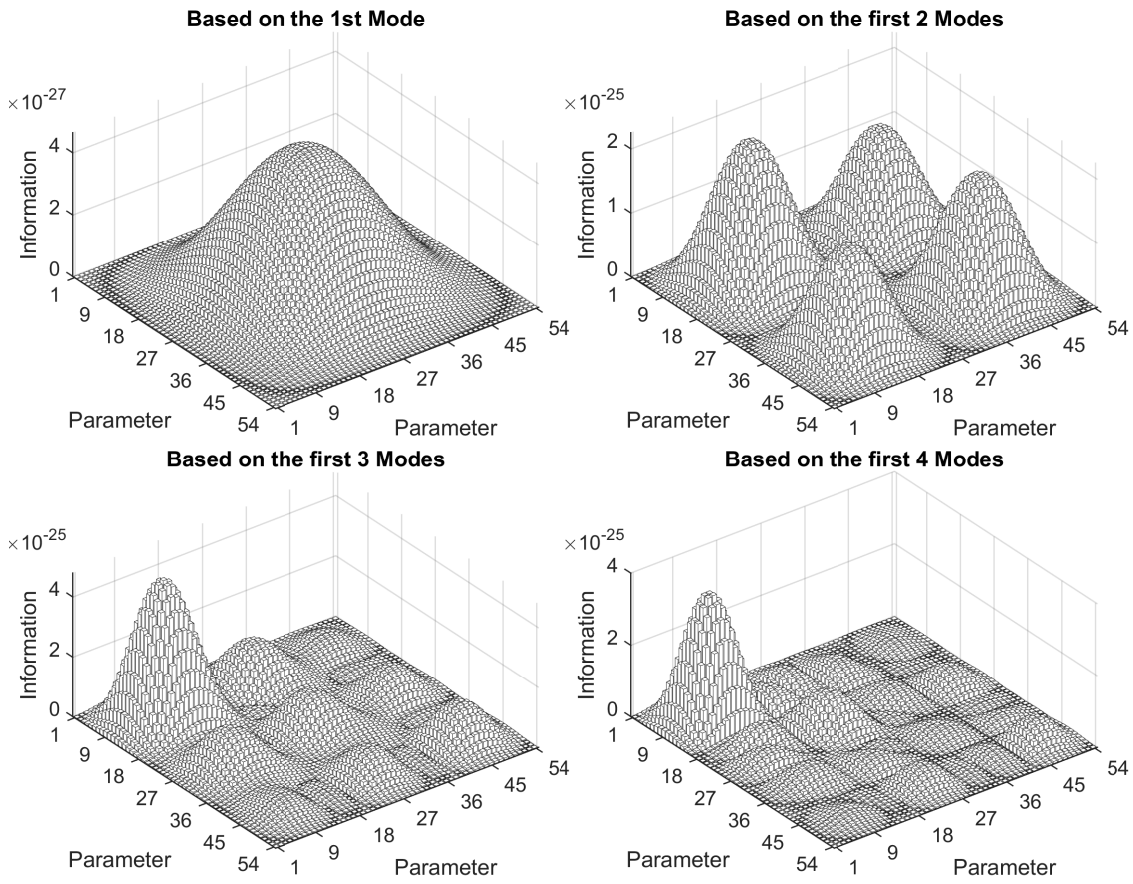

Figure 10.6: Fisher information for a simply supported beam with asymmetrical excitation

detectability depends on the number of modes and the mode shape amplitude at the examined structural parameters, as well as the signal-to-noise ratio.

Example 10.5. Damage Detectability Gain

This example calculates the minimum detectable damage for an increasing number of modes of vibration. In Table 10.2 and Fig. 10.7, the predicted detectable damage is illustrated for 1 - 8 of modes of vibration. For example, the minimum detectable damage in Parameter 7 based on a single mode of vibration is $\Delta_7 = 128.1\%$. Since this is beyond the physical limit of 100%, damage cannot be detected in this parameter. Increasing the number of modes to two causes the minimum detectable damage to drop to $\Delta_7 = 8.4\%$, which corresponds to a detectability gain of 119.8%. Adding a third mode causes the minimum detectable damage to increase to 9.8%, so an increased number of modes does not lead to a higher detectability in all cases. For detecting damages in monitoring parameter 7, Mode 6 appears to be crucial, as it exhibits the highest damage detectability gain of 11.2%. For most other parameters, Mode 3 appears to be more important. The takeaway from this study is that a minimum number of modes is required for the numerical conditioning of the Jacobian matrix, and an increasing number of modes increases the damage

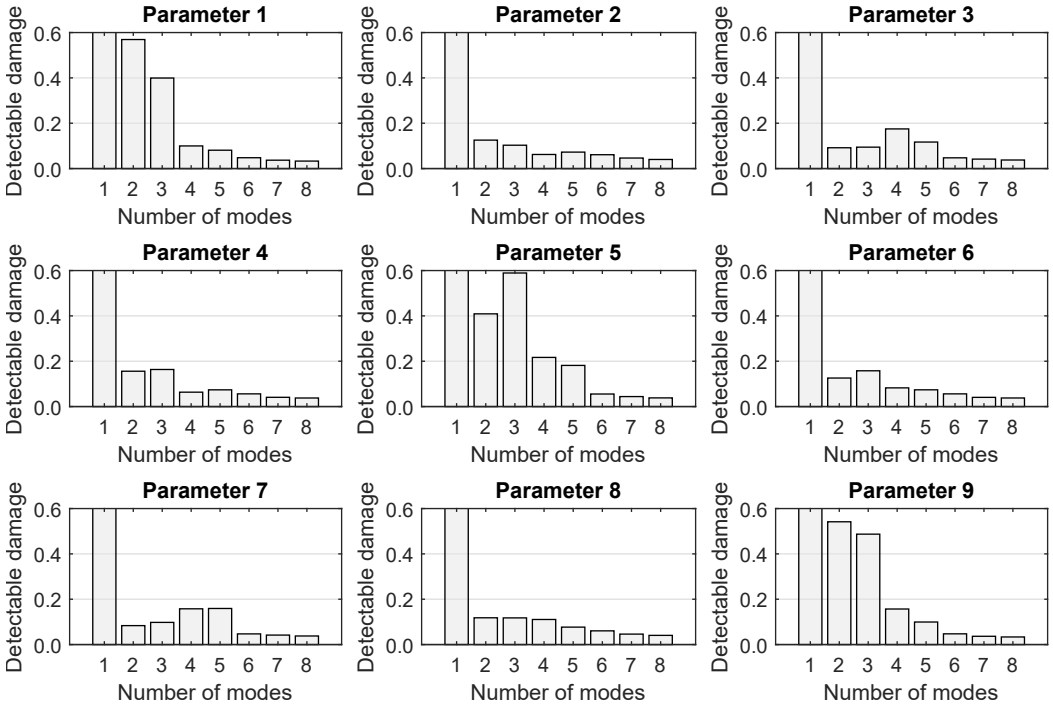

Figure 10.7: Relation between the detectable damage and the number of modes

Minimum Detectable Damage [%]									
Parameter	1	2	3	4	5	6	7	8	9
1 Mode	1675.7	290.4	128.1	85.9	76.0	85.9	128.1	290.4	1675.7
2 Modes	56.9	12.5	9.2	15.6	40.9	12.6	8.4	11.8	54.2
3 Modes	39.9	10.3	9.4	16.4	58.9	15.8	9.8	11.8	48.7
4 Modes	10.0	6.2	17.5	6.3	21.7	8.2	15.8	11.1	15.7
5 Modes	8.1	7.3	11.7	7.4	18.1	7.4	15.9	7.7	9.9
6 Modes	4.8	6.1	4.7	5.6	5.5	5.6	4.7	6.0	4.7
7 Modes	3.7	4.6	4.2	4.1	4.4	4.1	4.2	4.6	3.7
8 Modes	3.3	4.0	3.8	3.8	3.8	3.8	3.8	4.0	3.3
Damage Detectability Gain [%]									
Parameter	1	2	3	4	5	6	7	8	9
2 Modes vs. 1 Mode	1618.8	277.9	119.0	70.3	35.1	73.3	119.8	278.6	1621.5
3 Modes vs. 2 Modes	17.0	2.2	-0.3	-0.8	-18.0	-3.2	-1.4	0.0	5.57
4 Modes vs. 3 Modes	30.0	4.1	-8.0	10.0	37.2	7.5	-6.0	0.7	33.0
5 Modes vs. 4 Modes	1.9	-1.0	5.8	-1.0	3.5	0.9	-0.1	3.4	5.7
6 Modes vs. 5 Modes	3.3	1.2	7.0	1.8	12.6	1.8	11.2	1.6	5.2
7 Modes vs. 6 Modes	1.1	1.5	0.6	1.5	1.1	1.5	0.5	1.4	1.1
8 Modes vs. 7 Modes	0.4	0.6	0.4	0.3	0.6	0.3	0.4	0.6	0.3

Table 10.2: Relation between the detectable damage and the number of modes

detectability differently for each monitoring parameter.

Example 10.6. Unobservable Modes in the Reference State
Unobservable modes of vibration deserve special attention. A mode of vibration is defined as non-observable if all sensors are placed at vibrational nodes, as sufficient excitation is always assumed. Unobservable modes are inevitable during sensor placement optimization, where all possible sensor combinations are explored. For example, placing two sensors at position P3 and P6 in Fig. 10.2 would cause Mode 3 to become non-observable. The first issue is related to the sensitivity matrix. Non-observable modes cause the derivative of multiple modal parameters to be close to zero, and thus, linear dependencies arise in the column space of the sensitivity matrix (Jacobian $\boldsymbol{\mathcal{J}}^{(1)}$). The redundancies are numerical in nature, so they mislead the automated substructuring approach and falsify the damage diagnosis and prediction. Another issue is related to the left null space. If the null space is extracted from the block Hankel matrix, it is not orthogonal to non-observable modes. However, if modes become observable in the damaged state, because damage causes a shift of the vibration nodes, the damage-sensitive residual does not approximate the Gaussian properties and the prediction of the minimum detectable damage is biased. The issue related to the sensitivity matrix can be remedied by over-writing the entries with zero values. Since this does not remedy the issue regarding the left null space, it is generally recommended to remove sensor layouts with non-observable modes from the analysis. Ultimately, these layouts are likely to have a low damage detectability, because non-observable modes do not carry structural information.

10.2.4 Number of Data Segments

Based on the theoretical properties of the underlying χ^2-distribution, meaningful statements regarding the minimum detectable damage can be made. The pursued approach is to split the vibration record into multiple data segments, to repeatedly apply the test to each segment in a Monte Carlo experiment, and to evaluate reliability-based quantities such as the PFA and the POD. An interesting question is how many data segments it takes for the empirical distribution to approximate the theoretical properties. This is important for practical applications, because the number of data segments influences the data length requirements.

Example 10.7. Accuracy of the Empirical Distribution
This example analyzes how many samples are required for the NCR to converge toward 100%. It is based on a idealized χ^2- distribution with $\nu = 18$ degrees of freedom, and a non-central χ^2-distribution with $\nu = 18$ degrees of freedom and a non-centrality of $\lambda = 52.5$. The overlap between the two distributions corresponds to a PFA of 5% and a POD of 99.6%. For the analysis, the number of samples n_s is gradually increased, while re-evaluating the number of degrees of freedom as the sample mean $\nu_{emp} = \mathrm{E}[\chi^2(\nu)]$ and the empirical safety threshold t_{crit} based on a PFA of 5%. Subsequently, the minimum non-centrality λ_{min} is estimated based on a POD of 99.6%, and finally, the predicted non-centrality is divided by the actual non-centrality of 52.5 and plotted over n_s. On the left side of Fig. 10.8, the sample mean values (black dots) are plotted over

the number of samples n_s. The sample mean gradually converges, with acceptable results with less than 5% deviation to the true mean value after 100 - 110 data segments. On the right side of Fig. 10.8, the NCRs (black dots) are displayed over n_s. The predicted non-centrality converges faster than the mean value with acceptable results with less than 5% deviation after about 30 samples. Moreover, a 1 - 2% error in the non-centrality appears inevitable even for large sets with 1,000 data samples. To highlight this, the experiment is repeated 10 times, and a grey envelope is drawn over all data points. To conclude, the number of data segments should exceed 30, but larger sample sizes with $n_s = 100$ are advisable.

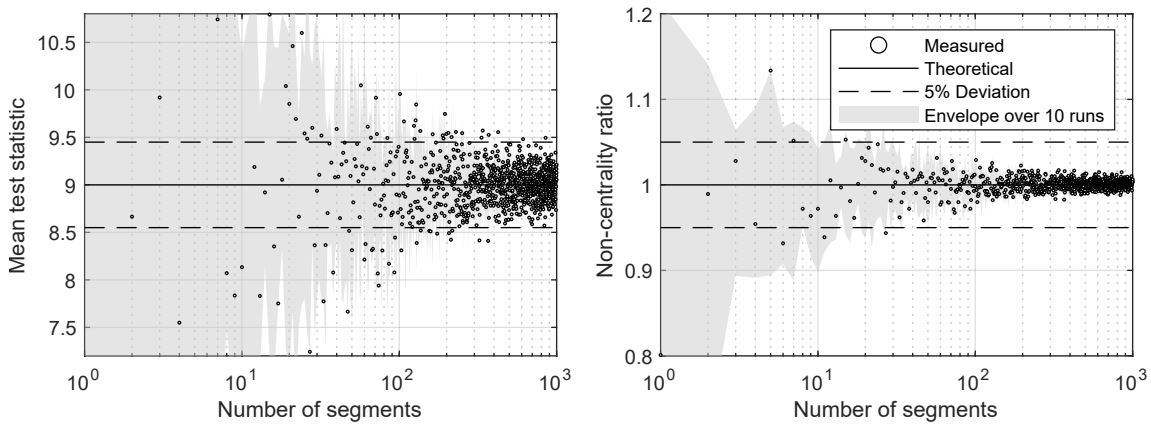

Figure 10.8: Convergence of the predictions for a varying number of data segments

10.3 Minimum Data Length

Damage detection and localization based on the asymptotic local (AL) approach is based on the assumption of a large sample size N, which leads to the rather significant question of whether there is a lower bound for N. In general, the residual's distribution is approximated through a Gaussian distribution, and the approximation becomes more accurate for larger N. All quantities, including the test statistics, the Fisher information, and the formula for minimum detectability are based on the normally distributed residual. Vice versa, there must be a lower bound for the sample size below which the predictive framework is invalid because Gaussianity is not given anymore. This is particularly relevant for sensor placement optimization, where the optimal sensor layout is found as the one with the minimum measurement duration. The sample size N is the product of the measurement duration and the sampling frequency

$$N = T f_s$$

meaning the sample size could be increased by increasing the sampling frequency or increasing the measurement duration. The effect of both input parameters is studied in this section, starting with the sampling frequency.

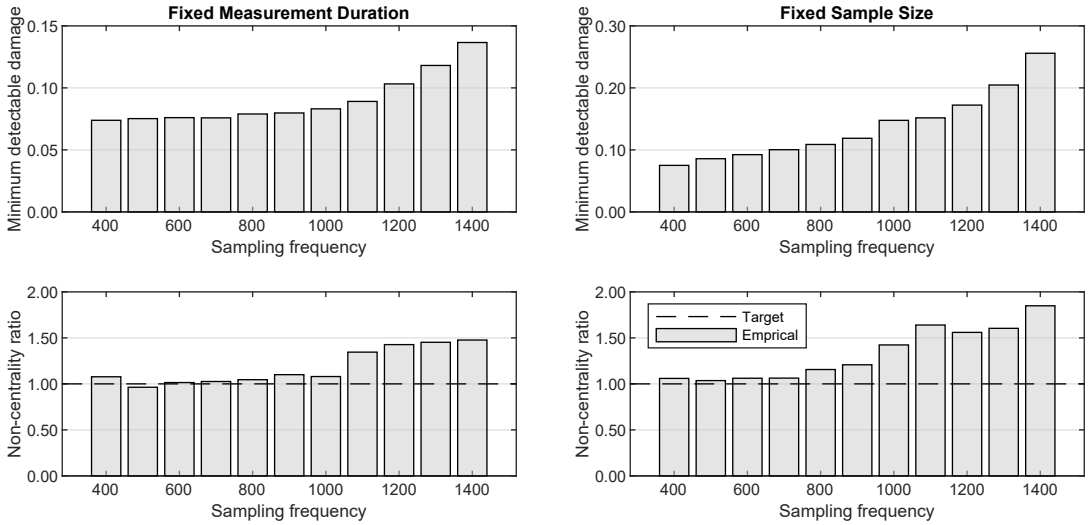

Figure 10.9: Increasing the sampling frequency for a fixed measurement duration T (left side) and a fixed sample size (right side). Refer to Table 10.3 for input parameters

Fixed Measurement Duration											
Frequency f_s [kHz]	0.4	0.5	0.6	0.7	0.8	0.9	1.0	1,1	1,2	1,3	1,4
Duration T [s]	10	10	10	10	10	10	10	10	10	10	10
Sample size $N/1000$ [-]	4	5	6	7	8	9	10	11	12	13	14
Fixed Sample Size											
Frequency f_s [kHz]	0.4	0.5	0.6	0.7	0.8	0.9	1,0	1,1	1,2	1,3	1,4
Duration T [s]	10.0	8.0	6.7	5.7	5.0	4.4	4.0	3.6	3.3	3.1	2.9
Sample size $N/1000$ [-]	4	4	4	4	4	4	4	4	4	4	4

Table 10.3: Input parameters for the evaluation of the minimum detectable damage and the non-centrality ratio in Fig. 10.9

10.3.1 Sampling Frequency

Increasing the sampling frequency does not increase the damage detectability if the same number of modes is considered. This is unsurprising, as the information on the structural parameters primarily depends on the number of modes in the sensitivity matrix. The premise is to set the sampling frequency (after downsampling) high enough, so the highest mode of vibration is sufficiently captured—even in the damaged state—and low enough so no unwanted modes of vibration are captured that are not considered in the sensitivity matrix.

Example 10.8. Increasing the Sampling Frequency
The effect of a changing sampling frequency can be shown by means of an example using the HSS beam from Fig. 10.1. To avoid having high-frequency modes become observable, the vibration data is generated based on a modal reduction approach that considers only the first four modes of vibration. In the first case, the measurement duration is fixed to $T = 10$ s. Increasing the

sampling frequency from 400 Hz to 1,400 Hz for a fixed measurement duration means that the sample size increases as well, see Table 10.3. The resulting minimum detectable damage and the non-centrality are shown on the left side of Fig. 10.9. The minimum detectable damage remains unchanged if the sampling frequency is increased from 400 Hz to 1,000 Hz. Consequently, the sampling frequency is not a tuning parameter for damage detectability, although it is part of the predictive formula. Increasing the sampling frequency beyond 1,000 Hz leads to detectability changes, but the predictions also become inaccurate (which is indicated through the non-centrality ratio beyond 100%), so the results are biased for some reason. In the second case, the sample size is fixed to $N = 4{,}000$, so varying the sampling frequency now changes the measurement duration, see Table 10.3. The results for the minimum detectable damage and the non-centrality ratio are shown on the right side of Fig. 10.9. The measurement duration appears to be a powerful tuning parameter to increase the detectability for changes between 400 Hz and 1,000 Hz. More studies on the effect of the measurement duration follow in the subsequent section.

10.3.2 Measurement Duration

The measurement duration during testing is a powerful tuning parameter for damage detectability. According to the predictive formula, the mean test response is proportional to the measurement duration, see Eq. (10.3). The minimum measurement duration varies for the reference state and the testing state. In the reference state, a long measurement duration is required to guarantee that all matrices converge toward their final matrix, where the measurement duration during training and testing can be significantly shorter because the matrices are not re-evaluated. Consequently, the measurement duration in the testing state depends on how fast the residual attains the Gaussian properties. To analyze the lower bound for the measurement duration, two additional convergence criteria are introduced, i.e., the induced matrix norms and the Gaussianity check.

The induced matrix norm is a standard measure to verify the convergence behaviour of matrices. In the Euclidean vector space, the matrix norm of a matrix $\mathbf{A}$ can be approximated through its maximum singular value σ_{max} with (Atkinson, 1989)

$$||\mathbf{A}||_2 = \sigma_{max}(\mathbf{A}). \tag{10.5}$$

The Gaussianity check is a method-specific technique to verify that the distribution of the damage-sensitive feature approximates a Gaussian distribution. In theory, Gaussianity is only given if the sample size is infinite, because then, the central limit theorem (CLT) from Eq. (4.28) holds true with

$$\sqrt{N} \cdot (\hat{\boldsymbol{\varepsilon}} - \mathrm{E}[\hat{\boldsymbol{\varepsilon}}]) \longrightarrow \mathcal{N}(\mathbf{0}, \boldsymbol{\Sigma}). \tag{10.6}$$

One way to validate that the Gaussian properties are well-approximated is to transform the residual into standard Gaussian form and to check its mean vector and covariance. This is done by pre-

multiplying the inverse square root of the covariance matrix

$$\mathbf{z} = \sqrt{N} \cdot \hat{\mathbf{\Sigma}}^{-1/2} \hat{\boldsymbol{\varepsilon}} \longrightarrow \mathcal{N}(\mathbf{0}, \mathbf{I}). \tag{10.7}$$

In the following, the index i is introduced to clarify that each residual entry approximates a standard Gaussian distribution $z_i \longrightarrow \mathcal{N}(0,1)$. By evaluating the residual multiple times in a Monte Carlo experiment, the mean value and the standard deviation can be plotted for each entry. Since the standard deviation is a statistical quantity of higher order than the mean value, it converges slower. Another way to verify the Gaussianity is to transform the residual into standard Gaussian form while considering the parametrization and the estimated Jacobian matrix $\hat{\boldsymbol{\mathcal{J}}}$:

$$\begin{aligned} \sqrt{N} \cdot \hat{\mathbf{\Sigma}}^{-1/2} \hat{\boldsymbol{\varepsilon}} &\longrightarrow \mathcal{N}(\mathbf{0}, \mathbf{I}) \\ \sqrt{N} \cdot \hat{\boldsymbol{\mathcal{J}}}^T \hat{\mathbf{\Sigma}}^{-1/2} \hat{\mathbf{\Sigma}}^{-1/2} \hat{\boldsymbol{\varepsilon}} &\longrightarrow \mathcal{N}(\mathbf{0}, \hat{\boldsymbol{\mathcal{J}}}^T \hat{\mathbf{\Sigma}}^{-1} \hat{\boldsymbol{\mathcal{J}}}) \\ \mathbf{z} = \sqrt{N} \cdot (\hat{\boldsymbol{\mathcal{J}}}^T \hat{\mathbf{\Sigma}}^{-1} \hat{\boldsymbol{\mathcal{J}}})^{-1/2} \hat{\boldsymbol{\mathcal{J}}}^T \hat{\mathbf{\Sigma}}^{-1} \hat{\boldsymbol{\varepsilon}} &\longrightarrow \mathcal{N}(\mathbf{0}, \mathbf{I}) \end{aligned} \tag{10.8}$$

with $z_i \longrightarrow \mathcal{N}(0,1)$. Repeatedly evaluating the residual from Eq. (10.8) and evaluating the mean and the standard deviation of each entry gives insight into whether the Gaussian residual, the covariance, and finally, the Jacobian matrix have converged. As the residual is projected onto the monitoring parameters through the Jacobian matrix, the number of residual entries reduces to the number of monitoring parameters. Ultimately, statistical hypothesis tests can be applied to verify the Gaussianity with the null hypothesis $H_0: \; z_i \longrightarrow \mathcal{N}(0,1)$. For this purpose, the distribution is divided into N_{bin} number of bins, so the χ^2-goodness-of-fit test can be applied to each bin with

$$\chi^2 = \sum_{i=1}^{N_{bin}} (O_i - E_i)^2 / E_i. \tag{10.9}$$

The test verifies whether the observed residual entries O_i in the bins are likely to be drawn from a standard Gaussian distribution with expected bin count E_i. For clarification, Example 10.9 visualizes the mean and standard deviation of the non-parametric and parametric CLT, as well as the goodness-of-fit tests.

Example 10.9. Gaussianity Checks in the Training State

For visualization, this example performs the non-parametric and the parametric zero mean check, unit variance check, and Gaussianity check in the training state of the HSS beam. In the training state, the test statistic from Eq. 10.1 is repeatedly applied to 100 data segments of 10 s length in a Monte Carlo experiment, so the test distribution can be plotted in histograms. In the same way, the residuals from Eq. (10.7) and (10.8) can be evaluated in a Monte Carlo experiment, so the mean value and the standard deviation of each residual entry can be plotted. In the top left and the bottom left plot of Fig. 10.10, the mean and the standard deviation of each residual entry is shown. As expected, the mean values are close to zero but only a few entries of the standard deviation approximate the expected value of one, because the covariance is not of full rank. The mean

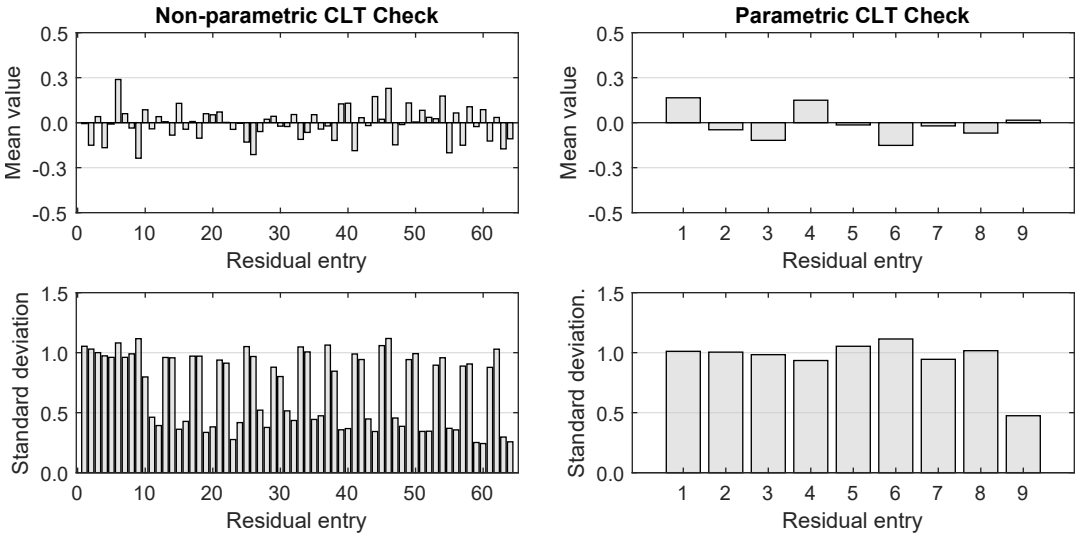

Figure 10.10: Zero mean and unit variance checks in the training state

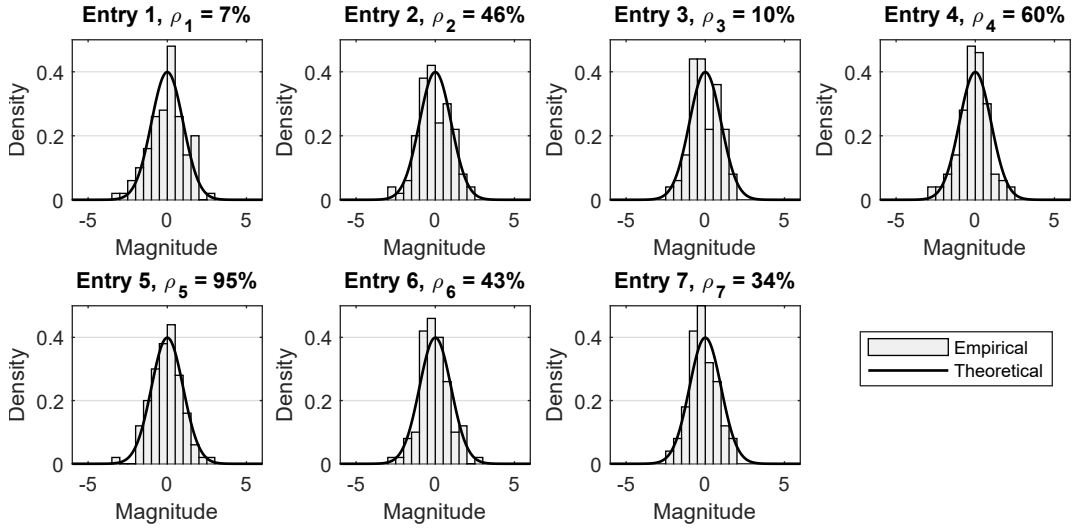

Figure 10.11: Gaussianity check, goodness-of-fit test on the parametric residual

values and the standard deviations of the parametric residual, where the residual is projected onto the monitoring parameter through the Jacobian matrix, approximate the theoretical distributions $\mathcal{N}(0,1)$ for 8/9 residual entries, as shown on the right side of Fig. 10.10. The deviation in the covariance of the ninth entry comes at no surprise, as the Jacobian matrix is column-rank deficient. This demonstrates how relevant the newly developed damage detection test from Section 5.3 is, as it can also handle Jacobian matrices with column-rank deficiency. Moreover, it demonstrates that the Gaussianity check or unit variance check is a suitable tool to get insight into the conditioning of the damage diagnosis problem. In Figure 10.11, the distributions for the parametric test are shown, after QR-decomposition and column pivoting, see Section 5.3. The first observation is that the number of distributions reduces from nine to seven, as the Fisher information has a rank of seven.

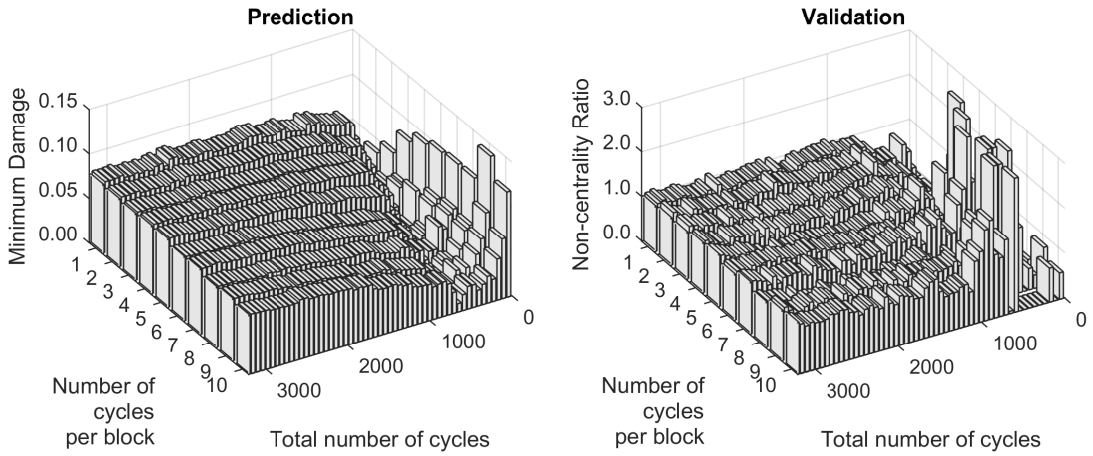

Figure 10.12: Convergence of the minimum detectable damage

Applying the χ^2-goodness-of-fit test to the distributions leads to $\rho-$values that range between 7% and 95%. Using a standard threshold of ρ=5%, the goodness-of-fit test verifies the Gaussianity for all seven entries, so the measurement duration of 10 s is long enough.

Example 10.10. Convergence of the Minimum Detectable Damage
This example studies the convergence behaviour of the minimum detectable damage in Parameter 5, so Δ_5. Where the measurement duration during testing is fixed to $T = 10$ s, the measurement duration in the reference state is varied from 0.1 s to 300 s, which corresponds to one and 3,090 cycles of the fundamental mode of vibration with a period of $T_{0,1} = 1/10.3\ s$. Moreover, the block length for the covariance computation N_b (see Eq. 4.10) is varied from one cycle per block to ten, because it affects the convergence behaviour. Fig. 10.12 shows the corresponding minimum detectable damage (left plot). It converges toward the same value regardless of the chosen block length, but it converges faster for a block length with one cycle per block compared to a block length with 10 cycles per block. The observation is confirmed by the NCR (right plot), as it converges faster toward the optimal value of one for a short block length with one cycle. For a large block length with ten cycles, singularities occur, with NCRs up to three and higher. The singularities are further discussed in the subsequent examples. For the structure under consideration, a measurement duration of $T^0 = 500$ cycles (48.8 s) appears sufficient, provided the short block size of one cycle is used. This example suggests it is beneficial to keep the block length low, where a block length that corresponds to one cycle of the fundamental mode of vibration appears sufficient.

Example 10.11. Convergence of the Matrix Norm
To further analyze the convergence behaviour of the matrices from the reference state, this example evaluates the matrix norm of all three matrices, i.e., the Fisher information, the covariance, and the Jacobian matrix. The goal is to find out which matrix critically determines the measurement duration in the reference state. This time, the measurement duration is varied from one cycle to 1,000 cycles of the fundamental mode of vibration, and the block length is varied from one cycle to ten. In Fig. 10.13, the norm of the Fisher information and the norm of the covariance are

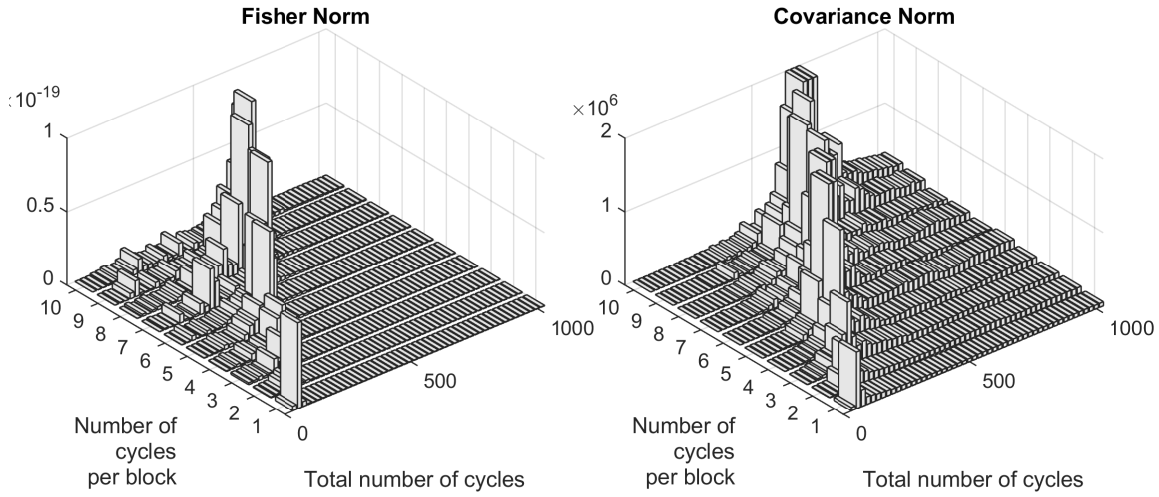

Figure 10.13: Convergence of the Fisher information matrix norm and the covariance matrix norm

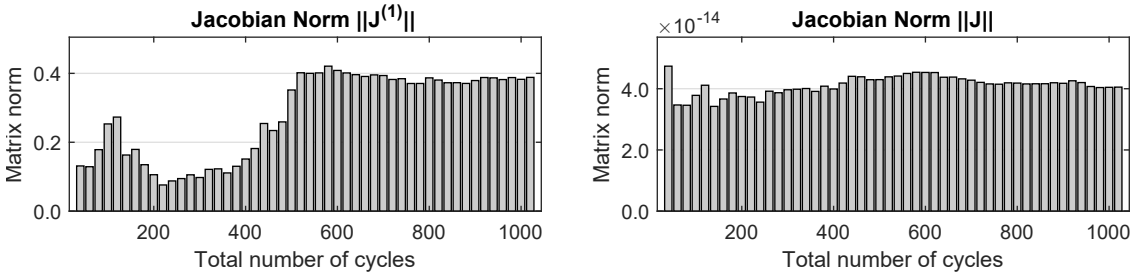

Figure 10.14: Convergence of the Jacobian matrix norm

plotted. The plot highlights singularities in the norm of the Fisher information (peaks), which form a diagonal when plotted over the measurement duration and block length. That means that, for varying block length, the singularities occur for varying measurement duration, but for the same number of blocks, see Eq. (4.10). The number of blocks can be calculated by dividing the total number of cycles by the number of cycles per block, where the peaks occur at $n_b = N/N_b = 66$. The Fisher information is calculated based on the covariance matrix, which shows the singularities at the same locations, implying that the singularities are caused by the covariance matrix. If the measurement duration is increased beyond the singularity, the matrix norm converges toward a constant value for all block lengths, but the convergence is faster for a short block length with one cycle compared to a block length with 10 cycles. This confirms the finding from Example 10.10. For a block length of one cycle, the matrix norm of the Fisher information converges after 100 cycles, and the covariance matrix after 200.

The covariance is a statistical quantity of higher order in comparison to the mean value. Therefore, it is expected that the Jacobian matrix converges faster than the covariance matrix, as it links the mean value of the data-driven residual to modal parameters and structural parameters.

However, the matrix norm on the right side of Fig. 10.14 clarifies that the Jacobian matrix $\boldsymbol{\mathcal{J}}$ converges after 600 cycles of the fundamental mode of vibration, so significantly slower compared to the covariance matrix (with 100 cycles). On close inspection of the Jacobian matrix components, it can be understood that the first Jacobian matrix $\boldsymbol{\mathcal{J}}^{(1)}$ (which links the data-driven residual to the modal parameters) causes the slow convergence, see left side of Fig 10.14. In other words, although a data-driven modal analysis is circumvented by taking the modal parameters from the model, the Jacobian matrix only converges if the measurement duration is sufficiently long, due to the covariance approximation in the estimated block Hankel matrix, see Eq. (4.17). For the considered HSS beam, the minimum measurement duration is equivalent to 600 cycles of the fundamental mode of vibration, which corresponds to 48.5 s and 19,400 data points. The same results are obtained for the convergence studies regarding the minimum detectable damage, see Fig. 10.12. The findings can be cross-checked with a rule of thumb from stochastic system identification, where the measurement duration is approximated through $T^0 \approx 1000$ cycles (Brincker and Ventura, 2015). Another way to validate that the Jacobian matrix critically determines the measurement duration in the reference state is to check the non-parametric and parametric Gaussianity check, which is done in the subsequent example.

Example 10.12. Convergence Toward Gaussianity (Reference State)
In this example, the unit variance checks are applied to training data while varying the measurement duration in the reference state. Figure 10.15 plots the standard deviation of the non-parametric and parametric test, from Eq. (10.7) and (10.8), over the measurement duration (i.e., the number of cycles of the fundamental mode) and the residual entries. For the non-parametric test, all residual entries converge toward the standard Gaussian distribution with a standard deviation of one after 200 cycles. For the parametric test, the minimum measurement duration is equivalent to 300 cycles, so a longer measurement duration is required if the Jacobian matrix is considered. Comparing this measurement duration to the measurement duration from Example 10.10 and 10.11 shows that the residual converges faster toward its assumed statistical properties than the minimum detectable damage and the matrix norms, where convergence was achieved after $T^0 = 600$ cycles. Moreover, this example illustrates that the residual converges slower toward its assumed statistical properties if the parametric version is considered, confirming that the convergence behaviour of the Jacobian matrix is decisive for the measurement duration in the reference state.

Example 10.13. Convergence Toward Gaussianity (Testing State)
In this example, the unit variance checks are applied to vibration data in the testing state, where the mean value of the Gaussian distribution has changed. The covariance is taken from the reference state and the non-parametric and parametric tests are applied to see when the standard deviation approximates the theoretical value of one, see Eq. (10.7) and (10.8). Fig. 10.16 plots the standard deviation over the residual entries and the number of cycles of the fundamental mode of vibration. The non-parametric version converges within 10 cycles (left side), where the parametric version required more than 80 cycles (right side). The NCR in Fig. 10.17 confirms that the residual converges after T = 80 cycles. To conclude, for the Gaussian framework to come into effect, a lower

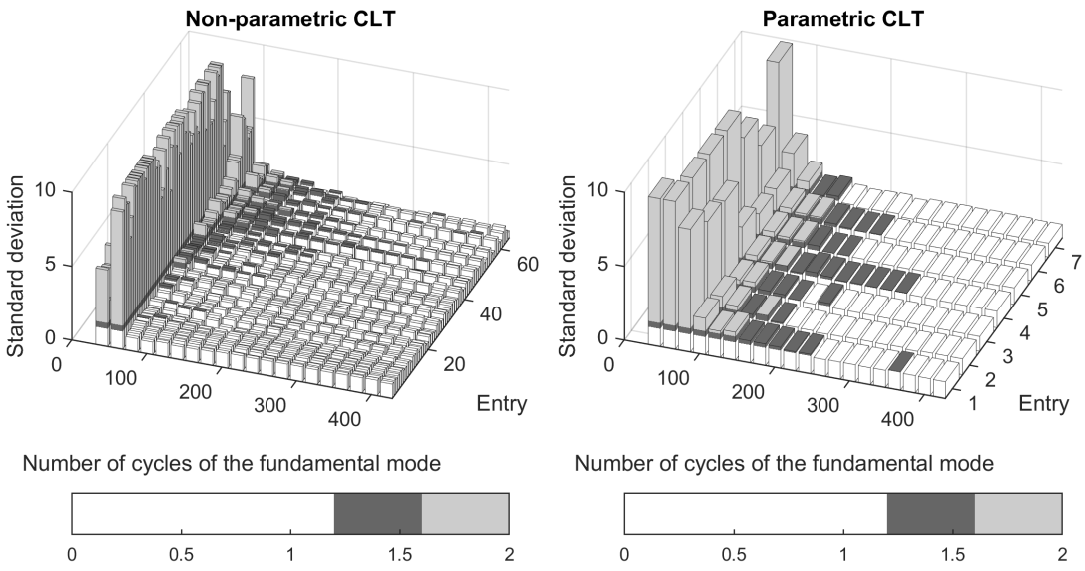

Figure 10.15: Gaussianity convergence studies in the reference state

bound for the measurement duration in the testing state is to be considered. However, this lower bound is sufficiently low, so it does not limit the theories developed in this thesis.

All studies regarding the minimum data length can be summarized as follows:

- The measurement duration in the reference state does not affect the damage diagnosis results once the reference matrices have converged.
- The Jacobian matrix dictates the measurement duration in the reference state with a minimum measurement duration corresponding to 600 cycles of the fundamental mode of vibration (58 s or 23,300 data points).
- The covariance matrix converges fast if the block length is kept short. A block length that corresponds to one cycle appears sufficient. Longer block lengths may cause non-structural long-term effects to be considered.
- There is a lower bound for the measurement duration during testing. Below this threshold the damage-sensitive residual does not attain the Gaussian properties.
- The lower bound for the examined HSS beam is 80 cycles (7.77 s or 3,100 data points), which is sufficiently low, so it does not limit the predictive framework.

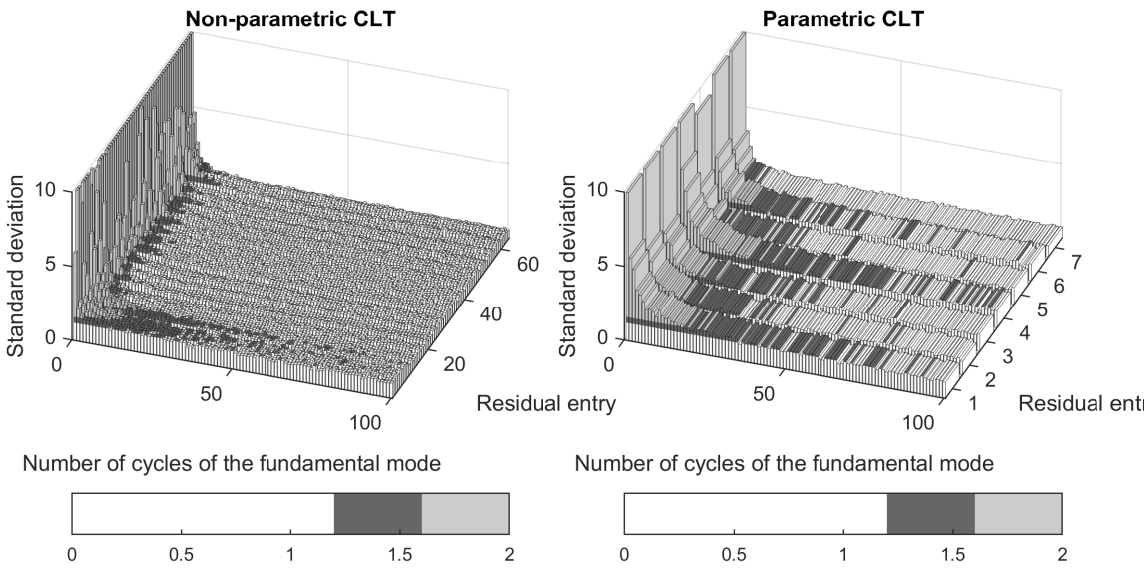

Figure 10.16: Gaussianity convergence studies in the testing state

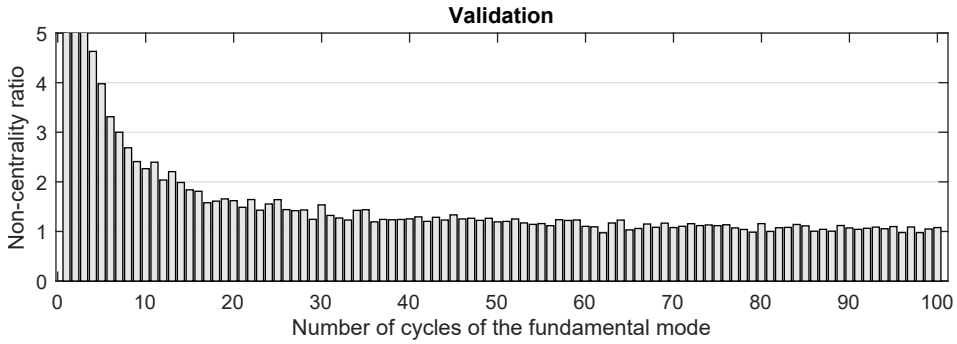

Figure 10.17: Convergence of the non-centrality ratio in the testing phase

10.4 Small Damage Assumption

The AL approach assumes that the residual converges toward a Gaussian distribution, for a very long measurement duration and small changes, and the Jacobian matrix is linearized. This linearization allows for the minimum detectable damage to be predicted, but the prediction is only accurate if the damage extent is small. Vice versa, there may be an upper bound for the minimum detectable damage, and this section introduces validation techniques to identify this upper bound. As explained in Chapter 4, the sensitivity matrix of the residual vector toward structural parameters is split into three parts

$$\boldsymbol{\mathcal{J}} = \left.\frac{\partial E_{\boldsymbol{\theta}}[\boldsymbol{\varepsilon}]}{\partial \boldsymbol{\theta}}\right|_{\boldsymbol{\theta}=\boldsymbol{\theta}^0} = \boldsymbol{\mathcal{J}}^{(1)} \cdot \boldsymbol{\mathcal{J}}^{(2)} \cdot \boldsymbol{\mathcal{J}}^{(3)}. \tag{10.10}$$

The first sensitivity matrix $\boldsymbol{\mathcal{J}}^{(1)}$ links the data-driven residual to modal parameters. The second sensitivity matrix links data-driven modal parameter to model-based ones (through $\boldsymbol{\mathcal{J}}^{(2)}$), and the third on links model-based modal parameter to structural parameters through $\boldsymbol{\mathcal{J}}^{(3)}$.

10.4.1 Jacobian Prediction Error

The Jacobian prediction error (JPE) employs the Jacobian matrix to predict changes in modal parameters based on changes in structural parameters, and subsequently evaluates the relative deviation in the predicted and the measured frequencies and mode shapes. As shown in this section, the JPE can be applied to verify individual components of the Jacobian matrix from Eq. (10.10), making it the most universal validation technique for the small damage assumption. For the prediction, the structural parameter change $\Delta\theta_h = \theta_h - \theta_h^0$ is multiplied with the corresponding Jacobian matrix column $\boldsymbol{\mathcal{J}}_h^{(3)}$ to predict the modal parameter change vector

$$\Delta\eta^{pred} = \boldsymbol{\mathcal{J}}_h^{(3)} \Delta\theta_h. \tag{10.11}$$

Adding the modal parameter vector from the reference state

$$\eta_{pred} = \eta^0 + \Delta\eta^{pred}, \tag{10.12}$$

and re-combining the vector components corresponding to poles (they are split into real and imaginary parts), the poles can be converted into predicted natural frequencies f^{pred}. Subsequently, the predicted natural frequencies can be compared to the measured ones from the FE model, using the Jacobian prediction error

$$\text{JPE} = \frac{f^{pred} - f}{f}[\%]. \tag{10.13}$$

Equivalently, the mode shape entries can be compared using the JPE. This is more tedious, in particular when many sensors are considered, because the number of mode shape derivatives is $N_m \times r$, where N_m is the number of modes of vibration for damage screening, and r is the number of sensor locations.

$$\text{JPE} = \frac{\Psi_{ij}^{pred} - \Psi_{ij}}{\Psi_{ij}}[\%] \tag{10.14}$$

The same idea can be applied to verify the Jacobian matrix for a data-driven parametrization $\boldsymbol{\mathcal{J}}^{(1)}$. For that purpose, the mean residual vector has to be generated by running a Monte Carlo simulation. Based on the inverted Jacobian matrix and the mean residual, the change in modal parameters can be predicted to

$$\Delta\eta^{pred} = \boldsymbol{\mathcal{J}}_h^{(1)\dagger}(\mathrm{E}[\boldsymbol{\varepsilon}] - \mathrm{E}[\boldsymbol{\varepsilon}^0])\sqrt{N}. \tag{10.15}$$

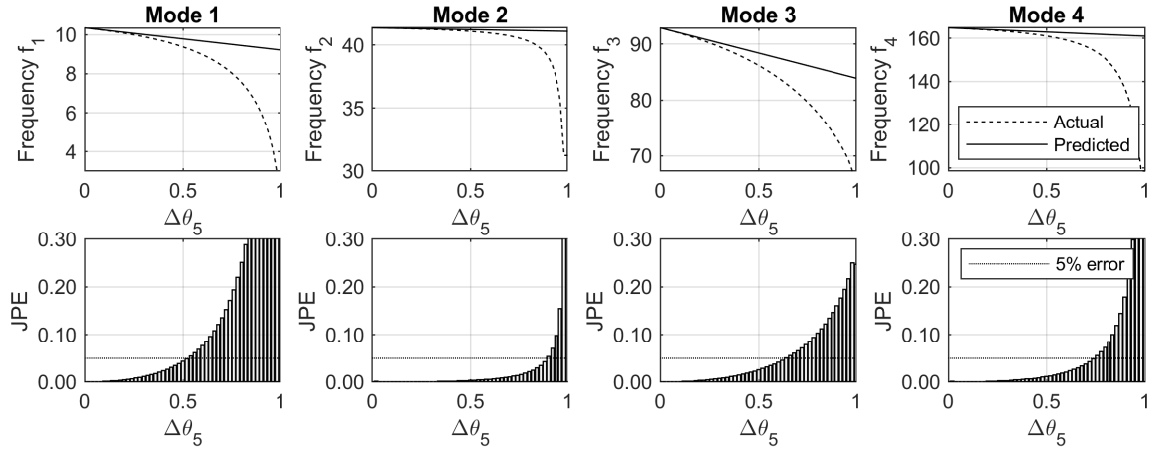

Figure 10.18: Jacobian prediction error (JPE) for the change prediction in natural frequencies (shown for Parameter θ_5)

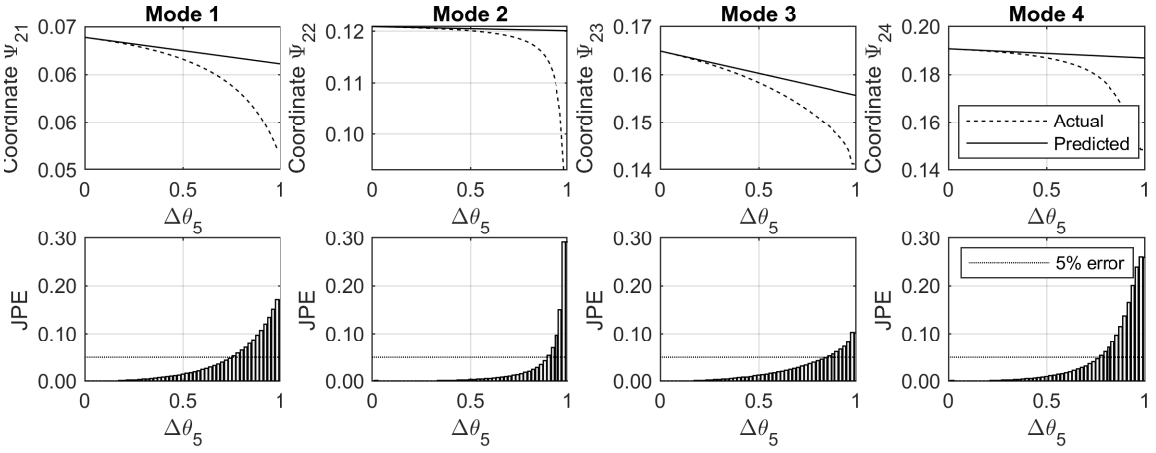

Figure 10.19: Jacobian prediction error (JPE) for the change prediction in mode shape coordinates (shown for Parameter θ_5)

Ultimately, the steps in Eq. (10.12), Eq. (10.13), and Eq. (10.14) can be repeated to verify the prediction based on the Jacobian matrix $\boldsymbol{\mathcal{J}}^{(1)}$.

Example 10.14. JPE for a Model-based Parametrization

In this example, the Jacobian prediction error is evaluated for the HSS beam from Fig. 10.1 to verify the bias that is introduced through the linearization of the model-based Jacobian matrix $\boldsymbol{\mathcal{J}}^{3}$. The example focuses on structural changes in Parameter 5 (the stiffness of the HSS beam at midspan) and its effect on modal parameters. The applied parameter change in the FE model is varied between 0% and 100%, and the predicted natural frequencies are compared to the measured ones from the model in Fig. 10.18. The measured frequencies (dotted line) non-linearly change with increasing damage extent, where the Jacobian matrix linearizes the curve at $\theta_5 = \theta_5^0$ (solid line). The plot also shows the JPE (in the bar plots below) for all four modes of vibration. Up to a damage extent of $\Delta_5 = 50\%$, the error stays below 5%, so the Jacobian matrix $\boldsymbol{\mathcal{J}}^{(3)}$ introduces

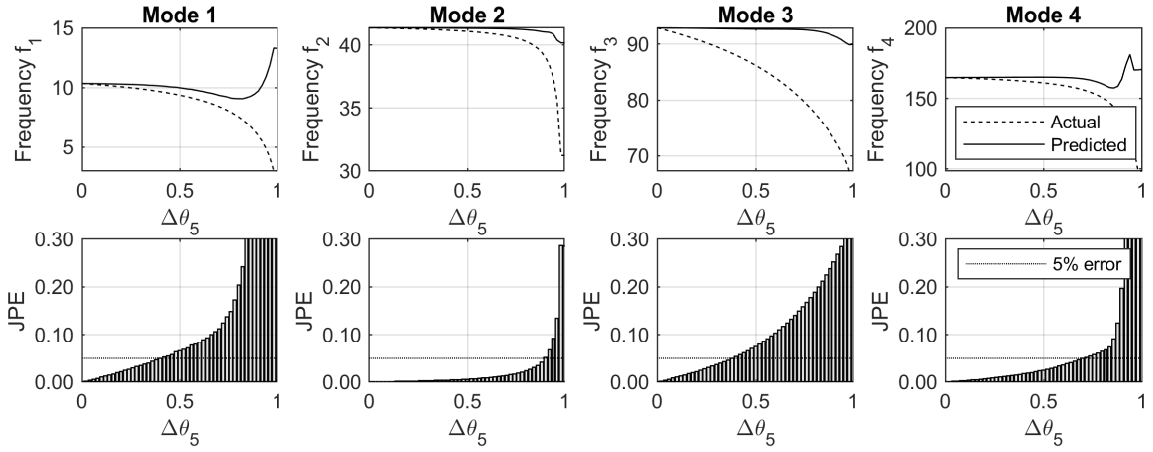

Figure 10.20: Jacobian prediction error (JPE) for the change prediction in natural frequencies (shown for Parameter θ_5)

little bias in the prediction of the minimum detectable damage. Fig. 10.19 illustrates the JPE for mode shapes. Up to a damage extent of 75%, the JPE remains below 5%, so the mode shape linearization is more accurate than the linearization of the natural frequencies.

Example 10.15. JPE for a Data-driven Parametrization
This example evaluates the JPE for the Jacobian matrix $\boldsymbol{\mathcal{J}}^1$, which links the data-driven mean residual to data-driven modal parameters. A single parameter change in the FE model causes all modal parameters to change, as well as multiple entries in the Gaussian residual to deviate from the zero mean conditions. Therefore, none of the natural frequency curves form a straight line when plotted over the structural parameter change in Parameter 5, which varies from 0% to 100%, see Fig. 10.20. The JPE is meaningful nonetheless, and up to a damage extent of 50%, the JPE stays below 5%, so the predictions are very accurate.

10.4.2 Degeneration Check

Another default test is the degeneration check. It analyzes whether the Jacobian matrix is of full column rank. One way to verify this is to perform the parametric Gaussianity test from Eq. (10.8), where the convergence of the standard deviation toward the theoretical value of one is analyzed (see Example 10.9). Another way is to plot the singular values of the Fisher information and to evaluate the Fisher matrix rank (FMR).

$$\text{FMR} = \text{rank}\left(\boldsymbol{\mathcal{J}}^T \boldsymbol{\Sigma}^{-1} \boldsymbol{\mathcal{J}}\right) \tag{10.16}$$

If the Jacobian matrix is column-rank deficient, i.e., if the number of dominant singular values is smaller than the number of monitoring parameters, the damage detection test has to be modified using a QR-decomposition with column pivoting. Moreover, the minmax localization test is not applicable without previously substructuring the Jacobian matrix (see Chapter 6).

Parameter	Effect / Importance	Recommendation
Time lag parameter p and q	- p captures the number of time steps of a freely decaying system and q is the shift parameter for the evaluation of the covariance functions - Affects the covariance matrix and the minimum detectability	- Set as high as necessary to consider the physics of the problem - Set as low as possible for numerical efficiency
System order n	- Determines the size of the left null space - Affects noise rejection capabilities	- Over-determine the system order over the minimum value of $n > 2N_m$
Modes of vibration N_m in the Jacobian matrix	- The number of modes and mode shape amplitudes at structural parameters affect the detectability - Affects the localization resolution - A minimum number is required to obtain full rank sensitivity matrices	- Ensure that all observable modes are considered in the Jacobian - Disregard sensor layouts with non-observable modes
Number of data segments	- Affects the accuracy of the prediction - Even for idealized processes, the accuracy varies by 1-2%	- Use 100 or more data segments - Use no less than 30 data segments
Sampling frequency f_s	- It is an application-specific input parameter for signal processing - Does not affect the detectability	- Set appropriately, so all modes in the Jacobian matrix are captured, even in the damaged state
Duration in reference state T^0	- Must be long enough for the Jacobian, the covariance, and the Fisher information matrix to converge - Does not affect the damage diagnosis once convergence is achieved	- Use sufficiently long data sets - If only short data sets are available, consider running a numerical simulation to evaluate the minimum data length. Verify convergence of the Jacobian matrix $\boldsymbol{\mathcal{J}}^{(1)}$, or the Fisher information
Duration in testing state T	- Must be long enough for the Gaussian framework to come into effect - Is a tuning parameter for damage detectability and localizability	- Consider applying the Gaussianity check, in particular after sensor placement optimization
Small damage assumption	- There is an upper bound for the minimum detectable damage - Beyond the threshold the predictions become inaccurate - Damage diagnosis is still possible	- Check the Jacobian prediction error for every application

Table 10.4: Best practices for stochastic subspace-based damage diagnosis

10.5 Summary

This chapter demonstrates that the predictive framework can be employed for model validation studies. Model validation includes the verification of crucial input parameters, such as the time lag parameters, the system order, the number of modes of vibration, and the number of data segments for the distribution evaluation. Moreover, several convergence criteria are introduced to study the lower bound for the measurement duration in the reference state and in the testing state, e.g., the standard Gaussianity check. The results from numerical case studies are reassuring, as the lower bound does not impose significant limitations to the theories developed in this thesis. The results further illustrate that the convergence behaviour of the covariance matrix depends on the block length, and the Jacobian matrix dictates the measurement duration in the reference state. Ultimately, multiple analysis tools are developed to analyze the small damage assumption of the asymptotic local (AL) approach, including the limitations of the change linearization through the Jacobian matrix. It appears that there is an upper bound for the minimum detectable damage beyond which the predictions become inaccurate. However, damage detection and localization is still possible. All case studies are based on a numerical hollow structural steel (HSS) beam, but the tools are universally applicable to other structures provided a finite element (FE) model is available. In this sense, this chapter summarizes the best practices for stochastic subspace-based damage diagnosis, with a concise summary in Table 10.4.

Chapter 11

Conclusions

"Damage assessment requires a comparison between two system states."

— Axiom II of SHM
(Farrar and Worden, 2012)

This thesis builds a framework to analyze the minimum diagnosable damage, which is defined as the minimum changes in local structural components that can be reliably detected and localized based on changes in global damage-sensitive features under consideration of statistical uncertainties related to ambient excitation and noise. All considerations are made based on vibration data from the undamaged structure in combination with a finite element (FE) model. This avoids empirical and structure-specific experiments, and makes the framework universally applicable to a wide range of civil and mechanical engineering structures (all structures that can be modelled in FE software). Damage is defined as a change in a model-based design parameter and numerous damage scenarios are considered, including changes in material constants or cross-sectional values, support displacements, or changes in prestressing forces. The framework is developed for stochastic subspace-based residuals because of its real-time capabilities, but it is universally applicable to any damage-sensitive feature whose distribution can be approximated through a Gaussian distribution. Traditionally, vibration-based structural health monitoring (SHM) is divided into four stages: the instrumentation of structures with vibration sensors, vibration measurements, the extraction of damage-sensitive features, and the damage diagnosis. This thesis suggests adding two building blocks to this procedure, i.e., the performance evaluation before a SHM system is installed and the model validation to perform quality control checks on existing instrumentation. Performance evaluation means that the diagnosability of damages can be assessed before they occur, even for unique structures, such as bridges, and unprecedented damage events, such as megathrust earthquakes. Based on the results in this thesis, the value of a SHM system can be assessed even if no vibration data from the damaged state is available, which is a powerful amendment to Axiom II of SHM. Model validation means that by comparing the predicted to the measured test response to extra masses, the effectiveness of existing instrumentation can be checked, input parameters can be verified, and the limitation of underlying damage diagnosis methods can be analyzed.

The applied damage detection and localization tests are based on the asymptotic local (AL) approach, which provides parametric and non-parametric tests. More importantly, the AL is not a black-box machine learning tool, but can be linked to structural models of the examined structures through analytical sensitivity vectors. This allows one to evaluate the global vibration while

focusing the damage diagnosis on local structural components that are critical for the safety and the serviceability of the structure. Other advantages are that the damage localization resolution can be manually adjusted and that false localization alarms can be quantified. In contrast to other methods, the statistical uncertainties due to short measurement records and the unknown system excitation can be quantified and propagated through the damage diagnosis, allowing for a reliability-based approach to evaluate the damage diagnosis results.

This last chapter summarizes the contributions of this thesis and ties them back to the research objectives from the introduction (see Section 11.1). Moreover, particular strengths and limitations of the developed theories are highlighted (Section 11.2), and possible future research topics are addressed (Section 11.3).

11.1 Contributions

This work's objective was to resolve a series of practical issues related to vibration-based damage diagnosis on civil engineering structures. Table 11.1 summarizes the main contributions, with more comments on the significance and the degree of maturity of individual methods in the subsequent paragraphs.

(1) **Minimum Detectable Damage.** The core of this thesis is a formula to predict the test response to damage based on vibration measurements from the undamaged structure in combination with a FE model. Moreover, it introduces a reliability concept for global vibration monitoring based on the acceptable probability of false alarms (PFA) and the minimum probability of detection (POD), where the latter is tied back to the national safety standards for assessing engineering systems. By combining the predictive formula with the reliability concept, the minimum detectable damage can be calculated. The predictive framework is developed based on the subspace-based residual but is applicable to any damage-sensitive feature whose distribution approximates a Gaussian distribution. According to the derived formula, damage detectability depends on the following aspects:

- The sensitivity of the feature
- The signal-to-noise ratio
- The reliability requirements toward the test results
- The measurement duration
- The complexity of the monitoring problem

The formula can also be solved for the measurement duration if the user fixes the minimum detectable damage. It is demonstrated that the prediction holds true for both model-based and data-driven tests, so the FE model is only necessary for calculating the minimum detectable damage, but not in the active monitoring phase. To avoid numerical issues, the damage detection test is modified, so it can efficiently be applied to large mechanical structures in

	Contributions	Methodology	Ref.
(1)	Proposed a method to determine the minimum detectable damages	Derived a formula to predict the mean test response to damage and developed a reliability concept for vibration-based damage detection	Ch. 5
(2)	Developed a method to determine the minimum localizable damages	Proposed mathematical expressions to quantify the minimum identifiable damage, and the false alarm susceptibility	Ch. 6
(3)	Proposed a performance criterion that optimizes damage detectability	Derived a formula for the minimum measurement time and used it as a measure for the detectability of damage in local structural components	Ch. 7
	Proposed a performance criterion for optimal damage localizability	Proposed a compromise function to find the optimal compromise between damage localization resolution, damage identifiability, and false alarm susceptability	Ch. 7
	Combined the proposed performance criteria with a genetic algorithm to efficiently find an optimal sensor layout for large structures	Implemented single-objective and multi-objective versions of the genetic algorithm including the 2nd generation of the non-dominated sorting genetic algorithm (NSGA-II)	Ch. 7
(4)	Expanded the damage detection method to diagnose changes in prestress and support displacements	Modified the direct sensitivity method based on the geometric stiffness matrix (stress stiffening)	Ch. 8
(5)	Proposed non-destructive validation techniques for quality control of existing instrumentation	Proposed extra masses to verify the efficiency of the damage diagnosis module and to verify the predicted minimum diagnosable damages	Ch. 9
	Developed tools to verify the input parameter settings	Put forward tools to quantify the absolute minimum measurement during training and testing, the system order, the time lags, and the number of modes of vibration	Ch. 10
	Devised tools to quantify the error due to the small damage assumption	Introduced the Jacobian prediction error as well as degeneration checks	Ch. 10

Table 11.1: List of contributions of this thesis

combination with a low number of modes of vibration (this determines the "complexity" of the monitoring problem).

The findings address multiple fundamental problems related to SHM. Firstly, the damage detectability can be evaluated for unique structures, without having to perform resource-consuming laboratory experiments, and remedies the issue of transferring findings from one structure to another. Quantifying the detectable damage based on the POD alleviates doubts on the sensitivity of global monitoring approaches to small and local damages (Brownjohn et al., 2011). Therefore, it is a powerful tool to convince decision-makers of the benefit of implementing a SHM system. Besides, the formula for the minimum measurement duration may replace the existing rules of thumbs. Ultimately, the predictive framework links SHM to structural reliability analysis (Thöns et al., 2018) and helps to evaluate the value of monitoring information in general (Long et al., 2020).

Non-parametric damage detection based on the AL approach is a mature technology established in commercially available computer software. The predictive formula has shown to be

highly accurate in numerical simulations of various structures and applicable to laboratory tests on a pin supported beam. The next step is to validate the predictions based on vibration data from a full-scale bridge.

(2) **Minimum Localizable Damage.** Damage localization poses additional challenges compared to damage detection. However, this thesis extends the predictive framework to damage localization tests, enabling the mean test response, the minimum identifiable damage, and the corresponding measurement duration to be predicted. Moreover, a method is devised to predict the test response of parameters that have not changed due to damage (false localization alarms). This is achieved for multiple damage localization tests, including the direct localization test or the minmax localization test.

This addresses another fundamental issue of SHM, i.e., the over-parametrization of FE models. The problem is that multiple monitoring parameters in the model have a similar effect on the damage-sensitive feature, and, vice versa, it is challenging to identify the structural parameters that have changed. A remedy is to cluster monitoring parameters with similar sensitivities (Balmès et al., 2008b; Allahdadian et al., 2019). Clustering the monitoring parameters is equivalent to dividing the FE models into substructures, in which damage can be isolated. However, this thesis gives evidence that finding the optimal number of clusters is a multi-objective optimization problem. It appears that with an increasing number of clusters, the damage localization resolution increases, but the damage identifiability in each parameter decreases, and the number of false alarms changes.

The method is robust when applied to numerical simulations and shows encouraging results when optimizing the damage localization on a laboratory steel beam. Therefore, it constitutes an important step toward real-time damage localization using the AL approach. However, additional studies are required, including laboratory tests and full-scale tests on bridges to increase its robustness and mature the technology.

(3) **Sensor Placement Optimization.** A criterion for sensor placement is proposed that optimizes the damage *detectability*. It is combined with a state-of-the-art optimization method, i.e., a genetic algorithm (GA), to efficiently find a close-to-optimal solution in large mechanical systems, such as bridges. The sensor placement strategy takes as input the requested detectable damage in individual FE model components, and yields as output the optimal sensor layout. By combining the proposed criterion with the considerations regarding the optimal substructure arrangement from the previous paragraph, a sensor placement strategy is proposed to optimize the damage *localizability*. The developed framework is capable of finding the optimal sensor layout and an appropriate number of sensors. Ultimately, a multi-objective GA is implemented to overcome the problem of combinatorial explosion.

The sensor placement strategy addresses two primary issues. Firstly, only a few method-specific criteria exist that directly optimize the damage detectability. None of the existing

criteria appears to consider the relative degradation of engineering design parameters, although this is the decisive quantity for structural design and safety. By proposing the minimum detectable damage as a criterion for sensor placement optimization, the purpose of vibration analysis is brought in line with structural design philosophies. Secondly, most sensor placement strategies optimize the criteria on a global vibration level, but the structural health depends on the integrity of local components that are critical for the structural safety and serviceability (such as joints), and damage tends to accumulate at well-known hotspots, see Fig. 1.4. Since the minimum detectable damage is defined components-wise, the sensor layout can be tuned to become more sensitive to damage hotspots.

The developed tools and the literature review on existing sensor placement strategies can enforce a transition in the British Columbia Smart Infrastructure Monitoring System (BCSIMS) from sensor layout based on engineering judgment to highly efficient layouts with optimal damage diagnosability tuned to address the specific service requirements of individual structures.

(4) **Monitoring Boundary Conditions.** Prior to this work, the damage diagnosis methods from the previous paragraphs have focused on changes in structural parameters, while changes in boundary conditions remained unconsidered. This thesis puts forward an approach to diagnose support displacements or changes in prestress, by considering the geometric stiffness matrix (stress stiffening) in the calculation of the sensitivity matrix. This way, changes in boundary conditions can be incorporated into the established diagnosis framework, so they can be localized and distinguished from changes in cross-sectional values or material properties, and their minimum diagnosable change can be predicted.

Multiple damage scenarios during extreme events such as earthquakes cause changes in boundary conditions, e.g., ground failure (see Fig. 1.4). Moreover, excessive support settlements or loss of tension in prestressing tendons (due to slippage or stress corrosion) are common problems in bridge monitoring, making the developments particularly relevant.

The monitoring of boundary conditions is studied based on numerical examples, such as an individual prestressing tendon and the Shipshaw cable-stayed bridge. However, it has not been applied to any laboratory or real-life applications. Further laboratory tests and real-life applications are required to achieve a sufficient degree of maturity.

(5) **Model Validation.** This thesis's more practice-oriented contributions are the non-invasive validation technique using extra masses as well as a series of checks for model validation. The employed damage diagnosis method is universal in that it can be applied to a wide range of structures and any model-based parameter. This allows one to define damage as changes in mass and to conduct non-invasive validation studies based on extra masses. Moreover, a series of studies on the input parameter settings are conducted that give guidance on how to set crucial signal processing parameters. Tools are introduced to verify the minimum data length requirements and the minimum number of data segments for reliable damage diagnoses.

Additional tools are introduced to verify the small damage assumption that is made in the considered damage diagnosis method.

This remedies another fundamental issue of SHM systems and the BCSIMS. Bridges are vital links in primary infrastructure, and damaging them for research purposes is not an option. Due to each structure's uniqueness, it is challenging to assess whether the theoretical assumptions are fulfilled and whether input parameters for signal processing are set appropriately. To check this, the developed tools can be applied (without having to damage the structure or interrupt its operation) and routinely scheduled tests based on extra masses could aid in the evaluation of the fitness of aging instrumentation.

A laboratory experiment based on extra masses has shown encouraging results validating the theoretical developments of this thesis. The next step to transition this approach into engineering practice is to evaluate the magnitude of extra masses to real bridges and to conduct a full-scale experiment.

11.2 Strengths and Limitations

Below, the particular strengths and limitations of the predictive framework are categorized.

Reliability. One of the main strengths of the developed method to analyze the minimum detectable damages is its comprehensiveness, as it considers many aspects that are typically criticized about global vibration monitoring: the sensitivity to local damages, the uncertainties in the estimation of the data-driven features, and the reliability of the damage diagnosis results. A damage diagnosis is considered "reliable" if the PFA is close to zero and the POD is close to one-hundred percent. Likewise, a damage scenario is considered "detectable" if the test result is reliable–while considering the uncertainties due to stochastic loads, measurement noise, and limited sample size. In other words, the distributions of the data-driven features in the undamaged and damaged states are considered, and a decision is made by comparing the tests against a safety threshold.

Universality. Another strength of the developed framework is its universality. In contrast to most other approaches that analyze the minimum diagnosable damages, the predictive formula is universally applicable to a wide range of structures and element types (i.e., to all structures that can be modelled in FE software). Secondly, the framework can be applied to analyze a wide range of damage scenarios, including changes in material constants, cross-sectional values, support displacements, and prestressing forces. The framework is derived based on the subspace-based residual vector, but it is applicable to numerous damage-sensitive features, the distribution of which can be approximated by a Gaussian distribution.

Gaussianity. The methods in this thesis are developed for damage-sensitive features with Gaussian distributions. It is important to keep in mind that the Gaussian framework is invalid if the

damage-sensitive feature is not normalized, meaning if it changes due to environmental and operational variables (EOVs) (where the next paragraph explains how to handle EOVs). Another case, where the Gaussian assumption is violated is when the inputs are strongly correlated, e.g., if rotating machinery is placed on or near the structure, so periodic signals are introduced. Weakly correlated inputs (with temporal correlations) are unproblematic, because the system dissipates energy, and the correlations decay over time. The fact that damage-sensitive features can be approximated by a Gaussian distribution after applying the central limit theorem (CLT) is shown through several laboratory experiments. For output covariance estimates of stable linear systems, Gaussianity is not an assumption but a consequence from the CLT, and it is not a limitation for damage-sensitive features. Viewed from a different perspective, the assumption of Gaussianity is a strong point because many features can be approximated by a Gaussian distribution, possibly even features derived from a non-linear system response. The premise is that the Taylor series expansion can be applied to the feature with respect to structural design parameters, and that higher order terms can asymptotically be neglected.

Environmental and Operational Variables. Depending on the effect that changing operational loads (e.g., wind or traffic loads) or environmental changes (e.g., temperature fluctuations) have on the statistical distribution of the features, the Gaussian distribution may no longer be given. Moreover, the associated uncertainties are not captured in the covariance matrix, which only considers the stochastic loads, measurement noise, and limited sample size. However, this does not mean that the predictive framework cannot be applied to real structures under changing EOVs; it means that the damage-sensitive features have to be normalized prior to the analysis of the minimum diagnosable damages. Data normalization approaches have not been considered in this thesis, but several solutions are available in the literature on stochastic subspace-based methods (Balmès et al., 2008a, 2009; Magalhães et al., 2012; Oliveira et al., 2018; Viefhues et al., 2020). By applying these approaches, the effect of EOVs can be eliminated and the Gaussian characteristics of the features can be preserved. This widens the applicability of the predictive framework from numerical simulations and laboratory studies to real world structures under changing environmental conditions.

Excitation Properties. For damage diagnosis based on the subspace-based residual, the minimal detectable damage and the optimal sensor placement depend on the excitation characteristics and the extent of noise contamination. This is because the predictive framework considers the sensitivity of the damage-sensitive feature and the uncertainty in its estimation. In general, this means that bias is introduced if the excitation characteristics change significantly between training and testing, or if the noise characteristics on the real structure are significantly different to the modelled excitation environment. The fact that the excitation properties matter is also an advantage because the application-specific signal-to-noise ratio can be considered when assessing the damage detectability. What is more, this alleged weakness is compensated by another strength of the predictive framework, which is the universal applicability to different damage-sensitive features. One

way to enhance the robustness is to use a different damage-sensitive residual that is more robust to changes in the excitation characteristics (Döhler et al., 2014b).

Small Damage Assumption. Another point is the small damage assumption made in the AL approach, including the change linearization through the first-order sensitivity matrix. The decisive formula of the AL approach is the CLT stating that, for very large measurement durations and small damages, the distribution of the damage-sensitive residual converges toward a Gaussian distribution. On the downside, this means that system changes (in modal parameters or structural parameters) cannot exceed a specific limit, otherwise, the prediction becomes inaccurate. In theory, higher-order terms could be considered in the Jacobian (Adhikari and Friswell, 2001) but they would require an entirely different framework for the prediction of the minimum detectable damage. On the upside, this makes the AL approach highly sensitive to small and local damages, and a slight modification of modal parameters may correspond to significant damage in structural design parameters for large structures. The limitations of the small damage assumption underline the importance of the developed validation techniques to verify that the predicted detectable damage does not exceed the limitation superimposed by change linearization.

Data Requirements. One aspect is that the sensor placement strategy requires vibration data from the undamaged structures (real data or simulated data), where many other approaches do not. Another aspect is that the developed methods are reliability-based, meaning they focus on the in-depth analysis of statistical test distributions rather than individual test samples for performance evaluation. Because of this, more extended data sets might be required, in particular, for the performance evaluation based on simulated data. Having said that, no vibration data from the damaged state is required to analyze the performance of the damage diagnosis module, and the diagnostic runtime during testing is one of the most compelling arguments to use the subspace-based residual, as it is formed in the time-domain without a time-consuming modal system identification. The shortest documented measurement time in this thesis is 3.0 s for damage localization in the hollow structural steel (HSS) steel beam and diagnosis runs with less than 2 s have been successful for the down-scaled laboratory model of the St. Nazaire bridge with considered natural frequencies up to 150.9 Hz. Considering the dynamic similitude requirements, the measurement time for full-scale bridges is longer; however, Monte Carlo experiments with 100 runs or more are feasible. In summary, the approach is particularly suited for damage-sensitive features that can be evaluated based on short measurement durations.

Multiple Damage Scenarios. The analysis of the minimum detectable damages is built on the assumption of individual parameter changes. Suppose multiple damages occur simultaneously at different locations across the structure. In that case, the minmax localization test should manage to isolate parameters that have changed, and the direct localization test may fail because it does not consider the interdependencies between different parameters. This does not mean that the predictive framework is not applicable for multiple damage scenarios. For parametric and non-parametric

damage detection tests, the prediction based on the individual parameter changes is conservative, as multiple parameter changes usually cause the tests to respond stronger than the predictions for individual damages. Moreover, the minimum detectability or localizability for multiple damage scenarios can straightforwardly be derived based on the proposed framework if the damages have equal magnitudes and if they are considered in the preprocessing stage. The interdependencies become more complex if the damage magnitudes differ, and (although not shown in this thesis) they could be described based on the off-diagonal terms of the Fisher information. To summarize, the presented framework in this thesis has been derived for the analysis of damage scenarios that can be described by individual parameter changes, to ease the exposition, and the minimum diagnosable damages described by multiple parameter changes could be derived analogously.

Necessity of a FE Model. The prediction of the minimum diagnosable damage is based on data-driven tests, but for the computation of the sensitivity matrix, a FE model is required. Hence, one might argue that this causes additional modelling effort and introduces several problems that are known from the FE model updating literature. That being said, the mismatch between the modelled and the real structure may be less critical, as the quality of the sensitivities is more important than the accuracy of the model itself. Moreover, the predictive framework is not restricted to specific element types or components but can be applied in combination with FE models of arbitrary structures. In this sense, the requirement of a "regular" FE model is an advantage compared to other damage diagnosis methods that are tailored to specific types of structures, such as analytical Bernoulli beams. Moreover, the use of FE models is advantageous because modal parameters can be extracted from the model, and a data-driven identification can be circumvented, including typical issues related to insufficient excitation or closely-spaced modes. For many applications, the number of monitoring parameters in the model is lower than the number of (vectorized) modal parameters, or residual entries, which leads to higher damage sensitivity of damage diagnosis tests. The reason for this is that the developed reliability index depends on the number of monitoring parameters. Ultimately, it is worth reiterating that parametrization in the active monitoring phase is optional, as the prediction of the minimum detectable damage is also valid for non-parametric tests.

Completeness of the Parametrization. Another aspect is the requirement of a complete parametrization for both modal parameters and structural parameters. The predictive framework is only valid for damage scenarios modelled through changes in the predefined monitoring parameters, and no statements can be made about unconsidered structural parameters. This does not mean that damage detection is impossible, but leads to bias in the statistical properties of the parametrized and non-parametrized detection test, as well as a loss of sensitivity. Moreover, it causes damage localization tests to fail. So, it is up to the user to provide a complete parametrization for him or her to be able to analyze the minimum detectability based on the devised tools from this thesis. Equivalently, every mode of vibration that is observable in the data also has to be considered in the null space and the sensitivity computation for the predictions to be accurate. However, this thesis expands the diagnostic capabilities to all anticipated damage scenarios, including change in cross-

sectional values, material properties, mass distribution values, change in prestress, and support displacements—meaning a complete parametrization is possible. Besides, damage parametrization is a suitable way to focus the damage diagnosis onto selective design parameters and to increase the damage detectability in them, provided changes in other parameters can be excluded. A selective parametrization reduces the number of monitoring parameters which, in turn, leads to a more lenient reliability index and higher damage detectability. In addition, a selective parametrization is crucial for sparse sensor layouts because it improves the numerical conditioning of the localization problem. Among the considered parametrizations, the model-based one appears to be the most sensitive to damage and robust toward noise effects. For data-driven monitoring, it is recommended to choose the parametrization with respect to modal parameters over the non-parametric test for robustness, whenever possible.

Efficiency of the Sensor Placement Strategy. Ultimately, the minimum measurement duration is an expensive objective function for sensor placement optimization, particularly, in comparison to low-level criteria such as the mode shape amplitude or the kinetic energy per mode, see Chapter 2. Consequently, it is impossible to assess all sensor configurations and to find the optimal solution in an exhaustive search approach. However, this problem is common to many state-of-the-art optimization criteria. It merely underlines the importance of a smart optimization method, such as the implemented GA, to efficiently find a close-to-optimal solution within a reasonable time.

11.3 Future Research

Besides the future research topics that are specific to the stochastic subspace-based method and that have already been discussed in the previous sections, the following points could be addressed.

Full-scale Case Study. An important step to transition the developed methods into engineering practice is to perform full-scale tests on cable-stayed bridges using extra masses or existing damage scenarios with single-damage scenarios and well-defined damage extent. Such case studies could verify the efficiency of all developed tools, could help to improve the robustness of the automated substructuring approach, and verify the practicability of extra masses for large structures. Furthermore, the limitations regarding the assumed excitation properties could be analyzed, as well as the effect of environmental and operational variables, and the numerical issues that might occur for very large mechanical structures. Large structures generally exhibit lower natural frequencies, lower sampling frequencies, a lower damage sensitivity (Jacobian), as well as higher noise components (covariance). Consequently, the damage detectability is lower and the measurement duration is longer, so the diagnostic runtime must be verified to ensure it is still practical.

Feature Comparison. The predictive framework for the minimum detectable damage is applicable to any damage-sensitive feature whose distribution can be approximated by a Gaussian distribution. Several such features have been proposed in the literature to which the approach

could be readily applicable, e.g., in (Parloo E. et al., 2003; Yan and Golinval, 2006; Döhler et al., 2014b; Bhuyan et al., 2017c; Gres et al., 2017). Since the subspace-based residual is directly formed in the subspace of the block Hankel matrix, which all modal parameters are derived from, many more such residuals likely exist. An interesting research topic would be a comparative study, where the minimum detectability for multiple such residuals is evaluated, and the most sensitive one is determined.

Strain Monitoring. An interesting future research topic is the expansion of the predictive framework to strain-based measurements. This thesis focuses on acceleration, velocity, or displacement measurements, or combinations thereof, which are combined into a stochastic state space model. Stochastic state space models for strain-based methods are available as well, and future research should focus on the evaluation of appropriate sensitivity matrices with respect to structural design parameters.

Bibliography

Adams, R. D., Cawley, P., Pye, C. J., and Stone, B. J. (1978). A vibration technique for non-destructively assessing the integrity of structures. *Journal of Mechanical Engineering Science*, 20(2):93–100.

Adhikari, S. and Friswell, M. I. (2001). Eigenderivative analysis of asymmetric non–conservative systems. *International Journal for Numerical Method in Engineering*, 51(6):709–733.

Afshari, M., Butrym, B. A., and Inman, D. J. (Jan, 2009). On quantifying detectable fatigue crack size in aluminum beams using vibration and impedance-based methods. In *Smart Materials, Adaptive Structures and Intelligent Systems*, volume 48975, pages 541–547.

Akima H. (1970). A new method of interpolation and smooth curve fitting based on local procedures. *Journal of the ACM (JACM),*, 17(4):589–602.

Allahdadian, S., Döhler, M., Ventura, C., and Mevel, L. (2019). Towards robust statistical damage localization via model-based sensitivity clustering. *Mechanical Systems and Signal Processing*, 134:106341.

Allemang, R. J. and Brown, D. L. (May, 1982). A correlation coefficient for modal vector analysis. In *Proceedings of the IMAC - 1st International Modal Analysis Conference*, pages 110–116, Orlando, United States.

An, Y., Chatzi, E., Sim, S.-H., Laflamme, S., Blachowski, B., and Ou, J. (2019). Recent progress and future trends on damage identification methods for bridge structures. *Structural Control and Health Monitoring*, 26(10):e2416.

Asgari, B., Osman, S. A., and Adnan, A. (2013). Sensitivity analysis of the influence of structural parameters on dynamic behaviour of highly redundant cable-stayed bridges. *Advances in Civil Engineering*, 2013:1–11.

Atkinson, K. E. (1989). *An introduction to numerical analysis*. John Wiley & Sons, New York, United States, 2nd edition.

Avci, O., Abdeljaber, O., Kiranyaz, S., Hussein, M., Gabbouj, M., and Inman, D. J. (2021). A review of vibration-based damage detection in civil structures: From traditional methods to machine learning and deep learning applications. *Mechanical Systems and Signal Processing*, 147:107077.

Balmès, É., Basseville, M., Bourquin, F., Mevel, L., Nasser, H., and Treyssède, F. (2008a). Merging sensor data from multiple temperature scenarios for vibration monitoring of civil structures. *Structural Health Monitoring*, 7(2):129–142.

Balmès, É., Basseville, M., Mevel, L., and Nasser, H. (2009). Handling the temperature effect in vibration monitoring of civil structures: A combined subspace-based and nuisance rejection approach. *Control Engineering Practice*, 17(1):80–87.

Balmès, É., Basseville, M., Mevel, L., Nasser, H., and Zhou, W. (2008b). Statistical model-based damage localization: A combined subspace-based and substructuring approach. *Structural Control and Health Monitoring*, 15(6):857–875.

Baruch, M. (1978). Optimization procedure to correct stiffness and flexibility matrices using vibration tests. *AIAA journal*, 16(11):1208–1210.

Basseville, M. (1997). Information criteria for residual generation and fault detection and isolation. *Automatica*, 33(5):783–803.

Basseville, M., Abdelghani, M., and Benveniste, A. (2000). Subspace-based fault detection algorithms for vibration monitoring. *Automatica*, 36(1):101–109.

Basseville, M., Benveniste, A., Goursat, M., and Meve, L. (2007). In-flight vibration monitoring of aeronautical structures. *IEEE Control Systems*, 27(5):27–42.

Basseville, M., Benveniste, A., Moustakides, G., and Rougee, A. (1987). Optimal sensor location for detecting changes in dynamical behavior. *IEEE Transactions on Automatic Control*, 32(12):1067–1075.

Basseville, M., Mevel, L., and Goursat, M. (2004). Statistical model-based damage detection and localization: Subspace-based residuals and damage-to-noise sensitivity ratios. *Journal of Sound and Vibration*, 275(3-5):769–794.

Bathe, K.-J. (2014). *Finite element procedures*. K.J. Bathe, Watertown, United States, 2nd edition.

Beck, J. L. and Au, S. K. (2002). Bayesian updating of structural models and reliability using Markov chain Monte Carlo simulation. *Journal of Engineering Mechanics*, 128(4):380–391.

Beck, J. L. and Katafygiotis, L. S. (1998). Updating models and their uncertainties. I. Bayesian statistical framework. *Journal of Engineering Mechanics*, 124(4):455–461.

Behmanesh, I. and Moaveni, B. (2015). Probabilistic identification of simulated damage on the Dowling Hall footbridge through Bayesian finite element model updating. *Structural Control and Health Monitoring*, 22(3):463–483.

Benveniste, A., Basseville, M., and Moustakides, G. (1987). The asymptotic local approach to change detection and model validation. *IEEE Transactions on Automatic Control*, 32(7):583–592.

Benveniste, A. and Mevel, L. (2007). Nonstationary consistency of subspace methods. *IEEE Transactions on Automatic Control*, 52(6):974–984.

Bernal, D. (2010). Load vectors for damage location in systems identified from operational loads. *Journal of Engineering Mechanics*, 136(1):31–39.

Bernal, D. (2013). Kalman filter damage detection in the presence of changing process and measurement noise. *Mechanical Systems and Signal Processing*, 39(1-2):361–371.

Bernal, D. (2014). Damage localization and quantification from the image of changes in flexibility. *Journal of Engineering Mechanics*, 140(2):279–286.

Bhuyan, M. D. H., Allahdadian, S., Döhler, M., Lecieux, Y., Mevel, L., Schoefs, F., and Ventura, C. (September, 2017a). Transfer matrices-based output-only statistical damage localization and quantification on a frame structure. In *IWSHM - 11th International Workshop on Structural Health Monitoring*, Stanford, United States.

Bhuyan, M. D. H., Döhler, M., Lecieux, Y., Mevel, L., and Schoefs, F. (2017b). Statistical damage localization with stochastic load vectors using multiple mode sets. *Structural Health Monitoring*, 16(5):518–535.

Bhuyan, M. D. H., Lecieux, Y., Thomas, J.-C., Lupi, C., Schoefs, F., Döhler, M., and Mevel, L. (September, 2018). Statistical vibration-based damage localization on Saint-Nazaire Bridge mockup. In *40th IABSE Symposium*, pages 1–8, Nantes, France.

Bhuyan, M. D. H., Viefhues, E., Döhler, M., Lecieux, Y., Mevel, L., Hille, F., and Schoefs, F. (2017c). Output-only subspace and transfer matrix-based damage localization and quantification. In *Proceedings of the IOMAC - 7th International Operational Modal Analysis Conference*, Ingolstad, Germany.

Boller, C., Chang, F.-K., and Fujino, Y., editors (2009). *Encyclopedia of structural health monitoring*. John Wiley & Sons, Chichester, United Kingdom.

Breccolotti, M., Ubertini, F., and Venanzi, I. (4-6 May, 2009). Natural frequencies of prestressed concrete beams: Theoretical prediction and numerical validation. In *3rd International Operational Modal Analysis Conference*, Portonovo, Italy.

Brehm, M., Zabel, V., and Bucher, C. (2013). Optimal reference sensor positions using output-only vibration test data. *Mechanical Systems and Signal Processing*, 41(1-2):196–225.

Brincker, R. and Ventura, C. E. (2015). *Introduction to operational modal analysis*. John Wiley & Sons, Chichester, United Kingdom.

Brownjohn, J. M. W., Stefano, A. D., Xu, Y.-L., Wenzel, H., and Aktan, A. E. (2011). Vibration-based monitoring of civil infrastructure: Challenges and successes. *Journal of Civil Structural Health Monitoring*, 1(3-4):79–95.

Brownjohn, J. M. W. and Xia, P. Q. (2000). Dynamic assessment of curved cable-stayed bridge by model updating. *Journal of Structural Engineering*, 126(2):252–260.

Cadoret, A., Freyssinet, C., and Lecieux, Y. (2020). Fault detection using modal analysis (in French). Technical report, University of Nantes, Nantes.

Cantero-Chinchilla, S., Beck, J. L., Chiachío, M., Chiachío, J., Chronopoulos, D., and Jones, A. (2020). Optimal sensor and actuator placement for structural health monitoring via an efficient convex cost-benefit optimization. *Mechanical Systems and Signal Processing*, 144:106901.

Cao, T. T. and Zimmerman, D. C. (1999). Procedure to extract ritz vectors from dynamic testing data. *Journal of Structural Engineering*, 125(12):1393–1400.

Carden, E. P. and Fanning, P. (2004). Vibration based condition monitoring: A review. *Structural Health Monitoring*, 3(4):355–377.

Cavalagli, N., Comanducci, G., and Ubertini, F. (2018). Earthquake-induced damage detection in a monumental masonry bell-tower using long-term dynamic monitoring data. *Journal of Earthquake Engineering*, 22(sup1):96–119.

Cawley, P. and Adams, R. D. (1979). The location of defects in structures from measurements of natural frequencies. *The Journal of Strain Analysis for Engineering Design*, 14(2):49–57.

Censor, Y. (1977). Pareto optimality in multiobjective problems. *Applied Mathematics and Optimization*, 4(1):41–59.

Chang, P. C., Flatau, A., and Liu, S. C. (2003). Health monitoring of civil infrastructure. *Structural Health Monitoring*, 2(3):257–267.

Chen, C.-T. (1999). *Linear system theory and design*. Oxford University Press, New York, United States, 3rd edition.

Chen, W.-F. and Duan, L., editors (2014). *Bridge Engineering Handbook: Seismic Design*. CRC Press, Boca Raton, United States, 2nd edition.

Chopra, A. K. (2017). *Dynamics of structures: Theory and Applications to Earthquake Engineering*. Prentice Hall, Upper Sadlle River, United States, 5th edition.

Chow, H. M., Lam, H. F., Yin, T., and Au, S. K. (2011). Optimal sensor configuration of a typical transmission tower for the purpose of structural model updating. *Structural Control and Health Monitoring*, 18(3):305–320.

Chung, Y. T. and Moore, J. D. (February, 1993). On-orbit sensor placement and system identification of space station with limited instrumentations. In *Proceedings of the IMAC - 11th International Modal Analysis Conference*, Kissimmee, United States.

Clague, J. J., Luternauer, J. L., and Mosher D. C., editors (1998). *Geology and natural hazards of the Fraser river delta, British Columbia*. Geological Survey of Canada.

Coppolino, R. and Rubin, S. (January, 1980). Detectability of structural failures in offshore platforms by ambient vibration monitoring. In *Proceedings of the Offshore Technology Conference*, Houston, United States.

Corana, A., Marchesi, M., Martini, C., and Ridella, S. (1987). Minimizing multimodal functions of continuous variables with the simulated annealing algorithm. *ACM Transactions on Mathematical Software (TOMS)*, 13(3):262–280.

Cornwell, P., Farrar, C. R., Doebling, S. W., and Sohn, H. (1999). Environmental variability of modal properties. *Experimental Techniques*, 23(6):45–48.

Crosier, R. B. (1988). Multivariate generalizations of cumulative sum quality-control schemes. *Technometrics*, 30(3):291–303.

Cross, E. J., Worden, K., and Chen, Q. (2011). Cointegration: A novel approach for the removal of environmental trends in structural health monitoring data. *Proceedings of the Royal Society A: Mathematical, Physical and Engineering Sciences*, 467(2133):2712–2732.

Cury, A. and Cremona, C. (2012). Assignment of structural behaviours in long-term monitoring: Application to a strengthened railway bridge. *Structural Health Monitoring*, 11(4):422–441.

de Clerck, J. P. and Avitable, P. (1996). Development of several new tools for pre-test. In *Proceedings of SPIE 2768*, pages 1272–1277.

Deb, K. (2001). *Multi-objective optimization using evolutionary algorithms*. John Wiley & Sons, Ltd, Chichester, United Kingdom.

Deng, Z., Guo, Z., and Zhang, X. (2017). Interval model updating using perturbation method and radial basis function neural networks. *Mechanical Systems and Signal Processing*, 84:699–716.

Deraemaeker, A., Reynders, E., de Roeck, G., and Kullaa, J. (2008). Vibration-based structural health monitoring using output-only measurements under changing environment. *Mechanical Systems and Signal Processing*, 22(1):34–56.

Dervilis, N., Cross, E. J., Barthorpe, R. J., and Worden, K. (2014). Robust methods of inclusive outlier analysis for structural health monitoring. *Journal of Sound and Vibration*, 333(20):5181–5195.

Dervilis, N., Worden, K., and Cross, E. J. (2015). On robust regression analysis as a means of exploring environmental and operational conditions for SHM data. *Journal of Sound and Vibration*, 347:279–296.

Ding, Y. and Li, A. (2008). : Finite element model updating for the Runyang cable-stayed bridge tower using ambient vibration test results. *Advances in Structural Engineering*, 11(3):323–335.

Ding, Y. and Li, A. (2011). Temperature-induced variations of measured modal frequencies of steel box girder for a long-span suspension bridge. *International Journal of Steel Structures*, 11(2):145–155.

Doebling, S. W., Farrar, C. R., Prime, M. B., and Shevitz, D. W. (1996). Damage identification and health monitoring of structural and mechanical systems from changes in their vibration characteristics: A literature review. Technical Report LA-13070-MS512, Los Alamos National Lab., Los Alamos, United States.

Döhler, M., Hille, F., Mevel, L., and Rücker, W. (2014a). Structural health monitoring with statistical methods during progressive damage test of S101 Bridge. *Engineering Structures*, 69:183–193.

Döhler, M., Kwan, K., and Bernal, D. (February, 2013). Optimal sensor placement with a statistical criterion for subspace-based damage detection. In *Proceedings of the IMAC - 31st International Modal Analysis Conference*, pages 219–229, Garden Grove, United States.

Döhler, M. and Mevel, L. (2015). Fault isolation and quantification from gaussian residuals with application to structural damage quantification. *IFAC-PapersOnLine*, 48(21):640–645.

Döhler, M., Mevel, L., and Hille, F. (2014b). Subspace-based damage detection under changes in the ambient excitation statistics. *Mechanical Systems and Signal Processing*, 45(1):207–224.

Döhler, M., Mevel, L., and Zhang, Q. (2016). Fault detection, isolation and quantification from Gaussian residuals with application to structural damage diagnosis. *Annual Reviews in Control*, 42:244–256.

Döhler, M., Zhang, Q., and Mevel, L. (2015). Vibration monitoring by eigenstructure change detection based on perturbation analysis. *IFAC PapersOnLine*, 48(28):999–1004.

Döhler, M., Zhang, Q., and Mevel, L. (2017). Change detection and isolation in mechanical system parameters based on perturbation analysis. *IFAC PapersOnLine*, 50(1):419–424.

Duda, R. O., Hart, P. E., and Stork, D. G. (2012). *Pattern classification*. John Wiley & Sons, New York, United States.

Earthquakes Canada (2020). Geological Survey of Canada, Earthquake Search (On-line Bulletin). www.earthquakescanada.ca.

Eberhart, R. and Kennedy, J. (4-6 Oct. 1995). A new optimizer using particle swarm theory. In *MHS'95. Proceedings of the Sixth International Symposium on Micro Machine and Human Science*, pages 39–43, Nagoya, Japan. IEEE.

Elsaid, A. and Seracino, R. (2014). Rapid assessment of foundation scour using the dynamic features of bridge superstructure. *Construction and Building Materials*, 50:42–49.

Erdogan, S. Y. and Bakir, G. P. (2013). Inverse propagation of uncertainties in finite element model updating through use of fuzzy arithmetic. *Engineering Applications of Artificial Intelligence*, 26(1):357–367.

Eyre, R. and Tilly, G. P. (May, 1997). Damping measurements on steel and composite bridges. In *Proceeding of a Symposium on Dynamic Behaviour of Bridges at the Transport and Road Research Laboratory*, volume 275.

Fan, W. and Qiao, P. (2011). Vibration-based damage identification methods: A review and comparative study. *Structural Health Monitoring*, 10(1):83–111.

Fang, S.-E., Zhang, Q.-H., and Ren, W.-X. (2015). An interval model updating strategy using interval response surface models. *Mechanical Systems and Signal Processing*, 60-61:909–927.

Fanning, P. J. and Carden, E. P. (2001). Auto-regression and statistical process control techniques applied to damage indication in telecommunication masts. *Key Engineering Materials*, 204-205:251–260.

Farrar, C. and Worden, K. (2012). *Structural health monitoring: A machine learning perspective*. Wiley, Oxford, United Kingdom.

Feng, S. and Jia, J. (2018). Acceleration sensor placement technique for vibration test in structural health monitoring using microhabitat frog-leaping algorithm. *Structural Health Monitoring*, 17(2):169–184.

Figueiredo, E., Figueiras, J., Park, G., Farrar, C. R., and Worden, K. (2011). Influence of the autoregressive model order on damage detection. *Computer-Aided Civil and Infrastructure Engineering*, 26(3):225–238.

Filiatrault, A., Tinawi, R., and Massicotte, B. (1993). Damage to cable–stayed bridge during 1988 saguenay earthquake. I: Pseudostatic analysis. *Journal of Structural Engineering*, 119(5):1432–1449.

Foster, L. T., Keller, P., McKee, B., and Ostry, A., editors (2011). *British Columbia atlas of wellness*. Western Geographical Press, Victoria, British Columbia, Canada, 2nd edition.

Frieden, B. R., editor (2004). *Science from Fisher Information: A unification*. Cambridge University Press, Cambridge.

Friswell, M. and Mottershead, J. E. (1995). *Finite element model updating in structural dynamics*. Springer Science & Business Media, Dordrecht, Netherlands.

Gautier, G., Mencik, J.-M., and Serra, R. (2015). A finite element-based subspace fitting approach for structure identification and damage localization. *Mechanical Systems and Signal Processing*, 58-59:143–159.

Gautier, G., Mevel, L., Mencik, J.-M., Serra, R., and Döhler, M. (2017). Variance analysis for model updating with a finite element based subspace fitting approach. *Mechanical Systems and Signal Processing*, 91:142–156.

Gautier, G., Serra, R., and Mencik, J.-M. (2013). Vibratory diagnosis by finite element model updating and operational modal analysis. *Mechanics & Industry*, 14(2):145–149.

Georges, D. (13-15 December, 1995). The use of observability and controllability gramians or functions for optimal sensor and actuator location in finite-dimensional systems. In *Proceedings of 1995 34th IEEE Conference on Decision and Control*, pages 3319–3324, New Orleans, United States. IEEE.

Glad, T. and Ljung, L. (2000). *Control Theory: Multivariable and Nonlinear Methods*. CRC Press, London, 1st edition.

Gladwell, G. M. L. and Ahmadian, H. (1995). Generic element matrices suitable for finite element model updating. *Mechanical Systems and Signal Processing*, 9(6):601–614.

Goldfinger, C., Nelson, C. H., Morey, A. E., Johnson, J. E., Patton, J. R., Karabanov, E., Gutiérrez-Pastor, J., Eriksson, A. T., Gràcia, E., Dunhill, E., Enkin, R. J., Dallimore, A., and Vallier, T. (2012). Turbidite event history—Methods and implications for holocene paleoseismicity of the Cascadia subduction zone. Technical Report 1661–F, US Geological Survey, Reston, United States.

Gomes, G. F., da Cunha, S. S., Alexandrino, P. S. L., de Sousa, B. S., and Ancelotti, A. C. (2018). Sensor placement optimization applied to laminated composite plates under vibration. *Structural and Multidisciplinary Optimization*, 58(5):2099–2118.

Greś, S., Döhler, M., Andersen, P., and Mevel, L. (2021). Kalman filter-based subspace identification for operational modal analysis under unmeasured periodic excitation. *Mechanical Systems and Signal Processing*, 146:106996.

Gres, S., Ulriksen, M. D., Döhler, M., Johansen, R. J., Andersen, P., Damkilde, L., and Nielsen, S. A. (2017). Statistical methods for damage detection applied to civil structures. *Procedia Engineering*, 199:1919–1924.

Haag, T., Herrmann, J., and Hanss, M. (2010). Identification procedure for epistemic uncertainties using inverse fuzzy arithmetic. *Mechanical Systems and Signal Processing*, 24(7):2021–2034.

Hać, A., & Liu, L. (1993). Sensor and actuator location in motion control of flexible structures. *Journal of Sound and Vibration*, 167(2):239–261.

Hannan, E. J. (1970). *Multiple Time Series*. Wiley, New York, United States.

Hemez, F. M. (1993). *Theoretical and experimental correlation between finite element models and modal tests in the context of large flexible space structures*. Ph.D. Thesis, University of Colorado at Boulder, Department of Aerospace Sciences, Boulder, United States.

Hemez, F. M. and Doebling, S. W. A validation of Bayesian finite element model updating for linear dynamics. Technical Report LA-UR-98-4574, Los Alamos National Lab., Los Alamos, United States.

Heylen, W. and Sas, P. (1997). *Modal analysis theory and testing*. Katholieke Universiteit Leuven, Leuven, Belgium.

Hoell, S. and Omenzetter, P. (2016). Optimal selection of autoregressive model coefficients for early damage detectability with an application to wind turbine blades. *Mechanical Systems and Signal Processing*, 70-71:557–577.

Holland, J. H. (1975). *Adaptation in natural and artificial systems*. Ann Arbor: University of Michigan Press, Cambridge, United Kingdom.

Huang, M., Li, J., and Zhu, H. (10-12 December, 2009). Optimal sensor layout for bridge health monitoring based on dual-structure coding genetic algorithm. In *2009 International Conference on Computational Intelligence and Software Engineering*, pages 1–4, Wuhan, China. IEEE.

Inman, D. J. (2017). *Vibration with control*. Wiley, Chichester, United Kingdom, 2nd edition.

Janberg, N. (2020). Structurae. https://structurae.net/en/structures/saint-nazaire-bridge.

Jang, S., Spencer Jr, B. F., and Sim, S.-H. (2012). A decentralized receptance-based damage detection strategy for wireless smart sensors. *Smart Materials and Structures*, 21(5):055017.

Jin, C., Li, J., Jang, S., Sun, X., and Christenson, R. (March, 2015). Structural damage detection for in-service highway bridge under operational and environmental variability. In *Proceedings of SPIE 9435*, Smart Structures and Materials + Nondestructive Evaluation and Health Monitoring, San Diego, United States. International Society for Optics and Photonics.

Juneja, V, Haftka, R. T., and Cudney, H. H. (1997). Damage detection and damage detectability—analysis and experiments. *Journal of Aerospace Engineering*, 10(4):135–142.

Kalman, R. E. (1959). On the general theory of control systems. *IRE Transactions on Automatic Control*, 4(3):110.

Kalman, R. E. (1963). Mathematical description of linear dynamical systems. *Journal of the Society for Industrial and Applied Mathematics, Series A: Control*, 1(2):152–192.

Kammer, D. C. (1991). Sensor placement for on-orbit modal identification and correlation of large space structures. *Journal of Guidance, Control, and Dynamics*, 14(2):251–259.

Kang, F., Li, J.-j., and Xu, Q. (2008). Virus coevolution partheno-genetic algorithms for optimal sensor placement. *Advanced Engineering Informatics*, 22(3):362–370.

Kaouk, M. and Zimmerman, D. C. (10-12 May, 1994). Assessment of damage affecting all structural properties. In *Proceedings of the 9th VPI & SU Symposium on Dynamics and Control of Large Structures*, pages 445–455, Blacksburg, United States.

Kaouk, M., Zimmerman, D. C., and Simmermacher, T. W. (2000). Assessment of damage affecting all structural properties using experimental modal parameters. *Journal of Vibration and Acoustics*, 122(4):456–463.

Kaya, Y., Ventura, C., Huffman, S., and Turek, M. (2017). British columbia smart infrastructure monitoring system. *Canadian Journal of Civil Engineering*, 44(8):579–588.

Khodaparast, H. H., Mottershead, J. E., and Badcock, K. J. (2011). Interval model updating with irreducible uncertainty using the kriging predictor. *Mechanical Systems and Signal Processing*, 25(4):1204–1226.

Kim, C. W., Morita, T., Oshima, Y., and Sugiura, K. (2015). A Bayesian approach for vibration-based long-term birdge monitoring to conisder environmental and operational changes. *Smart Structures and Systems*, 15(2):395–408.

Kim, H. M. and Bartkowicz, T. J. (2001). An experimental study for damage detection using a hexagonal truss. *Computers & Structures*, 79(2):173–182.

Kim, K. O., Yoo, H. S., and Choi, Y. J. (June 11-14, 2001). Optimal sensor placement for dynamic testing of large structures. In *19th AIAA Applied Aerodynamics Conference*, page 1232, Anaheim, United States.

Ko, B., Tongue, B. H., and Packard, A. (1994). A method for determining the optimal location of a distributed sensor/actuator. *Shock and Vibration*, (1):357–374.

Kramer, M. A. (1991). Nonlinear principal component analysis using autoassociative neural networks. *AIAA journal*, 37(2):233–243.

Kulla, J. (2003). Damage detection of the z24 bridge using control charts. *Mechanical Systems and Signal Processing*, 17(1):163–170.

Kulla, J. (July, 2004). Structural health monitoring under variable environmental or operational conditions. In *Proceedings of the EWSWH - 2nd European Workshop on Structural Health Monitoring*, pages 1262–1269, Munich, Germany. DEStech Publications Inc.

Kumar, S. and Seinfeld, J. H. (1978). Optimal location of measurements in tubular reactors. *Chemical Engineering Science*, 33(11):1507–1516.

Larson, C. B., Zimmermann, D. C., and Marek, E. L. (January, 1994). A comparison of modal test planning techniques: Excitation and sensor placement using the NASA 8 bay truss. In *Proceedings of the IMAC - 12th International Modal Analysis Conference*, pages 205–211, Honolulu, Hawaii.

Lee, J. J., Lee, J. W., Yi, J. H., Yun, C. B., and Jung, H. Y. (2005). Neural networks-based damage detection for bridges considering errors in baseline finite element models. *Journal of Sound and Vibration*, 280(3-5):555–578.

Li, D.-S., Fritzen,, C.P, and Li, H.-N. (February, 2008). Extended minmac algorithm and comparison of sensor placement methods. In *Proceedings of the IMAC - 26th International Modal Analysis Conference*, Orlando, United States.

Li, D. S., Li, H. N., and Fritzen, C. P. (June, 2009a). On optimal sensor placement criterion for structural health monitoring with representative least squares method. In *Key Engineering Materials*, volume 413-414, pages 383–391. Trans Tech Publications, Switzerland.

Li, H., Li, S., Ou, J., and Li, H. (2009b). Modal identification of bridges under varying environmental conditions: Temperature and wind effects. *Structural Control and Health Monitoring*, 17:495–512.

Lieven, N. A. J. and Ewins, D. J. (1 - 4 February, 1988). Spatial correlation of mode shapes, the coordinate modal assurance criterion (COMAC). In *Proceedings of the IMAC - 6th International Modal Analysis Conference*, volume 1, pages 690–695, Kissimmee, United States.

Lieven, N. A. J. and Greening, P. (2001). Effect of experimental pre–stress and residual stress on modal behaviour. *Philosophical Transactions of the Royal Society of London. Series A: Mathematical, Physical and Engineering Sciences*, 359(1778):97–111.

Lim, T. W. and Kashangaki, T. A. L. (1994). Structural damage detection of space truss structures using best achievable eigenvectors. *AIAA journal*, 32(5):1049–1057.

Lindner, D. K. and Goff, R. M. (September, 1993). Damage detection, location, and estimation for space trusses. In *Proceedings of SPIE*, North American Conference on Smart Structures and Materials, pages 1028–1039, Albuquerque, New Mexico. International Society for Optics and Photonics.

Lindquist, A. and Picci, G. (2015). *Linear Stochastic Systems: A geometric approach to modeling, estimation and identification*. Springer, Heidelberg, Germany.

Liu, Y., Duan, Z. D., and Li, H. (2009). Updating of finite element model in considering mode errors with fuzzy theory. *Key Engineering Materials*, 413-414:785–792.

Long, L., Döhler, M., and Thöns, S. (2020). Determination of structural and damage detection system influencing parameters on the value of information. *Structural Health Monitoring*, 147592171990091:1–18.

Lowry, C. A., Woodall, W. H., Champ, C. W., and Rigdon, S. E. (1992). A multivariate exponentially weighted moving average control chart. *Technometrics*, 34(1):46–53.

Magalhães, F. and Cunha, Á. (2011). Explaining operational modal analysis with data from an arch bridge. *Mechanical Systems and Signal Processing*, 25(5):1431–1450.

Magalhães, F., Cunha, A., and Caetano, E. (2012). Vibration based structural health monitoring of an arch bridge: From automated OMA to damage detection. *Mechanical Systems and Signal Processing*, 28:212–228.

Magalhães, F., Cunha, A., and Caetano, E. (September, 2010). Continuous dynamic monitoring of an arch bridge: strategy to eliminate the environmental and operational effects and detect damages. In *Proceedings of the ISMA - 24th International Conference on Noise and Vibration Engineering*. Leuven, Belgium.

Mahalanobis, P. C. (1936). On the generalized distance in statistics. *National Institute of Science of India*, 2(1).

Marano, G. C., Monti, G., and Quaranta, G. (2011). Comparison of different optimum criteria for sensor placement in lattice towers. *The Structural Design of Tall and Special Buildings*, 20(8):1048–1056.

Marin, L., Döhler, M., Bernal, D., and Mevel, L. (2012). Uncertainty quantification for stoachstic damage localization for mechanical systems. In *Proceedings of the IFAC -8th Symposium on Fault Detection, Supervision and Safety of Technical Processes (SAFEPROCESS)*, pages 1017–1022, Mexico City, Mexico.

Marin, L., Döhler, M., Bernal, D., and Mevel, L. (2015). Robust statistical damage localization with stochastic load vectors. *Structural Control and Health Monitoring*, 22(3):557–573.

Marwala, T. (2010). *Finite element model updating using computational intelligence techniques: Applications to structural dynamics.* Springer Science & Business Media.

Mattson, S. G. and Pandit, S. M. (2006). Statistical moments of autoregressive model residuals for damage localisation. *Mechanical Systems and Signal Processing*, 20(3):627–645.

Mehra, R. K. and Peschon, J. (1971). An innovations approach to fault detection and diagnosis in dynamic systems. *Automatica*, 7(5):637–640.

Mellinger, P., Döhler, M., and Mevel, L. (2016). Variance estimation of modal parameters from output-only and input/output subspace-based system identification. *Journal of Sound and Vibration*, 379:1–27.

Meng, Z., Hao, P., Li, G., Wang, B., and Zhang, K. (2015). Non-probabilistic reliability-based design optimization of stiffened shells under buckling constraint. *Thin-Walled Structures*, 94:325–333.

Meo, M. and Zumpano, G. (2005). On the optimal sensor placement techniques for a bridge structure. *Engineering Structures*, 27(10):1488–1497.

Messac, A. (2015). *Optimization in practice with MATLAB: For engineering students and professionals*. Cambridge University Press, New York, United States.

Michaelewicvz, Z. (1994). *Book Genetic Algorithms + Data Structure = Evolution Programs.* Springer, Berlin, Heidelberg, Germany, 2nd edition.

Montgomery, D. C. (2007). *Introduction to Statistical Quality Control*. John Wiley & Sons, Jefferson City, United States, 6th edition.

Moore, B. (1981). Principal component analysis in linear systems: Controllability, observability, and model reduction. *IEEE Transactions on Automatic Control*, 26(1):17–32.

Morari, M. and Stephanopoulos, G. (1980). Studies in the synthesis of control structures for chemical processes: Part ii: Structural aspects and the synthesis of alternative feasible control schemes. *A.I.Ch.E. Journal*, 26(2):232–246.

Mordini, A., Savov, K., and Wenzel, H. (2007). The finite element model updating: A powerful tool for structural health monitoring. *Structural Engineering International*, 17(4):352–358.

Mordini, A., Savov, K., and Wenzel, H. (2008). Damage detection on stay cables using an open source-based framework for finite element model updating. *Structural Health Monitoring*, 7(2):91–102.

Moshtagh, N. (2005). Minimum volumne enclosing ellipsoid. *Convex Optimization*, 111:1–9.

Mottershead, J. E. (2001). Structural modification for the assignment of zeros using measured receptances. *Journal of Applied Mechanics*, 68(5):791–798.

Mottershead, J. E., Friswell, M. I., Ng, G. H. T., and Brandon, J. A. (1996). Geometric parameters for finite element model updating of joints and constraints. *Mechanical Systems and Signal Processing*, 10(2):171–182.

Mottershead, J. E., Link, M., and Friswell, M. I. (2011). The sensitivity method in finite element model updating: A tutorial. *Mechanical Systems and Signal Processing*, 25(7):2275–2296.

Moughty, J. J. and Casas, J. R. (2017a). Performance assessment of vibration parameters as damage indicators for bridge structures under ambient excitation. *Procedia Engineering*, 199:1970–1975.

Moughty, J. J. and Casas, J. R. (2017b). A state of the art review of modal-based damage detection in bridges: Development, challenges, and solutions. *Applied Sciences*, 7(5):510.

Muirhead, R. J. (1982). *Aspects of multivariate statistical theory.* John Wiley & Sons, New London, Canada.

Müller, P. C. and Weber, H. I. (1972). Analysis and optimization of certain qualities of controllability and observability for linear dynamical systems. *Automatica*, 8(3):237–246.

Mustafa, S., Debnath, N., and Dutta, A. (2015). Bayesian probabilistic approach for model updating and damage detection for a large truss bridge. *International Journal of Steel Structures*, 15(2):473–485.

Nguyen, V. H., Mahowald, J., Golinval, J.-C., and Maas, S. (2014). Damage detection in civil engineering structure considering temperature effect. In Catbas, F. N., editor, *Proceedings of the IMAC - 32nd International Modal Analysis Conference*, volume 4, pages 187–196. Springer, Orlando, United States.

Oh, C. K., Sohn, H., and Bae, I.-H. (2009). Statistical novelty detection within the Yeongjong suspension bridge under environmental and operational variations. *Smart Materials and Structures*, 18(12):125022.

Ojalvo, I. and Pilon, D. (18-20 April, 1988). Diagnostics for geometrically locating structural math model errors from modal test data: 1988: Smith. In *29th Structures, Structural Dynamics and Materials Conference*, page 2358, Williamsburg, United States.

Oliveira, G., Magalhães, F., Cunha, Á., and Caetano, E. (2018). Vibration-based damage detection in a wind turbine using 1 year of data. *Structural Control and Health Monitoring*, 25(11):e2238.

Onur, T. and Seemann, M. R. (1-6 August, 2004). Probabilities of significant earthquake shaking in communities across British Columbia: Implications for emergency management. In *Proceedings of the 13th World Conference on Earthquake Engineering*, volume 1065, Vancouver, British Colubia, Canada.

Overton, G. and Worden, K. (2004). Sensor optimisation using an ant colony metaphor. *Strain*, 40(2):59–65.

Pachaud, C., Salvetat, R., and Fray, C. (1997). Crest factor and kurtosis contributions to identify defects inducing periodical impulsive forces. *Mechanical Systems and Signal Processing*, 11(6):903–916.

Page, E. S. (1954). Continuous inspection schemes. *Biometrika*, 41(1/2):100–115.

Pandey, A. K. and Biswas, M. (1994). Damage detection in structure using change in flexibility. *Journal of Sound and Vibration*, 169(1):3–17.

Pandey, A. K., Biswas, M., and Samman, M. M. (1991). Damage detection from changes in curvature mode shapes. *Journal of Sound and Vibration*, 145(2):321–332.

Papadimitriou, C. (2004). Optimal sensor placement methodology for parametric identification of structural systems. *Journal of Sound and Vibration*, 278(4-5):923–947.

Papadimitriou, C., Beck, J. L., and Katafygiotis, L. S. (2001). Updating robust reliability using structural test data. *Probabilistic Engineering Mechanics*, 16(2):103–113.

Papadimitriou, C., Haralampidis, Y., and Sobczyk, K. (2005). Optimal experimental design in stochastic structural dynamics. *Probabilistic Engineering Mechanics*, 20(1):67–78.

Papadimitriou, C. and Papadioti, D.-C. (2013). Component mode synthesis techniques for finite element model updating. *Computers & Structures*, 126:15–28.

Papadopoulos, M. and Garcia, E. (1998). Sensor placement methodologies for dynamic testing. *AIAA journal*, 36(2):256–263.

Papatheou, E., Manson, G., Barthorpe, R. J., and Worden, K. (2010). The use of pseudo-faults for novelty detection in SHM. *Journal of Sound and Vibration*, 329(12):2349–2366.

Parloo E., Guillaume, P., and van Overmeire, M. (2003). Damage assessment using mode shape sensitivities. *Mechanical Systems and Signal Processing*, 17(3):499–518.

Pascual, R., Golinval, J.-C., and Razeto, M. (8 - 11 February,1999). On-line damage assessment using operating deflection shapes. In *Proceedings of the IMAC - 17th International Modal Analysis Conference*, pages 238–243. Kissimmee, United States.

Patterson, J. and Gibson, A. (2017). *Deep learning: A practitioner's approach*. O'Reilly Media, Inc, Sebastopol, United States.

Paultre, P. (2011). *Dynamics of Structures*. John Wiley & Sons, Hoboken, United States.

Pawar, P. M. and Ganguli, R. (2003). Genetic fuzzy system for damage detection in beams and helicopter rotor blades. *Computer methods in applied mechanics and engineering*, 192(16-18):2031–2057.

Penny, J. E. T., Friswell, M. I., and Garvey, S. D. (1994). Automatic choice of measurement locations for dynamic testing. *AIAA Journal*, 32(2):407–414.

Petersen, Ø. W. and Øiseth, O. (2017). Sensitivity-based finite element model updating of a pontoon bridge. *Engineering Structures*, 150:573–584.

Przemieniecki, J. S. (1968). *Theory of matrix structural analysis*. McGraw-Hill Book Company, New York, United States.

Rainieri, C. and Fabbrocino, G. (2014). *Operational modal analysis of civil engineering structures*. Springer, New York, United States.

Reynders, E. and de Roeck, G. (2008). Reference-based combined deterministic–stochastic subspace identification for experimental and operational modal analysis. *Mechanical Systems and Signal Processing*, 22(3):617–637.

Reynier, M. and Abou-Kandil, H. (1999). Sensors location for updating problems. *Mechanical Systems and Signal Processing*, 13(2):297–314.

Roberts, S. W. (1959). Control chart tests based on geometric moving averages. *Technometrics,*, 1(3):239–250.

Rosenblatt, F. (1962). *Principles of neurodynamics: Perceptrons and the theory of brain mechanisms*. Spartan, Washington, United States.

Rousseeuw, P. J. and van Driessen, K. (1999). A fast algorithm for the minimum covariance determinant estimator. *Technometrics*, 41(3):212–223.

Roy, T. and Chakraborty, D. (2009). Optimal vibration control of smart fiber reinforced composite shell structures using improved genetic algorithm. *Journal of Sound and Vibration*, 319(1-2):15–40.

Rytter, A. (1993). *Vibrational based inspection of civil engineering structures*. Ph.D. Thesis, Aalborg University, Aalborg.

S6-19 (2019). Canadian highway bridge design code. Technical report, CSA Group, Mississauga, Canada.

Sanda, M. S., Gauron, O., Turcotte, N., Lamarche, C. P., Paultre, P., Talbot, M., and Laflamme, J. F. (12-14 July, 2017). Efficient finite elements model updating for damage detection in bridges. In *Proceedings of the International Conference on Experimental Vibration Analysis for Civil Engineering*, pages 293–305, San Diego, United States.

Santos, J. P., Crémona, C., Orcesi, A. D., and Silveira, P. (2013). Multivariate statistical analysis for early damage detection. *Engineering Structures*, 56:273–285.

Santos, J. P., Orcesi, A. D., Crémona, C., and Silveira, P. (2015). Baseline-free real-time assessment of structural changes. *Structure and Infrastructure Engineering*, 11(2):145–161.

Schoefs, F., Clément, A., and Nouy, A. (2009). Assessment of ROC curves for inspection of random fields. *Structural Safety*, 31(5):409–419.

Scott, M. and Worden, K. (2015). A bee swarm algorithm for optimising sensor distributions for impact detection on a composite panel. *Strain*, 51(2):147–155.

Sepulveda, A. E., Jin, I. M., and Schmit, L. A. (1993). Optimal placement of active elements in control augmented structuralsynthesis. *AIAA journal*, 31(10):1906–1915.

Shi, H., Worden, K., and Cross, E. J. (2016). A nonlinear cointegration approach with applications to structural health monitoring. *Journal of Physics: Conference Series*, 744:012025.

Siddesha, H. and Hegde, M. N. (2017). Structural damage detection in framed structures using under foundation settlement/rotation of bases. *Structural Durability & Health Monitoring*, 11(1):17–41.

Siddiquee, K., Shahria, and Alam M. (2017). Highway bridge infrastructure in the province of British Columbia (BC), Canada. *Infrastructures*, 2(7):1–18.

Siegert, D., Döhler, M., Mekki, O. B., Mevel, L., Goursat, M., and Toutlemonde, F. (2010). Vibration monitoring of a small span composite bridge. In *Proceedings of the IMAC - 28th International Modal Analysis Conference*, Jacksonville, United States.

Simmermacher, T., Zimmerman, D. C., Mayes, R., Reese, G., and James, G. H. (10- 13 April, 1995). The effects of finite element grid density on model correlation and damage detection or a bridge. In *Proceedings of the 36th Structures, Structural Dynamics and Materials Conference*, page 1075. New Orleans, United States.

Simoen, E., de Roeck, G., and Lombaert, G. (2015). Dealing with uncertainty in model updating for damage assessment: A review. *Mechanical Systems and Signal Processing*, 56-57:123–149.

Smallwood, D. O. (1994). Characterization and simulation of transient vibrations using band limited temporal moments. *Shock and Vibration*, 1(6):507–527.

Smith, S. W. and Beattie, C. A. (1991). Secant-method adjustment for structural models. *AIAA journal*, 29(1):119–126.

Sohn, H. and Law, K. H. (1997). A Bayesian probabilistic approach for structure damage detection. *Earthquake Engineering and Structural Dynamics*, 26(12):1259–1281.

Sohn, H. and Law, K. H. (2000). Bayesian probabilistic damage detection of a reinforced–concrete bridge column. *Earthquake Engineering and Structural Dynamics*, 29(8):1131–1152.

Sohn, H. and Oh, C. K. (2009). Statistical pattern recognition. In Boller, C., Chang, F.-K., and Fujino, Y., editors, *Encyclopedia of structural health monitoring*. John Wiley & Sons, Chichester, United Kingdom.

Spiridonakos, M. D. and Chatzi, E. N. (2015). Metamodeling of dynamic nonlinear structural systems through polynomial chaos NARX models. *Computers & Structures*, 157:99–113.

Stubbs, N., Kim, J. T., and Topole, K. (13-15 April, 1992). An efficient and robust algorithm for damage localization in offshore platforms. In *Proceedings of the ASCE 10th Structures Congress*, volume 1, pages 543–546. San Antonio, United States.

Sutter, T. R., Camarda, C. J., Walsh, J. L., and Adelman, H. M. (1988). Comparison of several methods for calculating vibration mode shape derivatives. *AIAA journal*, 26(12):1506–1511.

Svensson, H. (2013). *Cable-Stayed Bridges: 40 Years of Experience Worldwide*. Wilhelm Ernst & Sohn, Berlin, Germany.

Swindlehust, A., Roy, R., Ottersten, B., and Kailath, T. (1995). A subspace fitting method for identification of linear state-space models. *IEEE Transactions on Automatic Control*, 40(2):311–316.

Teughels, A. and de Roeck, G. (2004). Structural damage identification of the highway bridge Z24 by fe model updating. *Journal of Sound and Vibration*, 278(3):589–610.

Thöns, S., Döhler, M., and Long, L. (2018). On damage detection system information for structural systems. *Structural Engineering International*, 28(3):255–268.

van Laarhoven, P. and Aarts, E. (1987). *Simulated annealing: Theory and applications*. Springer Science & Business Media, Dordrecht, Netherlands.

van Overschee, P. and de Moor, B. (1995). *Subspace identification for linear systems: Theory-Implementation-Application*. Kluwer Academic Publishers, Boston/London/Dordrecht.

Vanik, M. W., Beck, J. L., and Au, S. K. (2000). Bayesian probabilistic approach to structural health monitoring. *Journal of Engineering Mechanics*, 126(7):738–745.

Ventura, C., Andersen, P., Mevel, L., and Döhler, M. (15-17 July, 2014). Structural health monitoring of the Pitt River Bridge in British Columbia, Canada. In *Proceedings of the WCSCM - 6th World Conference on Structural Control and Monitoring*. Barcelona, Spain.

Viefhues, E., Döhler, M., Hille, F., and Mevel, L. (2020). Fault detection for linear parameter varying systems under changes in the process noise covariance. In *Proceedings of the IFAC - 21st World Congress of the International Federation of Automatic Control*, pages 1–6, Berlin, Germany.

Wenzel, H. (2009). *Health monitoring of bridges*. Wiley, Chichester, United Kingdom.

Worden, K. and Dulieu-Barton, J. M. (2004). An overview of intelligent fault detection in systems and structures. *Structural Health Monitoring*, 3(1):85–98.

Worden, K., MANSON, G., and FIELLER, N. (2000). Damage detection using outlier analysis. *Journal of Sound and Vibration*, 229(3):647–667.

Yam, L. H., Leung, T. P., Li, D. B., and Xue, K. Z. (1996). Theoretical and experimental study of modal strain analysis. *Journal of Sound and Vibration*, 191(2):251–260.

Yan, A.-M. and Golinval, J.-C. (2006). Null subspace-based damage detection of structures using vibration measurements. *Mechanical Systems and Signal Processing*, 20(3):611–626.

Yan, A.-M., Kerschen, G., de Boe, P., and Golinval, J.-C. (2005a). Structural damage diagnosis under varying environmental conditions—Part I: A linear analysis. *Mechanical Systems and Signal Processing*, 19(4):847–864.

Yan, A.-M., Kerschen, G., de Boe, P., and Golinval, J.-C. (2005b). Structural damage diagnosis under varying environmental conditions—Part II: Local PCA for non-linear cases. *Mechanical Systems and Signal Processing*, 19(4):865–880.

Yang, J. and Soh, C. K. (1997). Structural optimization by genetic algorithms with tournament selection. *Journal of computing in civil engineering*, 11(3):195–200.

Yao, L., Sethares, W. A., and KAMMER, D. C. (1993). Sensor placement for on-orbit modal identification via a genetic algorithm. *AIAA journal*, 31(10):1922–1928.

Yi, T.-H. and Li, H.-N. (2012). Methodology developments in sensor placement for health monitoring of civil infrastructures. *International Journal of Distributed Sensor Networks*, 8(8).

Yi, T.-H., Li, H.-N., and Wang, C.-W. (2016). Multiaxial sensor placement optimization in structural health monitoring using distributed wolf algorithm. *Structural Control and Health Monitoring*, 23(4):719–734.

Yi, T.-H., Li, H.-N., and Zhang, X.-D. (2015). Health monitoring sensor placement optimization for canton tower using immune monkey algorithm. *Structural Control and Health Monitoring*, 22(1):123–138.

Yin, S.-H. and Tang, C.-Y. (2011). Identifying cable tension loss and deck damage ina cable-stayed bridge using a moving vehicle. *Journal of Vibration and Acoustics*, 133(2):021007.

Yuen, K. V., Katafygiotis, L. S., Papadimitriou, C., and Mickleborough, N. C. (2001). Optimal sensor placement methodology for identification with unmeasured excitation. 123(4):677–686.

Yuen, M. (1985). A numerical study of the eigenparameters of a damaged cantilever. *Journal of Sound and Vibration*, 103(3):301–310.

Zárate, B. A. and Caicedo, J. M. (2008). Finite element model updating: Multiple alternatives. *Engineering Structures*, 30(12):3724–3730.

Zhang, Q. W., Chang, T. Y. P., and Chang, C. C. (2001). Finite-element model updating for the Kap Shui Mun cable-stayed bridge. *Journal of Bridge Engineering*, 6(4):285–293.

Zheng, B., Yu, K., Liu, S., and Zhao, R. (2020). Interval model updating using universal grey mathematics and Gaussian process regression model. *Mechanical Systems and Signal Processing*, 141:106455.

Zhou, G. D., Yi, T. H., and Li, H. N. (2014). Sensor placement optimization in structural health monitoring using cluster-in-cluster firefly algorithm. *Advances in Structural Engineering*, 17(8):1103–1115.

Zhou, S. and Song, W. (March, 2016). Updating finite element models considering environmental impacts. In *Proceedings of SPIE 9803*, Smart Structures and Materials + Nondestructive Evaluation and Health Monitoring, page 98031R, Las Vegas, United States. International Society for Optics and Photonics.

Zhou, W., Li, S., and Li, H. (2016). Damage detection for smc benchmark problem: A subspace-based approach. *International Journal of Structural Stability and Dynamics*, 16(04):1640025.

Zimmerman, D. C. and Kaouk, M. (1992). Eigenstructure assignment approach for structural damage detection. *AIAA journal*, 30(7):1848–1855.

Zouari, R., Mevel, L., and Basseville, M. (6-8 July, 2009). Subspace-based damping monitoring. In *Proceedings of the IFAC - 15th World Congress of the International Federation of Automatic Control*, volume 42, pages 850–855, Saint Malo, France.